Flow control of boundary layers and wakes

by

Jens H. M. Fransson

December 2003
Technical Reports from
Royal Institute of Technology
KTH Mechanics
SE-100 44 Stockholm, Sweden

Akademisk avhandling som med tillstånd av Kungliga Tekniska Högskolan i Stockholm framlägges till offentlig granskning för avläggande av teknologie doktorsexamen fredagen den 12 december 2003 kl 10.15 i Kollegiesalen, Administrationsbyggnaden, Kungliga Tekniska Högskolan, Vallhallavägen 79, Stockholm.

Universitetsservice US–AB, Stockholm 2003

Jens H. M. Fransson 2003, **Flow control of boundary layers and wakes**
KTH Mechanics, SE-100 44 Stockholm, Sweden

Abstract

Both experimental and theoretical studies have been considered on flat plate boundary layers as well as on wakes behind porous cylinders. The main thread in this work is control, which is applied passively and actively on boundary layers in order to inhibit or postpone transition to turbulence; and actively through the cylinder surface in order to effect the wake characteristics.

An experimental set-up for the generation of the asymptotic suction boundary layer (ASBL) has been constructed. This study is the first, ever, that report a boundary layer flow of constant boundary layer thickness over a distance of 2 metres. Experimental measurements in the evolution region, from the Blasius boundary layer (BBL) to the ASBL, as well as in the ASBL are in excellent agreement with boundary layer analysis. The stability of the ASBL has experimentally been tested, both to Tollmien–Schlichting waves as well as to free stream turbulence (FST), for relatively low Reynolds numbers (Re). For the former disturbances good agreement is found for the streamwise amplitude profiles and the phase velocity when compared with linear spatial stability theory. However, the energy decay factor predicted by theory is slightly overestimated compared to the experimental findings. The latter disturbances are known to engender streamwise elongated regions of high and low speeds of fluid, denoted streaks, in a BBL. This type of spanwise structures have been shown to appear in the ASBL as well, with the same spanwise wavelength as in the BBL, despite the fact that the boundary layer thickness is substantially reduced in the ASBL case. The spanwise wavenumber of the optimal perturbation in the ASBL has been calculated and is $\beta = 0.53$, when normalized with the displacement thickness. The spanwise scale of the streaks decreases with increasing turbulence intensity (Tu) and approaches the scale given by optimal perturbation theory This has been shown for the BBL case as well.

The initial energy growth of FST induced disturbances has experimentally been found to grow linearly as $Tu^2 Re_x$ in the BBL, the transitional Reynolds number to vary as Tu^{-2}, and the intermittency function to have a relatively well-defined distribution, valid for all Tu.

The wake behind a porous cylinder subject to continuous suction or blowing has been studied, where amongst other things the Strouhal number (St) has been shown to increase strongly with suction, namely, up to 50% for a suction rate of 2.5% of the free stream velocity. In contrast, blowing shows a decrease of St of around 25% for a blowing rate of 5% of the free stream velocity in the considered Reynolds number range.

Descriptors: Laminar-turbulent transition, asymptotic suction boundary layer, free stream turbulence, Tollmien–Schlichting wave, stability, flow control, cylinder wake.

Preface

This doctoral thesis in fluid mechanics is a paper-based thesis of both experimental and theoretical character. The thesis treats of boundary layers on flat plates as well as wakes behind porous cylinders. The main thread in the thesis is control, which is applied passively and actively on boundary layers in order to inhibit or postpone transition to turbulence; and actively through the cylinder surface in order to effect the wake characteristics. The thesis is divided into two parts in where the first part, starting with an introductory essay, is an overview and summary of the present contribution to the field of fluid mechanics. The second part consists of ten papers, which are adjusted to comply with the present thesis format for consistency. However, their contents have not been changed compared to published or submitted versions except for minor refinements. In chapter 7 of the first part in the thesis the respondent's contribution to all papers are stated.

November 2003, Stockholm
Jens Fransson

You asked, 'What is this transient pattern?' If we tell the truth of it, it will be a long story; It is a pattern that came up out of an ocean and in a moment returned to that ocean's depth.

Omar Khayyam (1048–1131)

Contents

Part I

Overview and summary

CHAPTER 1

Introduction

–You push the ends of the seat belt together and you hear the familiar click. You are ready for take off. The cabin attendant walks through the aisle showing the safety equipment while the plane taxes of to the runway. You are full of expectations but also somewhat tense for the trip and you look out through the window. The rain rattles on the wing. You feel the acceleration pulling you back into your seat when the plane speeds up and rises. On twenty thousand metres the plane levels out and the seat belt lights are switched off. The air-hostess serves you the longed-for single malt and you lean back into your seat. Within a few minutes you doze off. The plane flies smoothly through air and rain. How is it possible for this huge machine to rise up into the sky and fly you to your destination?

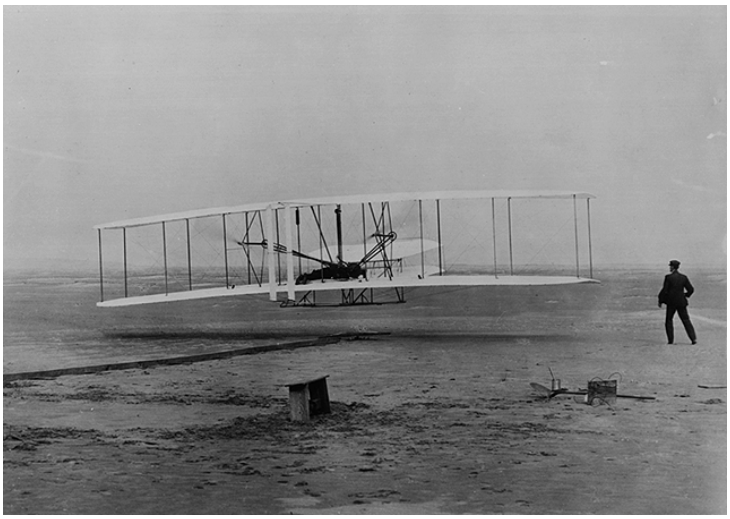

FIGURE 1.1. On December 17, 1903, in Kitty Hawk, North Carolina, Orville Wright performed the first ever airplane flight and this was the breakthrough to airplane development. The image was downloaded from http://www.wam.umd.edu/.

The explanation of the ability of an airplane to fly is the lift force. Feeling the lift force is an event you most likely faced as a kid. You probably remember how you stretched out your arm through the car window, and how you by tilting your hand could feel an upward or downward pointing force. In this context the tilting angle of your hand is usually denoted angle of attack, whereas your hand can be seen as a wing. The wellspring of the lift force on your hand is caused by air accelerating around your thumb which gives rise to a low pressure, whilst it decelerates along the palm causing a high pressure. This pressure difference creates an upward pointing force, which is the lift force. When dad accelerated the car you immediately felt how your hand reacted faster and stronger on a small change of tilting angle. One can experimentally and theoretically show that the velocity in square of the car is proportional to the lift force, which explains the reaction of above acceleration. Exchanging a kids arm with a real wing, specially designed to cause high lift, on both sides of the car you almost have an airplane.

–Suddenly the plane is shaking and the ride feels extremely bumpy. You wake up with your drink all over your trousers. Through the window you hardly see the wing tip. Dark clouds and heavy rain are all that can be distinguished. The seat belt lights are turned on and the captain instructs you to remain seated. What is happening?

Strictly speaking there are two air flow states, laminar and turbulent. The former can be described as smooth and regular flow like if the air was moving in a series of layers sliding over one another without mixing. The latter state is a flow in which the velocity at any point fluctuates irregularly and there is continual mixing rather than a steady flow pattern. In other words, laminar flow produces smooth and regular flying conditions whilst turbulent flow is associated with a rough and irregular condition. Further, turbulence is a multi-eddy scale flow, ranging from swirling air of hundreds of metres in scale to the tiny *Kolmogorov*[1] scale (i.e. the smallest length scale of eddies in a turbulent flow) only a few microns in the perspective of a flying commercial airliner.

Your intuition of a rough flight is easier justified with the presence of bad weather, but the fact is that turbulence can be present even in clear visible air. The bumpy feeling caused by turbulence is in everyday language often denoted 'air-pockets'. Literally speaking this denomination is a myth. You may draw the parallel when sitting in a speedy boat on heavy sea. The waves appearing from all directions makes you jump around just as an airplane does in strong turbulent air. Thus, similarly to the boat surrounded with water without any 'water-pockets' you have air everywhere preventing you from falling down from the sky. The only difference in the parallel above is that in air the large velocity and pressure fluctuations are invisible, in contrary to the surface water waves that you are able to both see and feel.

[1] Andrej N. Kolmogorov (1903-1987), a soviet mathematician.

There are many possible reasons that can make turbulence appear in an atmospheric perspective, such as heated earth (due to sun exposure) which makes warm air rise due to increasing pressure and a vertical movement of air is caused, mountainous terrain which makes the air unstable simply due to its geometrical presence, jet streams due to their high velocities (high velocity flows are more susceptible to transition), or meteorological reasons.

However, there is no universal theory for how turbulence appears. What is a common consensus is that the turbulence originates from some instability in the laminar state that grows in amplitude and eventually causes transition to turbulence. Natural occurring phenomena in fluid dynamics are complex and appears irregularly why these favourably are investigated in a more controlled manner and in a simpler configuration, such as on a flat plate positioned in a wind tunnel. The present thesis includes theoretical as well as experimental investigations on the transition process from laminar to turbulent state.

CHAPTER 2

Boundary layer transition

There are plenty of practical applications where fluid dynamics is involved. Knowledge in this area is preferred in many design studies on for instance on- and off shore vehicles, airplanes, and space shuttles. A common interest in vehicle design is to reduce drag in order to minimize the fuel consumption and/or to be able to go faster as the case of Formula 1 cars.

When studying big streamlined vehicles (with a lot of surface), such as an airliner, the major contribution to the drag comes from the skin friction. In figure 2.1a) the skin friction coefficient (c_f) over a flat plate (with zero pressure gradient) is plotted versus the Reynolds number (Re_x). These two non-dimensional quantities are defined as

$$c_f = \frac{\tau_w}{q} \quad ; \qquad Re_x = \frac{xU_\infty}{\nu}. \tag{2.1}$$

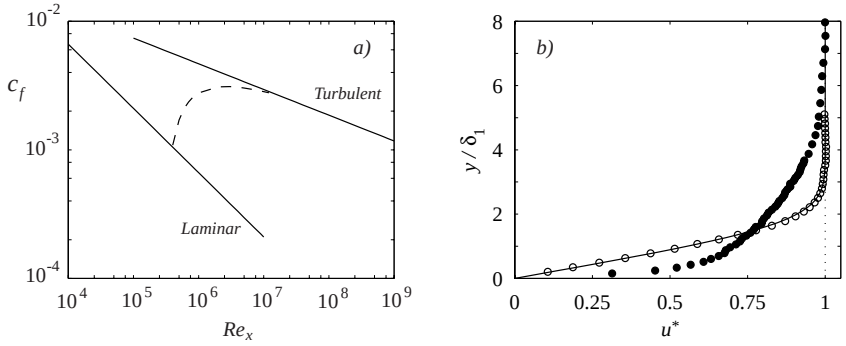

FIGURE 2.1. Laminar versus turbulent boundary layer. a) Skin friction coefficient versus Re_x. The dotted line describes a theoretical transition and is the Prandtl-Schlichting formula. b) Laminar- ($\circ$; $Re_x = 1.0 \times 10^5$) and turbulent ($\bullet$; $Re_x = 7.3 \times 10^5$) mean velocity profiles. $u^* = u/U_\infty$. Solid line is the theoretical Blasius profile.

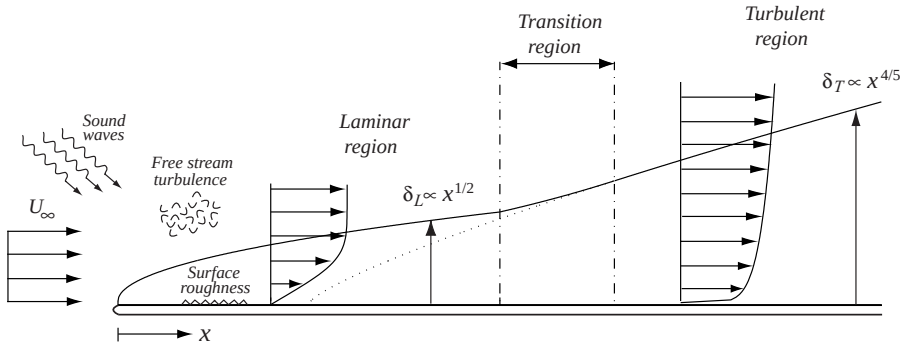

FIGURE 2.2. Sketch of a flat plate boundary layer.

In the expressions above τ_w is the wall shear stress, q the dynamic pressure, U_∞ is the free stream velocity, ν the kinematic viscosity, and x the downstream distance from the leading edge. As can be seen in figure 2.1a) for large Re_x-values the difference in skin friction between laminar and turbulent boundary layers becomes significant, more precisely, the skin friction may be reduced by one order of magnitude if transition can be inhibited. Even if this is not possible there is a lot to gain if one may succeed to postpone the transition, since the two curves are diverging. Figure 2.1b) shows typical wall normal distributions of the mean streamwise velocity component for a laminar (low Re_x) and a turbulent (high Re_x) measured profile.

Roughly speaking there are two accepted routes of transition to turbulence in boundary layer flows, with totally different driving physical mechanisms (cf. Kachanov 1994, for a thorough review). These are the classical scenario of exponential character and the by–pass transition scenario. In the present chapter these two scenarios are presented both theoretically and experimentally with typical examples, namely the Tollmien–Schlichting wave and the free stream turbulence induced transition scenarios, in order to elucidate their differences. Real life applications of fluid mechanics are usually of complex nature why many fundamental phenomena are studied in detail on the most simplified configuration one can imagine, namely a flat plate. In figure 2.2 a sketch of the boundary layer on a flat plate is shown. In the case of zero pressure gradient the laminar boundary layer grows as $x^{1/2}$ whilst the turbulent grows as $x^{4/5}$; this is indicated in the figure. The natural scenario is that a laminar boundary layer starts to grow from the leading edge. The receptivity process at the leading edge, which may constitute of one or a combination of the shown primary disturbance sources (namely sound waves, surface roughness, and free stream

turbulence), causes an instability in the laminar boundary layer. This disturbance grows in space and time to some amplitude, where it becomes hostile to secondary instabilities, and transition to turbulence takes place. Note, that a reverse scenario may also take place in boundary layer flows even though this type of process is more infrequent, an example of relaminarization is a turbulent boundary layer that is exposed to a steep favourable pressure gradient, i.e. an accelerated free stream (see e.g. Narasimha & Sreenivasan 1973; Parsheh 2000).

2.1. Tollmien–Schlichting wave scenario

For low environmental disturbances the transition scenario from laminar to turbulent flow on a flat plate boundary layer is rather well understood. This class of transition starts with instability waves that are generated in the receptivity process taking place close to the leading edge. The initial growth of these waves may be described by Fourier modes $\propto \mathrm{e}^{i(\alpha x+\beta z-\omega t)}$, where for spatially growing waves the streamwise wave number α is complex and the angular frequency ω and the spanwise wave number β are real. When assuming such a mode, in a two-dimensional parallel base flow, the Navier–Stokes equations linearized

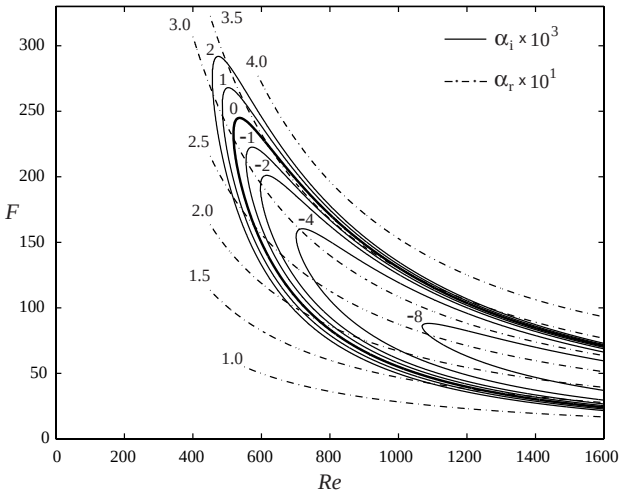

FIGURE 2.3. Spatial stability curves for two-dimensional waves in a Blasius boundary layer. Solid lines are for constant imaginary parts of the streamwise wave number (α_i) and dash-dotted for constant real parts (α_r). The bold solid line is the neutral stability curve. The displacement thickness (δ_1) is the characteristic length scale.

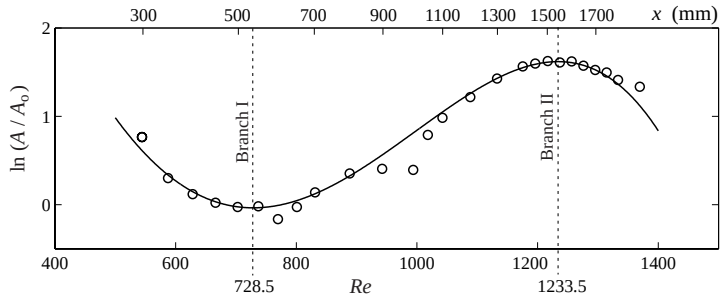

FIGURE 2.4. Amplitude evolution of the TS-wave at $F = 100$. In this and subsequent figures the symbols are experimental results, and solid lines are the OS-solution of the Blasius profile.

about the base state give rise to the well known Orr–Sommerfeld (OS) and Squire (S) equations according to

$$\left[(-i\omega + i\alpha U)(\mathcal{D}^2 - k^2) - i\alpha U'' - \frac{1}{Re}(\mathcal{D}^2 - k^2)^2\right]\hat{v} = 0 \ , \tag{2.2}$$

and

$$\left[(-i\omega + i\alpha U) - \frac{1}{Re}(\mathcal{D}^2 - k^2)\right]\hat{\Omega} = -i\beta U'\hat{v} \ , \tag{2.3}$$

respectively. Here $\mathcal{D} = \partial/\partial y$, $k^2 = \alpha^2 + \beta^2$ and $\hat{v}$ and Ω denote the wall normal amplitude and vorticity functions of the eigenmode. From the continuity and the vorticity equations the streamwise and spanwise perturbation components may be derived (see for instance Fransson 2001, for a full derivation of above equations). Solution procedures for this semi-coupled system may be found in e.g. Drazin & Reid (1981); Schmid & Henningson (2001).

These waves grow/decay exponentially (according to the ansatz) and the critical Reynolds number is, according to *Squire's theorem*, obtained for a two-dimensional wave (i.e. for $\beta \equiv 0$) and is called a Tollmien–Schlichting (TS) wave. In figure 2.3 the stability diagram (based on linear parallel theory) is given for the Blasius profile. The solid lines are contours of the growth factor (α_i) where the bold solid line shows the neutral stability curve, i.e. the contour line of $\alpha_i = 0$. The dash-dotted lines correspond to contour lines of constant wave number (α_r). Here, the Reynolds number (Re) is based on the displacement thickness (δ_1), and F is the non-dimensionalized frequency defined as

$$F = (\omega\nu/U_\infty^2) \times 10^6 \ .$$

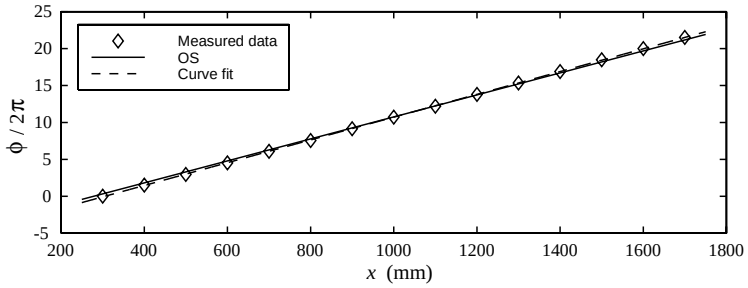

FIGURE 2.5. Phase distribution in the streamwise direction at $F = 100$.

If a TS-wave in a Blasius boundary layer reaches high enough amplitude ($\gtrsim$1% of U_∞), three-dimensional waves and vortex formations develop (still laminar) that give rise to the appearance of turbulent spots which merge and bring the whole flow into a fully turbulent one. The first successful wind tunnel experiment on TS-waves was carried out and reported by Schubauer & Skramstad (1948). However, these results were not in full agreement with theory and for long the discrepancy between linear parallel stability theory and experiments were believed to be due to the non-parallel effect of a growing boundary layer. However, Fasel & Konzelmann (1990) found out through direct numerical integration of the Navier–Stokes equations that this effect is quite small and that it hardly influences the amplitude and phase distributions. Later, parabolized stability calculations by Bertolotti (1991) showed that the non-parallel effect becomes significantly stronger for three-dimensional disturbances. Finally, the experiments by Klingmann *et al.* (1993), performed with a special designed asymmetric leading edge (in order to get rid of the pressure suction peak), could show excellent agreement with non-parallel theory, which is close to the parallel theory for two-dimensional disturbances.

In the following controlled stability experiments, where the studied disturbance is generated with a known frequency, together with theoretical results are shown. In figure 2.4 the amplitude distribution of the TS-wave at $F = 100$ is shown (in this and following figures A corresponds to the maximum measured amplitude in the profile). The experiment ($\circ$-symbols) shows good agreement with linear parallel theory (solid line), where both the first and the second branch are well captured by the experiment. The TS-wave is generated at $x = 205$ mm and decays until reaching the first branch at approximately Re=728.5. From there on it grows in amplitude until reaching the second branch at approximately Re=1233.5 where it starts to decay.

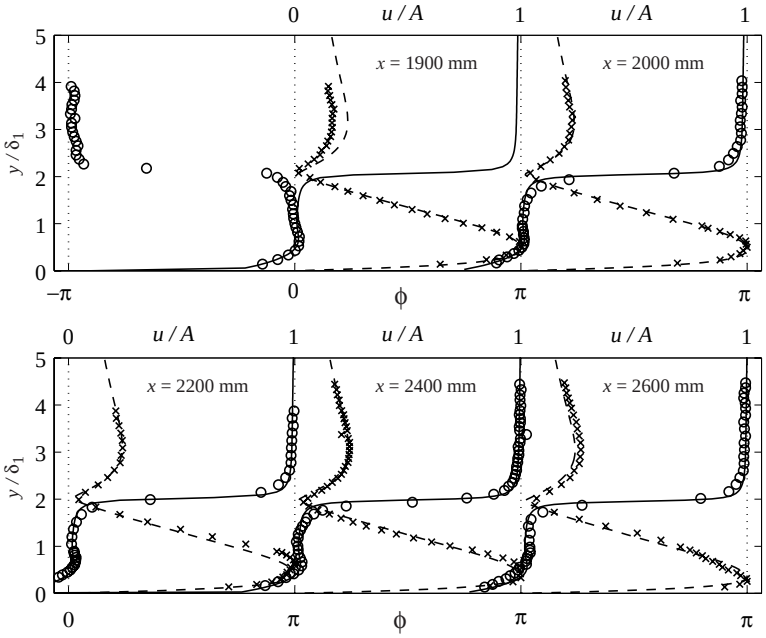

FIGURE 2.6. Amplitude- and phase distribution profiles for $F = 59$ at different x-positions. ($\times$)-symbols and dashed lines correspond to measured and theoretical amplitude profiles respectively. ($\circ$)-symbols and solid lines are the corresponding phase profiles.

The phase velocity ($c = \omega/\alpha_r$) of the wave can be determined simply by determining the real part of the wave number (α_r) since the angular frequency (ω) is known. In figure 2.5 the phase distribution in the streamwise direction is plotted. The phase is taken at the wall-normal distance above the plate where the inner maximum amplitude appears. α_r is then determined by calculating the phase gradient ($\partial\phi/\partial x$), and it is seen to be constant throughout the whole investigated downstream distance. The symbols are experimental data, the solid curve is the OS-solution, and the dashed line is the curve fit for the determination of the gradient. This curve fit gives us a phase velocity of $0.34U_\infty$ compared with the theoretical based on the Blasius profile of $0.36U_\infty$.

In figure 2.6 the amplitude distribution profiles are plotted for F=59 at five different downstream positions. The first x-position closest to the disturbance source, in fact only 50 mm from the source (here located at x=1850 mm or at Re=1350), is not fully developed in the upper part of the profile when compared to the OS-solution. However, from the second x-position the agreement is excellent in this part. Further, in figure 2.6 the corresponding phase

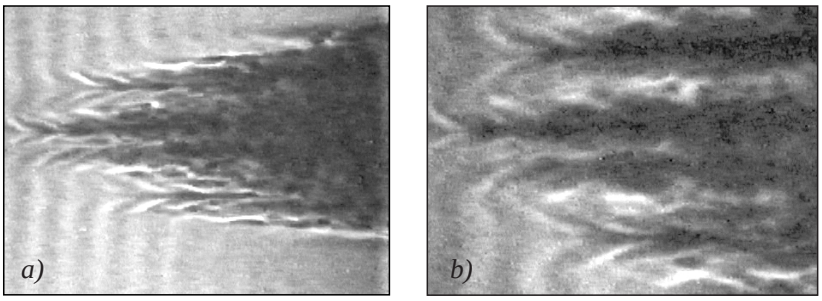

FIGURE 2.7. Smoke visualization of Tollmien–Schlichting wave breakdown. The flow is from left to right. b) is a blow up of a section in a). $U_\infty = 7.5$ m/s, F=168, $u_{TS}/U_\infty = 0.8\%$, and $\lambda_x \approx 2.9$ cm.

distribution profiles are also plotted, and they clearly show the phase shift of π radians which can be shown to appear where $\partial\hat{v}/\partial y$ changes sign, i.e. at the wall-normal amplitude ($\hat{v}$) maxima. The experimental data are in good agreement with the OS-solution (solid line).

2.1.1. *Flow visualization of TS-wave breakdown*

The non-linear breakdown of TS-waves have been mapped out during the last decades and can today be considered known (cf. Herbert 1983; Kachanov 1994, for reviews on the topic). When the amplitude of the TS-wave is large enough ($\sim 1\%$ in u_{rms} of U_∞) the wave becomes three-dimensional. Klebanoff *et al.* (1962) observed a spanwise scale of the same order as the streamwise wavelength which later became known as the K-type transition after Klebanoff but also fundamental since the frequency of the secondary spanwise periodic matched the original two-dimensional TS-wave. In this scenario Λ-shaped vortices appear in the non-linear stage that are aligned in both the streamwise and spanwise directions. Another "similar" breakdown was observed by Kachanov *et al.* (1977) that differs in the secondary frequency which is half of the original TS-wave frequency. This type is known as the N-type[1] transition after Novosibirsk or the subharmonic scenario, in where the Λ-shaped structures are arranged in a staggered pattern. In figure 2.7 a smoke visualization is shown of a TS-wave dominated transition scenario. The breakdown seams to occur localized in the spanwise direction which is due to the nature of the two-dimensional wave generating device, namely a vibrating ribbon, that provides the wave with a higher amplitude in the centre. In figure 2.7b) it is possible to discern that a K-type transition scenario is present in the experiment, which is to be expected at this high initial amplitude of the TS-wave (u_{TS}), namely 0.8% of U_∞.

[1]Note that this type of transition is sometimes referred to as H-type after Herbert (1983).

2.2. Free stream turbulence scenario

It is well known that for the Blasius boundary layer free stream turbulence (FST) induces disturbances into the boundary layer which give rise to streamwise oriented structures of low and high speed fluid (see e.g. Kendall 1985; Westin 1997; Jacobs & Durbin 2001; Matsubara & Alfredsson 2001; Brandt & Henningson 2002; Fransson & Alfredsson 2003*a*; Brandt 2003, for thorough investigations of such a flow). These structures grow in amplitude and establish a spanwise size which is of the order of the boundary layer thickness far away

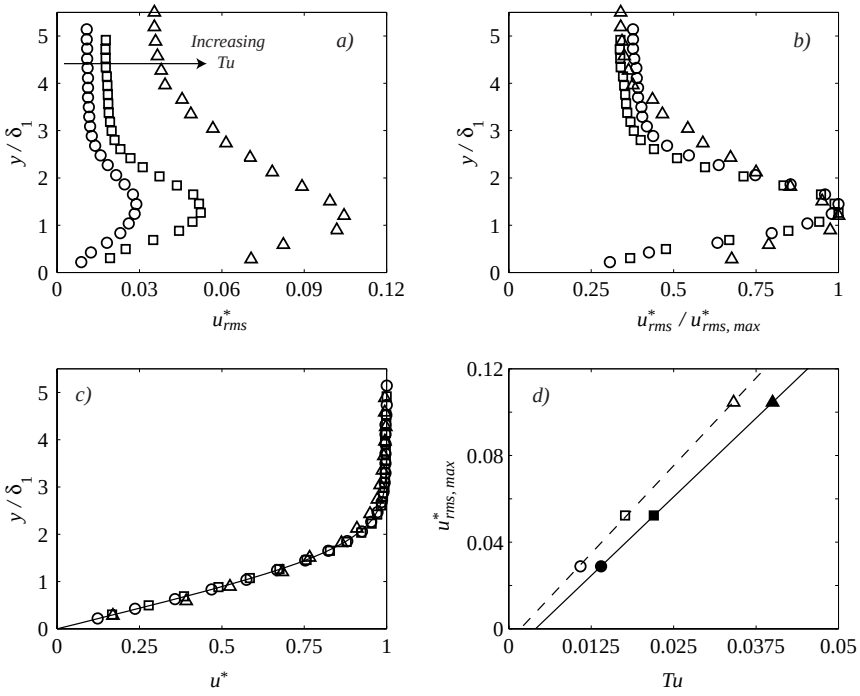

FIGURE 2.8. Wall normal perturbation- and mean velocity profiles for different Tu-levels at $Re = 544$ (based on δ_1) or $Re_x = 10^5$, $u^* = u/U_\infty$ and $u^*_{rms} = u_{rms}/U_\infty$. a) and c) show the perturbation- and the mean velocity profile for different Tu. b) correspond to the data in a) but normalized to unity and d) shows the normalization value versus the local (open symbols) and the leading edge (filled symbols) Tu-value, respectively. (◯) $Tu = 1.4\%$, (□) $Tu = 2.2\%$, and (△) $Tu = 4.0\%$.

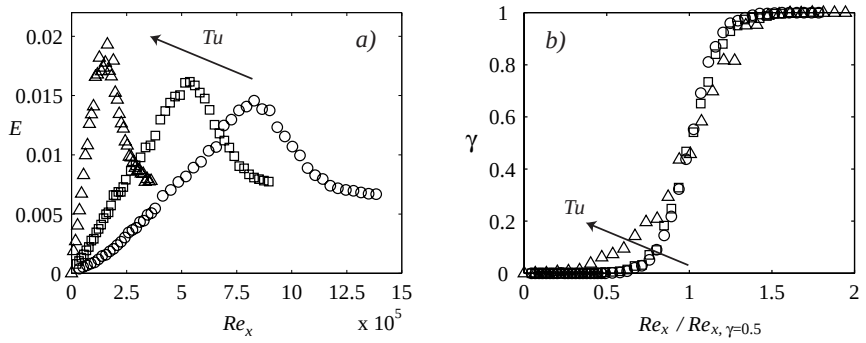

FIGURE 2.9. a) Energy growth ($E = u_{rms}^2/U_\infty^2$) as function of Re_x for three different Tu-levels. Measurements are made at y/δ_1=1.4. b) The corresponding intermittency distribution of the data in a) versus Re_x normalized with ditto for $\gamma = 0.5$. ($\bigcirc$) $Tu = 1.4\%$, ($\square$) $Tu = 2.2\%$, and ($\triangle$) $Tu = 4.0\%$.

from the leading edge. When the streaks reach a certain amplitude they break down to turbulence, probably through a secondary instability mechanism (see e.g. Andersson *et al.* 2001). This type of boundary layer disturbance was originally called the breathing mode by Klebanoff (1971), since the wall-normal disturbance profile resembles that which would result from a locally continuous thickening and thinning of the boundary layer edge (see Taylor 1939). However, this mode is nowadays recognized as the Klebanoff mode which was proposed by Kendall (1985), and can be viewed as one scenario of by–pass transition (Morkovin 1969). It is a relatively rapid process by–passing the traditional TS-wave dominated transition scenario resulting in breakdown to turbulence at subcritical Reynolds numbers when compared with the predicted value by traditional theory. Nonlinear theories were tested (see e.g. Orszag & Patera 1983) in order to find a theory that matched experimental results. However, the nonlinear terms of the Navier–Stokes equations can be shown not to be part of the growth mechanism (see e.g. Drazin & Reid 1981). A possible mechanism governing this type of transition scenario is the transient growth, i.e. an algebraic growth of the disturbance energy until viscosity becomes significant which eventually causes an exponential decay of the energy.

Algebraic growth is a consequence of the non-normality of the governing differential operator: as the normal modes are not orthogonal, constructive and destructive interference may give rise to transients before the asymptotic state described by modal theory sets in (Schmid & Henningson 2001). Butler & Farrell (1992) pioneered the study of optimal perturbations (OP) in shear

flows; their findings and those of later workers indicate that the initial conditions which maximize perturbation kinetic energy are streamwise-oriented vortices which produce streaks (variations in the streamwise perturbation velocity). Ever since the transient growth and its linear physical mechanism was described by Ellingsen & Palm (1975), and Landahl (1980) a number of works has been done on the topic. Among the earlier ones are e.g. Hultgren & Gustavsson (1981), Gustavsson (1991), Reddy & Henningson (1993), and Trefethen *et al.* (1993). For more recent publications on the subject see e.g. Luchini (2000), Reshotko (2001), and Andersson *et al.* (2001). A physical explanation for this was advanced by Landahl (1980), who noted that such initial configurations of perturbation velocity are ideally suited to 'lift-up' low-speed fluid into relatively faster flow and vice versa, exchanging momentum and generating a streak.

In figure 2.8 streamwise disturbance and mean velocity wall normal distributions are plotted for different Tu-levels. In figure 2.8a) it is clear that the presence of higher FST intensity causes a higher disturbance level inside as well as outside the boundary layer, without affecting the mean velocity (cf. figure 2.8c). It is both the Reynolds number and the Tu-level that sets the state, i.e. whether the flow is in the sub-transitional, transitional, or in the post-transitional state. At least up to the transitional state one can expect a self similar disturbance profile through the boundary layer. Thereafter, the disturbance peak moves towards the wall and the disturbance level spreads out more in the entire boundary layer, this may be observed in figure 2.8b). An interesting observation is that the level of the disturbance peak inside the boundary layer increases linearly with Tu which is shown in figure 2.8d), where solid lines are curve fits to the data (see caption for more information).

In figure 2.9a) the energy distribution versus the downstream distance for the three different Tu-levels are shown. It is seen that the disturbance (u_{rms}/U_∞) reaches levels around 14% for Tu=4.0% before it starts to decrease, which is connected to the transitional nature of the boundary layer. It should be observed that this decrease has nothing to do with the exponential viscous decay mentioned earlier in connection with transient growth, which is a purely linear mechanism. What is observed in figure 2.9a) is the algebraic growth followed by transition. That the peak becomes smaller with decreasing Tu is probably connected to the relation between turbulent scales in the free stream (that are different for all three cases), the disturbance level, the streak spacing, and the boundary layer thickness. Note, also that the energy seems to asymptote to a constant level around $E = 0.007$ independent of the Tu-level after reaching the maximum value. The intermittency function for the three different cases in a) are shown in figure 2.9b). The maximum (in figure 2.9a) is closely related to the point of γ=0.5, i.e. the point where the flow alternatively consists of laminar portions and turbulent spots which explains the high u_{rms} value. In a) it is seen that the higher the Tu the smaller the Re_x for which

the maximum occurs, and figure 2.9b) shows that the relative extent of the transitional zone is larger for Tu=4.0% than the other two.

2.2.1. *Flow visualization of free stream turbulence breakdown*

The photograph in figure 2.10 shows the free stream turbulence induced transition scenario. The flow is from left to right and the white smoke regions have been shown to correspond to low velocity streaks (see Alfredsson & Matsubara 2000). Secondary instabilities on the streaks triggers turbulent spots according to a Dirac probability density function (cf. Dhawan & Narasimha 1957) which causes a fully turbulent flow further downstream (see the right end in the photograph). In figure 2.11 an image sequence from the primary instability, the streaks, to a fully developed turbulent spot is shown. From studying video recordings, taken in the MTL wind tunnel at KTH, of this transition scenario one may conclude that the naturally occurring secondary instability is of sinuous-type and acts on a low speed streak. This is clearly visualized in the particular sequence shown in figure 2.11.

FIGURE 2.10. Smoke visualization of free stream turbulence induced transition in a flat plate boundary layer. Flow direction is from left to right. Tu = 2.2%, U_∞ = 6 m/s, and the streamwise extent of the photograph is 220–700 mm. From Alfredsson & Matsubara (2000).

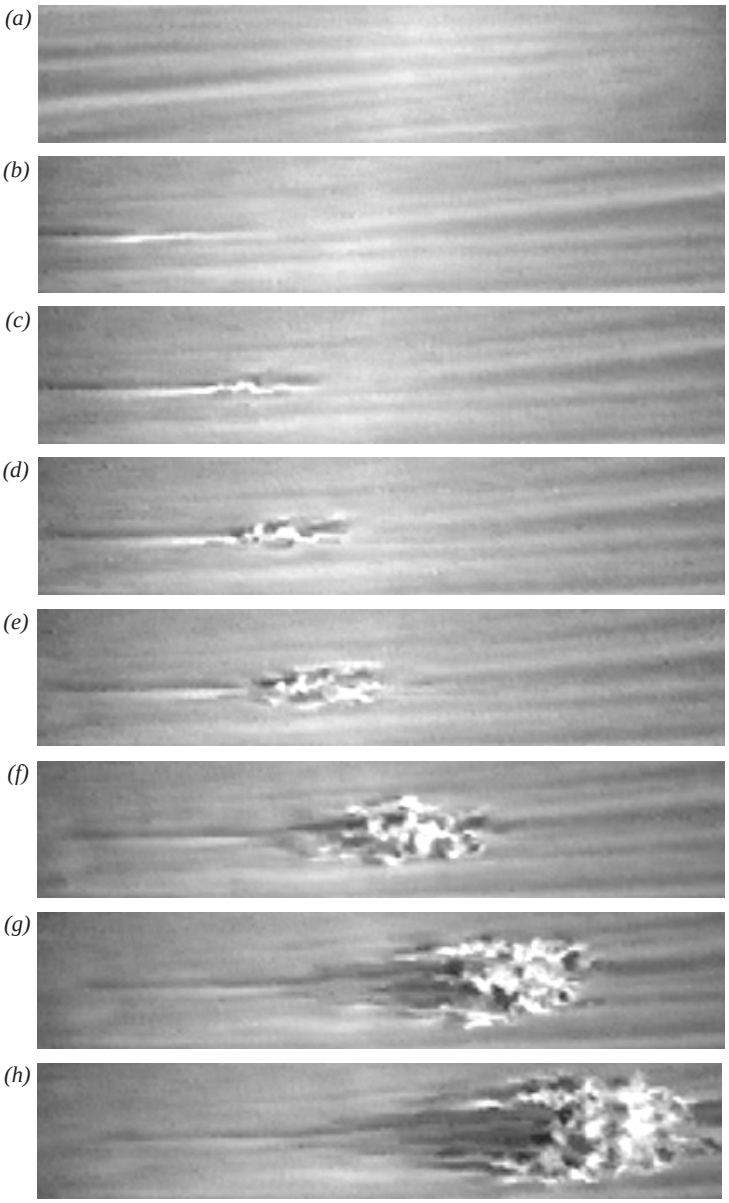

FIGURE 2.11. Smoke visualization of free stream turbulence induced transition in a flat plate boundary layer. Sequence of a typical breakdown. $U_\infty = 3$ m/s and $Tu = 2.2\%$. Note that this is a natural scenario, i.e. there is no artificial triggering on the streak.

CHAPTER 3

Boundary layer flow control

One area of significant recent interest in fluid dynamics is laminar flow control (LFC). A possible method of LFC is to apply suction at the wall. A definition of this control method is given in Joslin (1998), where it is pointed out that LFC is a method to delay the laminar-turbulent transition and not to relaminarize the flow. The energy cost is typically one order of magnitude higher in the latter case, which makes the definition appropriate since the optimal performance is not obtained (as one may believe) when the suction completely absorbs the boundary layer. The more suction that is used the steeper the velocity gradient of the boundary layer at the wall implying an increase in skin-friction. Therefore, the balance between retaining the flow laminar and keeping low energy consumption is actually the optimal performance.

The viscous drag accounts for 50% of the total drag of a commercial transport aircraft, and since the difference between the turbulent and the laminar skin-friction typically is one order of magnitude at the same Reynolds number the interest in LFC (or hybrid laminar flow control HLFC) is motivated by the reduced fuel consumption that may be achieved (see Saric 1985; Joslin 1998).

In connection to drag reduction experiments (i.e. LFC) suction through spanwise slots, porous panels and discrete holes has been applied (see e.g. Pfenninger & Groth 1961; Reynolds & Saric 1986; and MacManus & Eaton 2000 as well as Roberts *et al.* 2001, respectively). A general review of various types of surfaces and of the results achieved in wind tunnel tests is given by Gregory (1961), where pros and cons for practical applications on aircraft are discussed. The flow characteristics through laser drilled titanium sheets were investigated by Poll *et al.* (1992*b*) and was shown to be laminar, incompressible and pipe like. Poll *et al.* (1992*a*) conducted a cylinder experiment made of a similar laser drilled titanium sheet. The effect of suction was found to have a powerful effect upon cross-flow induced transition.

In an experimental and numerical study performed by MacManus & Eaton (2000) the flow physics of boundary layer suction through discrete holes was investigated. The aim was to use a realizable design and find a critical suction criterion for transonic cruise conditions. They showed that the suction may destabilize the flow by introduction of contra-rotating streamwise vortices but

that for small enough perforations ($d/\delta_1 < 0.6$) transition is not provoked by suction independent of suction velocity.

Roberts *et al.* (2001) found that two types of instability are possible when non-uniformities of suction are present. The first one is connected to the classical TS-wave that is modified due to the non-uniformities and the second one are streamwise vortices that are induced due to the non-uniformities alone. The latter instability was triggered by a finite band of suction wave numbers and the strength of this instability was shown to increase almost linearly with the amplitude of the suction non-uniformities and flow Reynolds number.

The application of optimal control theory to laminar flow control has sparked a renaissance in the field (Bewley & Liu 2001). An extensive amount of work has been done on the subject of flow control in general and the interested reader is addressed to Moin & Bewley (1994); Joslin *et al.* (1996); Joslin (1998); Lumley & Blossey (1998); Balakumar & Hall (1999); Högberg (2001); Lundell (2003), just to mention a few works on both experimental and numerical control. Pralits *et al.* (2002); Pralits (2003) and Airiau *et al.* (2003) have recently outlined methods in which modifications to the boundary layer flow by spatially-varying steady suction create conditions which stabilize linear disturbances.

The difficulties of sensing boundary layer disturbances in an aerospace setting on the one hand, and the inherent complexity of a system capable of delivering variable suction at an arbitrary position on a lifting surface on the other, pose formidable implementation challenges with technology available today. The simple case where the boundary layer is subject to uniform, constant suction, as initially envisioned by the pioneers in the field, is far more likely to find application in practice (see also Amoignon *et al.* 2003, in where shape optimization is used in order to theoretically delay transition).

3.1. Asymptotic suction boundary layer

When uniform wall-normal surface suction is applied over a large area the well known asymptotic suction profile will be reached after some evolution region. According to Schlichting (1979) it was Meridith and Griffith that first derived the asymptotic suction profile, which is an exact solution of the Navier–Stokes equations in the asymptotic limit of constant suction. Assuming that the streamwise velocity varies only in y and that the wall-normal velocity is constant the subsequent simplification of the x-momentum equation permits its direct integration to,

$$U(y) = U_\infty \left(1 - e^{y\,V_0/\nu}\right) \ , \tag{3.1}$$

where V_0 is the normal velocity applied at the wall. Physical solutions are associated only with the suction case $V_0 < 0$ (see Schlichting 1979; White 1991,

and their references for more details). Since the streamwise velocity is given by an analytic expression (3.1) the characteristic boundary layer scales may be calculated exactly and the result is shown below

$$\delta_1 = -\frac{\nu}{V_0} \; ; \qquad \delta_2 = -\frac{1}{2}\frac{\nu}{V_0} \; ; \tag{3.2}$$

$$\delta_{0.99} = \frac{\nu}{V_0}\log(0.01) = \delta_1 \log(100) \; ;$$

$$u_\tau = \sqrt{-V_0 U_\infty} \; ; \qquad \ell = \frac{\delta_1}{\sqrt{Re}} \; ;$$

where u_τ and ℓ are the viscous velocity and length scales, respectively. Re is the Reynolds number based on δ_1 and is solely determined by U_∞ and V_0 according to

$$Re = \frac{U_\infty \delta_1}{\nu} = -\frac{U_\infty}{V_0} \; . \tag{3.3}$$

Note that the exponent in equation (3.1) is equivalent to $-y/\delta_1$, and that the shape factor of the asymptotic suction boundary layer becomes exactly 2.

In figure 3.1 experimentally measured velocity profiles are shown at different Re both in a Blasius boundary layer and in three asymptotic suction boundary layers (see caption for symbols).

The measured profiles in figure 3.1 verifies the similarity profile feature that both these boundary layers possess. Iglisch[1] extended the asymptotic work by Meridith and Griffith to the non-similar flow arising before the asymptotic state establishes itself, and outlined a method for finding the velocity profile corresponding to an arbitrary suction distribution. Later, Rheinboldt (1956) developed this further to include an impermeable entry length followed by a region of uniform suction through the surface, and the problem was solved through series expansion. This impermeable entry length approach is considered below.

If an impermeable area is considered from the leading edge to where the suction starts the boundary layer will be allowed to grow and a Blasius velocity profile will be developed for a zero pressure gradient flow. In the evolution region the profile will then undergo a transformation from the Blasius state to the asymptotic suction state. This spatial evolution can from a simple approach be described through a non-dimensional evolution equation. The first step is to introduce a stream function according to

[1] See Schlichting (1979) for reference.

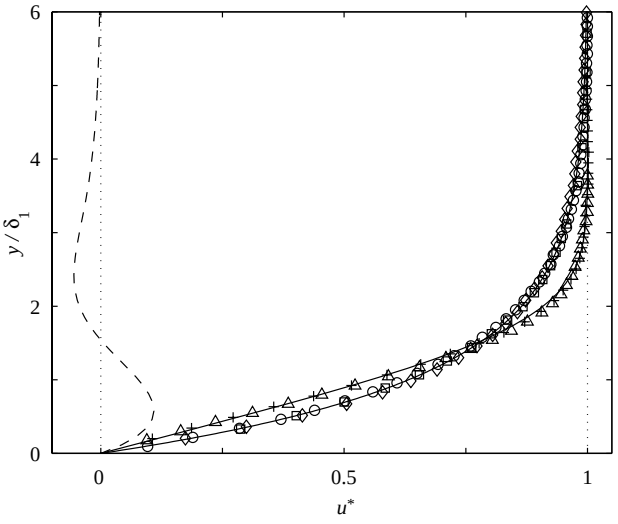

FIGURE 3.1. Velocity profiles for the Blasius and the asymptotic suction boundary layers at different Re. The Blasius profiles with (+)- and (△)-symbols correspond to $Re = 544$ and 1333, respectively. The asymptotic suction profiles are shown for $Re = 250, 357$, and 500 with the symbols (♢), (□), and (◯) respectively. The solid lines are the corresponding theoretical Blasius- and asymptotic suction profiles, and the dashed line shows the difference between the two profiles.

$$\psi = \sqrt{\nu x U_\infty} f(\xi, \eta) \ ,$$

$$\xi = x \frac{-V_0}{U_\infty} \sqrt{\frac{U_\infty}{\nu x}} \ ; \qquad \eta = y \sqrt{\frac{U_\infty}{\nu x}} \ .$$

The streamwise and normal velocity components are recovered through

$$u(\eta) = U_\infty \frac{\partial f}{\partial \eta} \qquad \text{and} \qquad v(\eta) = \sqrt{\frac{U_\infty \nu}{4x}} \left(\eta \frac{\partial f}{\partial \eta} - \xi \frac{\partial f}{\partial \xi} - f \right) \ ,$$

respectively. When applied to the boundary layer equations we get the following third order non-linear partial differential equation

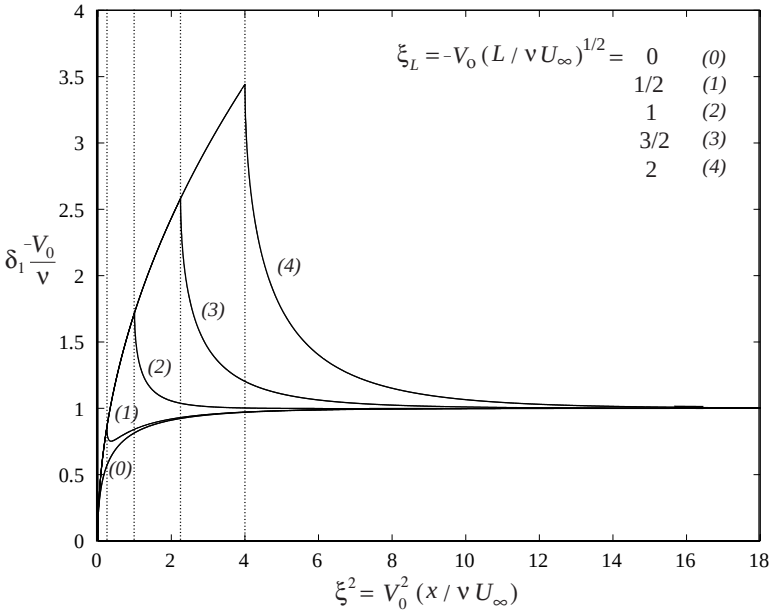

FIGURE 3.2. The displacement thickness evolution from the evolution equation (3.4) vs the downstream distance to the power of two. See text for comments.

$$\frac{\partial^3 f}{\partial \eta^3} + \frac{1}{2} f \frac{\partial^2 f}{\partial \eta^2} + \frac{1}{2} \xi \left(\frac{\partial f}{\partial \xi} \frac{\partial^2 f}{\partial \eta^2} - \frac{\partial f}{\partial \eta} \frac{\partial^2 f}{\partial \eta \partial \xi} \right) = 0, \tag{3.4}$$

with the corresponding boundary conditions

$$\left.\begin{array}{rcll} f & = & \xi & \text{(suction)} \\ \frac{\partial f}{\partial \eta} & = & 0 & \text{(no-slip)} \end{array}\right\} \quad \text{at} \quad \eta = 0 \quad \text{and} \quad \frac{\partial f}{\partial \eta} \to 1 \quad \text{as} \quad \eta \to \infty \, .$$

Along the impermeable entry length a Blasius boundary layer is assumed to develop and is given as input to the evolution equation.

In figure 3.2 the displacement thickness (δ_1) of the profiles in the evolution region is plotted. The different curves (0, 1, 2, 3, and 4) can be seen as different impermeable entry lengths shown with the dotted lines, i.e. they belong to different values of the initial length (ξ_L). Independently of the impermeable entry length all curves asymptotes to unity, which corresponds to the asymptotic suction condition (cf. expression 3.2 and note the scaling).

The skin–friction coefficient defined in expression 2.1 can in the asymptotic limit be expressed as

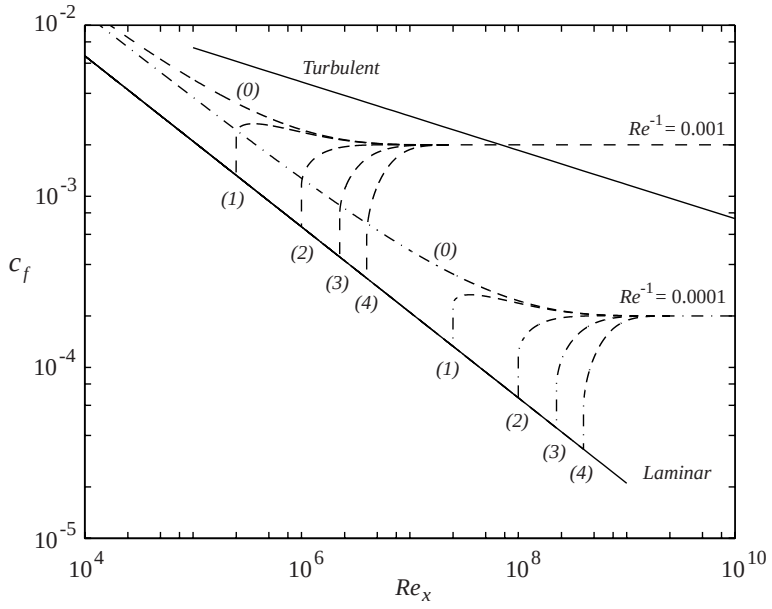

FIGURE 3.3. Skin–friction coefficient versus Re_x. Solid lines correspond to laminar and turbulent values of c_f. Dash-dotted and dashed lines correspond to the suction rates 0.01% and 0.1% of U_∞, and the different curves belong to different impermeable entry lengths (see figure 3.2).

$$c_f = \frac{\tau_w}{q} = \frac{2\nu}{U_\infty^2}\frac{\partial u}{\partial y}\Big|_{y=0} = \frac{2\nu}{U_\infty \delta_1} = 2Re^{-1} \ . \tag{3.5}$$

Note that in the asymptotic limit c_f is x independent and thus becomes constant. Another interesting observation is that c_f is viscosity independent. As mentioned earlier the more suction that is applied (at a constant U_∞) the higher becomes the c_f value, and for strong enough suction the skin–friction actually becomes larger than the turbulent boundary layer. This is illustrated in figure 3.3 where suction rates of 0.01% and 0.1% of the free stream velocity have been considered and are plotted with dash-dotted and dashed lines, respectively. The different curves belong to different impermeable entry lengths and are the same as in figure 3.2.

A fuller velocity profile compared with the Blasius, such as a turbulent profile or the exponentially asymptotic suction profile, carries more momentum close to the wall and is therefore more resistant to flow separation. This feature is of course preferable at large angles of attack of an aircraft wing in order to

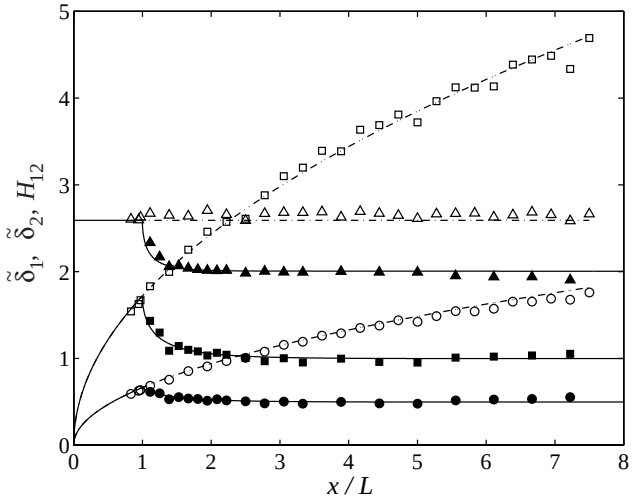

FIGURE 3.4. Experimental and theoretical results of integral boundary layer parameters. No suction (unfilled-) and suction (filled symbols). (□) $\tilde{\delta}_1$ and (○) $\tilde{\delta}_2$ are the displacement- and momentum thickness, respectively, normalized with $\frac{1}{L}(\frac{UL}{\nu})^{1/2}$. (△) H_{12} is the shape factor. $L = 360$ mm.

avoid the wing from stalling and maintain a high lift force. The draw back is the higher skin–friction that has to be balanced accordingly to meet the requirements on the wing performance.

The experimental results of the integral boundary layer parameters show excellent agreement with theoretical results (see figure 3.4). The dash-dotted lines are from the Blasius solution and the solid lines originate from the evolution equation (3.4). L is the impermeable entry length.

3.1.1. *Tollmien–Schlichting waves*

Additional terms in the familiar Orr–Sommerfeld/Squire system (eqs. 2.2–2.3) describing linear stability appear as a consequence of the normal velocity component in the asymptotic suction boundary layer, from here on these new equations are denoted the modified OS- and S-equation. However, it has long been known that the change in shape of the mean streamwise velocity profile is the main reason for the altered stability characteristics of the flow (Drazin & Reid 1981). That this change is considerable is reflected by a two order of magnitude increase in critical Reynolds number (Hocking 1975; Fransson & Alfredsson 2003*a*). In turn, this indicates that modal Tollmien–Schlichting disturbances are significant in flows where the free stream velocity dominates the suction velocity.

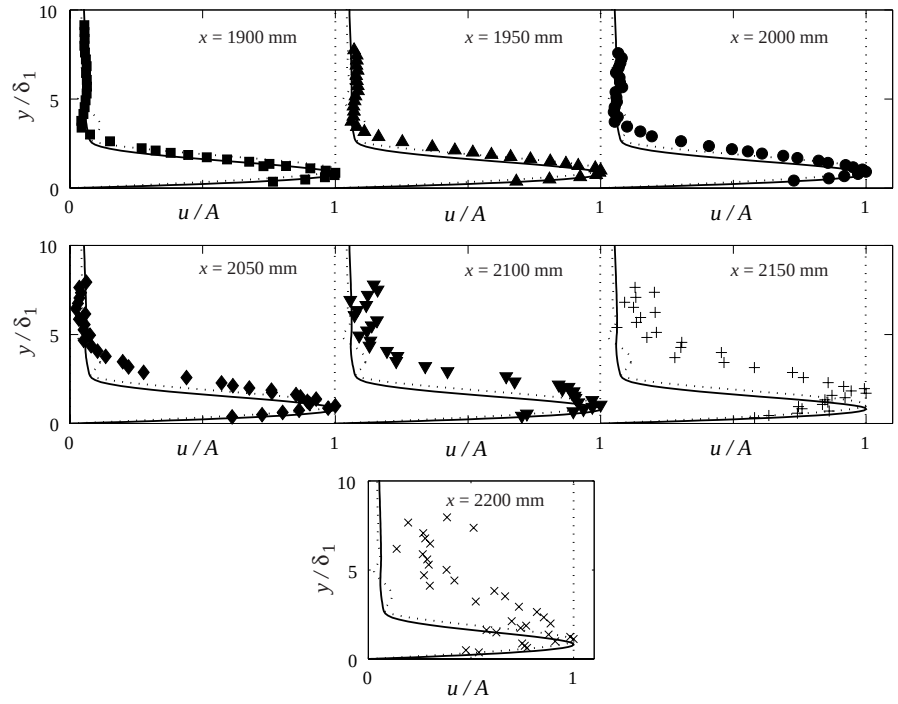

FIGURE 3.5. Amplitude distribution profiles for different downstream positions in an asymptotic suction boundary layer for F=59 and Re = 347. Symbols are measured data, solid line is the modified OS-solution and dotted line the OS-solution.

One should be aware of that the cross flow does not have a stabilizing effect in all flow configurations. Fransson & Alfredsson (2003*b*) showed that for the case of channel flow with permeable walls and cross flow the situation becomes more complicated and can give rise to both stabilization and destabilization depending on the rate of cross flow. The critical Reynolds number is lowered by an order of magnitude (Re_c = 667.4) as compared to plane Poiseuille flow at a cross flow velocity of 5.7% of the streamwise velocity.

In figure 3.5 experimental and theoretical amplitude distribution profiles are compared at different downstream positions. Here, Re = 347 which implies that the TS-wave will decay rapidly after its generation. The solid line is the solution from the modified OS-equation and the dotted is the ordinary OS-equation. Note that the last profile shown is only 350 mm from the disturbance source. Close to the disturbance source the experimental results show

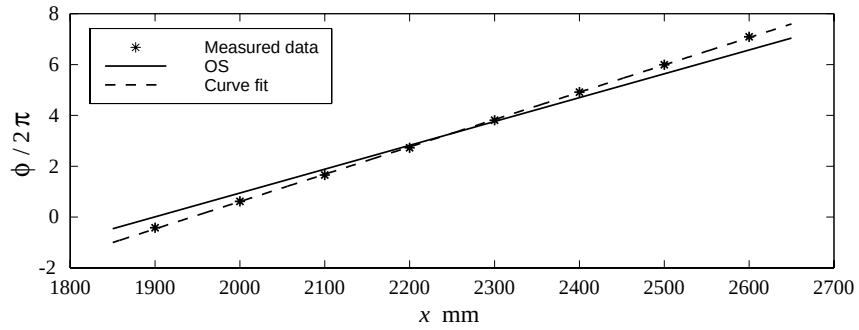

FIGURE 3.6. Phase distribution in the streamwise direction at F=59 and $Re = 347$ in the asymptotic suction boundary layer.

quite good agreement with the modified OS-solution, whereas further downstream the disturbance is seen to be spread out towards the upper part of the boundary layer and from x=2100 mm the measured data start to appear somewhat scattered.

The phase velocity of the TS-wave with F=59 is determined in figure 3.6. The solid line is the modified OS-solution and this solution almost corresponds to a curve fit to the measured data. The dotted line is the ordinary OS-solution. The experimental phase velocity is determined to be $c = 0.48U_\infty$, which is the phase velocity predicted by the modified OS-solution.

In figure 3.7 the amplitude decay is shown together with theoretical results. The theoretical results overpredicts the stability of the TS-wave. The experimental result gives a damping factor of $\alpha_i = 0.0153$ mm^{-1}, when the

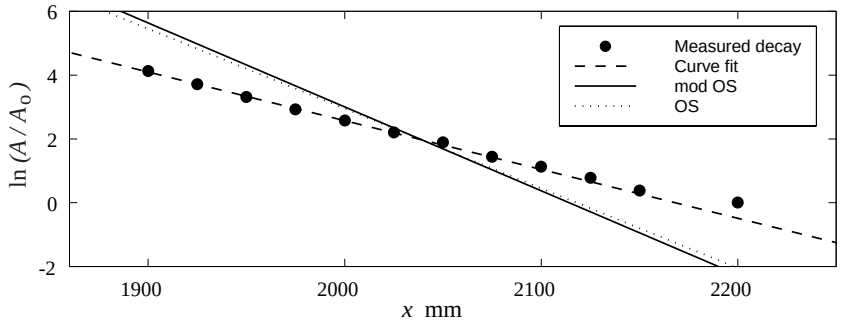

FIGURE 3.7. Amplitude decay versus the downstream distance for F=59 and $Re = 347$.

first six points are used for the curve fit, and the modified OS-solution predicts $\alpha_i = 0.0263\ \mathrm{mm}^{-1}$, i.e. a factor 1.72 higher.

3.1.2. *Free stream turbulence*

As already mentioned free stream turbulence gives rise to regions of high and low velocity (streaky structures) and in a Blasius boundary layer the streamwise disturbance energy grows in linear proportion to the downstream distance. These streaky structures move slowly in the spanwise direction and if the streamwise disturbance amplitude is measured (u_{rms}) it is seen to increase with the downstream distance when no suction is applied. However, in the suction case (for this typical suction rate 0.3% of U_∞) this amplitude increase is found to be eliminated and the u_{rms}-profiles more or less collapse on each other independent of the downstream position with a fix free stream turbulence intensity applied. This can be observed in figure 3.8 where the u_{rms}-profiles are plotted for both cases, i.e. with and without suction, for the $Tu = 1.4\%$. The position above the plate, where the maximum u_{rms}-value appears, does hardly change in y/δ_1-units and is approximately 1.5, this corresponds to 1/2- and 1/3 of the boundary layer thickness without suction and with suction, respectively. Similar results are found for other free stream turbulence intensities.

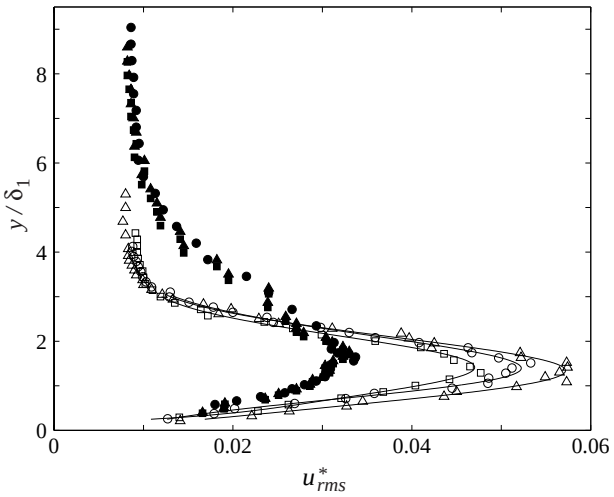

FIGURE 3.8. u_{rms}-profiles for different downstream positions from the leading edge with $Tu = 1.4\%$. No suction (unfilled-) and suction (filled markers). (□) $Re = 889$ mm; (◯) $Re = 994$ mm and (△) $Re = 1088$ mm. Solid lines are curve fits to data. $Re = 347$ in the suction case.

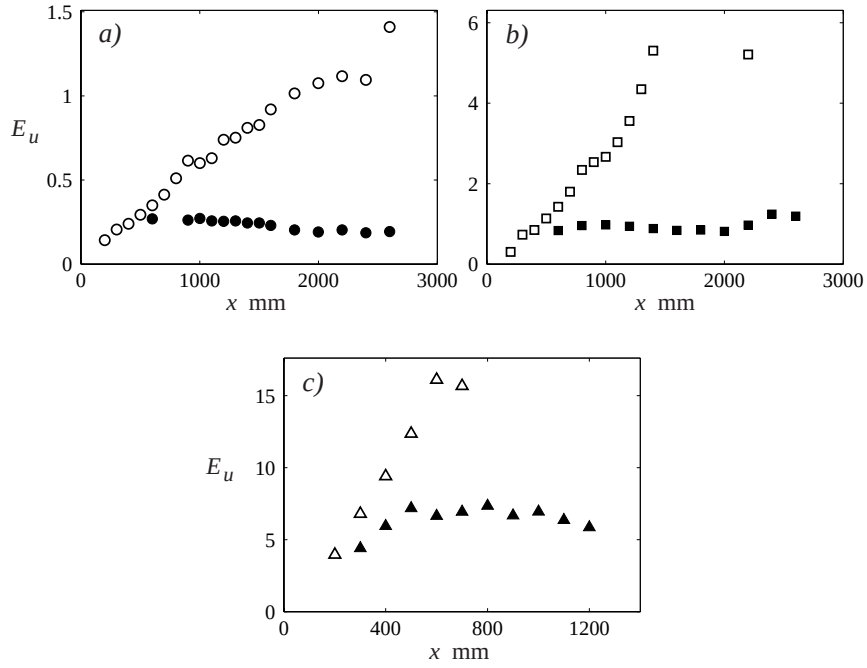

FIGURE 3.9. The growth of the average disturbance energy inside the boundary layer, defined as $E_u = \frac{1}{\delta U_\infty^2} \int_0^\delta u_{rms}^2 \mathrm{dy}$ (where $\delta = \delta_{0.99}$). a) $Tu = 1.4$ %, b) $Tu = 2.2\%$, and c) $Tu = 4.0\%$.

In figure 3.9 the averaged disturbance energy (E_u) inside the boundary layer is plotted versus the downstream distance from the leading edge. This figure reflects the growth elimination observed in figure 3.8 in the suction case. The figures show the well known linear growth of the disturbance energy with the downstream distance for the no suction case and for all Tu-levels. In the case with suction the energy growth ceases and a more or less constant level for each grid is obtained. Note that a larger suction would make the energy disturbance level decay whilst smaller suction rates would simply dampen the growth Yoshioka, Fransson & Alfredsson (2003).

The spanwise scale of the streaks can be determined through two-point correlation measurements of the streamwise velocity component, defined as

$$R_{uu} = \frac{\overline{u(z)u(z+\Delta z)}}{\overline{u(z)^2}} \ , \tag{3.6}$$

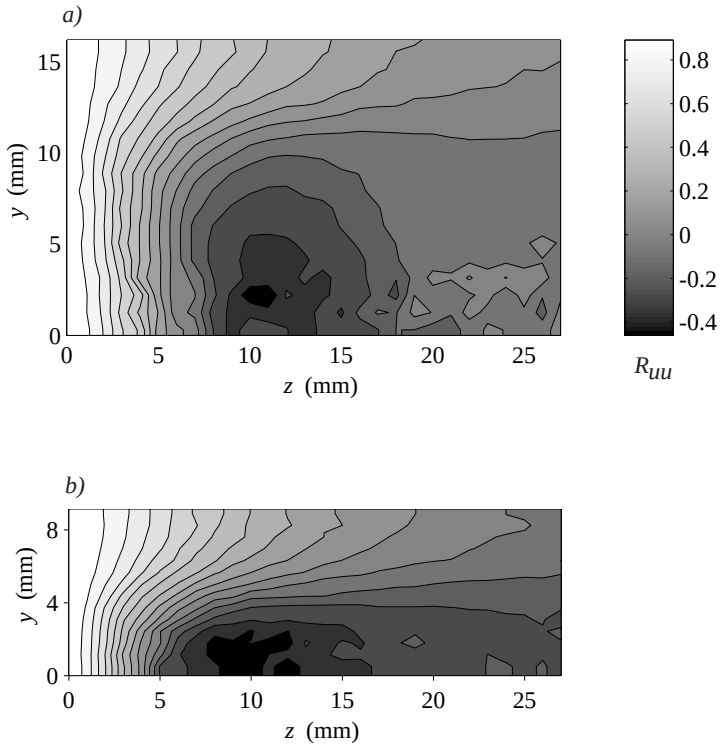

FIGURE 3.10. Contour plots of the correlation coefficient in the (y, z)-plane. a) Blasius boundary layer $x = 1800$ mm ($Re = 1333$), and b) asymptotic suction boundary layer $x = 1800$ mm ($Re = 347$). $Tu = 1.4$ %.

where Δz is the distance between the two probes. It is well known that the position where the streamwise correlation coefficient shows a distinct minimum can be interpreted as half the dominating spanwise wavelength of the streaks (see e.g. Westin 1997; Matsubara & Alfredsson 2001). From contour plots of R_{uu} in the (y, z)-plane an overview of the structure inside the boundary layer is achieved. In figure 3.10 such contour plots are shown for both the Blasius an the asymptotic suction boundary layer at $Tu = 1.4\%$. These show that the spanwise scale of the streaky structures is only slightly decreased by suction, despite a twofold reduction in boundary layer thickness. This indicates that disturbances inside the boundary layer is strongly dependent of the scale of the FST.

So far only the streamwise velocity fluctuation component has been considered and it has been shown to be strongly damped when suction is applied

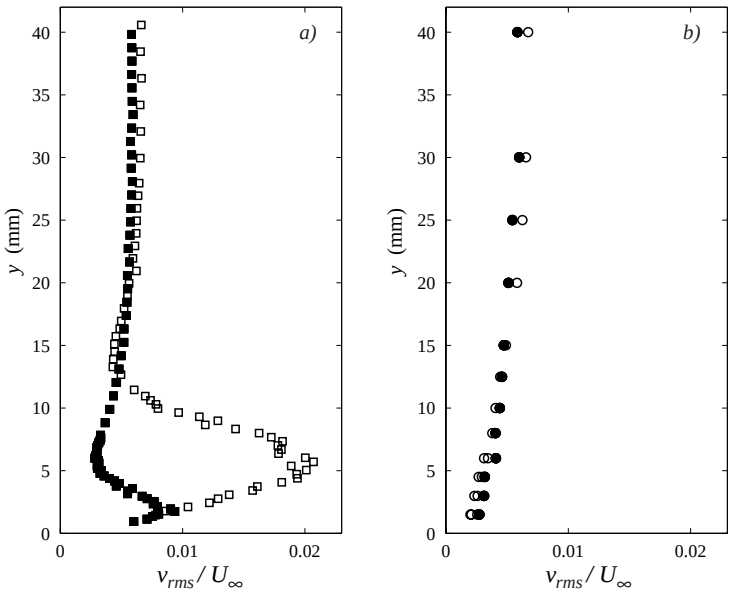

FIGURE 3.11. X-probe versus LDV measurements in boundary layers influenced by free stream turbulence. a) HW-measurements, (□) no suction and (■) with suction. b) LDV-measurements, (○) no suction and (●) with suction. Measurements with no suction applied are performed at $x = 1800$ mm ($\delta_{0.99} = 11.6$ mm) and when suction applied at $x = 2400$ mm ($\delta_{0.99} = 5$ mm).

compared with the no suction case. In figure 3.11 both Hot-Wire (HW) data (X-probe) in a) and Laser-Doppler-Velocimetry (LDV) data in b) of the wall-normal velocity fluctuation are shown. The wall-normal distance has been chosen to be dimensional for direct comparison between the no suction and suction case. The peculiar peak observed in the HW-data inside the boundary layer is a measurement error due to unsteady velocity gradients when using X-probes (see Fransson & Westin 2002, for details). The difference in v_{rms} measured by the X-probe is a direct consequence of a much smaller amplitude of the streaks in the suction case. Aronson, Johansson & Löfdahl (1997) showed that the wall-normal velocity component is damped over a region extending roughly one macroscale out from the wall in a shear free boundary, i.e. it is actually the presence of the wall that dampens v_{rms} and not the shear layer that is created due to the wall (see also Hunt & Graham 1978). The shear free boundary was created by having a moving wall at the same speed as the free stream. Figure 3.11 show that in the no suction and the suction cases

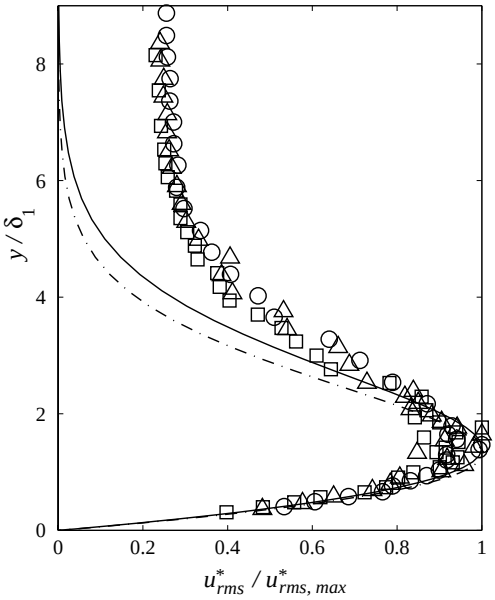

FIGURE 3.12. Streamwise perturbation velocity profiles at $R = 347$. Lines are OP response (i.e. disturbance at t_γ: solid line for $\beta = 0.33$, the measured streak separation; dash-dotted for $\beta = 0.53$, the maximum global optimal), symbols represent experimental data ($u_{\rm rms}$) at different downstream positions, $x = 1$m (◯), 1.6 m (△), 2m (□) for a flow with $Tu = 1.4\%$.

the v_{rms}-profiles are similar and decrease monotonously from the free stream towards the wall. This indicates that the suction does not strongly influence the normal velocity fluctuations close to the wall.

As shown by Fransson & Westin (2002) X-probe measurements to get the wall-normal fluctuation in streaky boundary layers is not an alternative (see also Talamelli *et al.* 2000, for further complications). LDV give accurate data but it is difficult to get high concentration of smoke close to the wall which implies that the sampling time increases enormously when approaching the wall. Due to difficulties in measuring the wall-normal fluctuation it has unfortunately been passed over. A large eddy simulation performed by Yang & Voke (1993) show that it is the pressure- and wall normal velocity fluctuations that are most efficient in exciting perturbations in the boundary layer, whereas streamwise fluctuations are rather harmless. This means that a high correlation between the disturbances (and their scales) inside the boundary layer and the wall-normal fluctuation in the free stream is to be expected, and should be investigated in more detail.

The asymptotic suction boundary layer is one case in which the algebraic growth mechanism presents the only viable linear route to transition at Reynolds numbers of practical interest. In this context it is reasonable to compare the optimal response state to disturbances measured inside the boundary layer (cf. §6 of Luchini (2000) for more details). Figure 3.12 compares perturbation velocity profiles of two different optimal perturbations (OP) with measurements at three different streamwise stations when $Tu = 1.4\%$. The agreement is good between the theoretical predictions, corresponding to the maximum global optimal for this flow and the global optimal at the measured streak spacing, and measurements carried out at three x-stations. As might be expected the concordance is slightly better for the optimal whose spanwise periodicity matches the experimental conditions (for further details and results see Fransson & Corbett 2003).

Fransson & Alfredsson (2003*a*) report a decrease of the spanwise scale inside the boundary layer with increasing Tu for a Blasius flow, and good agreement of the spanwise scale with spatially predicted OP-scales by Andersson *et al.* (1999) and Luchini (2000). In Fransson & Corbett (2003) this hypothesis is strengthened since it is shown that for high enough Tu (if directly connected to the streak spacing) the boundary layer preferentially amplifies disturbances whose scales are close to that of the optimal disturbance. However, it should be remembered that the free stream scales are important and that the FST level does probably not set the spanwise scale inside the boundary layer by itself.

3.2. Steady streaks and its effect upon stability

The stability properties of the streaky three-dimensional (3D) boundary layers may strongly differ from those of the two-dimensional (2D) Blasius boundary layer and depend on the streak amplitude and shape.

For streaks of sufficiently large amplitude the inflection points, appearing in the 3D basic flow, are able to support high frequency secondary instabilities of inviscid nature. Andersson *et al.* (2001) analyzed the linear inviscid stability of a family of streaky boundary layers parameterized by the amplitude of the linearly-optimal vortices, which are forced at the leading edge of the flat plate . They found that the inflectional instability sets in when the maximum streak amplitude exceeds a critical value of 26% of the free stream velocity.

The viscous stability of the same family of basic flows considered by Andersson *et al.* (2001) has been recently explored in the case of moderate amplitudes of the streaks ($< 26\%U_\infty$), which are therefore stable to inviscid instability. It was found (Cossu & Brandt 2002; Brandt *et al.* 2003) that, in that case, the streaks have a stabilizing effect on the viscous Tollmien-Schlichting waves. It was therefore suggested to artificially force such moderate amplitude, steady streaks in the 2D Blasius boundary layer in order to delay the onset of the viscous TS instability, and, hopefully the onset of turbulence, to larger values of the Reynolds number.

Preliminary wind tunnel tests have been performed in order to verify the stabilization effect of TS-waves, which show promising results. However, it is important to define a proper measure of the energy growth/decay in order to "prove" the stabilization effect, and to get rid of the higher harmonics in the initial generation process of the steady streaks, which otherwise will undesirely influence the stability and comparison with theory will be difficult.

White (2002) shows by Fourier decomposition of the velocity field into different modes that roughness elements induce harmonics in a wide range of spanwise wavenumbers. Furthermore, comparison with optimal perturbation theory is done and turns out to disagree, implying that the streaks generated by White (2002) were not the optimal. The question whether it is possible to generate an optimal streak or not still remains unanswered. However, the generated streaks in Fransson *et al.* (2003*a*) were shown to agree with suboptimal theory. Here, both the optimized initial perturbation's position (corresponding to the position of the experimental roughness elements) as well as the perturbation's location in the wall-normal direction was considered. The former

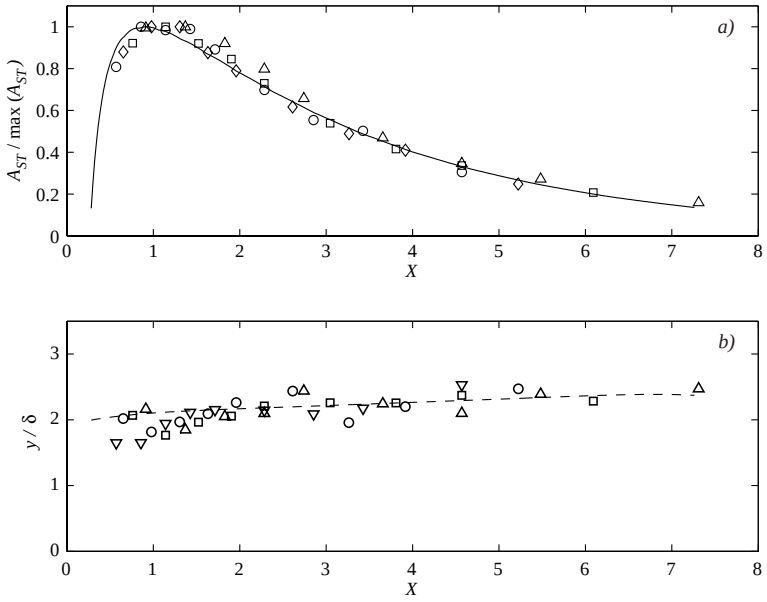

FIGURE 3.13. Comparison between the experimental results and suboptimal perturbation theory. a) Wall-normal maximum of the streak amplitude, and its corresponding position above the wall in b). For further information consult **Paper 6**.

consideration was investigated by Levin & Henningson (2003), but can not alone explain the suboptimal streaks observed in experiments. The latter consideration was implemented by stretching or compressing the the wall-normal velocity profile of the optimal upstream perturbation. The result is shown in figure 3.13 where the stretching/compressing parameter has been tuned to match the experimental data, and it turns out that the optimal perturbation has to be compressed (i.e. the maxima in the initial perturbation is found closer to the wall) in order to agree with the amplitude evolution of the experimental streaks.

3.2.1. *Generation mechanisms*

A comparison of the present results with similar experimental studies in literature shows that two distinct flow configurations can be induced by the presence of roughness elements; they are both characterised by the formation of streamwise elongated velocity perturbations and differ in the relative position of the high- and low speed streaks with respect to the roughness elements. In the experiments by Kendall (1990), Gaster *et al.* (1994) and related simulations by Joslin & Grosch (1995), White (2002), and Asai *et al.* (2002), a region of defect velocity is formed straight behind the element. This is most likely due to the presence of the wake, which persists downstream forming the low speed streak. Conversely, in the present experiment, similarly to what was observed by Bakchinov *et al.* (1995), a high-speed region is induced behind the roughness element. Two different generation mechanisms are therefore dominating and in **Paper 6** of the present thesis we attempt an explanation for this behaviour by considering the perturbation induced by a roughness element in a wall-bounded shear flow (see Acarlar & Smith 1987). For other streak generation techniques see Fransson *et al.* (2003*a*), **Paper 6**.

CHAPTER 4

Porous cylinder and flow control

A flow configuration that has attracted researchers and scientists over many years is the flow past bluff bodies. This configuration offers the interaction of three shear layers to be studied (cf. e.g. Williamson 1996), namely the boundary layer, the separating free shear layer, and the wake flow. From a fundamental research point of view it is a very complex flow geometry that can advance many flow phenomena in different Reynolds number ranges, such as boundary layer separation, periodic vortex shedding, wake transition, boundary layer transition, flow reattachment, separation bubbles etc. These flow phenomena are of direct relevance to many practical and industrial applications, where the vortex shedding in particular plays an important role, such as in telecom masts, aircraft and missile aerodynamics, civil and wind engineering, marine structures, and underwater acoustics. The periodic vortex shedding can lead to devastating structural vibrations that finally lead to material fatigue and structural failure in this context denoted vortex induced vibrations.

The vortex shedding instability is a self excited oscillation that will set in even if all sources of noise are removed (see Gillies 1998), and can be shown to be attributed to the local stability property of the two-dimensional mean velocity wake profile behind a bluff body. Monkewitz (1988) identified a sequence of stability transitions by using a family of wake profiles, that resulted in $Re_C < Re_A < Re_K$, where Re_C (≈ 5), Re_A (≈ 25), and Re_K (≈ 47) are critical Reynolds numbers that mark the onset of convective, absolute, and von Kármán shedding instability, respectively. This sequence was in fully agreement with the qualitative model predictions by Chomaz *et al.* (1988) the same year. The onset of the global von Kármán shedding mode occurs via a so-called supercritical Hopfh bifurcation (see e.g. Provansal *et al.* 1987). For a review on the stability properties of open flows in general the interested reader is referred to Huerre & Monkewitz (1990), and for reviews on cylinder flows in particular see e.g. Williamson (1996); Buresti (1998); Norberg (2003); Zdravkovich (1997, 2003).

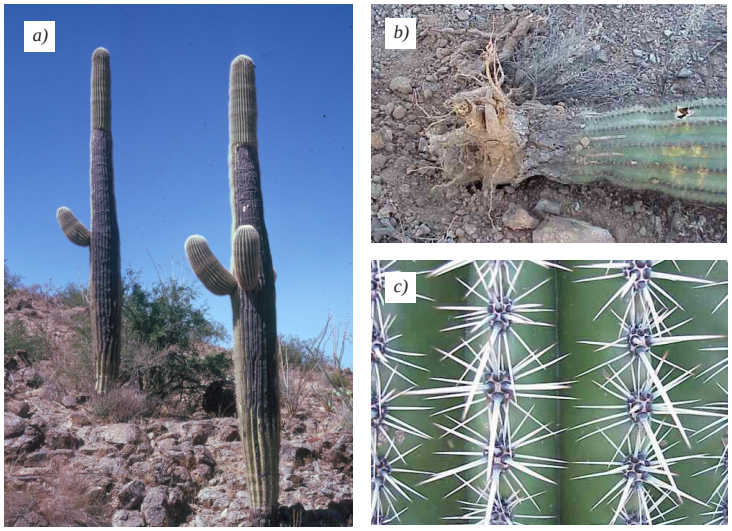

FIGURE 4.1. Saguaro cactus. a) Two fairly young Saguaros (approximately 85 years of age). b) A toppled Saguaro. c) Close-up of the Saguaro's spines and cavities.

4.1. Biological example of flow control

A good example of geometrical flow control, by thousands of years of evolution, is the Saguaro cactus (see figure[1] 4.1a). The Saguaro is the largest cactus in USA and reaches commonly heights of 12 m with a diameter of 0.5 m. However, due to their heights the Saguaro is vulnerable to high speed winds (storms) which sometimes make them topple but not necessarily brake (cf. figure 4.1b). The Saguaro can be viewed as a giant cylindrical structure and as mentioned above the wake will become unstable and a von Kármán eddy street will develop in the wake which will cause huge side forces on the cactus. Years and years of evolution has provided the Saguaro with a very complex outer geometry wich is most probably the optimal by means of minimizing induced side forces. This geometry has taken the form of longitudinal V-shaped cavities and spines (see figure 4.1c). For references on the topic the interested reader is referred to Talley & Mungal (2002).

4.2. Vortex shedding control

The ability to control the wake and the vortex shedding of a bluff body can for instance be used to reduce drag, increase heat transfer and mixing, and

[1]The images were downloaded from http://helios.bto.ed.ac.uk/bto/desbiome/saguaro.htm and http://www.nps.gov/sagu/Saguaros/saguaro.htm

enhance combustion. Over the second half of the last century there has been a number of successful attempts to control the shedding wake behind bluff bodies with the practical goal of reducing the pressure drag on the body.

4.2.1. *Rectangular-based forebody*

A control approach that has shown to be effective in reducing the average strength of the vortices and the shedding frequency is base bleed (cf. e.g. Wood 1967; Bearman 1967). For successively increasing bleeding rates the regular shedding of vortices ceases, intermittently at first, and then completely. Hannemann & Oertel (1989) performed numerical simulations on the effect of uniform blowing from the base, and reported a critical value[2] ($c_q = 0.214$) for which vortex shedding was suppressed. Uniform suction from the base was considered numerically by Hammond & Redekopp (1997) and they report a continuous decline of the wake shedding frequency with a gradual increase of suction until an abrupt suppression occurs at a sufficiently high suction rate.

4.2.2. *Cylinder*

A simple passive control method is to place a thin splitter plate aligned in the streamwise direction on the centreline of the near wake (see Roshko 1955, 1961). For a specific length of the splitter plate the sinuous von Kármán mode is altered for a varicouse mode that causes a pair of twin–vortices to be formed, one on each side of the plate. More recently, Grinstein *et al.* (1991) carried out numerical simulations on the effect of an interference plate in the wake of a thick plate and found that the base pressure coefficient could decrease by a factor of 3 depending on the length of the interference plate and its separation from the base.

Experiments on circular cylinders with forced rotary oscillations have shown to give a drag reduction of up to 80% at $Re = 15000$ for certain ranges of frequency and amplitude of the sinusoidal rotary oscillation (see Tokumaru & Dimotakis 1991). Shiels & Leonard (2001) performed numerical simulations of this control approach, where the above experimental foundings were verified, and showed indications that this kind of control could be even more efficient at higher Re.

Control approaches using feedback control have also been attempted. Roussopoulos (1993) carried out experiments in a wind tunnel with acoustic waves from a loudspeaker as actuation as well as by vibrating the cylinder. In a numerical study by Park *et al.* (1994) blowing and suction through slots on the rear part of the cylinder were utilized as actuation. However, this investigation

[2] $c_q = m^*/U_\infty D^*$, were m^* is the mass flow rate divided by density and for unit depth which is blown into the wake at the base of the plate, U_∞ is the free stream velocity, and D^* is the thickness of the plate.

were performed at relatively low Reynolds numbers (< 300) and so far it does not exist any results on higher Re-flows.

Glezer & Amitay (2002) used synthetic jets, which provide a localized addition of momentum normal to the surface, on selected positions over the cylinder in order to delay separation in both laminar and turbulent boundary layers. They argued that this delay was caused by increased mixing within the boundary layer. In addition, the interaction between the jet and the cross flow has a profound effect both on the separated shear layer and on the wake; the magnitude of the Reynolds stresses is reduced indicating that the delay in separation is not merely the result of a transition to turbulence in the boundary layer.

Experiments with suction or blowing through the entire surface of the cylinder in order to control the vortex shedding have been considered by e.g. Pankhurst & Thwaites (1950); Hurley & Thwaites (1951); Mathelin *et al.* (2001*a*,*b*); Fransson *et al.* (2003*b*). Pankhurst & Thwaites (1950) made combined experiments with continuous suction through the surface and a flap in form of a short splitter plate at different angles. They showed through surface pressure and wake velocity measurements that with the flap directed in the streamwise direction and for sufficient suction[3] ($C_q\sqrt{R} \gtrsim 10$) the separation is entirely prevented and a remarkable close approximation to the potential flow solution is achieved. Further, Hurley & Thwaites (1951) performed boundary layer measurements on the same porous cylinder and found in general good agreement with laminar boundary layer theory. However, no time resolved measurements to determine the vortex shedding frequency were reported.

The von Kármán frequency is Reynolds number dependent, whilst the dimensionless frequency known as the Strouhal number is constant (≈ 0.2) in the range $10^2 \lesssim Re \lesssim 10^5$. Mathelin *et al.* (2001*a*,*b*) considered the case of continuous blowing through the entire cylinder surface. Among the effects observed are the wider wake and a decrease of the Strouhal number with increasing blowing. They report an analytical relation of an equivalent Reynolds number of the canonical case which produces the same flow characteristics in terms of vortex shedding instability as the case with blowing. The decrease of the Strouhal number with blowing result was experimentally verified by Fransson *et al.* (2003*b*), who also considered the effect of continuous suction which turns out to have the contrary effect on the Strouhal number. Note that uniform suction from the base of a rectangular-based forebody, interestingly, gives the opposite behaviour (cf. Hammond & Redekopp 1997). In Fransson *et al.* (2003*b*) the changes in the flow due to blowing or suction was analyzed in terms of mean and fluctuating velocity profiles in the wake through hot-wire

[3]Here C_q is a suction coefficient defined as the suction velocity per unit area divided by the free stream velocity.

anemometry, pressure distributions on the cylinder, and drag and vortex shedding measurements. Furthermore, smoke visualizations of the flow field in the near wake of the cylinder for different blowing or suction rates were reported. Image averaging enabled the retrieval of quantitative information, such as the vortex formation length, which showed that the vortex formation length is decreased by 75% and increased by 150% for 5% of suction and blowing of the free stream velocity, respectively.

4.3. The effect of applying continuous suction or blowing

In the following section some results of applying continuous suction or blowing through the cylinder surface will be shown briefly. The amount of suction or blowing applied through the cylinder surface is characterized by the parameter Γ. This parameter is simply defined as the velocity through the cylinder surface $V_{\text{surf.}}$ (being negative for suction and positive for blowing) in percentage of of the free stream velocity U_∞, i.e. $\Gamma = 100 \times V_{\text{surf.}}/U_\infty$. Flow visualizations show a very complex flow around the cylinder at Reyndols numbers of the order of

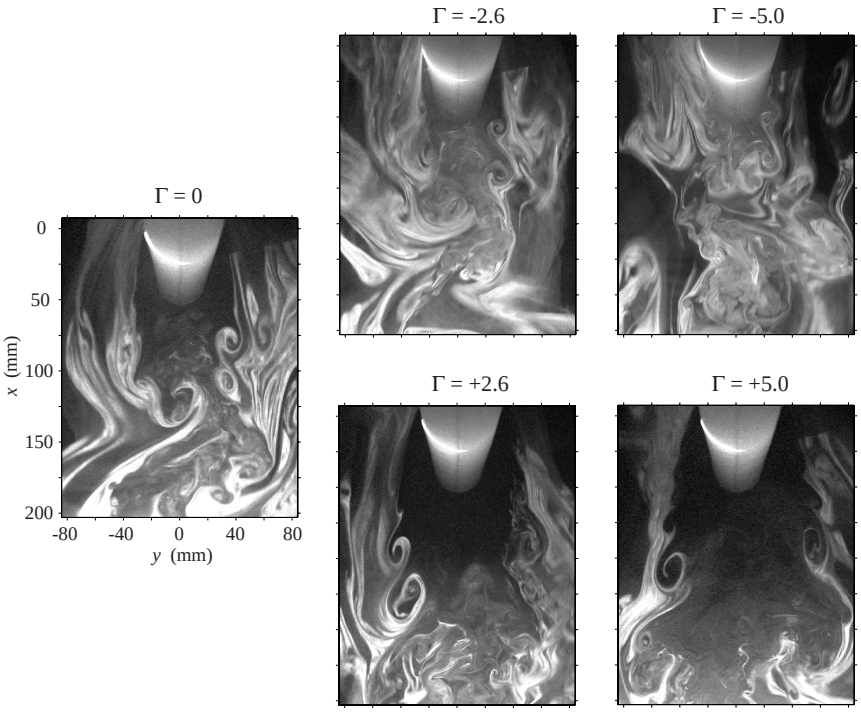

FIGURE 4.2. Instantaneous flow visualization images in the near wake of a porous cylinder subject to continuous suction or blowing for $R = 3300$.

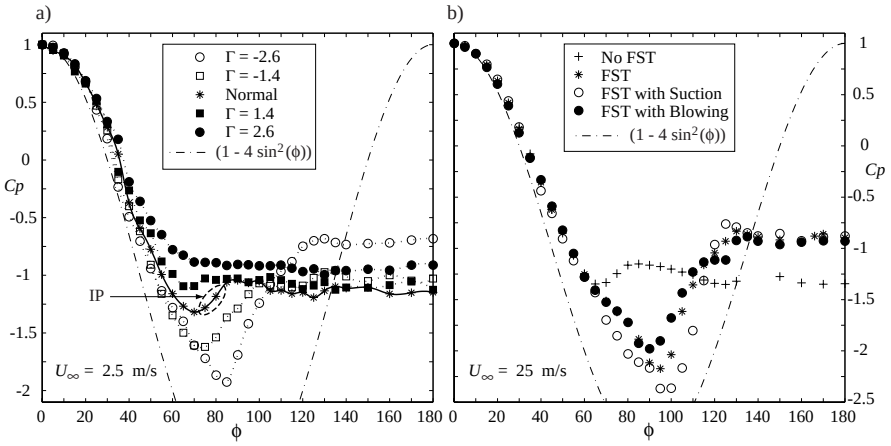

FIGURE 4.3. The pressure distribution around the cylinder is shown for different Γ-values. a) shows the effect of blowing/suction with a laminar oncoming flow ($U = 2.5$ m/s, $R^* = 8300$, $Tu = 0.5\%$). b) shows the effect of free stream turbulence generated by a turbulence generating grid, the blowing/suction is $\Gamma = \pm 0.4$ ($U = 25$ m/s, $R = 10 \times R^*$, $Tu = 3\%$). Dash-dotted line is the potential flow solution.

10^4, see figure 4.2. These images clearly show the effect of applying suction and blowing; with suction the wake shrinks and with blowing it enlarges.

In figure 4.3a) the effect of different suction and blowing rates on the C_p-distribution is shown and compared with the potential flow solution (dash-dotted line). There are three major remarks that can be made; firstly, one can observe how $C_{p,min}$ is reduced down to a value close to -2 for $\Gamma = -2.6$ and tends to -1 for $\Gamma = +2.6$; secondly for suction the separation point (ϕ_s) moves towards larger angles ($\phi_s \approx 105^o$ for $\Gamma = -2.6$), and when blowing is applied, the flow is seen to separate at lower angles; thirdly the base pressure coefficient ($C_{p,B}$) is increased for the case of suction producing a significant increase in the adverse pressure recovery ($C_{p,B} - C_{p,min}$), whilst for the case of sufficiently large blowing rates, the recovery region is eliminated.

The inflection point in region IP on the C_p-curve, marked with a dashed ellipse in figure 4.3a), is often used to estimate the location of the separation point and this is the criterion employed in the preceding paragraph. Suction makes the boundary layer profile fuller and hence more resistant to separation, in analogy to high Reynolds number flow. At $Re \sim 10^5$ transition in the boundary layer occurs (the exact Re-value depends on the flow quality and the surface roughness) and the separation point moves from the front part of the cylinder to the rear part, due to the turbulent boundary layer that can

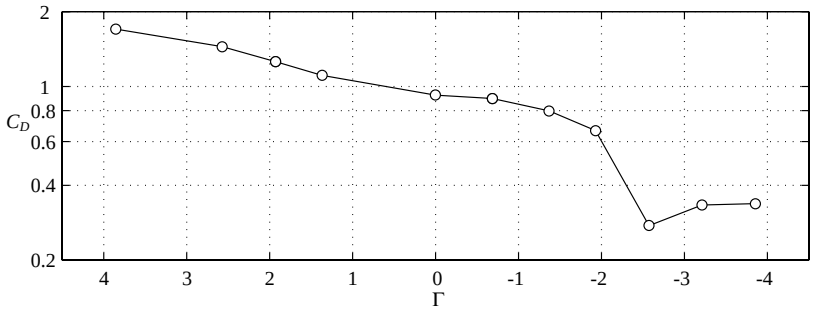

FIGURE 4.4. Shows the effect of the drag coefficient (C_D) when blowing or suction is applied. C_D is here estimated by calculating the momentum loss in the far wake.

make the flow adhere for a longer distance to the surface. In figure 4.3b) the free stream velocity is increased ten times and the C_p-distribution is compared with results when a turbulence intensity ($Tu = u_{rms}/U_\infty$) of 3% is present (causing transition in the boundary layer at subcritical Reynolds numbers); this was done by installing a turbulence generating grid at the inlet of the test-section. It is clearly seen, by comparing the ($\circ$)-symbols in figure 4.3a) with the ($*$)-symbols in b), that suction and high levels of free stream turbulence have the same impact on the C_p-distribution. Furthermore, in b), one can observe how a small blowing/suction rate ($\Gamma = \pm 0.4$) effects the location of $C_{p,min}$ and consequently the separation point, but not the base pressure coefficient. In figure 4.4 the drag coefficient (C_D) is plotted versus different blowing and suction rates. The shape of the drag distribution vs Γ may be compared with that obtained for different Reynolds numbers in the case of a solid cylinder, see e.g. Schlichting (1979) (page 17 figure 1.4.) with experimental data from Wieselsberger.

The drop in C_D for $\Gamma \approx -2.5$ is related to the shift of the separation point as described previously in connection with figure 4.3, which is also present for high Reynolds numbers ($Re \sim 10^5$) due to the laminar-turbulent boundary layer transition. Both the turbulent profile and the fuller laminar profile due to suction are more resistent to separation which is the actual cause for the shift. For further results the intereseted reader is referred to Fransson *et al.* (2003*b*) and Fransson (2003).

CHAPTER 5

Experimental techniques and set-ups

In this thesis experiments have been performed in three different wind-tunnels, in where eight different experimental configurations or techniques have been used. This chapter will provide a short summary for the interested reader of the tunnels, experimental set-ups and experimental techniques that have been used.

5.1. Wind-tunnels

All three wind-tunnels are low-speed tunnels of closed loop circuit type. The MTL tunnel[1] is specially designed for transition and turbulence research studies and is located at KTH Mechanics, Stockholm. The test section is 7 m long, 0.8 m high and 1.2 m wide, and the maximum speed is 70 m/s. The background disturbance level is considered low with a streamwise turbulence intensity lower than 0.025% of the free stream velocity and with both the cross flow turbulence intensities lower than 0.035% at $U_\infty = 25$ m/s. The tunnel is equipped with a heat exchanger and the desired temperature is easily set by the user on the control panel of the tunnel. At 25 m/s the temperature and pressure variations over the cross section area are less than ± 0.05 °C and $\pm 0.06\%$, respectively. For further details see Lindgren (2002).

The BL wind tunnel[2] is located at KTH Mechanics, Stockholm, and the test section has a cross sectional area of 0.5×0.75 m^2, and a length of 4.2 m. The maximum speed is 48 m/s. The flow quality in this tunnel is also considered good with a turbulence intensity (of all three components) of less than 0.04% of the free stream velocity. The tunnel was successfully designed with expanding corners (larger outlet than inlet cross section area) in order to reduce the total wind-tunnel circuit length with only a negligible increase of the total pressure loss. The interested reader is referred to Lindgren (2002).

The S4 wind-tunnel is located at IMFT in Toulouse and is equipped with a three-dimensional traversing mechanism and allows automatized computer controlled measuring and traversing in one of the cross sectional directions with an accuracy of 1/80 mm. The dimension of the cross sectional area of the

[1] Minimum Turbulence Level or Mårten Theodore Landahl named after its late initiator.
[2] Boundary Layer or Björn Lindgren named after its designer.

test section is 0.7×0.6 m^2 and the length is 1.8 m. The background streamwise disturbance level amounts to 0.1% at a free stream velocity of 25 m/s.

5.2. Experimental set-ups

The asymptotic suction boundary layer has been created over a porous flat plate in the MTL wind-tunnel, and this plate has been used for paper 1 & 4. For this set-up a removable asymmetric leading edge was specially designed and built (see paper 10). The plate is of sandwich-construction type, and in the front of the plate the removable leading edge is mounted and in the back there is a possibility to extend the plate by additional plates of aluminium. The plate is constructed on a base plate of aluminium with a frame, and is designed having two 250 mm long plenum chambers starting 360 mm from the leading edge followed by a 1750 mm long plenum chamber. The subdivision into three chambers is for future work in where the suction rate then is allowed to change with the downstream distance. Inside the plenum chamber spacing elements made of hollowed T-profiles are glued, with a spanwise separation of 50 mm, in order to support the porous plates and avoid bending the plates when suction is applied. On these T-profiles three porous plates with the total dimension $2250 \times 1000 \times 3.2$ mm^3 (length, width, thickness) were mounted into the frame plate. See Fransson (2001) and paper 1 for details and schematics of the experimental set-up. The disturbance generating device based on blowing and suction through a slot in the plate has been used previously and was designed by Elofsson (1998) in where the interested reader will find all details.

For paper 5 an active turbulence generating grid was designed and built to fit the MTL wind-tunnel. The grid is active in the sense that it ejects secondary fluid jets into the fluid upstream, i.e. counterflow injection. By regulating the injection rate the free stream turbulence intensity can be changed without changing the set-up in the test section and with a small change of the characteristic turbulence scales. This grid has been used successfully in paper 1 & 4 as well. Consult Fransson (2001) appendix B and paper 5 for details and schematics of the active turbulence generating grid.

In paper 7 a porous cylinder with four inner chambers and connection pipes for tube connections to a high/low pressure source, and pressure holes on the surface, was designed and built. This cylinder was designed in order to fit both the S4 and the BL wind-tunnel. The experimental set-ups are described in paper 7 & 8.

Steady streaks may be generated by different means. One way of doing this is outlined in paper 6 where the method of roughness elements have been applied. The elements were made at KTH Mechanics and are standing cylinders (cylinder axis perpendicular to the plate) glued to the plate with a diameter and height of 2 mm and 777 μm, respectively. The plate used in this investigation is named the "Laminar plate" and has been used for several transition

experiments over the past years in the MTL wind-tunnel. See paper 6 for further details of the experimental set-up.

5.3. Experimental techniques

5.3.1. *Velocity measurements*

Hot-Wire Anemometry (HWA) is an old technique from the beginning of last century and is based on the heat convection from an infinitely long cylinder. This technique permits high time resolved data and is even today the most attractive technique for transition and turbulence measurements. A drawback is its inability to be applied in back flow regions, such as separation bubbles and near wake flows. However, there exist HWA based techniques – or – tricks that are developed for these kinds of flow measurements, such as pulsed hot-wires, flying probes, and multi-wire probes (see e.g. Bruun 1995; Häggmark *et al.* 2000; Häggmark 2000). Another complication with this method is the need of calibration. Here, the single wire probe calibration was done against a Prandtl tube using a modified King's law (cf. Johansson & Alfredsson 1982) taking into account the natural convection which becomes significant at low velocities. For the X-probe an angle calibration was carried out and two fifth-order polynomials were fitted to the calibration data (cf. eg. Österlund 1999). In this thesis close to all hot-wire measurements were carried out with an AN–1003 anemometer apparatus. The hot-wire probes both single wire- and X-probes were manufactured by the author at KTH Mechanics, except for the measurements carried out at IMFT, Toulouse, where a commercial single wire Dantec probe was used.

The Laser Doppler Velocimetry (LDV) is based on the detection of the doppler frequency shift that appears from scattered light from particles that follow the stream. The frequency shift is directly proportional to the velocity and the proportionality constant is solely determined by geometry and the wave length of the scattered light, which makes this device easy to use since it does not need any calibration. Other advantages are for instance the insensitivity to the temperature and the compound of the fluid as well as it is a nonintrusive technique in contrary to HWA. Drawbacks with this technique is for instance its relatively big measurement volume and the need of transparent fluids. Furthermore, the fluid has to be seeded with particles correctly, since the actual measured velocity is not the fluid's – it is the particles'. The LDV-system used in paper 9 is an integrated one dimensional laser-optics unit, including a 10 mW He-Ne laser of wavelength 632.8 nm. A beam expander was mounted to the lens to reduce the measurement volume, which can be approximated as an ellipsoid with axes lengths 0.14 mm and 2.4 mm. See paper 9 for further details.

Particle Image Velocimetry (PIV) is a relatively new technique which allows capturing a whole field of instantaneous velocities. This technique is based

on the simple equation speed equals distance over time. With a laser sheet illuminating the seeded flow a camera is used to capture two fast images with a known time interval. The images are decomposed into interrogation areas that are correlated to produce an average particle displacement vector, from where the velocity and direction is achieved. A drawback is the temporal resolution, however, today there exist high speed PIV-systems that allows sampling rates of around 1 kHz. The PIV-system used consists of a Spectra Physics 400 mJ double pulsed Nd:Yag laser operating at 15 Hz as a light source and the camera is a double-frame Kodak ES1.0 8-bit CCD camera with 1018×1008 pixels (cf. Angele 2003, for use of this system in the MTL and in the BL wind-tunnels). See paper 8 for a schematic of the experimental set-up.

5.3.2. *Flow visualization technique*

Many fluids are of transparent media, i.e. their motion remains invisible, why flow visualization is such an important tool in fluid mechanics research. An image says more than thousand words and a movie says more than thousand images is a qualified truth, but the fact is that insights into any flow phenomenon will be improved if this process may be observed visually. In this thesis a flow visualization technique has been developed and applied on the flow around a porous circular cylinder in the BL wind-tunnel. The technique is reported in paper 7. In figure 5.1 the flow visualization setup is shown. A horizontal smoke sheet was created by injecting smoke through a slot in a wing-profile, which was located over the whole spanwise distance in the stagnation chamber of the windtunnel. The profile has two tubing inlets, one on each side close to the walls. The smoke was generated by heating a glycol based liquid with a

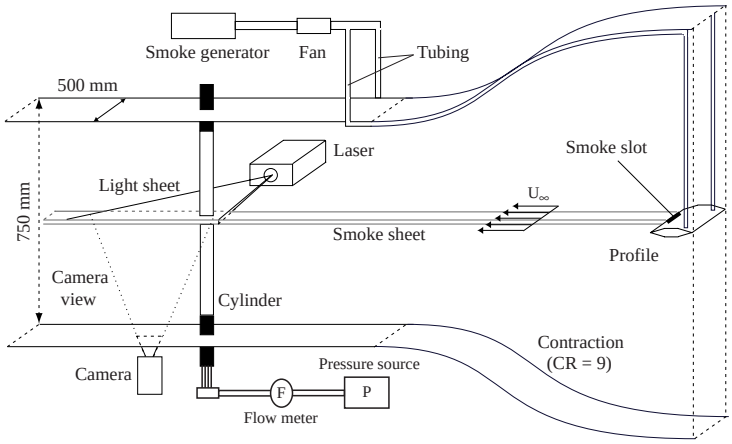

FIGURE 5.1. Flow visualization set-up of the porous cylinder.

disco smoke generator, JEM ZR20 Mk II, and forced by a small fan through the tubing into the profile enabling a steady leakage of smoke through the slot.

The light source was a continuous Ar–ion laser, LEXEL 95–4, which gave the high light intensity needed for the short camera shutter times. The laser beam (1.5 W) was aligned through a cylinder lens creating a light sheet intersecting with the smoke sheet from the side (perpendicular to the flow field and the test section). The collection of flow visualization images was taken with a digital video camera, SONY TRV900 576×720 pixels, with a shutter time of 2 ms and with a rate of 20 images per second.

CHAPTER 6

Conclusions

In this chapter the most important conclusions from the different investigations are summarized. For further results the reader is referred to the separate papers in Part II of the present thesis.

Asymptotic suction boundary layer

- *Base flow.* The mean flow development from the leading edge of the plate is shown to be in good agreement with a theoretical boundary layer analysis and when the asymptotic suction region is reached there is an excellent agreement between the theoretical and experimental boundary layer profiles.
- *Tollmien–Schlichting waves.* The correspondence, of the streamwise amplitude profiles and the phase velocity is good, between linear spatial stability analysis and experimental results. However, the decay factor predicted by theory is slightly overestimated compared to the experimental results.
- *Optimal perturbation.* The spanwise wavenumber of the optimal perturbation in the asymptotic suction boundary layer is $\beta = 0.53$, when normalized with the displacement thickness.

Free stream turbulence induced transition

- In the initially laminar, but disturbed region, it has been found that the disturbance energy grows linearly as $Tu^2 Re_x$.
- The transitional Reynolds number was found to vary as Tu^{-2}.
- It was found that the length of the transitional zone has a minimum value and it increases linearly with Re_{tr}. This result puts earlier attempts to model the length of the transitional zone into doubt.
- The relative length of the transitional zone increases with increasing Tu.
- The intermittency function is found to have a relatively well-defined distribution, valid for all Tu.
- The spanwise scale of the streaks decreases with increasing level of free stream turbulence and approaches the scale given by optimal perturbation theory.
- The spanwise scale of the streaks is maintained when suction is applied compared with the no suction case, despite the fact that the boundary

layer thickness can decrease substantially depending on the suction rate. The streaks are compressed but not splitted, indicating the importance of the receptivity process.
- The disturbance energy growth of the streaks are inhibited or even become negative in the asymptotic suction boundary layer, it may be possible that the streaks initiated at the leading edge become mainly passive disturbances which are convected downstream by the flow.
- The optimal perturbation velocity profile agrees well with experimentally measured disturbance profiles in the asymptotic suction boundary layer.

Porous cylinder with continuous suction/blowing

- Strong enough suction moves the separation line to the rear part of the cylinder in a similar way as it does when the cylinder boundary layer becomes turbulent. This results in a narrower wake.
- When blowing is applied the separation point moves forward on the cylinder and the drag is shown to increase linearly with increasing magnitude of blowing. Correspondingly this is shown to result in a widening of the wake.
- The turbulence on the wake centreline decreases throughout the whole wake (at least up to $x/D = 20$) if suction is applied on the cylinder, whereas there is hardly any effect from blowing beyond $x/D = 5$.
- The Strouhal number increases strongly with suction (up to 50% for a suction rate of 2.5% of the free stream velocity), whereas blowing has the opposite effect (decrease of around 25% for a blowing rate of 5% of the free stream velocity).
- It has been shown that it is possible to find a relation between an effective Reynolds number and the blowing/suction rate. The relation proposed was verified in the Reynolds number range $Re \sim 10^2 - 10^6$.
- The position of maximum back-flow behind the cylinder and the position where the two stationary vortices (appearing in the mean field) confluence, i.e. the stagnation point in the flow field, have been shown to be related by a factor of 1.4 (in average) for different blowing and suction rates.
- The vortex formation length have been shown to decrease and increase with suction and blowing, respectively. However, the absolute size in the streamwise direction of the recirculating region is not significantly influenced by suction nor blowing.
- For high enough suction and blowing rates a compression and an extension, respectively, of the vortices across the wake have been found.

Other results

- The energy growth and streamwise wall-normal disturbance peak location of experimentally generated steady streaks have been found to agree well with sub–optimal perturbation theory.
- The critical Reynolds number for channel flows with uniform cross flow has been found to be lowered by an order of magnitude as compared to plane Poiseuille flow. This critical value occurs when the cross flow velocity to the maximum streamwise velocity ratio is 5.7%.

CHAPTER 7

Papers and authors contributions

Paper 1

On the disturbance growth in an asymptotic suction boundary layer.
J. H. M. Fransson (JF) & P. H. Alfredsson (HAL). *J. Fluid Mech.* **482**, 51–90.

This work is of both experimental and theoretical character on the asymptotic suction boundary layer and was published as part of the Licentiate thesis of JF. The experimental set-up was designed and built by JF. The experimental and theoretical investigations were performed by JF under supervision of HAL and the writing was done by JF and HAL jointly. Parts of these results have been presented at ERCOFTAC Nordic Pilot Center Meeting 2000, Dalarö, Sweden, American Physical Society 53rd annual meeting Division of Fluid Dynamics 2000, Washington D.C., USA, and at Euromech 423rd Colloquium 2001 Stuttgart, Germany.

Paper 2

Optimal linear growth in the asymptotic suction boundary layer.
J. H. M. Fransson & P. Corbett (PC). *Eur. J. Mech. B/Fluids* **22**, 259–270.

In this paper a variational technique in the temporal framework is used to study initial configurations of disturbance velocity which maximize perturbation kinetic energy in the asymptotic suction boundary layer. Comparisons were made between the state of the theoretical optimal perturbation and wind tunnel experiments (performed by JF). The numerical code was originally written by PC for the Falkner–Skan–Cooke family of boundary layers. The derivation of the equations and extension of the existing code was done by JF under guidance of PC. Computations and post-processing were performed by JF and the paper was written by JF and PC jointly.

Paper 3

On the hydrodynamic stability of channel flow with cross flow.
J. H. M. Fransson & P. H. Alfredsson. *Phys. Fluids* **15**, 436–441.

This work is a theoretical investigation of the linear stability problem of an ordinary Poiseuille flow with uniform cross flow. The theoretical approach was

done by JF (supervised by HAL) and the numerical code was written by JF. The computations and the post-processing were performed by JF and the analysis of the results, and the writing were done in cooperation with HAL. Part of this work was presented as a model problem in the Licentiate thesis of JF.

Paper 4

Free stream turbulence induced disturbances in boundary layers with wall suction. S. Yoshioka (SY), J. H. M. Fransson & P. H. Alfredsson

This paper is an extension study of Paper 1. The original set-up was designed and built by JF. Modifications and improvements of the porous plate was performed by SY with help from JF. The experiments were mainly performed by SY but also by JF. Post-processing and figure generation was done by SY. A shorter version of this paper was published as a proceeding of TSFP3, Sendai, Japan, where JF participated in the writing. This paper is based on the proceeding and was written by SY and HAL with feed-back from JF. These results were further presented at the European Fluid Mechanics Conference 2003, Toulouse, France.

Paper 5

Transition induced by free stream turbulence
J. H. M. Fransson, M. Matsubara (MM) & P. H. Alfredsson

This paper deals with free stream turbulence induced transition on a flat plate boundary layer. In this experimental investigation JF helped MM during the collection of data. Most of the data evaluation was done by MM, whereas most of the data analysis was done by JF under supervision of HAL. The paper was written by JF and HAL with input from MM.

Paper 6

On streamwise streaks generated by roughness elements in the boundary layer on a flat plate.
J. H. M. Fransson, L. Brandt (LB), A. Talamelli (AT) & C. Cossu (CC)

This paper treats of the generation of high amplitude steady streaks in a flat plate boundary layer by means of roughness elements. Both wind tunnel experiments as well as suboptimal perturbation calculations have been carried out. The experiments were performed by JF and AT with input from CC, and the calculations was performed by LB. The paper was written jointly by all authors. This work was presented at the 17th AIMETA Congress of Theoretical and Applied Mechanics, and at the American Physical Society 56th annual meeting Division of Fluid Dynamics 2003, New York, USA.

Paper 7

Flow around a porous cylinder subject to continuous suction or blowing.
J. H. M. Fransson, P. Konieczny (PK) & P. H. Alfredsson

In this paper the flow past a porous cylinder and the effect of applying continuous suction or blowing through the porous surface was investigated. The cylinder (with pressure tabs, blowing/suction chambers, outlet piping etc.) was designed by JF. The experimental set-up in Toulouse, as well as the pressure and hot-wire measurements, were performed by JF with help from PK. The original idea of the visualization set-up in Stockholm came from HAL and the design and set-up was performed by JF & PK. The final flow visualization images were taken by JF. The post-processing and figures were made by JF. The introduction part of the paper was written by PK and the rest by JF together with HAL. This work has been presented at the European Fluid Mechanics Conference 2003, Toulouse, France, and at the ERCOFTAC Nordic Pilot Center Meeting 2003, Marstrand, Sweden.

Paper 8

PIV–measurements in the wake of a cylinder subject to continuous suction or blowing. J. H. M. Fransson

This work was performed by the author.

Paper 9

Errors in hot-wire X-probe measurements induced by unsteady velocity gradients. J. H. M. Fransson & K. J. A. Westin (JW). *Exp. Fluids* **32**, 413–415.

The experimental set-up, measurements, evaluation and writing were performed jointly by JF and JW. This work was presented at the 15th AIMETA Congress of Theoretical and Applied Mechanics.

Paper 10

Leading edge design process using a commercial flow solver. J. H. M. Fransson

This work was performed by the author.

Acknowledgements

In my walks, every man I meet is my superior in some way, and in that I learn from him.

Ralph Waldo Emerson (1803–1882)

My supervisor Prof. Henrik Alfredsson has been an inspiring source and a role model for me in fluid dynamics even before my graduate studies started. Your knowledge and experience in the field never stop impressing me. I am also happy to have had the opportunity to share other experiences than fluid dynamics with you, such as skiing in the Pyrenees, dinners along the River Garonne, and waxing the cross country skis in your garden shed.

However, one got to have several role models in order not to become a travesty of one. Special thanks go to Prof. Alessandro Bottaro who was my supervisor during my six month stay at Institut de Mécanique des Fluides de Toulouse. You made my stay in France pleasant and enlightening in many perspectives. Dr. Masaharu Matsubara, you were my first tutor in experimental fluid dynamics and you taught me many useful things about hot-wire probe construction. The video sequences of TS-wave and FST break downs were kindly lent by Dr. Matsubara, which resulted in the visualization photos present in the introduction part of this thesis. Dr. Johan Westin, it is always a pleasure to work with you even five o'clock in the morning. I would especially like to thank you for being such an excellent host in Providence, Rhode Island, arranging visits to Brown University and Massachusetts Institute of Technology. Prof. Alessandro Talamelli, you did not only teach me in vehicle aerodynamics and wake flows, you also gave me several appreciated lectures in italian cooking. I have also enjoyed your guided tours of the universities in Pisa and Forli.

Furthermore, I would like to thank my co-authors Peter Corbett, Luca Brandt, Philippe Konieczny, and Carlo Cossu, for nice collaborations and for sharing their knowledge. Marcus Gällstedt and Ulf Landén, you are gratefully acknowledged for your patience, laughs, and skilful construction works.

Dr. Nils Tillmark and Dr. Barbro Muhammad–Klingmann, you are acknowledged for sharing your experiences and providing fruitful discussions during working hours as well as lunch breaks. Dr. Ardeshir Hanifi, you are thanked for fruitful discussions, and explanations regarding theoretical stability analysis. Furthermore, I wish to thank all lab colleagues during the years for contributing to a pleasant working place and good laughs.

I wish to express my gratitude to my family and friends who have encouraged me during my education. Special thanks are directed to my lovely wife Annika for all her love and support. Without you, neither I nor this thesis would have been the same.

The Swedish Research Council (VR) is acknowledged for the financial support. The six months stay in Toulouse was kindly supported by an EU Marie Curie Training Site Fellowship.

References

Acarlar, M. S. & Smith, C. R. 1987 A study of hairpin vortices in a laminar boundary layer. Part 1. Hairpin vortices generated by a hemisphere protuberance. *J. Fluid Mech.* **175**, 1–41.

Airiau, C., Bottaro, A., Walther, S. & Legendre, D. 2003 A methodology for optimal laminar flow control: A application to the damping of Tollmien-Schlichting waves in a boundary layer. *Phys. Fluids* **15**, 1131–1145.

Alfredsson, P. H. & Matsubara, M. 2000 Free-stream turbulence, streaky structures and transition in boundary layer flows. *AIAA Paper* 2000-2534.

Amoignon, O., Pralits, J. O., Hanifi, A., Berggren, M. & Henningson, D. S. 2003 Shape optimization for delay of laminar-turbulent transition. Tech. Rep. FOI-R-0919-SE. FOI, Aeronautics Division, FFA, Stockholm.

Andersson, P., Berggren, M. & Henningson, D. S. 1999 Optimal disturbances and bypass transition in boundary layers. *Phys. Fluids* **11**, 134–150.

Andersson, P., Brandt, L., Bottaro, A. & Henningson, D. S. 2001 On the breakdown of boundary layer streaks. *J. Fluid Mech.* **428**, 29–60.

Angele, K. 2003 Experimental studies of turbulent boundary layer separation and control. PhD thesis, KTH, Stockholm, TRITA-MEK Tech. Rep. 2003:08.

Aronson, D., Johansson, A. V. & Löfdahl, L. 1997 Shear-free turbulence near a wall. *J. Fluid Mech.* **338**, 363–385.

Asai, M., Minagawa, M. & Nishioka, M. 2002 The instability and breakdown of a near-wall low-speed streak. *J. Fluid Mech.* **455**, 289–314.

Bakchinov, A. A., Grek, G. R., klingmann, B. G. B. & Kozlov, V. V. 1995 Transition experiments in a boundary layer with embedded streamwise vortices. *Phys. Fluids* **7**, 820–832.

Balakumar, P. & Hall, P. 1999 Optimum suction distribution for transition control. *Theor. Comput. Fluid Dynamics* **13**, 1–19.

Bearman, P. W. 1967 On vortex street wakes. *J. Fluid Mech.* **28**, 625–641.

Bertolotti, F. P. 1991 Linear and Nonlinear Stability of Boundary Layers with Streamwise Varying Properties. PhD thesis, The Ohio State University, Department of Mechanical Engineering , Columbus, Ohio.

Bewley, T. R. & Liu, S. 2001 Optimal and robust control and estimation of linear paths to transition. *Progress in Aerospace Sciences* **37**, 21–58.

Brandt, L. 2003 Numerical studies of bypass transition in the Blasius boundary layer. PhD thesis, KTH, Stockholm, TRITA-MEK Tech. Rep. 2003:04.

Brandt, L., Cossu, C., Chomaz, J.-M., Huerre, P. & Henningson, D. S. 2003 On the convectively unstable nature of optimal streaks in boundary layers. *J. Fluid Mech.* **485**, 221–242.

Brandt, L. & Henningson, D. S. 2002 Transition of streamwise streaks in zero-pressure-gradient boundary layers. *J. Fluid Mech.* **472**, 229–262.

Bruun, H. H. 1995 *Hot-wire anemometry*. Oxford University Press Inc., NY.

Buresti, G. 1998 Vortex shedding from bluff bodies. *Wind Effects on Buildings and Structures,* pp. 61–95, Riera & Davenport (eds.), Balkema, Rotterdam.

Butler, K. M. & Farrell, B. F. 1992 Three-dimensional optimal perturbations in viscous shear flow. *Phys. Fluids A* **4**, 1637–1650.

Chomaz, J. M., Huerre, P. & Redekopp, L. G. 1988 Bifurcations to local and global modes in spatially developing flows. *Phys. Rev. Lett.* **60**, 25–28.

Cossu, C. & Brandt, L. 2002 Stabilization of Tollmien-Schlichting waves by finite amplitude optimal streaks in the Blasius boundary layer. *Phys. Fluids* **14**, L57–L60.

Dhawan, S. & Narasimha, R. 1957 Some properties of boundary layer flow during the transition from laminar to turbulent motion. *J. Fluid Mech.* **3**, 418–436.

Drazin, P. G. & Reid, W. H. 1981 *Hydrodynamic stability*. Cambridge University Press.

Ellingsen, T. & Palm, E. 1975 Stability of linear flow. *Phys. Fluids* **18**, 487–488.

Elofsson, P. 1998 Experiments on oblique transition in wall bounded shear flows. PhD thesis, KTH, Stockholm, TRITA-MEK Tech. Rep. 1998:05.

Fasel, H. & Konzelmann, U. 1990 Non-parallel stability of a flat-plate boundary layer using the complete Navier-Stokes equations. *J. Fluid Mech.* **221**, 311–347.

Fransson, J. H. M. 2001 Investigations of the asymptotic suction boundary layer. TRITA-MEK Tech. Rep. 2001:11. KTH, Stockholm, licentiate Thesis.

Fransson, J. H. M. 2003 PIV–measurements in the wake of a cylinder subject to continuous suction or blowing, **Paper 8**.

Fransson, J. H. M. & Alfredsson, P. H. 2003*a* On the disturbance growth in an asymptotic suction boundary layer. *J. Fluid Mech.* **482**, 51–90, **Paper 1**.

Fransson, J. H. M. & Alfredsson, P. H. 2003*b* On the hydrodynamic stability of channel flow with cross flow. *Phys. Fluids* **15**, 436–441, **Paper 3**.

Fransson, J. H. M., Brandt, L., Talamelli, A. & Cossu, C. 2003*a* On streamwise streaks generated by roughness elements in the boundary layer on a flat plate, **Paper 6**.

Fransson, J. H. M. & Corbett, P. 2003 Optimal linear growth in the asymptotic suction boundary layer. *Eur. J. Mech. B/Fluids* **22**, 259–270, **Paper 2**.

Fransson, J. H. M., Konieczny, P. & Alfredsson, P. H. 2003*b* Flow around a porous cylinder subject to continuous suction or blowing. *J. Fluids Struc.* (Submitted for publication) **Paper 7**.

Fransson, J. H. M. & Westin, K. J. A. 2002 Errors in hot-wire X-probe measurements induced by unsteady velocity gradients. *Exp. Fluids* **32**, 413–415, **Paper 9**.

Gaster, M., Grosch, C. E. & Jackson, T. L. 1994 The velocity field created by a shallow bump in a boundary layer. *Phys. Fluids* **6** (9), 3079–3085.

Gillies, E. A. 1998 Low–dimensional control of the circular cylinder wake. *J. Fluid Mech.* **371**, 157–178.

Glezer, A. & Amitay, M. 2002 Synthetic jets. *Annu. Rev. Fluid Mech.* **34**, 503–529.

Gregory, N. 1961 Research on suction surfaces for laminar flow. *Boundary Layer and Flow Control II* , 924–957.

Grinstein, F. F., Boris, J. P. & Griffin, O. M. 1991 Passive pressure-drag control in a plane wake. *AIAA J.* **29**, 1436–1442.

Gustavsson, L. H. 1991 Energy growth of three-dimensional disturbances in plane Poiseuille flow. *J. Fluid Mech.* **224**, 241–260.

Häggmark, C. 2000 Investigations of disturbances developing in a laminar separation bubble flow. PhD thesis, KTH, Stockholm, TRITA-MEK Tech. Rep. 2000:03.

Häggmark, C. P., Bakchinov, A. A. & Alfredsson, P. H. 2000 Measurements with a flow direction boundary-layer probe in a two-dimensional laminar separation bubble. *Exp. Fluids* **28**, 236–242.

Hammond, D. A. & Redekopp, L. G. 1997 Global dynamics of symmetric and asymmetric wakes. *J. Fluid Mech.* **331**, 231–260.

Hannemann, K. & Oertel, H. 1989 Numerical simulation of the absolutely and convectively unstable wake. *J. Fluid Mech.* **199**, 55–88.

Herbert, T. 1983 Secondary instability of plane channel flow to subharmonic three-dimensional disturbances. *Phys. Fluids* **26**, 871–874.

Hocking, L. M. 1975 Non-linear instability of the asymptotic suction velocity profile. *Quart. J. Mech. Appl. Math.* **28**, 341–353.

Högberg, M. 2001 Optimal control of boundary layer transition. PhD thesis, KTH, Stockholm, TRITA-MEK Tech. Rep. 2001:13.

Huerre, P. & Monkewitz, P. A. 1990 Local and global instabilities in spatially developing flows. *Annu. Rev. Fluid Mech.* **22**, 473–537.

Hultgren, L. S. & Gustavsson, L. H. 1981 Algebraic growth of disturbances in a laminar boundary layer. *Phys. Fluids* **24**, 1000–1004.

Hunt, J. C. R. & Graham, J. M. R. 1978 Free-stream turbulence near plane boundaries. *J. Fluid Mech.* **84**, 209–235.

Hurley, D. G. & Thwaites, M. A. 1951 An experimental investigation of the boundary layer on a porous circular cylinder. *Brit. Aero. Res. Council,* Rep. and Memo. 2829.

Jacobs, R. G. & Durbin, P. A. 2001 Simulations of bypass transition. *J. Fluid Mech.* **428**, 185–212.

Johansson, A. V. & Alfredsson, P. H. 1982 On the structure of turbulent channel flow. *J. Fluid Mech.* **122**, 295–314.

Joslin, R. D. 1998 Aircraft laminar flow control. *Annu. Rev. Fluid Mech.* **30**, 1–29.

Joslin, R. D., Erlebacher, G. & Hussaini, M. Y. 1996 Active control of instabilities in laminar boundary layers – overview and concept validation. *J. Fluids Eng.* **118**, 494–497.

Joslin, R. D. & Grosch, C. E. 1995 Growth characteristics downstream of a shallow bump: Computation and experiment. *Phys. Fluids* **7** (12), 3042–3047.

Kachanov, Y. S. 1994 Physical mechanisms of laminar-boundary-layer transition. *Annu. Rev. Fluid Mech.* **26**, 411–482.

Kachanov, Y. S., Kozlov, V. V. & Levchenko, V. Y. 1977 Nonlinear development of a wave in a boundary layer. *Izv. Akad. Nauk SSSR Mekh. Zhid. Gaza* **3**, 49–58, in Russian.

Kendall, J. M. 1985 Experimental study of disturbances produced in a pretransitional laminar boundary layer by weak free stream turbulence. *AIAA Paper* 85-1695.

Kendall, J. M. 1990 The effect of small-scale roughness on the mean flow profile of a laminar boundary layer. In *Instability and transition* (ed. Hussaini & Voigt), pp. 296–302.

Klebanoff, P. S. 1971 Effect of freestream turbulence on the laminar boundary layer. *Bull. Am. Phys. Soc.* **10**, 1323.

Klebanoff, P. S., Tidstrom, K. D. & Sargent, L. M. 1962 The three dimensional nature of boundary layer instability. *J. Fluid Mech.* **12**, 1–34.

Klingmann, R. G. B., Boiko, A. V., Westin, K. J. A., Kozlov, V. V. & Alfredsson, P. H. 1993 Experiments on the stability of Tollmien-Schlichting waves. *Eur. J. Mech., B/Fluids* **12**, 493–514.

Landahl, M. T. 1980 A note on an algebraic instability of inviscid parallel shear flows. *J. Fluid Mech.* **98**, 243–251.

Levin, O. & Henningson, D. S. 2003 Exponential vs algebraic growth and transition prediction in boundary layer flow. *Flow, Turbulence and combustion.* In press.

Lindgren, B. 2002 Flow facility design and experimental studies of wall-bounded turbulent shear-flows. PhD thesis, KTH, Stockholm, TRITA-MEK Tech. Rep. 2002:16.

Luchini, P. 2000 Reynolds number independent instability of the boundary layer over a flat surface: optimal perturbations. *J. Fluid Mech.* **404**, 289–309.

Lumley, J. & Blossey, P. 1998 Control of turbulence. *Annu. Rev. Fluid Mech.* **30**, 311–327.

Lundell, F. 2003 Experimental studies on bypass transition and its control. PhD thesis, KTH, Stockholm, TRITA-MEK Tech. Rep. 2003:03.

MacManus, D. G. & Eaton, J. A. 2000 Flow physics of discrete boundary layer suction-measurements and predictions. *J. Fluid Mech.* **417**, 47–75.

Mathelin, L., Bataille, F. & Lallemand, A. 2001*a* Near wake of a circular cylinder submitted to blowing - I Boundary layers evolution. *Int. J. Heat Mass Transf.* **44**, 3701–3708.

Mathelin, L., Bataille, F. & Lallemand, A. 2001*b* Near wake of a circular cylinder submitted to blowing - II Impact on the dynamics. *Int. J. Heat Mass Transf.* **44**, 3709–3719.

Matsubara, M. & Alfredsson, P. H. 2001 Disturbance growth in boundary layers subjected to free-stream turbulence. *J. Fluid Mech.* **430**, 149–168.

Moin, R. & Bewley, T. R. 1994 Feedback control of turbulence, part 2. *Appl. Mech. Rev.* **47**, S3–S13.

Monkewitz, P. A. 1988 The absolute and convective nature of instability in two–dimensional wakes at low Reynolds numbers. *Phys. Fluids* **31**, 999–1006.

Morkovin, M. V. 1969 *The many faces of transition*. In Viscous Drag Reduction, Plenum Press.

Narasimha, R. & Sreenivasan, K. R. 1973 Relaminarization in highly accelerated turbulent boundary layers. *J. Fluid Mech.* **61**, 417–447.

Norberg, C. 2003 Fluctuating lift on a circular cylinder: review and new measurements. *J. Fluids Struc.* **17**, 57–96.

Orszag, S. A. & Patera, A. 1983 Secondary instability in wall-bounded shear flows. *J. Fluid Mech.* **128**, 347–385.

Österlund, J. M. 1999 Experimental studies of zero pressure-gradient turbulent boundary layer flow. PhD thesis, KTH, Stockholm, TRITA-MEK Tech. Rep. 1999:16.

Pankhurst, R. C. & Thwaites, M. A. 1950 Experiments on the flow past a porous circular cylinder fitted with a Thwaites flat. *Brit. Aero. Res. Council,* Rep. and Memo. 2787.

Park, D. S., Ladd, D. M. & Hendricks, E. W. 1994 Feedback control of von Karman vortex shedding behind a circular cylinder at low Reynolds numbers. *Phys. Fluids* **6**, 2390–2405.

Parsheh, M. 2000 Flow in contractions with application to headboxes. PhD thesis, KTH, Stockholm, TRITA-MEK Tech. Rep. 2000:16.

Pfenninger, W. & Groth, E. 1961 Low drag boundary layer suction experiments in flight on a wing glove of an F-94A airplane with suction through a large number of fine slots. *Boundary Layer and Flow Control* **II**, 981–999.

Poll, D. I. A., Danks, M. & Davies, A. J. 1992*a* The effect of surface suction near the leading edge of a swept-back wing. *First European Forum on Laminar Flow Technology* pp. 278–293.

Poll, D. I. A., Danks, M. & Humphreys, B. E. 1992*b* The aerodynamic performance of laser drilled sheets. *First European Forum on Laminar Flow Technology* pp. 274–277.

Pralits, J. 2003 Optimal design of natural hybrid laminar flow control on wings. PhD thesis, KTH, Stockholm, TRITA-MEK Tech. Rep. 2003:13.

Pralits, J., Hanifi, A. & Henningson, D. S. 2002 Adjoint-based optimization of steady suction for disturbance control in incompressible flows. *J. Fluid Mech.* **467**, 129–161.

Provansal, M., Mathis, C. & Boyer, L. 1987 Benard-von Karman instability: transient and forced regimes. *J. Fluid Mech.* **182**, 1–22.

Reddy, S. C. & Henningson, D. S. 1993 Energy growth in viscous channel flows. *J. Fluid Mech.* **252**, 209–238.

Reshotko, E. 2001 Transient growth: A factor in bypass transition. *Phys. Fluids* **13**, 1067–1075.

Reynolds, G. A. & Saric, W. S. 1986 Experiments on the stability of the flat-plate boundary layer with suction. *AIAA J.* **24**, 202–207.

Rheinboldt, W. 1956 Zur Berechnung stationärer Grenzschichten bei kontinuierlicher Absaugung mit unstetig veränderlicher Absaugegeschwindigkeit. *J. Rational Mech. Anal.* **5**, 539–604.

Roberts, P. J. D., Floryan, J. M., Casalis, G. & Arnal, D. 2001 Boundary layer instability induced by surface suction. *Phys. Fluids* **13**, 2543–2552.

Roshko, A. 1955 On the wake and drag of bluff bodies. *J. Aeronaut. Sci.* **22**, 124–132.

Roshko, A. 1961 Experiments on the flow past a circular cylinder at very high Reynolds number. *J. Fluid Mech.* **10**, 345–356.

Roussopoulos, K. 1993 Feedback control of vortex shedding at low Reynolds number. *J. Fluid Mech.* **248**, 267–296.

Saric, W. S. 1985 Laminar flow control with suction. *AGARD Report No* 723.

Schlichting, H. 1979 *Boundary layer theory*. McGraw-Hill.

Schmid, P. J. & Henningson, D. S. 2001 *Stability and transition in shear flows*. Springer.

Schubauer, G. B. & Skramstad, H. K. 1948 Laminar boundary layer oscillations and transition on a flat plate. *Technical Report Rep.* 909, NACA.

Shiels, D. & Leonard, A. 2001 Investigation of a drag reduction on a circular cylinder in rotary oscillation. *J. Fluid Mech.* **431**, 297–322.

Talamelli, A., Westin, K. J. A. & Alfredsson, P. H. 2000 An experimental investigation of the response of hot-wire X-probes in shear flows. *Exp. Fluids* **28**, 425–435.

Talley, S. & Mungal, G. 2002 Flow around cactus-shaped cylinders. In *Annual Research Briefs, Center of Turbulence Research* (ed. P. Bradshaw), pp. 363–376.

Taylor, G. I. 1939 Some recent developments in the study of turbulence. In *Proc. Fifth Int. Cong. Appl. Mech., 12-16 September 1938* (ed. J. P. den Hartog & H. Peters), pp. 294–310. Cambridge, MA, USA: Wiley.

Tokumaru, P. T. & Dimotakis, P. E. 1991 Rotary oscillation control of a cylinder wake. *J. Fluid Mech.* **224**, 77–90.

Trefethen, L. N., Trefethen, A. E., Reddy, S. C. & Driscoll, T. A. 1993 Hydrodynamic stability without eigenvalues. *Science* **261**, 578–584.

Westin, J. 1997 Laminar-turbulent boundary layer transition influenced by free stream turbulence. PhD thesis, KTH, Stockholm, TRITA-MEK Tech. Rep. 1997:10.

White, E. B. 2002 Transient growth of stationary disturbances in a flat plate boundary layer. *Phys. Fluids* **14**, 4429–4439.

White, F. M. 1991 *Viscous fluid flow*. McGraw-Hill.

Williamson, C. H. K. 1996 Vortex dynamics in the cylinder wake. *Annu. Rev. Fluid Mech.* **28**, 477–539.

Wood, C. J. 1967 Visualization of an icompressible wake with base bleed. *J. Fluid Mech.* **29**, 259–272.

Yang, Z. Y. & Voke, P. R. 1993 Large-eddy simulation of transition to turbulence. Tech. Rep. ME-FC/93.12. University of Surrey, Dept. Mech. Eng.

Yoshioka, S., Fransson, J. H. M. & Alfredsson, P. H. 2003 Free stream turbulence induced disturbances in boundary layers with wall suction. (Submitted for publication) **Paper 4**.

Zdravkovich, M. M. 1997 *Flow around circular cylinders, Vol 1: Fundamentals*. Oxford University Press.

Zdravkovich, M. M. 2003 *Flow around circular cylinders, Vol 2: Applications*. Oxford University Press.

Part II

Papers

1

Paper 1

On the disturbance growth in an asymptotic suction boundary layer

By Jens H. M. Fransson and P. Henrik Alfredsson

KTH Mechanics, SE-100 44 Stockholm, Sweden

Published in *J. Fluid Mech.* **482**, 51–90, 2003

An experimental and theoretical study on the effect of boundary layer suction on the laminar-turbulent transition process has been carried out. In the study an asymptotic suction boundary layer was established in a wind tunnel with a free stream velocity of 5.0 ms^{-1}. Wall normal suction (suction velocity 1.44 cm s^{-1}) was applied over a large area and the boundary layer was nearly constant over a length of 1800 mm. Measurements were made both with and without suction so comparisons between the two cases could easily be made. Measurements of the development of the mean velocity distribution showed good agreement with theory. The Reynolds number based on the displacement thickness for the suction boundary layer was 347. Both experiments on the development of forced Tollmien-Schlichting (TS) waves and boundary layer disturbances introduced by free stream turbulence were carried out. In connection to the TS-wave experiments spatial linear stability calculations, where the wall-normal velocity component is accounted for, were carried out for comparison with the experiments. This comparison shows satisfactory agreement even though the stability of the asymptotic suction profile is somewhat overpredicted by the theory. Free stream turbulence (FST) was generated by three different grids giving turbulence intensities at the leading edge of the plate between 1.4 % and 4.0 %. The FST induces disturbances into the boundary layer and it was shown that for the present suction rate the disturbance level inside the boundary layer is constant and becomes proportional to the FST intensity. In all cases transition was prevented when suction was applied although without suction the two highest levels of grid turbulence gave rise to transition. Despite a twofold reduction in the boundary layer thickness in the suction case compared to the no suction case the spanwise scale of the streaky structures was almost constant.

1. Introduction

One area of significant recent interest in fluid dynamics is laminar flow control (LFC). A possible method of LFC is to apply suction at the wall. A definition of

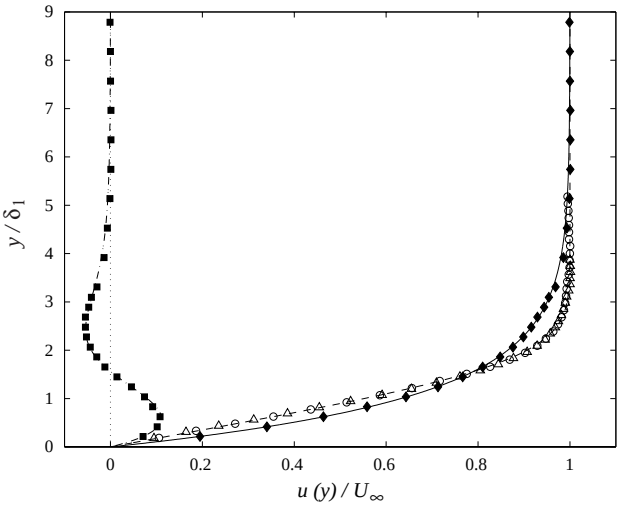

FIGURE 1. Velocity profiles for the Blasius and the asymptotic suction boundary layers. No suction (unfilled-), suction (filled symbols) and theory (lines). Asymptotic suction profile (solid line) (⧫) at $x = 1800$, Blasius profiles (dashed line) (○) at $x = 300$ mm and (△) at $x = 1800$ mm. (■) shows the difference (dash-dotted line) between the two velocity profiles.

this control method is given in Joslin (1998), where it is pointed out that LFC is a method to delay the laminar-turbulent transition and not to relaminarize the flow. The energy cost is typically one order of magnitude higher in the latter case, which makes the definition appropriate since the optimal performance is not obtained (as one may believe) when the suction completely absorbs the boundary layer. The more suction that is used the steeper the velocity gradient of the boundary layer at the wall implying an increase in skin-friction. Therefore, the balance between retaining the flow laminar and keeping a low energy consumption is actually the optimal performance.

The present paper describes theoretical and experimental work on the laminar-turbulent transition scenario on a flat plate boundary layer when uniform[1] suction through the surface is applied. A special case is when the so called asymptotic suction profile is obtained. This flow condition is obtained at some distance downstream the leading edge of a flat plate when uniform suction is applied over a large area. An interesting feature is that an analytic solution of the uniform suction problem may be derived from the boundary

[1] In a physical situation uniform suction is an idealization, since the pore size is finite. If the ratio between the boundary layer thickness and the pore size is large the suction will be close to uniform.

layer equations resulting in an exponential profile (the asymptotic suction profile). The suction has a similar influence on the profile as a favorable pressure gradient and makes the profile in the fully developed asymptotic region much more stable than the Blasius profile.

The asymptotic boundary layer flow has been dealt with extensively in text books, see for instance Schlichting (1979), and the theory for the mean flow is straightforward. One can easily show that the boundary layer profile $u(y)$ becomes

$$u/U_\infty = 1 - e^{-yV_0/\nu}$$

where U_∞, V_0 and ν are the constant free stream velocity, the suction velocity and the kinematic viscosity, respectively (x, y and z denotes the streamwise, wall-normal and spanwise coordinate directions). This expression was first derived by Griffith and Meredith (1936) according to both Jones & Watson (1963) and Schlichting (1979). In figure 1 experimental data with corresponding theoretical curves are plotted to show the comparison between the Blasius and the asymptotic suction profile. The asymptotic boundary layer thickness can be shown to be directly proportional to ν/V_0 and the Reynolds number (Re) based on the boundary layer displacement thickness (δ_1) becomes

$$Re = U_\infty/V_0 (= 1/C_\mathrm{q}),$$

where C_q is the suction coefficient.

To obtain the stability characteristics of the suction boundary layer the normal velocity component of the mean flow, i.e. the suction velocity at the wall, can be incorporated in the disturbance equation and this gives a slightly modified Orr-Sommerfeld (OS) equation. Also the boundary condition of the normal fluctuation velocity needs to be considered, but the standard boundary condition can be used in the limit when the permeability approaches zero. Hocking (1975) showed that the critical Reynolds number (Re_c), i.e. the lowest Reynolds number for which two-dimensional waves become amplified, increases by two orders of magnitude as compared to the Blasius boundary layer. Fransson & Alfredsson (2002) showed that for the case of channel flow with permeable walls and cross flow the situation becomes more complicated and can give rise to both stabilization and destabilization depending on the rate of cross flow. The critical Reynolds number is lowered by an order of magnitude ($Re_c = 667.4$) as compared to plane Poiseuille flow at a cross flow velocity of 5.7% of the streamwise velocity.

1.1. *Laminar-turbulent transition scenarios*

1.1a. *Tollmien-Schlichting wave dominated transition.* For low environmental disturbances the transition scenario from laminar to turbulent flow on a flat plate boundary layer is rather well understood. This class of transition starts with instability waves that are generated in the receptivity process taking place

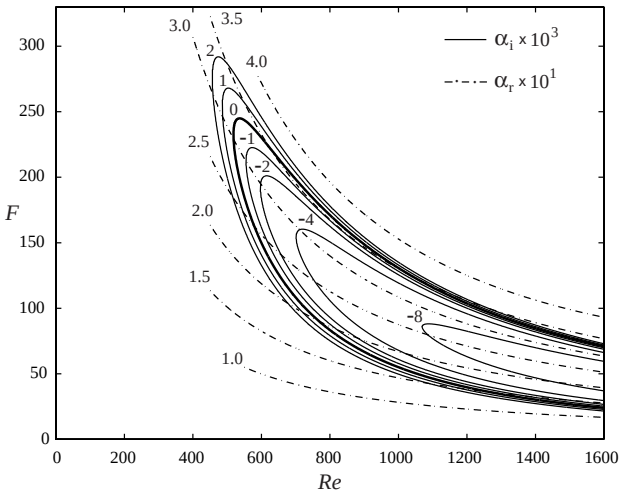

FIGURE 2. Spatial stability curves for two-dimensional waves in a Blasius boundary layer. Solid lines are for constant imaginary parts of the streamwise wavenumber (α_i) and dash-dotted for constant real parts (α_r). The bold solid line is the neutral stability curve. The displacement thickness (δ_1) is the characteristic length scale.

close to the leading edge. The initial growth of these waves may be described by Fourier modes $\propto e^{i(\alpha x-\omega t)}$, where for spatially growing waves the wavenumber α is complex. $\alpha = \alpha_r + i\alpha_i$ and the angular frequency ω is real. When assuming such a mode the linear disturbance equation gives rise to the well known OS-equation. These waves grow/decay exponentially and the critical Reynolds number, is according to *Squire's theorem*, obtained for a two-dimensional wave. In figure 2 the stability diagram (based on linear parallel theory) is given for the Blasius profile. The solid lines are contours of the growth factor (α_i) where the bold solid line shows the neutral stability curve, i.e. the contour line of $\alpha_i = 0$. The dash-dotted lines correspond to contour lines of constant wave number (α_r). The Reynolds number (Re) (which will be used throughout this paper) is based on the displacement thickness (δ_1), and F is the non-dimensionalized frequency defined as $F = (\omega\nu/U_\infty^2) \times 10^6$.

If a TS-wave in a Blasius boundary layer reaches high enough amplitude ($\gtrsim$1% of U_∞), three-dimensional waves and vortex formations develop (still laminar) that give rise to the appearance of turbulent spots which merge and bring the whole flow into a fully turbulent one. The first successful windtunnel experiment on TS-waves was carried out and reported by Schubauer & Skramstad (1948). However, these results were not in fully agreement with theory

and for long the discrepancy between linear parallel stability theory and experiments were believed to be due to the non-parallel effect of a growing boundary layer. However, Fasel & Konzelmann (1990) found out through direct numerical integration of the Navier-Stokes equations that this effect is quite small and that it hardly influences the amplitude and phase distributions. Later, parabolized stability calculations by Bertolotti (1991) showed that the non-parallel effect becomes significantly stronger for three-dimensional disturbances. Finally, the experiments by Klingmann *et al.* (1993), performed with a special designed asymmetric leading edge (in order to get rid of the pressure suction peak), could show excellent agreement with non-parallel theory, which is close to the parallel theory results for two-dimensional disturbances.

1.1b. *By-pass transition and streaky structure.* It is well known that for the Blasius boundary layer FST induces disturbances into the boundary layer which give rise to streamwise-oriented structures of low and high speed fluid (see e.g. Kendall 1985; Westin 1997; Jacobs & Durbin 2001; Matsubara & Alfredsson 2001; Fransson & Westin 2001, for thorough investigations of such a flow). These structures grow in amplitude and establish a spanwise size which is of the order of the boundary layer thickness far away from the leading edge. When the streaks reach a certain amplitude they break down to turbulence, probably through a secondary instability mechanism (see e.g. Andersson *et al.* 2001). This type of boundary layer transition can be viewed as one case of by-pass transition (Morkovin 1969). It is a relatively rapid process by-passing the traditional TS-wave dominated transition process resulting in breakdown to turbulence at subcritical Reynolds numbers when compared with the predicted value by traditional theory. Nonlinear theories were tested (see e.g. Orszag & Patera 1983) in order to find a theory that matched experimental results. However, the nonlinear terms of the Navier-Stokes equations can be shown not to be part of the growth mechanism (see Drazin & Reid 1981). A possible mechanism governing this type of transition scenario is the transient growth. An explanation of this mechanism is given in e.g. Schmid & Henningson (2001) and arises due to the non-orthogonality of the OS and Squire eigenmodes. Superposition of such decaying modes may first experience an algebraic growth followed by an exponential decay, denoted as transient growth. The "lift-up" mechanism proposed by Landahl (1980) is the cornerstone contributing to the algebraic growth in the study of transient growth. Small perturbations in the wall-normal direction induce large disturbances in the streamwise direction due to the lift-up of low speed fluid that originally maintains its horizontal momentum. The presence of viscosity will eventually damp the growth and finally make the disturbance decay. Some recent publications on the by-pass transition and the transient growth mechanism are Luchini (2000), Reshotko (2001), and Andersson *et al.* (2001).

1.2. *Previous work on suction*

Experimental work on the asymptotic suction boundary layer has to some extent been done earlier, but mainly devoted to determination of the mean flow (see Schlichting 1979, and references therein). TS-wave as well as FST experiments in a fully asymptotic suction boundary layer, that will be presented in this paper, have not been carried out earlier. However, in connection to drag reduction experiments (i.e. LFC) suction through spanwise slots, porous panels or discrete holes has been applied (see e.g. Pfenninger & Groth 1961, Reynolds & Saric 1986, and MacManus & Eaton 2000 as well as Roberts *et al.* 2001, respectively). A general review of various types of surfaces and of the results achieved in wind tunnel tests is given by Gregory (1961), where pros and cons for practical applications on aircraft are discussed. The flow characteristics through laser drilled titanium sheets were investigated by Poll *et al.* (1992*b*) and was shown to be laminar, incompressible and pipe like. Poll *et al.* (1992*a*) conducted a cylinder experiment made of a similar laser drilled titanium sheet. The effect of suction was found to have a powerful effect upon cross-flow induced transition.

In an experimental and numerical study performed by MacManus & Eaton (2000) the flow physics of boundary layer suction through discrete holes was investigated. The aim was to use a realizable design and find a critical suction criterion for transonic cruise conditions. They showed that the suction may destabilize the flow by introduction of contra-rotating streamwise vortices but that for small enough perforations ($d/\delta_1 < 0.6$) transition is not provoked by suction independent of suction velocity.

Roberts *et al.* (2001) found that two types of instability are possible when non-uniformities of suction are present. The first one is connected to the classical TS-wave that is modified due to the non-uniformities and the second one are streamwise vortices that are induced due to the non-uniformities alone. The latter instability was triggered by a finite band of suction wave numbers and the strength of this instability was shown to increase almost linearly with the amplitude of the suction non-uniformities and flow Reynolds number.

Applying continuously distributed suction over a large area may not be the optimal way of performing active control practically, since the energy consumption becomes relatively high. Another approach would be to use selective suction to control the growth of unstable fluctuations. This type of control must be done on a detectable quantity, such as e.g. low speed streaks. The appearance of streaks with alternate low and high speed velocity observed in a laminar boundary layer subjected to high levels of free stream turbulence is also found in the near-wall region of a turbulent boundary layer. Together with the intermittent bursts or turbulence production events these are usually referred to as coherent structures. Controlled experiments have been performed, see e.g. Myose & Blackwelder (1995) and Lundell (2000), in order to reduce the

instability and delay the breakdown of the low speed streaks in laminar flows. Myose & Blackwelder (1995) achieved successful control on the breakdown of Görtler vortices, by pointwise suction of low speed momentum from the low speed streak and in that manner delay the transition by producing a fuller profile in the normal direction and by eliminating the difference between low and high speed regions in the spanwise direction. A similar technique was used by Lundell (2000) who generated streaks in a plane channel flow by applying suction through streamwise slots. Secondary instabilities were then forced randomly by speakers and were then successfully controlled by localized suction some distance downstream.

1.3. *Layout of the paper*

In §2 the boundary layer equations for the evolution of the asymptotic suction boundary layer is put forward as well as the stability equations when the normal velocity is taken into account. Some results on both the mean profile evolution and stability are then given for the asymptotic suction boundary layer. The design philosophy of the leading edge of the experimental plate is described in §3 together with characterization of the porous material, the detailed construction of the flat plate, and the TS-wave excitation method. Herein the different turbulent length scales and energy spectra generated by the three different turbulence generating grids are also given. In §4 the experimental results are given both for the Blasius flow above the porous plate and the streamwise baseline flow of the suction case as well as the corresponding TS-waves results. Furthermore, results of the disturbance evolution in both the no suction and suction cases when FST is present are given and compared in detail. It is clearly shown that suction dramatically can change the disturbance growth rate and that transition to turbulence can be prevented.

2. Boundary layer evolution and stability concepts

2.1. *Evolution region*

When uniform wall-normal surface suction is applied over a large area the well known asymptotic suction profile will be reached after some evolution region. If an impermeable area is considered from the leading edge to where the suction starts the boundary layer will be allowed to grow and a Blasius velocity profile will be developed for a zero pressure gradient flow. In the evolution region the profile will then undergo a transformation from the Blasius state to the asymptotic suction state. This spatial evolution can from a simple approach be described through a non-dimensional evolution equation. The first step is to introduce a stream function according to

$$\psi = \sqrt{\nu x U_\infty} f(\xi, \eta) \ ,$$

$$\xi = x\frac{V_0}{U_\infty}\sqrt{\frac{U_\infty}{\nu x}}\ ; \qquad \eta = y\sqrt{\frac{U_\infty}{\nu x}}\ .$$

The streamwise and normal velocity components are recovered through

$$u(\eta) = U_\infty \frac{\partial f}{\partial \eta} \qquad \text{and} \qquad v(\eta) = \sqrt{\frac{U_\infty \nu}{4x}}\left(\eta\frac{\partial f}{\partial \eta} - \xi\frac{\partial f}{\partial \xi} - f\right)\ ,$$

respectively. When applied to the boundary layer equations we get the following third order non-linear partial differential equation

$$\frac{\partial^3 f}{\partial \eta^3} + \frac{1}{2}f\frac{\partial^2 f}{\partial \eta^2} + \frac{1}{2}\xi\left(\frac{\partial f}{\partial \xi}\frac{\partial^2 f}{\partial \eta^2} - \frac{\partial f}{\partial \eta}\frac{\partial^2 f}{\partial \eta \partial \xi}\right) = 0, \tag{1}$$

with the corresponding boundary conditions

$$\left.\begin{array}{rcll} f & = & \xi & \text{(suction)} \\ \frac{\partial f}{\partial \eta} & = & 0 & \text{(no-slip)} \end{array}\right\} \quad \text{at} \quad \eta = 0 \quad \text{and} \quad \frac{\partial f}{\partial \eta} \to 1 \quad \text{as} \quad \eta \to \infty\ .$$

Along the impermeable entry length a Blasius boundary layer is assumed to develop and is given as input to the evolution equation. The boundary conditions at permeable surfaces are not obvious. Taylor (1971) discussed the boundary conditions and concluded that due to the open structure of a porous solid with large pores the external surface stress may produce a tangential flow below the surface resulting in that the no-slip condition for the mean flow is not valid. This surface velocity is assumed to depend on the mean tangential stress in the fluid outside the porous material, the permeability and another material (porous) connected parameter. This model showed that experimental results agreed well with calculation but has only influence for large permeabilities.

The first solution from such an evolution equation with an impermeable entry length was obtained by Rheinboldt (1956) through series expansion. The ansatz of a stream function and non-dimensionalized variables for deriving the evolution equation are not to be confused with similarity solutions. The stream function is dependent on two variables and becomes 'similar' when the asymptotic suction state is reached. In figure 3 the displacement thickness (δ_1) of the profiles in the evolution region is plotted. The different curves can be seen as different impermeable entry lengths shown with the dotted lines, i.e. they belong to different values of the initial length (ξ_L). These are the positions where suction starts and what all the curves have in common is that after some evolution region they all merge together to a value of unity which corresponds to the asymptotic suction region. Recall that the asymptotic suction profile possesses an analytic expression which implies that all the characteristic length

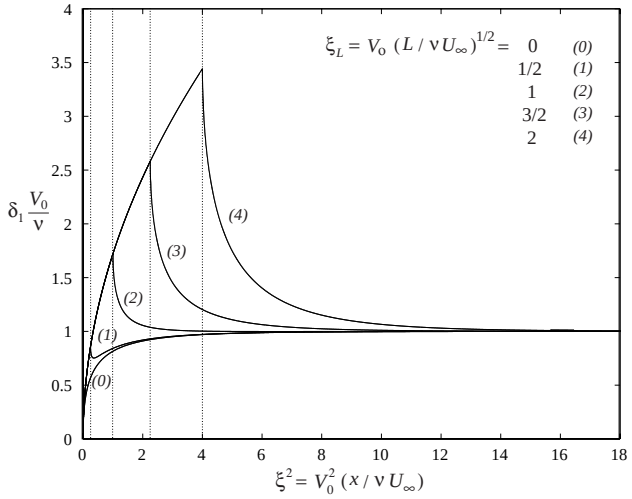

FIGURE 3. The displacement thickness evolution from the evolution equation (1) vs the downstream distance to the power of two. See text for comments.

scales are exact, e.g. $\delta_1 = \nu/V_0$, $\delta_2 = (1/2)\delta_1$ and $\delta_{0.99} = \delta_1 \log(100)$, where δ_2 and $\delta_{0.99}$ are the momentum thickness and the actual boundary layer thickness respectively.

2.2. *Modal stability characteristics*

When deriving the Orr-Sommerfeld (OS) and Squire equations the so called parallel flow assumption is made, which means that changes in x of the mean flow is neglected. For the continuous suction case where the mean wall-normal velocity component (V_0) is uniform and constant this assumption is exact, although the flow is not parallel to the wall. In order to neglect the V-component the suction rate has to be small. However, the parallel flow assumption is not needed since the cross-flow term easily can be considered.

When the following baseline flow, $\overline{U} = (U(y), V_0, 0)$, is introduced into the linearized stability equations one extra term is added to each equation, namely $V_0 \frac{\partial u}{\partial y}$, $V_0 \frac{\partial v}{\partial y}$, and $V_0 \frac{\partial w}{\partial y}$. Here (u, v, w) denotes the fluctuation velocity components in the (x, y, z) directions, respectively. The expression for the pressure, achieved by taking the divergence of the linearized momentum equations, does not change (compared to the no suction case) since the additional terms fulfill the continuity equation and therefore cancel out. After that the pressure expression is used in the v-equation of momentum we apply the normal mode hypothesis. Using the standard notations for the spatial theory, α represents the complex streamwise wave number, ω the real angular frequency and β the

real spanwise wave number which is used in order to possibly include oblique modes. The modified OS-equation can then be written as

$$\left[(-i\omega + i\alpha U - \frac{1}{Re}\mathcal{D})(\mathcal{D}^2 - k^2) - i\alpha U'' - \frac{1}{Re}(\mathcal{D}^2 - k^2)^2\right]\hat{v} = 0 \ ,$$

where $\mathcal{D} = \partial/\partial y$, $k^2 = \alpha^2 + \beta^2$ and $\hat{v}$ denotes the amplitude function of the eigenmode. This modified version of the OS-equation can e.g. be found in Drazin & Reid (1981). Continuing from here a modified Squire equation can equally be derived resulting in

$$\left[(-i\omega + i\alpha U - \frac{1}{Re}\mathcal{D}) - \frac{1}{Re}(\mathcal{D}^2 - k^2)\right]\hat{\Omega} = -i\beta U'\hat{v} \ ,$$

where Ω is the normal vorticity. So far no change of the boundary conditions of the disturbance quantities has been made and should indeed not be necessary as long as the permeability of the porous material has a reasonably low value.

In the present study the homogeneous boundary condition was used, i.e. $\hat{v} = \mathcal{D}\hat{v} = \hat{\Omega} = 0$, in all calculations since the permeability for the chosen material can be considered small.

Another boundary condition for the perturbations of a porous plate was suggested by Gustavsson (2000), where a pressure perturbation above the plate is added to Darcy's law. The result is an extra term for the boundary condition at the wall, which for small permeability would be negligible. This condition has so far not been verified experimentally.

Squire's theorem can be derived from the modified OS- and Squire equations in the usual way by identification of terms in the two-dimensional and three-dimensional cases. However, the extra terms do not contribute to any additional condition to Squire's theorem.

2.3. *Numerical methods*

The evolution equation was solved with a spectral approach, where Chebyshev expansion was made in the wall-normal direction and a backward finite difference method in the marching direction with a step size of $d\xi = 0.001$. A built in non-linear equation solver in the commercially available software Matlab was used.

The stability calculations carried out on the Blasius and the asymptotic suction boundary layer in the present chapter are for the spatial spectrum, i.e. the set of equations are solved for α given a real frequency ω.

The numerical method used for these calculations was also a spectral method with Chebyshev expansion of the dependent variable. The solution

is then represented by a truncated sum of Chebyshev polynomials according to

$$\hat{v}(\tilde{y}) = \sum_{n=0}^{N} a_n \mathbb{T}_n^j(\tilde{y}) \quad \text{for} \quad \tilde{y} \in [-1, 1] \ ,$$

where N is the truncated value, a_n is the coefficient of the n:th Chebyshev polynomial and the superscript ^{j} denotes the j:th derivative of the Chebyshev polynomials. A domain mapping from the finite Chebyshev domain ($[-1, 1]$) into the semi-infinite physical domain of the boundary layer was made through $y = \frac{y_\infty}{2}(1 - \tilde{y})$.

A spatial approach gives rise to a nonlinear eigenvalue problem where the eigenvalue appears as a fourth power in the normal velocity. This can be reduced to an eigenvalue equation of second power by a transformation of the independent variable according to Haj-Hariri (1988)

$$\begin{pmatrix} \hat{v} \\ \hat{\Omega} \end{pmatrix} = \begin{pmatrix} \hat{V} \\ \hat{E} \end{pmatrix} e^{-\alpha y}. \tag{2}$$

In order to get rid of the non-linearity in the eigenvalue problem, i.e. the now remaining second order α-terms of the $\hat{V}$-component, one can introduce a vector quantity according to

$$\mathbf{d} = \begin{pmatrix} \alpha\hat{V} \\ \hat{V} \\ \hat{E} \end{pmatrix}$$

which takes care of the non-linear α-terms, see e.g. Schmid & Henningson (2001). After applying the transformation of equation (2) on the perturbation equations we get a linear eigenvalue problem which in matrix form can be written

$$\mathcal{L}\mathbf{d} = \alpha\mathcal{M}\mathbf{d}, \tag{3}$$

where

$$\mathcal{L} = \begin{pmatrix} -R_1 & -R_0 & 0 \\ I & 0 & 0 \\ 0 & -S & -T_0 \end{pmatrix} \quad \text{and} \quad \mathcal{M} = \begin{pmatrix} R_2 & 0 & 0 \\ 0 & I & 0 \\ 0 & 0 & T_1 \end{pmatrix}. \tag{4}$$

The R_i, T_i and S elements represent a number of terms and the only difference between the OS and Squire equations and the modified OS and Squire equations is the appearance of some extra terms that are marked below

	Drazin & Reid		*Schmid & Henningson*	*Present*	
CASE	Blasius	Asymp.	Blasius	Blasius	Asymp.
Re_c	520	54370	519.4	518.7	54382
α_c	0.3012	0.1555	0.303	0.3036	0.1555
c_r^c	0.3961	0.150	0.3965	0.3966	0.1499
F	229.3	0.429	231.3	232.1	0.429

TABLE 1. Critical values for the Blasius and the asymptotic suction boundary layer.

$$
\begin{aligned}
R_2 &= 4\mathbb{T}^2 + 2iURe\mathbb{T}^1 + \underbrace{2\mathbb{T}^1}_{extra} \\
R_1 &= -4\mathbb{T}^3 - iURe\mathbb{T}^2 - \underbrace{3\mathbb{T}^2}_{extra} - 2i\omega Re\mathbb{T}^1 + 4\beta^2\mathbb{T}^1 + \\
&+ iURe\beta^2\mathbb{T}^0 + iU''Re\mathbb{T}^0 + \underbrace{\beta^2\mathbb{T}^0}_{extra} \\
R_0 &= \mathbb{T}^4 + \underbrace{\mathbb{T}^3}_{extra} + i\omega Re\mathbb{T}^2 - 2\beta^2\mathbb{T}^2 - \underbrace{\beta^2\mathbb{T}^1}_{extra} - i\omega\beta^2 Re\mathbb{T}^0 + \\
&+ \beta^4\mathbb{T}^0 \\
T_1 &= \mathbb{T}^1 + iURe\mathbb{T}^0 + \underbrace{\mathbb{T}^0}_{extra} \\
T_0 &= -\mathbb{T}^2 - \underbrace{\mathbb{T}^1}_{extra} - i\omega Re\mathbb{T}^0 + \beta^2\mathbb{T}^0 \\
S &= i\beta U' Re\mathbb{T}^0 \ .
\end{aligned}
$$

The notation of the elements in the matrixes (4) are chosen to be the same as used by Schmid & Henningson (2001).

The system of equations (3) was solved using a built-in eigenvalue problem solver in the mathematical software Matlab.

A (temporal) program using search routines was developed in order to provide high accuracy of the critical values given in table 1. For a given wave number (α) this program searches for the Reynolds number where the imaginary part of the phase velocity (c_i) is zero with an accuracy specified by the

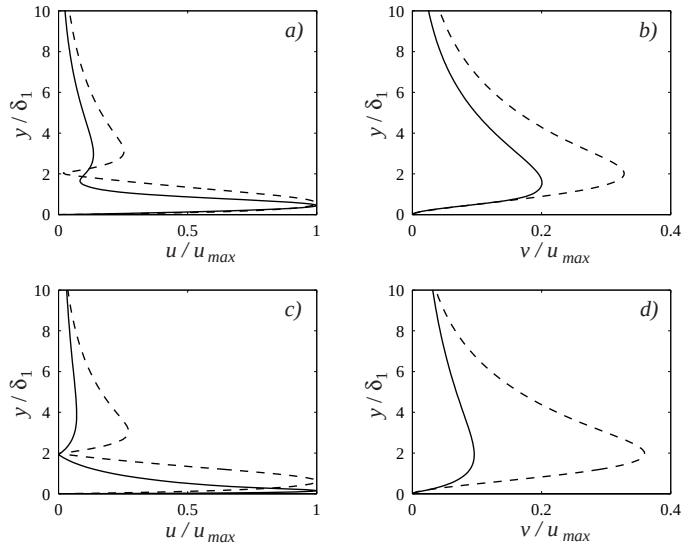

FIGURE 4. Eigenfunctions of both the Blasius (dashed lines) and the asymptotic suction case (solid lines) at $[Re, F] = [800, 125]$ in a) and b), and at their critical values (see table 1) in c) and d) respectively.

user and stops only for positive values of c_i. From there it chooses a new α by means of minimizing Re. The accuracy of α is also set by the user. The critical values in table 1 are in good agreement with other published values, see e.g. Drazin & Reid (1981) and Schmid & Henningson (2001), and the slightly varying values may be due to the solution method. Adding the V-component into the linearized stability equations, resulting in the modified OS-equation, has only a minor effect on the stability characteristics of the particular flow. The large stabilizing effect arises from the mean velocity profile change, see e.g. Fransson (2001).

In figure 4 the difference between the Blasius and the asymptotic suction boundary layer eigenfunctions (streamwise and wall-normal) are illustrated for two different parameter values. It is noteworthy that the maximum of the u-disturbance is found closer to the wall and that the ratio between the v- and the u-component is smaller for the asymptotic suction boundary layer as compared to the Blasius boundary layer.

3. Experimental design and set-up

This section deals with the design of the experimental set-up, the construction work, and the experimental techniques. In order to perform experiments in an

asymptotic suction boundary layer a plate had to be designed and built with a suitable permeable surface material. This material was investigated in order to get the characteristic properties of this porous material. In connection to the design a new asymmetric leading edge was built and investigated.

3.1. *Experimental set-up*

The experiments were carried out in the MTL-wind tunnel at KTH. The test section is 7 m long, 0.8 m high and 1.2 m wide. The maximum free stream velocity in the test-section is more than 60 m s^{-1}, however in the present study it is only used at low velocities. At these low velocities the turbulence intensity is around 0.02%-0.03%. The tunnel has good temperature stability characteristics due to a built in heat-exchanger and temperature control system. The wind tunnel is equipped with a computer controlled 5 degree of freedom traversing mechanism, which is convenient for boundary layer traverses as well as X-probe calibration. For a recent report on the tunnel characteristics see Lindgren & Johansson (2002).

A schematic of the experimental set-up is shown in figure 5, and is divided into two figures showing the FST experimental set-up and the TS-wave experimental set-up in a) and b), respectively. Everything present in a) is also present in b) except for the turbulence generating grids. A fine-meshed screen (mosquito type) was installed at the end of the test section just upstream the trailing edge flap (going into the diffuser). This was done in order to create a pressure drop to compensate for the extra blockage below the plate due to suction channels and tubing (the total blockage in the tunnel is about 7%). In the present experiments the wind tunnel ceiling was adjusted so that the pressure gradient along the test section was close to zero for the no suction (Blasius flow) case. When suction was applied less than 1 % of the flow in the test section was removed. This gives rise to a slight adverse pressure gradient, however the effect on the boundary layer flow is very small as compared to the suction itself. The suction is achieved by a centrifugal fan positioned outside the test section and is connected through a pressure vessel to the suction channels underneath the plate with vacuum cleaner tubing.

FST was generated by three different grids (two passive, B and E, and one active, G) mounted at different distances (x_{grid}) from the leading edge. The grids gave turbulence intensities ($Tu = u_{\mathrm{rms}}/U_\infty$) at the leading edge of the plate of 1.4%, 4.0% and 2.2%, respectively. In figures 6 and 7 the energy spectra (at x=400 mm) and the FST decay in the free stream for the three different grids are plotted respectively. To the Tu-decay data the typical power-law decay, $Tu = C(x - x_0)^b$, is applied and plotted with solid lines in figure 7 for the three different grids. Here $x = 0$ is at the leading edge of the plate, whereas x_0 is a virtual origin. The constant C and exponent b are parameters to be determined through curve fit to experimental data. In the curve fits b was set to -0.5 which is the value for fully isotropic turbulence. The virtual

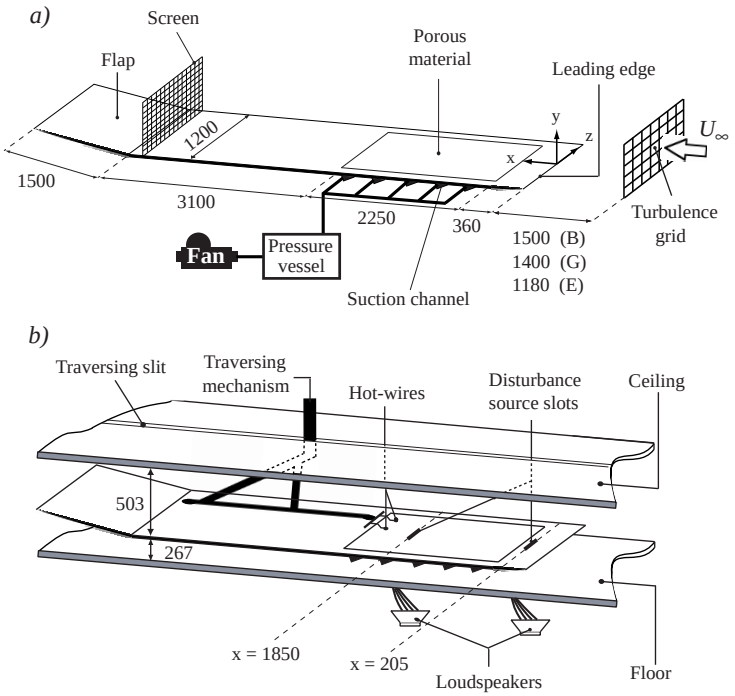

FIGURE 5. Schematic of the experimental set-up. a) The three turbulence generating grids give different turbulence intensities at the leading edge. $Tu_{\mathrm{B}} = 1.4\%$, $Tu_{\mathrm{E}} = 4.0\%$ and grid G being an active grid was used at $Tu_{\mathrm{G}} = 2.2\%$. b) 2D-waves were generated through two different slots in the plate.

origin has been determined consistently by taking the intersection point with the x/M-axis when $1/Tu^2 = x/M$ is plotted (M being the meshwidth of the grid). The fits are done to the unfilled symbols in figure 7, which corresponds to data collected when no suction was applied whilst the filled symbols are when suction was applied. The virtual origin is found to be displaced downstream of the grid for all cases (see figure 5a)).

The active turbulence generating grid, injecting secondary fluid upstream and in that way allowing different Tu-levels, is described thoroughly in Fransson (2001) and in figure 8 a sketch of the grid is shown. The secondary fluid was driven by a modified vacuum cleaner. In the present investigation only one injection rate was applied. In figure 9 both the evolution of the longitudinal Taylor micro lengthscale (γ) and of the integral lengthscale (Γ) are shown for the active grid. As expected the scales grow with the downstream distance due to the dissipation of the smallest scales. The flow behind the active grid

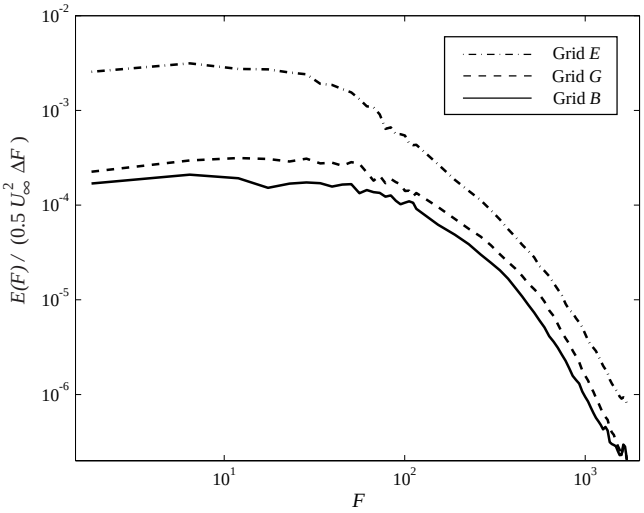

FIGURE 6. Energy spectra in the free stream from the three different grids at x=400 mm.

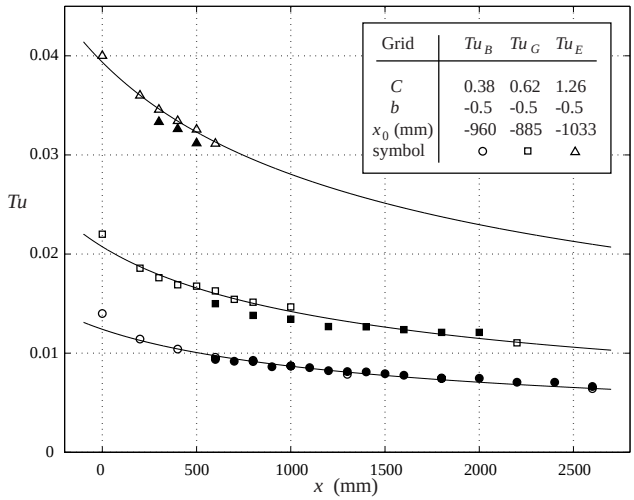

FIGURE 7. Turbulence decay in the free stream for the three different turbulence generating grids.

is homogeneous and isotropic $20M$ downstream the grid position, which was checked with X-probe measurements. The two passive grids have been used

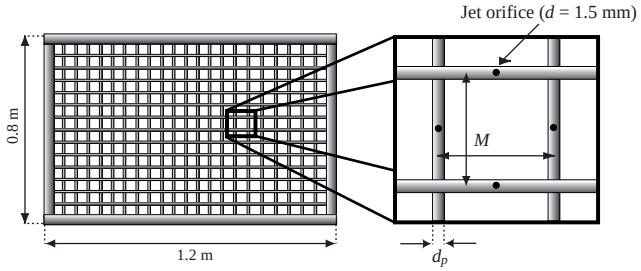

FIGURE 8. Active grid with main measures. $M = 50$ mm and $d_p = 5$ mm corresponding to a geometrical solidity (S_g) of 0.19. The total amount of jet orifices are 254 and these are concentrated to the middle section of the grid.

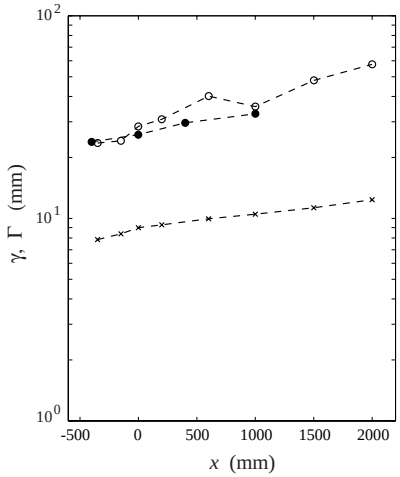

FIGURE 9. The Taylor (γ) and the integral (Γ) lengthscale evolution of the active grid (with injection) are plotted with ($\circ$) and ($\times$)-symbols respectively. Filled symbols of Γ are from spatial correlation measurements and unfilled from the autocorrelation. γ was determined from the autocorrelation alone which gives a better estimate of this scale (see Fransson 2001, for further details).

extensively in previous works and the Taylor microscale data have been obtained from Westin (1997). In table 2 the characteristic data of the turbulence generating grids are summarized.

TS-waves were generated by alternating suction and blowing at the wall through a slot in a plug mounted in the plate. The slot is 330 mm long in

Grid	Tu (%)	γ (mm)	M (mm)	d_p (mm)	S_g	Bar geometry	x_{grid} (mm)	
B	1.4	7±1	23	3.5	0.28	round	-1500	$(65M)$
E	4.0	7±1	50	10	0.36	square	-1180	$(23.5M)$
G	2.2	9±1	50	5	0.19	round	-1400	$(28M)$

TABLE 2. Characteristic data of the turbulence generating grids. For definitions of M, d_p and S_g see figure 8.

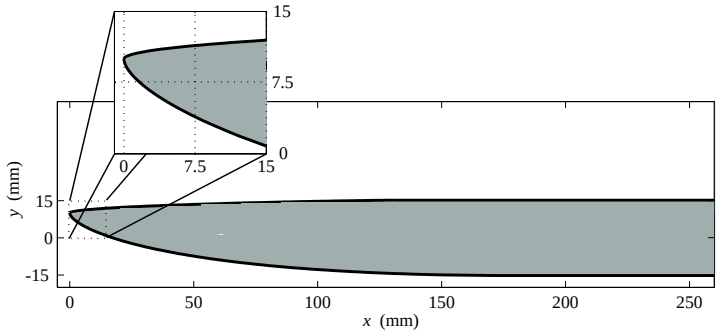

FIGURE 10. Final shape of the leading edge. The profile is described by two cubic Bézier curves.

the spanwise direction and 0.8 mm wide. Two plugs (slots) are present, one at x=205 mm from the leading edge and one at x=1850 mm. The latter is used for investigations in the fully developed asymptotic suction boundary layer. At the second plug the porous plate was made impermeable over the whole spanwise width by putting a tape underneath the plate over the 50 mm in the the flow direction where the plug was located (in order to keep the two-dimensionality of the flow). The disturbance signal was generated by the computer through a D/A-board to an audio amplifier driving the loudspeakers. The loudspeakers are connected to the disturbance source through ten flexible tubes. A more thorough description of the disturbance generating system can be found in Elofsson (1998).

An asymmetric leading edge was specially designed for this experimental set-up, which resulted in a relatively short pressure gradient region without any suction peak at the leading edge. The local pressure distribution near the leading edge influences the stability of the flow further downstream and therefore the design of the leading edge is an important issue, see e.g. Klingmann *et al.* (1993). In figure 10 the final shape of the present leading edge, which is described by two cubic Bézier-curves, is shown. The commercial flow

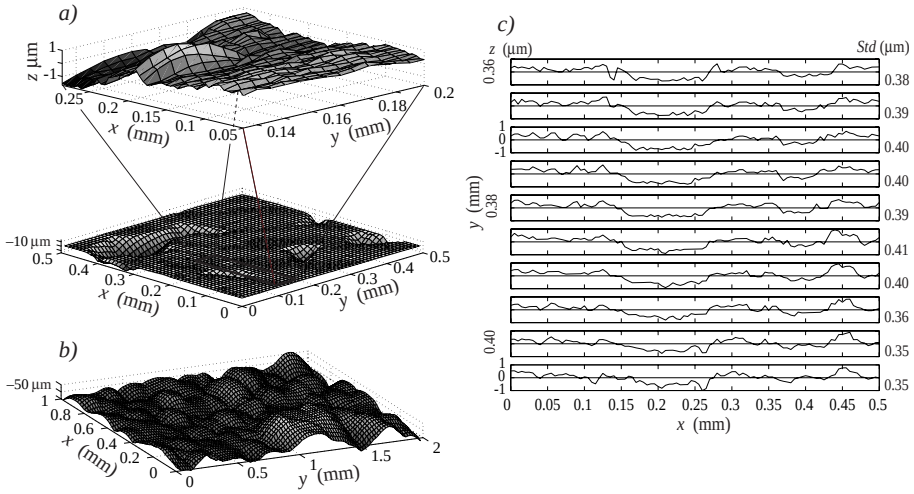

FIGURE 11. Surface roughness measurement of the porous material. a) smooth side with a blow-up area and b) rough side. c) shows the surface traces from a part of the area shown in a).

solver CFX 4.2 was used to design the leading edge for the present set-up. Two-dimensional laminar flow calculations were performed in the test section of the wind tunnel, i.e. the ceiling (upper wall) and the floor (lower wall) of the tunnel were simulated together with the plate. The present leading edge (with a thickness of 30 mm) gives a near Blasius profile as close as 100 mm from the leading edge, when the suction channel and the suction tubing are absent from the set-up. The analytic expression of the shape and further information about the design process together with experimental verification of the design can be found in Fransson (2001).

3.2. *Porous material*

As a permeable plate a porous plastic material was chosen. Compared to laser drilled plates (discrete holes) it is only one tenth of the price and it has some advantages. For instance, the plastic material allows quite accurate hot-wire readings close to the wall due to the low heat conductivity, and its pore size and pore spacing is small making the surface-normal velocity "uniform" over the surface area which is preferable in this experiment in contrast with what would be obtained in an experiment with a plate with discrete holes.

The porous plates consist of a sintered plastic material with an average pore size of 16 μm (given by the manufacturer). One of the surfaces can be considered smooth and the other rough (the smooth one was used as the upper

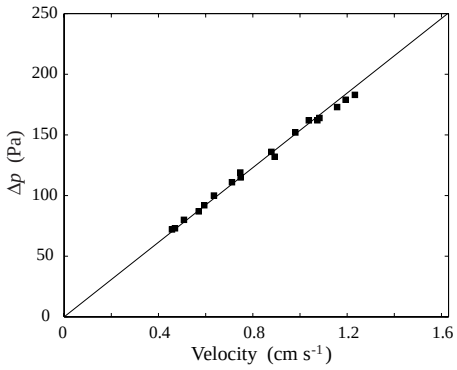

FIGURE 12. Piston-experiment result used to determine the permeability of the porous material.

surface). The standard deviation of the roughness is about 0.38 μm on the smooth side, which was calculated from a surface roughness measurement seen in figure 11a) and b) (note the scale). In figure 11c) the needle traces from the blow-up area in a) is shown.

The flow properties of the porous material were characterized through a piston-experiment where the permeability of the porous material was determined. This was done by placing a piece of the porous material (thickness t = 3.2 mm) at the end of a 0.9 meter, 4 cm diameter Plexiglass pipe and measuring the pressure drop over the porous material when a piston was forced through the pipe with a linear motor. This was done at various velocities (V) in the range 0.4-1.2 cm^{-1} and it was found that the pressure drop Δp varied in linear proportion to the flow velocity through the material (see figure 12 for the measurement result). From this the permeability (k) of the material was determined from Darcy's law as $k = Vt\mu/\Delta p$ where μ is the dynamic viscosity and was found to be $k = 3.7 \times 10^{-12}\mathrm{m}^2$.

A load-test of the porous material was performed in order to be able to design the inner structure of the plate such that the surface deformation was sufficiently small when suction was applied. Three tests were performed and the average modulus of elasticity was determined to be 974 MPa. On the suction side longitudinal T-profiles with a certain spanwise interval distance supported the plate. The spanwise distance (L_s) between the T-profiles, supporting the porous plates, was determined by assuming a 1.5 kPa pressure difference across the plate with a restriction of a bending deviation (w_b) of less than 1% of the boundary layer thickness (being 5 mm resulting in w_b = 50 μm). This gave L_s = 58 mm and the L_s finally used was 50 mm. Since the actual pressure difference that was applied in the final experiment was about 200-250 Pa there was a large margin in the load assumption.

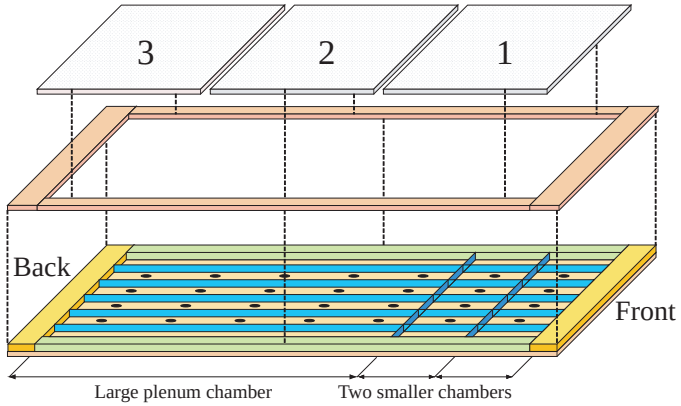

FIGURE 13. Schematic view of the plate construction. See text for comments.

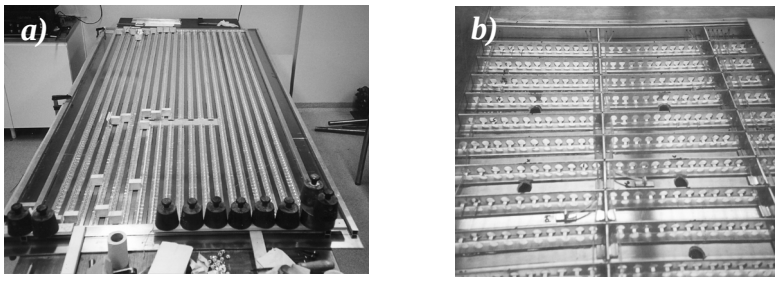

FIGURE 14. Photos of the construction work. Photo b) shows the two front plenum chambers together with the larger spanwise drilled suction holes and the pressure tubing for the static pressure measurements.

3.3. *Plate construction*

The test plate is built as a sandwich-construction and a schematic is shown in figure 13. In the front of the plate the removable leading edge is mounted and in the back there is a possibility to extend the plate by additional plates of aluminum. The plate is constructed on a base plate of aluminum with a frame, and is designed having two 250 mm long plenum chambers starting 360 mm from the leading edge followed by a 1750 mm long plenum chamber. The subdivision into three chambers is for future work in where the suction rate then is allowed to change with the downstream distance. Inside the plenum chamber spacing elements made of hollowed T-profiles are glued, with a spanwise separation of 50 mm, in order to support the porous plates and avoid bending the plates when suction is applied. On these T-profiles three porous plates with the

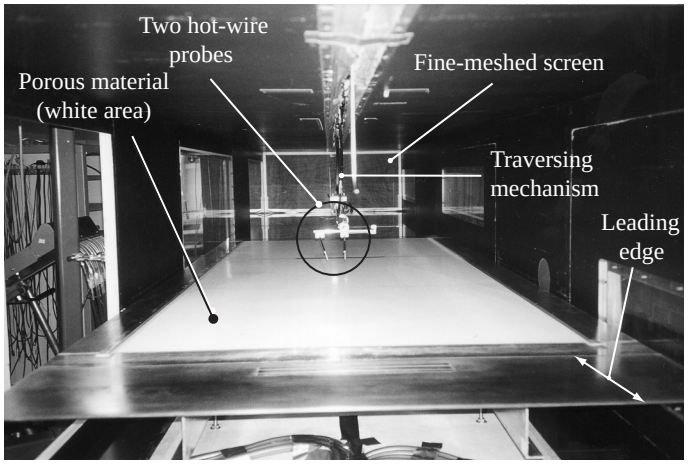

FIGURE 15. Photo of the plate together with the leading edge mounted in the windtunnel.

total dimension $2250 \times 1000 \times 3.2$ mm^3 (length, width, thickness) were mounted into the frame plate. On a spanwise line in the base plate five large holes (30 mm) were drilled at nine positions to where nine suction channels were connected. This secured a uniform pressure in the plenum chamber, which was checked by measuring the the static pressure at 40 different positions in the chamber. In figure 14 photos are shown of the construction process work. The two front chambers are seen in 14b) as well as the larger spanwise distributed suction holes. Finally, the finished plate mounted in the test-section of the MTL windtunnel is shown in figure 15.

3.4. *Measurement technique*

Single hot-wire probes operating at constant temperature were used to measure the streamwise velocity components. One probe could be traversed in all three spatial directions whereas a second probe was located at a specific spanwise position (in the centre of the tunnel). Both probes were traversed in the x and y-directions by the same traversing system and their x and y positions were the same. This made it possible to make two-point spanwise space correlation measurements.

The single probes were made of 2.5 μm platinum wires with a distance between the prongs of approximately 0.5 mm. The calibration function according to Johansson & Alfredsson (1982) was used, where an extra term is added to King's law for compensation of natural convection which makes it suitable for low speed experiments and is shown below,

$$U = k_1(E^2 - E_0^2)^{1/n} + k_2(E - E_0)^{1/2}.$$

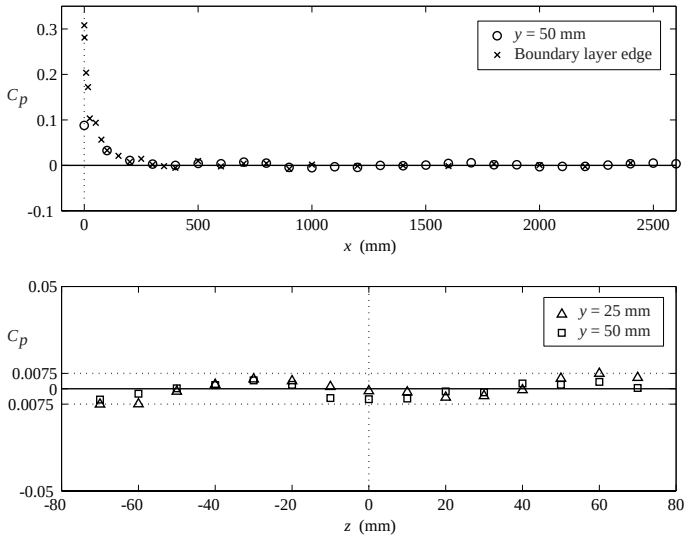

FIGURE 16. Pressure distribution in the test-section. a) Streamwise-, and b) spanwise distribution at $x = 300$ mm.

4. Experimental results

In the next three sections the experimental results will be shown and discussed. In the first section the results for the Blasius boundary layer will be presented showing the baseline flow properties and TS-wave experiments. The next section shows the evolution region (from the Blasius to the asymptotic suction state) followed by TS-wave experiments in the asymptotic suction region. Finally FST experiments will be presented where the Blasius and the asymptotic suction results are chosen to be presented together for direct comparisons.

The experiments reported here were made at a free stream speed of 5.0 m s^{-1}. Since stability experiments are sensitive to the Reynolds number Re, accurate determination of the viscosity is necessary meaning that both temperature and pressure has to be monitored and measured. For the suction case the suction speed was 1.44 cm s^{-1}, corresponding to a pressure difference across the porous plate of Δp=221 Pa. This gives an asymptotic boundary layer thickness of 5 mm and a Reynolds number based on the displacement thickness of 347, which corresponds to $C_{\mathrm{q}} = 2.88 \times 10^{-3}$.

4.1. *TS-waves in a Blasius boundary layer*

In order to verify the flow set-up, measurement technique and disturbance generation, the stability characteristics of the Blasius boundary layer for 2D-wave disturbances were determined and compared with previously reported results from the MTL-wind tunnel.

The pressure distribution over the plate was determined by traversing a hot wire close to the plate surface but outside the boundary layer using the Bernouilli equation to obtain the pressure. This method has earlier been used and verified by Klingmann *et al.* (1993) and gives better accuracy than a static pressure tube for low velocities. In figure 16a) the streamwise pressure distribution is plotted for the investigated downstream region on the flat plate. Two different measurements are shown, one at constant y(=50 mm) and the other by traversing the probe to a position just outside the boundary layer. As can be seen there is hardly any difference between the two measurements except at the leading edge, and the variation for x >300 mm is within $\pm 1\%$ of the dynamic pressure. The relatively long pressure gradient region observed in figure 16a) is due to the thickening of the plate due to suction channels and tubing underneath the plate that are present in this experiment. The suction channels alone contributes to an extra vertical blockage of 35 mm. In figure 16b) the spanwise pressure distribution is plotted over a spanwise distance of 140 mm at x=300 mm for two different y-positions in the free stream, and is shown to vary within $\pm 0.75\%$ of the dynamic pressure. As expected measured boundary layer profiles from x=300-2400 mm and z=$\pm$70 mm show excellent agreement with the Blasius profile, for details see Fransson (2001). It is notable that the hot-wire reading very close to the wall is quite accurate, making it possible to measure velocities down to 0.5 m s^{-1} without any deviation from the theoretical curve (cf. figure 1). This is due to the calibration function as well as the low heat conductivity of the porous material.

Controlled stability experiments were performed, where the studied disturbance is generated with a known frequency. The first slot located in the leading edge is used to verify the experimental set-up, and the second slot far downstream was used to perform experiments that later will be compared with the TS-wave study in an asymptotic suction boundary layer. In figure 17 the amplitude distribution of the TS-wave at $F = 100$ is shown (in this and following figures A corresponds to the maximum measured amplitude in the profile). The experiment ((○)-symbols) shows good agreement with linear parallel theory (solid line), where both the first and the second branch are well captured by the experiment. The TS-wave is generated at $x = 205$ mm and decays until reaching the first branch at approximately Re=728.5. From there on it grows in amplitude until reaching the second branch at approximately Re=1233.5 where it starts to decay.

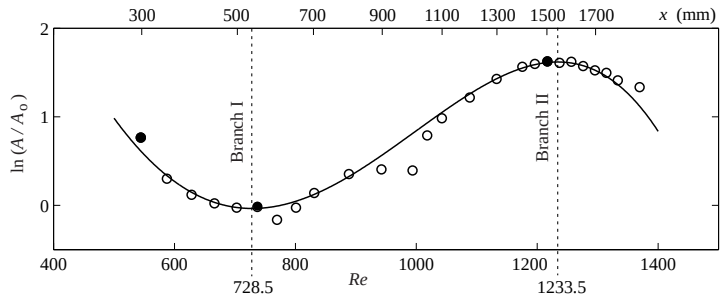

FIGURE 17. Amplitude evolution of the TS-wave at $F = 100$. In this and subsequent figures the symbols are experimental results, and solid lines are the OS-solution of the Blasius profile.

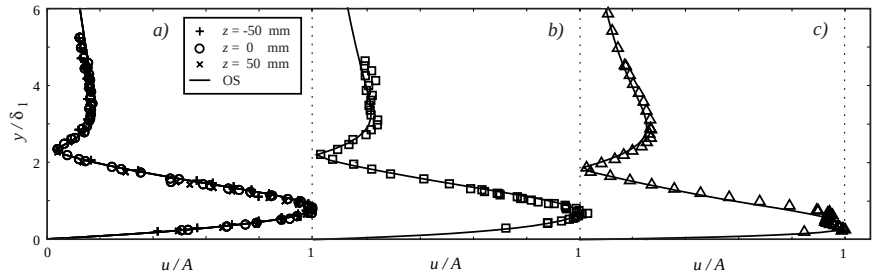

FIGURE 18. Amplitude distribution profiles for $F = 100$. a) $x = 300$ mm at three different spanwise positions ($A = 0.0094 - 0.0097$ m s^{-1}), b) $x = 550$ mm ($A = 0.0036$ m s^{-1}), and c) $x = 1500$ mm ($A = 0.0210$ m s^{-1}).

In figures 18 the disturbance amplitude distribution profiles are shown for the three filled symbols (•) in figure 17. In figure 18a) the two-dimensionality of the TS-wave is illustrated by plotting the profiles of three different spanwise positions together with the OS-solution. The other figures show the smallest (least amplified) and the largest (most amplified) profiles, and in b) (at x=550 mm) the smallness can be revealed near the boundary layer edge where the measured data appear more scattered than in c) (at x=1500 mm). Furthermore, in c) a deformation of the amplitude distribution at the inner maximum can be seen. This deformation has been observed in previous works, see e.g. Klingmann *et al.* (1993) and Ross *et al.* (1970), at downstream distances far from the disturbance source.

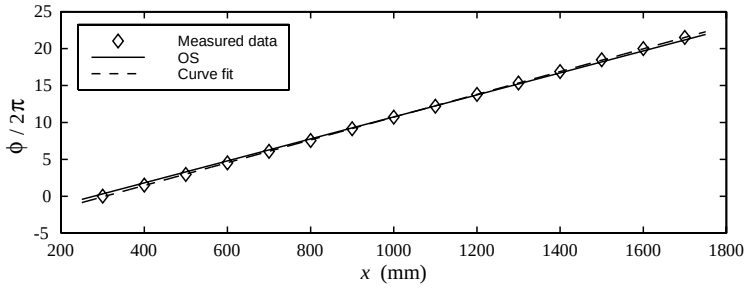

FIGURE 19. Phase distribution in the streamwise direction at $F = 100$.

The phase velocity ($c = \omega/\alpha_r$) of the wave can be determined simply by determining the real part of the wave number (α_r) since the angular frequency (ω) is known. In figure 19 the phase distribution in the streamwise direction is plotted. The phase is taken at the wall-normal distance above the plate where the inner maximum amplitude appears. α_r is then determined by calculating the phase gradient ($\partial\phi/\partial x$), and it is seen to be constant throughout the whole investigated downstream distance. The symbols are experimental data, the solid curve is the OS-solution, and the dashed line is the curve fit for the determination of the gradient. This curve fit gives us a phase velocity of $0.34U_\infty$ compared with the theoretical based on the Blasius profile of $0.36U_\infty$.

From now on all stability results are from the second disturbance slot in the plate located at x=1850 mm corresponding to Re=1350. This is also the region where the stability experiments were made for the asymptotic suction boundary layer. In figure 20 the amplitude distribution profiles are plotted for F=59 at five different downstream positions. The first x-position closest to the disturbance source, in fact only 50 mm from the source, is not fully developed in the upper part of the profile when compared to the OS-solution. However, from the second x-position the agreement is excellent in this part.

In figure 20 the corresponding phase distribution profiles are also plotted, and they clearly show the phase shift of π radians which can be shown to appear where $\partial v'/\partial y$ changes sign, i.e. at the wall-normal amplitude (v') maxima. The experimental data are in good agreement with the OS-solution (solid line).

For F=59, the TS-wave is unstable in this region which is in between branches I and II. The amplitude growth of the TS-wave is seen in figure 21 together with the predicted amplitude evolution by the OS-equation. The phase velocity is $c = 0.29U_\infty$ determined from figure 22 whereas the corresponding phase velocity obtained from the OS-solution is $c = 0.33U_\infty$. However, the agreement has to be judged as good since there are many external conditions that may influence the result this far downstream from the leading edge. When

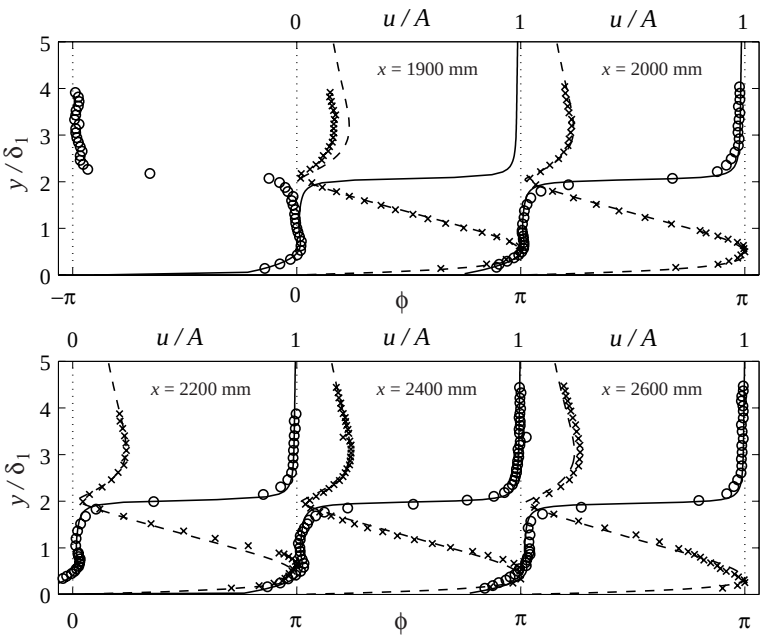

FIGURE 20. Amplitude- and phase distribution profiles for $F = 59$ at different x-positions. ($\times$)-symbols and dashed lines correspond to measured and theoretical amplitude profiles respectively. ($\circ$)-symbols and solid lines are the corresponding phase profiles.

compared with figure 19 one can observe that the phase velocity is larger just as for that frequency, but in this case the trend is somewhat stronger and the effect is more apparent.

Experiments were also made at two other frequencies ($F = 29$ and $F = 81$) which both showed good agreement with linear stability theory. The latter frequency (at the second slot) is close to the second branch and a clear decay of the amplitude growth was visible. To fit the experimental data to the OS-solution it was necessary to make a shift in the Reynolds number. The shift corresponds to a virtual ($_v$) origin at $x_v = -15.8$ mm, which can be considered small (recall the large distance from the leading edge).

In summary the results indicate that the presence of the passive porous plate itself does not seem to affect the stability characteristics of the boundary layer flow. The amplitude growth of the TS-wave agrees with linear parallel theory as well as the amplitude and phase distribution profiles.

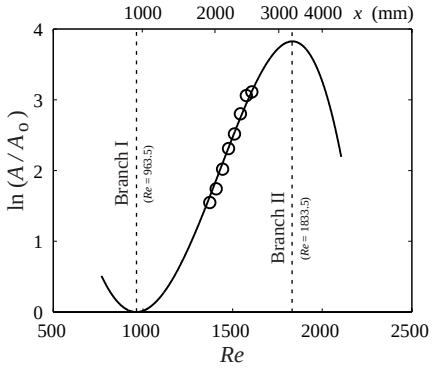

FIGURE 21. Amplitude evolution of the TS-wave at $F = 59$.

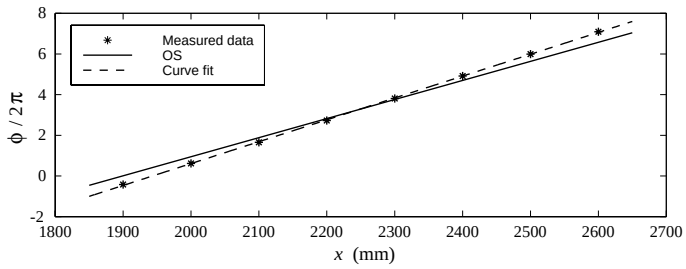

FIGURE 22. Phase distribution in the streamwise direction at F=59.

4.2. *TS-waves in an asymptotic suction boundary layer*

In the following section the baseline flow when continuous suction is applied will be presented together with TS-wave experiments in the fully developed asymptotic suction region.

For the present experiments the flat plate and wind tunnel test section were adjusted for zero-pressure gradient with no suction through the plate. Much effort was spent in order to achieve the zero pressure gradient by changing the floor and ceiling positions of the test-section. Recall that the thick plate together with its suction channels and additional blockage due to suction tubing makes the adjustments more difficult. Therefore, no additional geometrical adjustments of the test section were done for the suction case. The result of different suction rates on the pressure distribution along the streamwise direction is shown in figure 23.

All experimental results are for a pressure difference (Δp) over the porous plate of 221 Pa, which corresponds to a suction velocity of 1.44 cm s^{-1} using

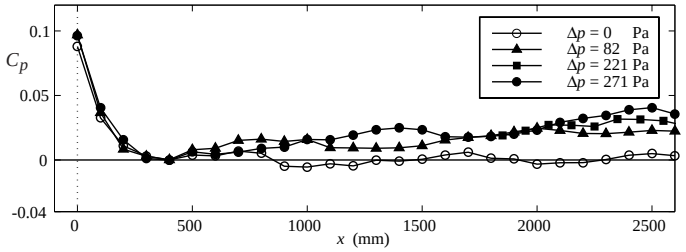

FIGURE 23. Pressure distribution along the streamwise direction for different suction rates. All cases are measured at $y =$ 50 mm, and ($\circ$)-symbols are the same data as in figure 16.

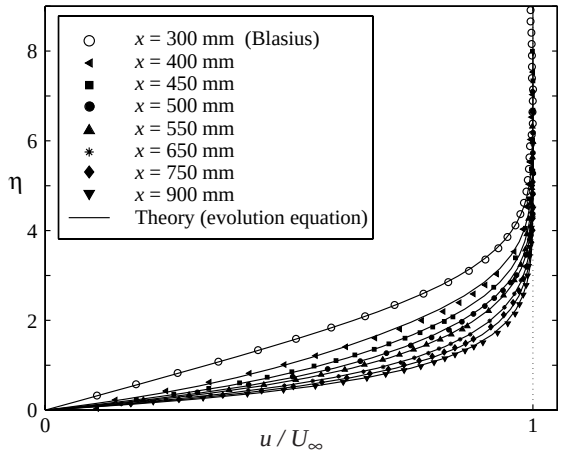

FIGURE 24. Experimental data versus the evolution equation (discussed in §2.1) in the evolution region. $\eta = y\sqrt{\frac{U_\infty}{x\nu}}$.

the permeability value determined through the piston-experiment described in §3.2.

In figure 24 several velocity profiles are plotted in the evolution region, where the wall-normal distance η ($= y\sqrt{U_\infty/x\nu}$) is chosen in order to clearly follow the profile evolution. The development of the boundary layer from the Blasius towards the asymptotic profile shows good agreement with theory, i.e. the evolution equation, and can be observed in figure 25 (note the scaling). The dash-dotted lines are from the Blasius solution and the solid lines originate from the evolution equation. L is the impermeable entry length.

The uniformness and two-dimensionality of the flow was checked in the asymptotic suction region by comparing the velocity profiles at different spanwise

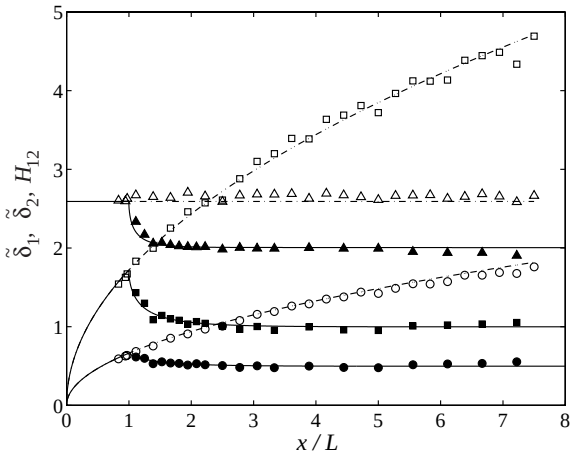

FIGURE 25. Experimental and theoretical results of integral boundary layer parameters. No suction (unfilled-) and suction (filled symbols). (□) $\tilde{\delta}_1$ and (○) $\tilde{\delta}_2$ are the displacement- and momentum thickness, respectively, normalized with $\frac{1}{L}(\frac{UL}{\nu})^{1/2}$. (△) H_{12} is the shape factor. $L = 360$ mm.

and downstream positions. There are in total fourteen mean velocity profiles plotted in figure 26, and they show excellent agreement with the theoretical exponential curve (solid line), i.e. the analytical asymptotic suction profile. The wall position (y_0) and the displacement thickness (δ_1) were determined by fitting the measured data ($u(y_{\text{meas}})$) to

$$\frac{u(y_{\text{meas}})}{U_\infty} = 1 - e^{-(y_{\text{meas}} - y_0)/\delta_1}$$

by means of the least square method. This is also a way to verify the actual suction velocity through the porous plate with the suction velocity corresponding to the pressure difference applied. Since the displacement thickness is $\delta_1 = \nu/V_0$, the suction velocity can easily be calculated once δ_1 is determined from the curve fit. Any profile chosen to verify the suction velocity 1.44 cm s^{-1} agrees within 9%.

In the TS-wave experiments for the asymptotic suction boundary layer the slot at x=1850 mm was used in order to study the wave in a fully developed boundary layer. However due to the presence of the slot (50 mm in the streamwise direction) the porous material was made impermeable over the whole spanwise length in order to ensure the two-dimensionality of the flow as was mentioned in 3.1. This allows the boundary layer to grow slightly and a small increase of δ_1 may be observed downstream of the slot. This results in a Reynolds number increase and for the theoretical comparison Re=382 was used,

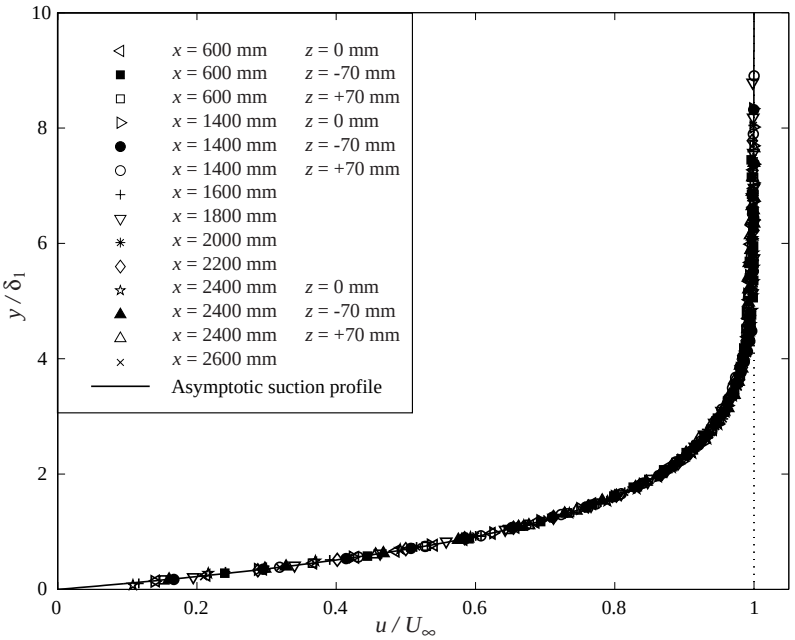

FIGURE 26. Mean velocity profiles for different downstream- and some different spanwise positions in the asymptotic suction boundary layer.

which was extracted from the profiles. For the present Re the TS-wave will decay rapidly after its generation. In figure 27 the amplitude distribution profiles are shown for different downstream positions. The solid line is the solution from the modified OS-equation and the dotted is the ordinary OS-equation. Note that the last profile shown is only 350 mm from the disturbance source. Close to the disturbance source the experimental results show quite good agreement with the modified OS-solution, whereas further downstream the disturbance is seen to be spread out towards the upper part of the boundary layer and from x=2100 mm the measured data start to appear somewhat scattered. The corresponding phase distribution profiles are plotted in figure 28 with the solid line belonging to the modified OS-solution. The agreement is good in the upper part of the boundary layer and in the free stream, but in the theoretical phase distribution there is a zigzag-formation in the middle of the boundary layer that is not clearly apparent in the experimental results. It is the quotient between the imaginary and real part of the eigenfunction that determines the shape of the phase distribution and it is a large decrease with a minimum of this quotient at $y/\delta_1 = 2.7$ followed by an increase that gives the zigzag-formation of the theoretical result.

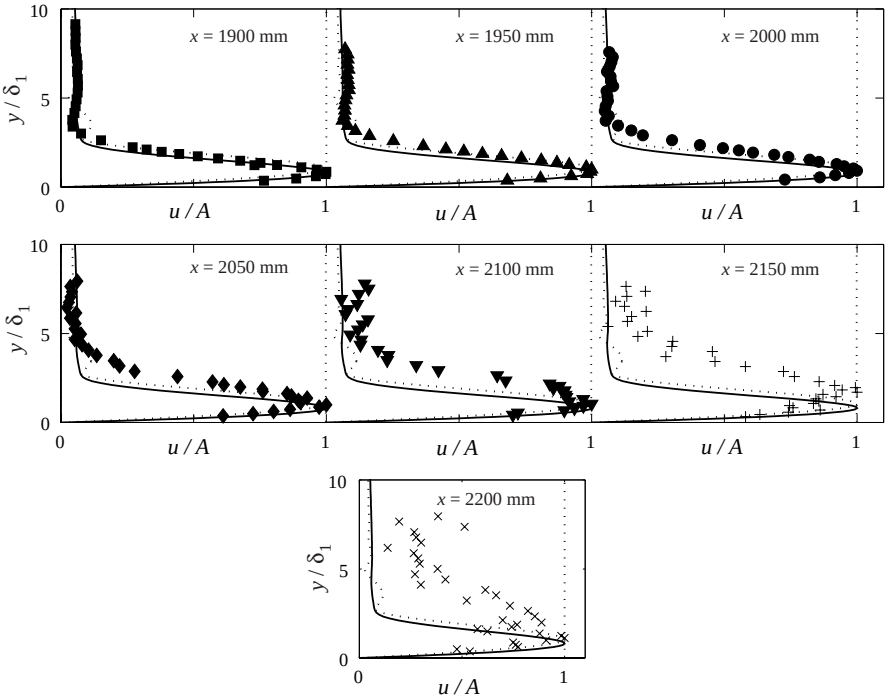

FIGURE 27. Amplitude distribution profiles for different downstream positions in an asymptotic suction boundary layer for F=59. Symbols are measured data, solid line is the modified OS-solution, and dotted line the OS-solution.

The phase velocity of the TS-wave with F=59 is determined in figure 29. The solid line is the modified OS-solution and this solution almost corresponds to a curve fit to the measured data. The dotted line is the ordinary OS-solution. The experimental phase velocity is determined to be $c = 0.48U_\infty$, which is the phase velocity predicted by the modified OS-solution.

The amplitude decay is shown in figure 30 together with theoretical results. The theoretical results overpredicts the stability of the TS-wave. The experimental result gives a damping factor of $\alpha_i = 0.0153$ mm^{-1}, when the first six points are used for the curve fit, and the modified OS-solution predicts $\alpha_i = 0.0263$ mm^{-1}, i.e. a factor 1.72 higher.

TS-wave measurements in the asymptotic suction boundary layer were also made for a higher frequency, F=84.4. The same conclusions are drawn as for the lower frequency experiment. Good agreement with theory is found for the amplitude distribution profile close to the disturbance source and the theoretical decay factor is still overpredicted compared with the experimental

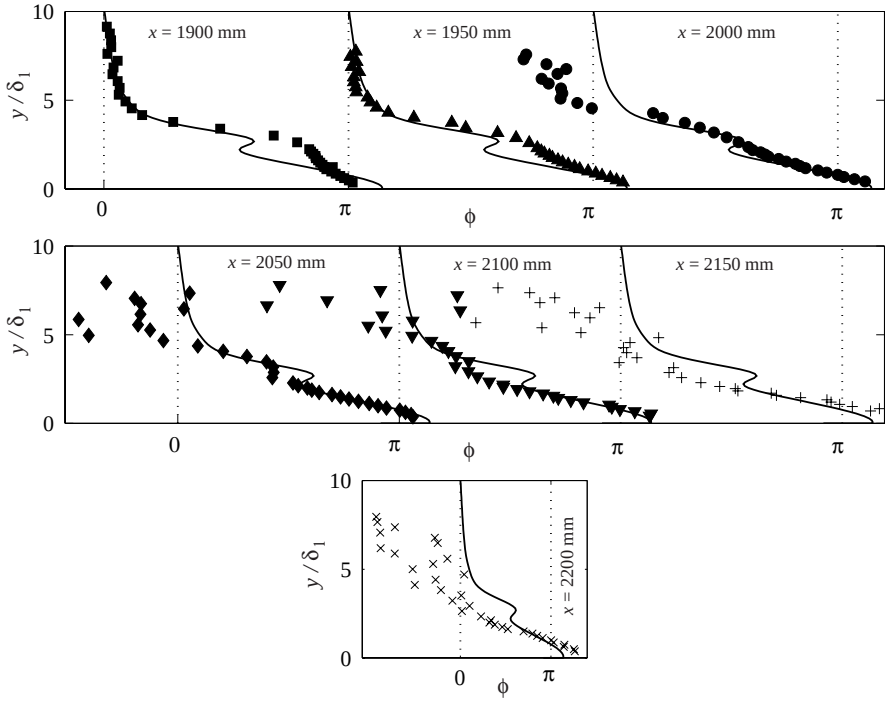

FIGURE 28. Corresponding phase distribution profiles to figure 27.

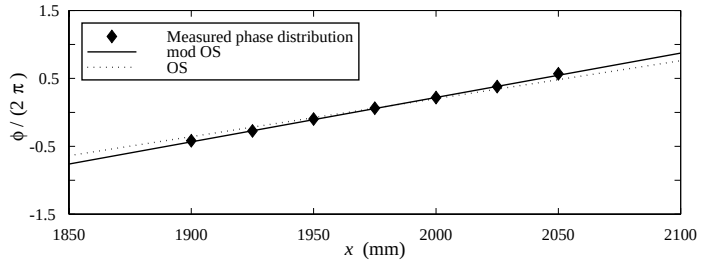

FIGURE 29. Phase distribution in the streamwise direction at F=59 in the asymptotic suction boundary layer.

results. Some possible explanations for this discrepancy will be discussed in section 5.

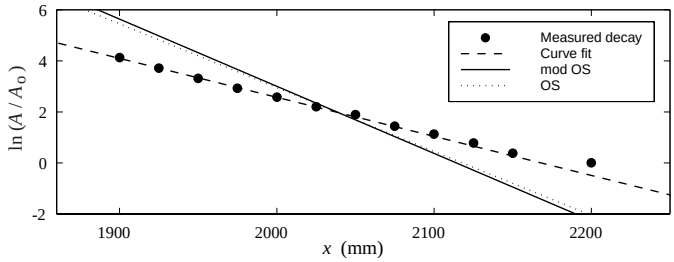

FIGURE 30. Amplitude decay versus the downstream distance for F=59.

4.3. *Experiments with free stream turbulence*

4.3a. *Disturbance growth.* Free stream turbulence (FST) gives rise to regions of high and low streamwise velocity (streaky structures) and in a Blasius boundary layer the streamwise disturbance energy grows in linear proportion to the downstream distance. These streaky structures move slowly in the spanwise direction and if the streamwise disturbance amplitude is measured ($u_{\rm rms}$) it is seen to increase with the downstream distance when no suction is applied, whereas in the suction case this amplitude increase was found to be eliminated. This can be observed in figures 31 & 32 where both the mean velocity and disturbance profiles are plotted for both cases, i.e. with and without suction respectively, for the Tu_B-level and for different downstream positions. The position above the plate, where the maximum $u_{\rm rms}$-value appears, does hardly change in y/δ_1-units and is approximately 1.5, this corresponds to 1/2- and 1/3 of the boundary layer thickness without suction and with suction, respectively. The results are similar for the other two grids (these data can be found in Fransson 2001).

In figure 31a) the mean velocity profiles hardly show any distortion from the theoretical Blasius profile despite disturbance levels up to 8% inside the boundary layer far downstream. Each solid curve in b) is a curve fit to data in order to more easily separate the different downstream positions from each other. It is clearly seen that the amplitude increases with increasing x.

For the suction case the mean flow is indistinguishable from the asymptotic suction profile as can be seen in figure 32a). A large difference is however, that the disturbance level amplitude inside the boundary layer is much smaller than for the no suction case, and that the level is decreasing slightly with increasing x for the profiles in figure 32b). Note that the decay is similar to the FST decay observed in the upper part of this figure.

Fransson (2001) reported $v_{\rm rms}$-data obtained from LDV-measurements both for the Blasius and the suction boundary layers. These results show that in

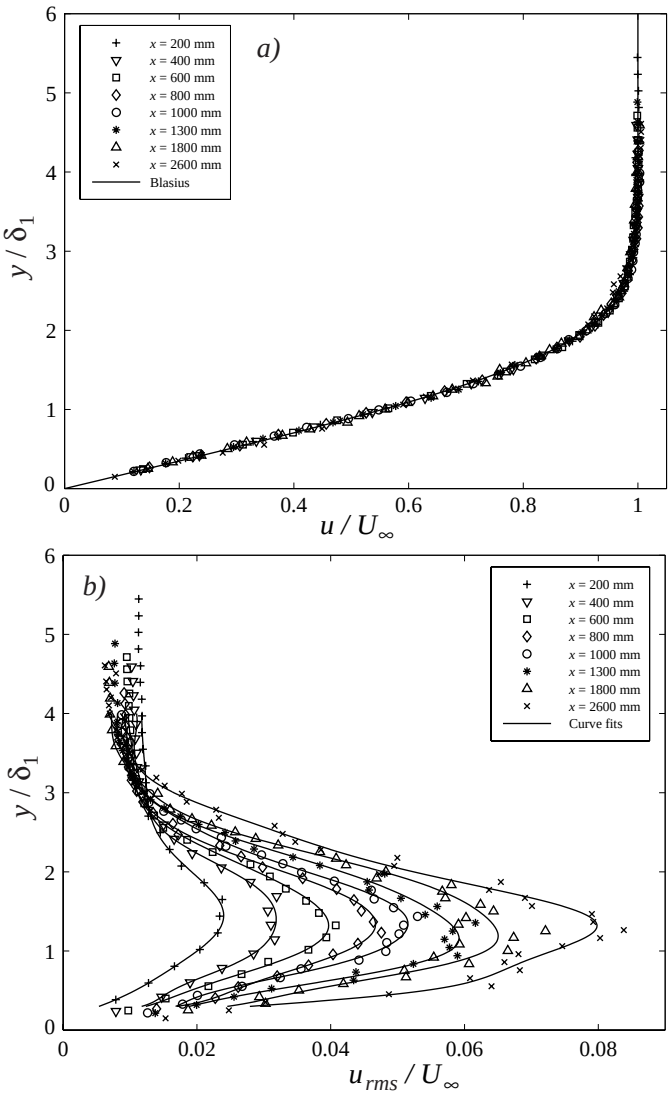

FIGURE 31. Data for different downstream positions from grid B without suction. a) Mean velocity profiles, and b) $u_{\rm rms}$-profiles for the same x-positions as in a).

both cases the $v_{\rm rms}$-profiles are similar and decrease monotonously from the free stream towards the wall. This indicates that the suction does not strongly influence the normal velocity fluctuations close to the wall.

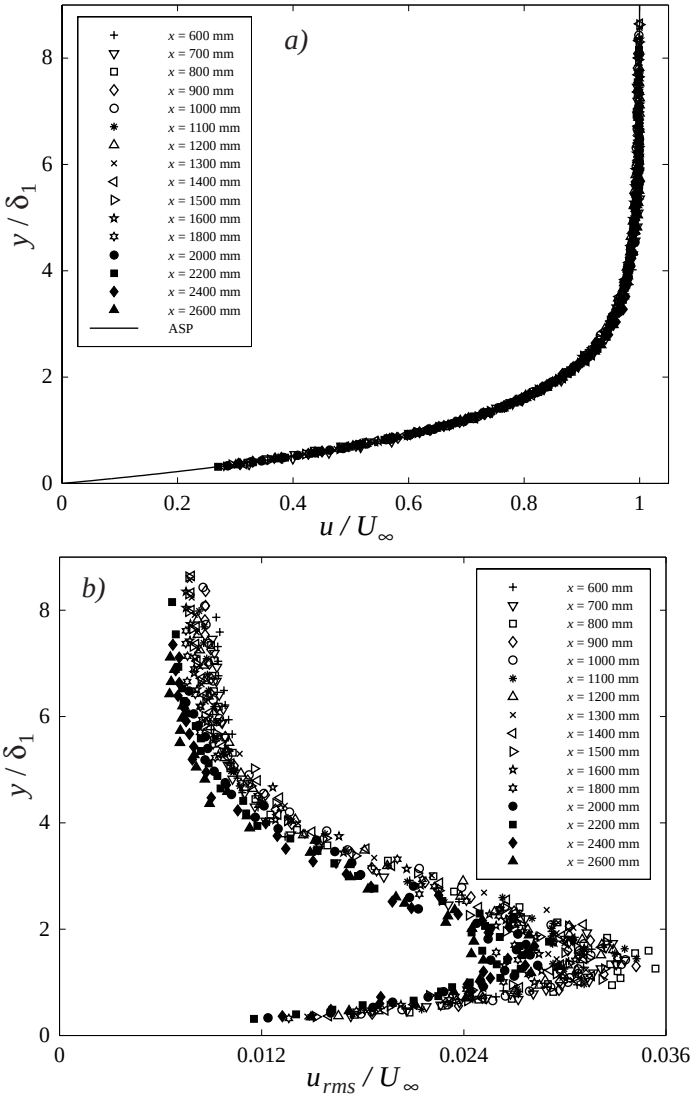

FIGURE 32. Data for different downstream positions from grid B with suction through the porous plate. a) Mean velocity profiles, and b) $u_{\rm rms}$-profiles for the same x-positions as in a).

In figure 33 the displacement thickness evolution, with and without suction, is plotted versus the downstream distance for different FST intensities. In a Blasius transition region when the profile approaches the turbulent one an

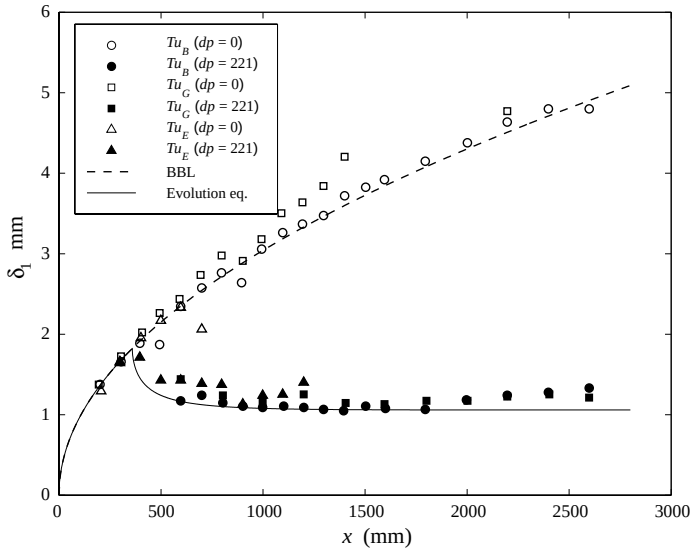

FIGURE 33. The displacement thickness evolution with and without suction when influenced by FST.

increase in the displacement thickness is expected. According to this figure the displacement thickness seems to increase somewhat in both the suction and no suction case when the Tu-level is increased. The dashed and solid lines in figure 33 correspond to the theoretical laminar δ_1-evolution of the Blasius and the suction case, respectively.

In figure 34 the disturbance amplitude, here chosen as the maximum value of the disturbance profiles, for the three different grids are plotted versus the downstream distance from the leading edge. For the no suction cases the disturbance amplitude has been found to grow in proportion to the $x^{1/2}$ and a similar development is observed here. For grid B transition does not occur over the length of the measured region, despite the fact that the $u_{\rm rms}$-level is above 8% at the end. For high enough Tu-levels the FST will force the flow to transition. For grid G a maximum of nearly 17% in the turbulence intensity is found at $x \approx 1800$ mm. Such a maximum is usually observed in the intermittent region where the flow consists both of laminar regions and turbulent spots. Further downstream the intensity decreases which is expected when the flow goes towards a fully developed turbulent stage. For grid E, measurements were only made until $x = 700$ mm where a similar high level was observed.

When applying the present rate of suction it is however found that transition does not occur for any of the grids, although the mean velocity profiles deviate from the asymptotic profile at the most downstream positions for grid

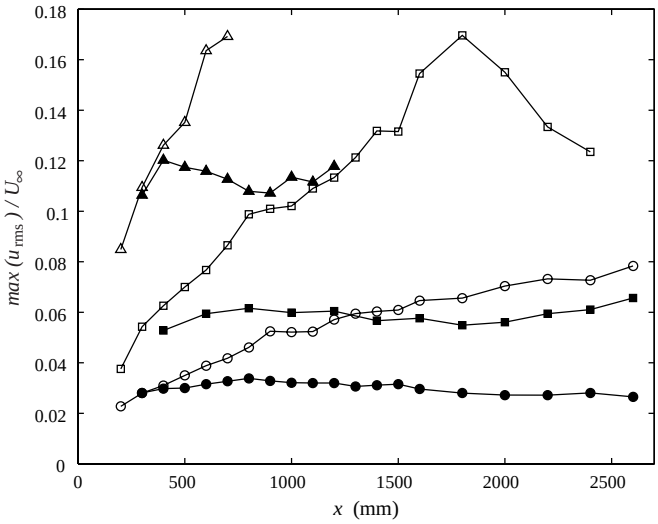

FIGURE 34. Peak disturbance amplitude vs downstream distance from the leading edge. No suction (unfilled-) and suction (filled symbols). (○) Tu_{B}, (□) Tu_{G} and (△) Tu_{E}.

E. Instead the fluctuation level inside the boundary layer reaches an almost constant level for all three grids and the level is in each case close to the level where the suction starts. An interesting observation is that this level is proportional to the level of the FST. This is shown in figure 35 where the maximum u_{rms}-values (or constant level in the suction case) versus the local Tu-level are plotted for both the suction and no suction case.

The data presented in figure 34 appear somewhat scattered and another way to plot the disturbance evolution is to evaluate the average disturbance energy (E_u) by integrating u_{rms}^2 across the boundary layer. This measure is plotted in figure 36 versus the downstream distance from the leading edge. The figures show the well known linear growth of the disturbance energy with the downstream distance for the no suction case and for all Tu-levels. In the case with suction the energy growth ceases and a more or less constant level for each grid is obtained.

4.3b. *Spanwise scale of the streaks.* The spanwise scale of the streaks can be determined through two-point correlation measurements of the streamwise velocity component. It is well known that the position where the streamwise correlation coefficient (R_{uu}) shows a distinct minimum can be interpreted as half the dominating spanwise wavelength of the streaks (see e.g. Matsubara

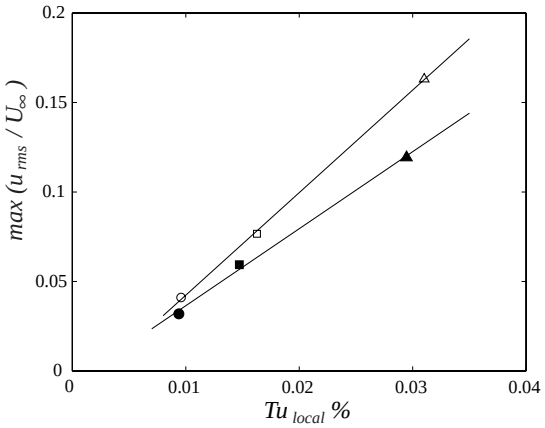

FIGURE 35. The maximum $u_{\rm rms}$-value versus the local Tu at x=600 mm. ($\circ$) $Tu_{\rm B}$, ($\Box$) $Tu_{\rm G}$ and ($\triangle$) $Tu_{\rm E}$. Filled symbols with suction and unfilled without.

& Alfredsson 2001), and will from here on be denoted $\lambda_z^{1/2}$. In order to determine this spanwise scale the correlation measurement has preferably to be done inside the boundary layer where the maximum $u_{\rm rms}$ appears, this is the position where the correlation coefficient will appear strongest. The spanwise correlation coefficient is defined as

$$R_{\rm uu} = \frac{\overline{u(z)u(z+\Delta z)}}{\overline{u(z)^2}} \ .$$

In figure 37 two correlation measurements are shown, one measured at the boundary layer edge ($\bullet$) and the other where the maximum $u_{\rm rms}$ appears ($\circ$). In the former the correlation is close to one at the first measuring point and it decays gradually to become uncorrelated far away. In the latter measurement the correlation coefficient shows the (previously mentioned) dinstinct minimum. An interesting observation is the zero crossing of the correlation coefficient that will be shown to be an equally good measure of the spanwise scale of the streaks as the minimum value. In figure 38 the correlation coefficient is plotted for gradually increasing distance (y) from the plate. Close to the surface the data seem to be somewhat scattered, which is due to the short sampling time (30 sec). From data such as shown in figure 38 one can make a contour plot in the yz-plane for an overview of the structure inside the boundary layer. This was done for different Tu-levels and x-positions with and without suction and are shown in figure 39 (for $Tu_{\rm B}$ and $Tu_{\rm G}$) and 40 (for $Tu_{\rm E}$ with suction). Figure 39 shows that the spanwise scale of the streaky structures is only slightly decreased by suction, despite a twofold reduction in boundary layer thickness. This indicates that disturbances inside the boundary layer is strongly dependent of the scale

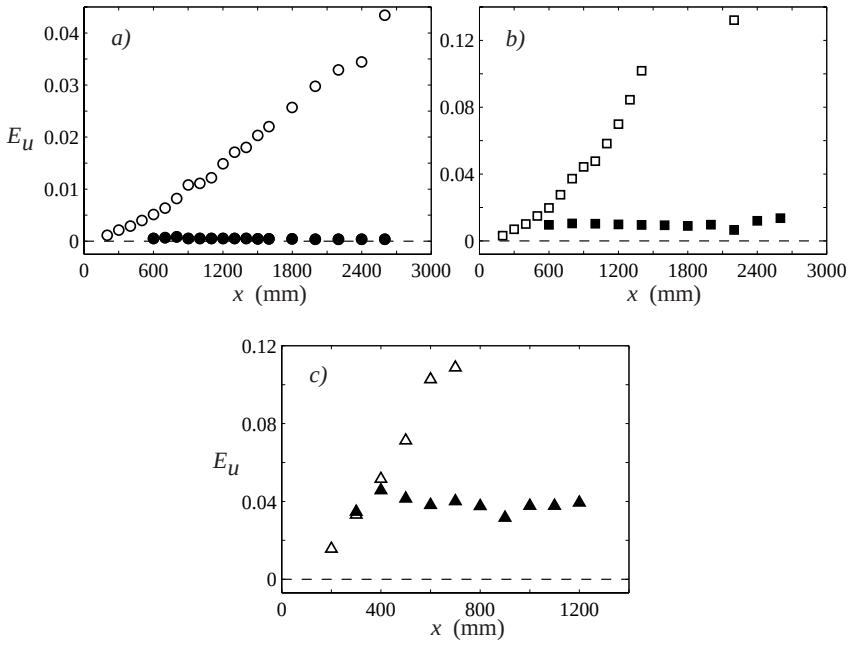

FIGURE 36. The growth of the average disturbance energy inside the boundary layer, defined as $E_{\rm u} = \frac{1}{\delta U_\infty^2}\int_0^\delta u_{\rm rms}^2 {\rm dy}$ (where δ is the boundary layer thickness). a) $Tu_{\rm B}$, b) $Tu_{\rm G}$, and c) $Tu_{\rm E}$.

of the FST. Note that the minimum value is clearly distinguishable in all cases, including figure 40 with $Tu_{\rm E}$ at $x = 500$ mm.

Matsubara & Alfredsson (2001) showed that the spanwise scale of the streaks observed near the leading edge seems to depend on the FST scales introduced into the boundary layer at an early stage of the receptivity process. Further downstream this scale seems to adapt to the boundary layer thickness and grows in proportion to this thickness. In the suction case the scenario is slightly different since the spanwise scale is hardly changed compared to the spanwise scale observed in the Blasius boundary layer, and this despite the fact that the boundary layer thickness is only half of that in a Blasius layer. This result was obtained for all three FST intensities tested. The conclusion from figure 39 is that the effect of suction on the streaks is compression, i.e. since the boundary layer thickness decreases the streaks are compressed in the wall-normal direction but the spanwise scale is preserved. This creates a wider structure in terms of boundary layer thickness as compared to the Blasius case.

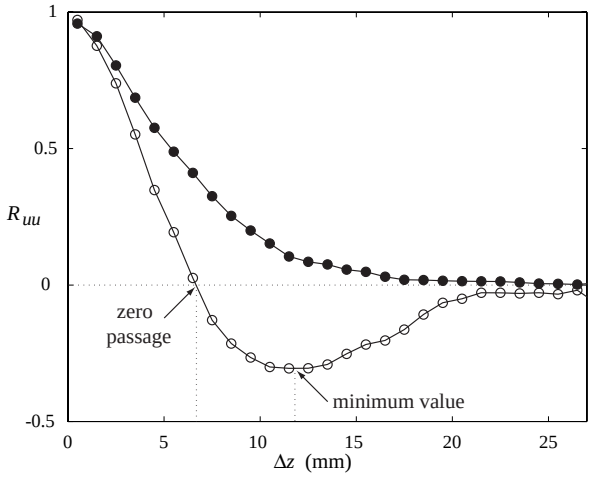

FIGURE 37. The spatial (spanwise) correlation coefficient ($R_{\rm uu}$) versus the separated distance (Δz). (•) Measured at the boundary layer edge, and (◦) measured at the position inside the boundary layer where the maximum $u_{\rm rms}$ appears. The two curves are obtained from smoothed data from a yz-plane measurement at $x = 1800$ mm with $Tu_{\rm B}$.

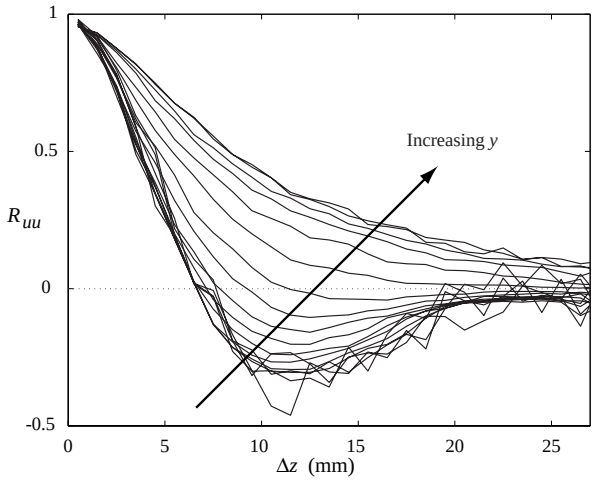

FIGURE 38. The spatial (spanwise) correlation coefficient ($R_{\rm uu}$) versus the separated distance (Δz) for different distances above the plate at $x = 1800$ mm with $Tu_{\rm B}$.

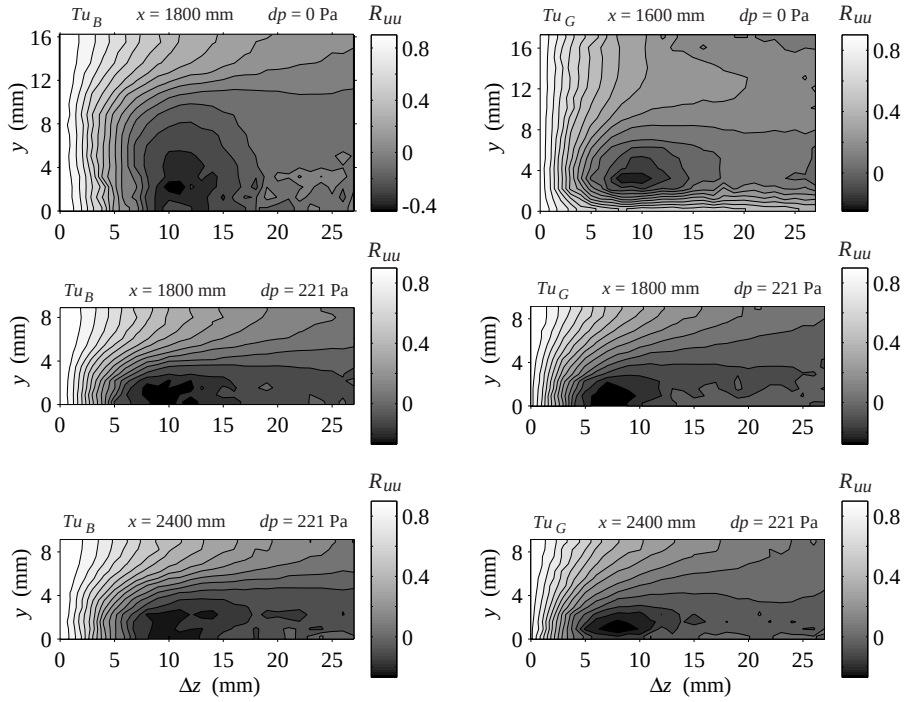

FIGURE 39. Contour plots of R_{uu} in the yz-plane for different downstream positions for both Tu_{B} and Tu_{G}. The no suction case consists of 504 measuring points and the suction case of 392. $\delta_{0.99} \approx 11$ and 5 mm for dp=0 and 221 Pa respectively.

In figure 41 the evolution of the spanwise scales of the streaks from all three grids are shown. The minimum values of the correlation coefficient (R_{uu}) were determined by fitting a third order polynomial to the measured data and the zero crossing of R_{uu} by fitting a second order polynomial. For all cases there is a tendency for the scales to increase with x, however the effect is strongest for grid B (figure 41a)). If a difference between the no suction- and suction cases should be pointed out, a tendency towards a slower growing spanwise scale in the suction case compared to the no suction case may be observed. The spanwise scale of the streaks seems to decrease with increasing FST intensities according to figure 41. As can be seen in figure 41d) the zero crossing is an equally good measure of the spanwise scale as the minimum value of the correlation coefficient. The zero crossing can not give a direct physical interpretation, but is easier to determine from an experimentalist's point of view. All ratios of the minimum value of the correlation coefficient and the zero crossing of the present data collapse at a value of 1.68 ± 0.23.

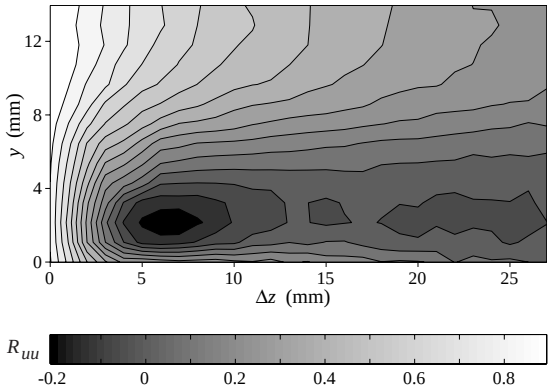

FIGURE 40. Contour plot of R_{uu} in the yz-plane at $x = 500$ mm with Tu_{E} and no suction. Total amount of measuring points are 392.

In figure 42 the evolution of the spanwise scales of the streaks are plotted again (same data as in figure 41) together with the Blasius boundary layer thickness evolution. This figure allows a direct comparison between all cases and confirms previous studies, see e.g. Matsubara & Alfredsson (2001), that the spanwise scale comes close to the boundary layer thickness for low Tu-levels in the Blasius boundary layer.

5. Discussion and summary

In the present work a successful experimental set-up to establish the asymptotic suction boundary layer in a wind tunnel is reported. The main interest of the study is not to develop a practical suction set-up but to establish a generic flow situation where the effect due to suction on disturbance development inside the boundary layer can be investigated. The suction coefficient C_{q} is fairly high compared to what is given in the literature as a reasonable value for flow control.

A test plate with a porous surface material was constructed and with a specially designed leading edge with a short region of non-zero pressure gradient. The mean flow development from the leading edge of the plate is shown to be in good agreement with a theoretical boundary layer analysis and when the asymptotic suction region is reached there is an excellent agreement between the theoretical and experimental boundary layer profiles.

The stability equations for modal disturbances are derived where the wall normal mean velocity modifies the standard OS-equation. The effect of this component as well as the change in mean velocity profile is discussed, and it is shown that the main effect is due to the profile change.

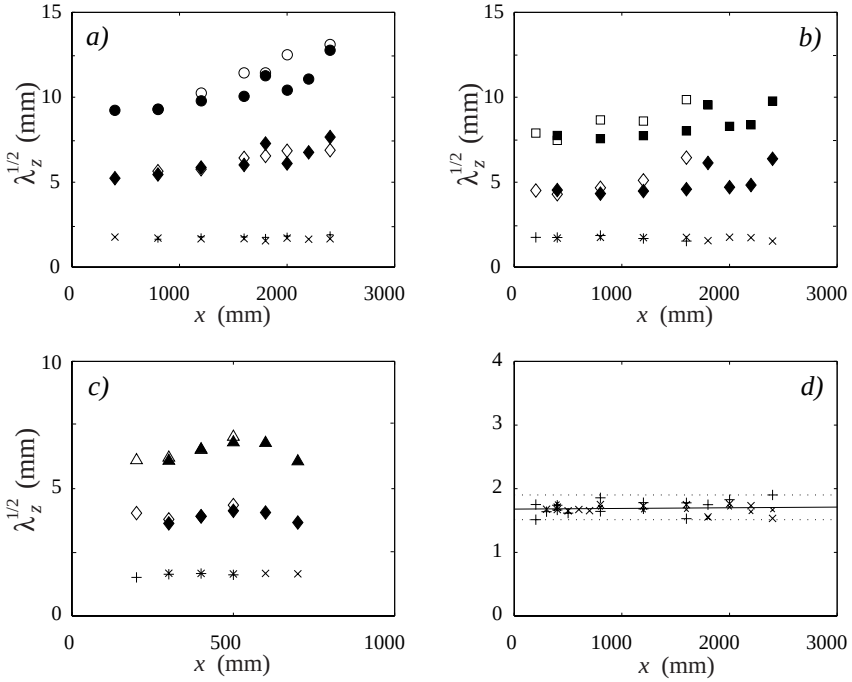

FIGURE 41. Evolution of the spanwise scale of the streaks. No suction (unfilled) and suction (filled symbols). a) ($\circ$) min(R_{uu}) and ($\diamond$) zero(R_{uu}) for Tu_B. b) ($\square$) min(R_{uu}) and ($\diamond$) zero(R_{uu}) for Tu_G. c) ($\triangle$) min(R_{uu}) and ($\diamond$) zero(R_{uu}) for Tu_E. d) min(R_{uu})/zero(R_{uu}) for all grids. ($+$) no suction and ($\times$) suction.

TS-waves are generated in the experiment through a spanwise slot and the development of the waves over the plate without suction is shown to be in good agreement with standard stability theory and previous experiments. The same conclusion can be drawn for the asymptotic suction boundary layer although in that case the waves are strongly damped. The correspondence of the streamwise amplitude profiles and the phase velocity is good, but the decay factor predicted by linear stability theory is slightly overestimated compared to the experimental results. It is not clear why this difference occurs but four main possibilties for the discrepancy of the decay rate as compared to the theoretical results have been identified, namely *i*) the adverse pressure gradient, *ii*) the disturbance introduced by the width of the slot which may give small

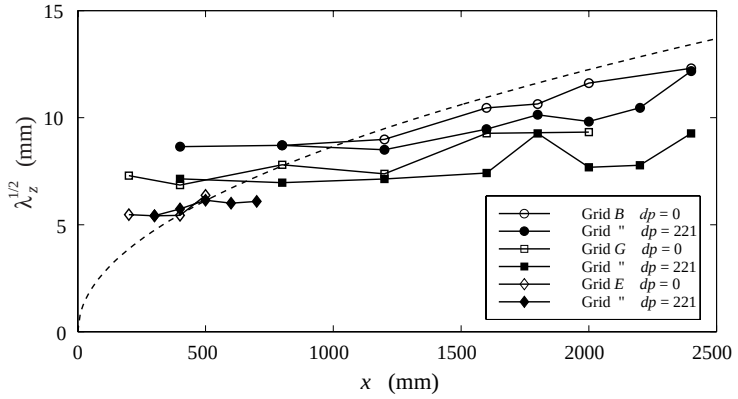

FIGURE 42. Evolution of the spanwise scale of the streaks for all cases are plotted together with the Blasius boundary layer thickness evolution (dashed line). Same data as in figure 41.

deviations of the mean profile, *iii*) the low wave amplitude, and *iv*) a possible obliqueness of the measured disturbance. The adverse pressure gradient that is present in the asymptotic suction region (due to the suction, see figure 23), influences the stability characteristics in such a way that the flow would be less stable. This would bring the theoretical results closer to the experimental ones. However, the pressure gradient is small and PSE calculations with the present pressure gradient, show hardly any effect on the stability characteristics (A. Hanifi, private communication).

Secondly, the profile is affected due to the impermeable streamwise length of 50 mm in connection with the disturbance slot. A sudden stop of the continuous suction over some streamwise distance would allow the boundary layer to grow and the profiles to become slightly disturbed when passing above the impermeable slot. It is well known that even small deviations can give large differences in the decay rate. Also the displacement thickness becomes larger as noted in the measurements. However, this latter effect was taken into account in the stability calculations by using a higher Reynolds number of Re=382 that was extracted from the profiles in the region of interest.

Thirdly, one cannot rule out the possibility that the small amplitude of the wave disturbances in the experiment, may make the measurements susceptible to noise. This would increase the measured level, especially at the more downstream positions, thereby giving a too low decay rate.

Finally, even though the generated disturbance is two-dimensional the circumstances with external disturbances and high noise level may cause an

oblique mode which is less stable than the corresponding two-dimesional disturbance. Three-dimensional disturbance analysis reveal that the theoretical disturbance growth approaches the experimental one as β increases (equal around β=0.25). However, this mode has a phase velocity of $0.70U_\infty$ (compared to $0.48U_\infty$) which in turn simply moves the mismatch to the phase velocity. An obliqueness can despite this not be excluded as a possible factor. A combination of all the suggested explanations is the most likely scenario making the situation rather complicated.

The second part of this study deals with the development of FST induced disturbances. Direct comparisons between the no suction (Blasius) and suction cases were made. In the no suction case the results were similar to earlier work, showing a linear growth of the disturbance energy in the downstream direction until spot formation occurs. However in the suction case the growth of the disturbance amplitude has been shown to cease, and that present amplitude level is essentially kept constant throughout the measured region for this particular suction velocity. In consequence, transition is inhibited for all cases with suction. The 'constant' level was found to be proportional to the FST level. Note that for larger suction rates the disturbance amplitude decays, and for smaller rates the growth is simply damped (cf. Yoshioka *et al.* 2002).

The spanwise scale of the streaks is maintained when suction is applied compared with the no suction case, and this despite a twofold boundary layer thickness reduction. In both cases the receptivity process at the leading edge is similar due to the Blasius boundary layer that develops during the impermeable entry length for both the suction and the no suction case. This might explain the development of similar spanwise scales in the two studied cases since the initial spanwise scale is probably set by the receptivity process.

The spanwise wavenumber of the optimal perturbation in a Blasius boundary layer is at $\beta = 0.775$ when normalized with the displacement thickness (see e.g. Andersson *et al.* 1999 and Luchini 2000). For the asymptotic suction boundary layer the optimum is at $\beta = 0.53$ (Fransson & Corbett 2002), i.e. a somewhat widened structure inside the boundary layer compared to the Blasius case. This is in agreement with the present experiments even though the experiment shows even more widened structures inside the boundary layer for low FST levels (see figure 39). In some recent papers (Andersson *et al.* 1999; Luchini 2000; Matsubara & Alfredsson 2001) comparisons have been made between the optimal perturbation theory and experiments at Tu=1.5 %. The streamwise disturbance profiles were found to agree well, but initially there is a mismatch in the spanwise wavelength of the streaks as pointed out by Matsubara & Alfredsson (2001). The results of Fransson & Corbett (2002) show similarily good agreement also for the asymptotic boundary layer when it comes to the disturbance distribution normal to the wall.

The experimental and theoretical results support the following hypothesis. When free stream turbulence of sufficient level is present, disturbances, which develop into streaks, are triggered inside the boundary layer. The scale of the triggered disturbances depends on both the level and the scale of the FST. Higher FST level implies that more energy is present over the whole range of scales (see figure 6). A certain level is needed to generate disturbances within a certain scale interval, but if this level is high enough the boundary layer would preferably amplify disturbances whose scales are close to that of the optimal disturbance. This is in accordance with the experiments which clearly show that the spanwise scale of the streaks decreases with increasing level of FST (as shown in figure 41) approaching the scale given by optimal perturbation theory. For instance for the Blasius boundary layer in the range $x = 200 - 500$ mm the streak spacing ($\lambda_z^{1/2}$) is between $6 - 7.5$ mm when subjected to Tu_{E} (see figure 41c) where the theory gives $\lambda_z^{1/2} = 5.4 - 8.5$ mm.

Finally one should bear in mind that for transition it is not only the streak amplitude and scale that is important. The streaks will not break down to turbulence without the development of a secondary instability. The triggering of the secondary instability may be due to the free stream turbulence working on top of the streaks. In order to obtain a growing instability the streak amplitude has to be sufficiently large. With the suction rate of the present experiments it seems that the amplitude of the streaks is not high enough for the secondary instability to be able to trigger breakdown to turbulence.

Acknowledgments

We wish to thank Mr. Marcus Gällstedt at the Department of Mechanics at KTH for his skillfull construction work of the leading edge. This work has been financially supported by The Swedish Research Council (VR) and is gratefully acknowledged.

References

Andersson, P., Berggren, M. & Henningson, D. S. 1999 Optimal disturbances and bypass transition in boundary layers. *Phys. Fluids* **11**, 134–150.

Andersson, P., Brandt, L., Bottaro, A. & Henningson, D. S. 2001 On the breakdown of boundary layer streaks. *J. Fluid Mech.* **428**, 29–60.

Bertolotti, F. P. 1991 Linear and Nonlinear Stability of Boundary Layers with Streamwise Varying Properties. PhD thesis, The Ohio State University, Department of Mechanical Engineering , Columbus, Ohio.

Drazin, P. G. & Reid, W. H. 1981 *Hydrodynamic stability*. Cambridge University Press.

Elofsson, P. 1998 Experiments on oblique transition in wall bounded shear flows. PhD thesis, KTH, Stockholm, TRITA-MEK Tech. Rep. 1998:05.

Fasel, H. & Konzelmann, U. 1990 Non-parallel stability of a flat-plate boundary layer using the complete Navier-Stokes equations. *J. Fluid Mech.* **221**, 311–347.

Fransson, J. H. M. & Alfredsson, P. H. 2002 On the hydrodynamic stability of channel flow with cross flow. *Accepted for publication in Phys. Fluids*.

Fransson, J. H. M. & Corbett, P. 2002 Optimal linear growth in the asymptotic suction boundary layer. *Submitted*.

Fransson, J. H. M. & Westin, K. J. A. 2001 Errors in hot-wire X-probe measurements induced by unsteady velocity gradients. *Exp. Fluids* **32**, 413–415.

Fransson, J. H. M. 2001 Investigations of the asymptotic suction boundary layer. TRITA-MEK Tech. Rep. 2001:11. Licentiate Thesis, KTH, Stockholm. Also available at www.mech.kth.se.

Gregory, N. 1961 Research on suction surfaces for laminar flow. *Boundary Layer and Flow Control II*, 924–957.

Gustavsson, C. 2000 Development of three-dimensional disturbances in boundary layers with suction. Master Thesis, Luleå University of Technology, Luleå.

Haj-Hariri, H. 1988 Transformations reducing the order of the parameter in differential eigenvalue problems. *J. Comp. Phys.* **77**, 472–484.

Hocking, L. M. 1975 Non-linear instability of the asymptotic suction velocity profile. *Quart. J. Mech. Appl. Math.* **28**, 341–353.

Jacobs, R. G. & Durbin, P. A. 2001 Simulations of bypass transition. *J. Fluid Mech.* **428**, 185–212.

Johansson, A. V. & Alfredsson, P. H. 1982 On the structure of turbulent channel flow. *J. Fluid Mech.* **122**, 295–314.

Jones, C. W. & Watson, E. J. 1963 Two-dimensional boundary layers. *Laminar boundary layers,* (ed. Rosenhead L.) Oxford University Press.

Joslin, R. D. 1998 Aircraft laminar flow control. *Annu. Rev. Fluid Mech.* **30**, 1–29.

Kendall, J. M. 1985 Experimental study of disturbances produced in a pre-transitional laminar boundary layer by weak free stream turbulence. *AIAA Paper* 85-1695.

Klingmann, R. G. B., Boiko, A. V., Westin, K. J. A., Kozlov, V. V. & Alfredsson, P. H. 1993 Experiments on the stability of Tollmien-Schlichting waves. *Eur. J. Mech., B/Fluids* **12**, 493–514.

Landahl, M. T. 1980 A note on an algebraic instability of inviscid parallel shear flows. *J. Fluid Mech.* **98**, 243–251.

Lindgren, B. & Johansson, A. V. 2002 Evaluation of the flow quality in the MTL wind-tunnel. TRITA-MEK Tech. Rep. 2002:13, KTH, Stockholm.

Luchini, P. 2000 Reynolds number independent instability of the boundary layer over a flat surface: optimal perturbations. *J. Fluid Mech.* **404**, 289–309.

Lundell, F. 2000 Streak breakdown and transition control in wall-bounded flows. TRITA-MEK Tech. Rep. 2000:06. Licentiate Thesis, KTH, Stockholm.

MacManus, D. G. & Eaton, J. A. 2000 Flow physics of discrete boundary layer suction-measurements and predictions. *J. Fluid Mech.* **417**, 47–75.

Matsubara, M. & Alfredsson, P. H. 2001 Disturbance growth in boundary layers subjected to free-stream turbulence. *J. Fluid Mech.* **430**, 149–168.

Morkovin, M. V. 1969 *The many faces of transition.* In Viscous Drag Reduction, Plenum Press.

Myose, R. Y. & Blackwelder, R. F. 1995 Control of streamwise vortices using selective suction. *AIAA J.* **33**, 1076–1080.

Orszag, S. A. & Patera, A. 1983 Secondary instability in wall-bounded shear flows. *J. Fluid Mech.* **128**, 347–385.

Pfenninger, W. & Groth, E. 1961 Low drag boundary layer suction experiments in flight on a wing glove of an F-94A airplane with suction through a large number of fine slots. *Boundary Layer and Flow Control* **II**, 981–999.

Poll, D. I. A., Danks, M. & Davies, A. J. 1992*a* The effect of surface suction near the leading edge of a swept-back wing. *First European Forum on Laminar Flow Technology* pp. 278–293.

Poll, D. I. A., Danks, M. & Humphreys, B. E. 1992*b* The aerodynamic performance of laser drilled sheets. *First European Forum on Laminar Flow Technology* pp. 274–277.

Reshotko, E. 2001 Transient growth: A factor in bypass transition. *Phys. Fluids* **13**, 1067–1075.

Reynolds, G. A. & Saric, W. S. 1986 Experiments on the stability of the flat-plate boundary layer with suction. *AIAA J.* **24**, 202–207.

Rheinboldt, W. 1956 Zur Berechnung stationärer Grenzschichten bei kontinuierlicher Absaugung mit unstetig veränderlicher Absaugegeschwindigkeit. *J. Rational Mech. Anal.* **5**, 539–604.

Roberts, P. J. D., Floryan, J. M., Casalis, G. & Arnal, D. 2001 Boundary layer instability induced by surface suction. *Phys. Fluids* **13**, 2543–2552.

Ross, J. A., Barnes, F. H., Burns, J. G. & Ross, M. A. 1970 The flat plate boundary layer. part 3. comparison of theory and experiments. *J. Fluid Mech.* **43**, 819–832.

Schlichting, H. 1979 *Boundary layer theory*. McGraw-Hill.

Schmid, P. J. & Henningson, D. S. 2001 *Stability and transition in shear flows*. Springer.

Schubauer, G. B. & Skramstad, H. K. 1948 Laminar boundary layer oscillations and transition on a flat plate. *Technical Report Rep.* 909, NACA.

Taylor, G. I. 1971 A model for the boundary condition of a porous material. part 1. *J. Fluid Mech.* **49**, 319–326.

Westin, J. 1997 Laminar-turbulent boundary layer transition influenced by free stream turbulence. PhD thesis, KTH, Stockholm, TRITA-MEK Tech. Rep. 1997:10.

Yoshioka, S., Fransson, J. H. M. & Alfredsson, P. H. 2002 Evolution of disturbances in a boundary layer with wall suction. *Unpublished results* .

2

Paper 2

Optimal linear growth in the asymptotic suction boundary layer

By Jens H. M. Fransson[1] and Peter Corbett

IMFT, Allée du Pr. Camille Soula, F-31400 Toulouse, France

Published in *Eur. J. Mech. B/Fluids* **22**, 259–270, 2003

A variational technique in the temporal framework is used to study initial configurations of disturbance velocity which maximize perturbation kinetic energy in the asymptotic suction boundary layer (ASBL). These optimal perturbations (OP) excite significant and remarkably persistent transient growth, on the order of that which occurs in the Blasius boundary layer (BBL). In contrast, classical modal analysis of the ASBL predicts a critical Reynolds number two orders of magnitude larger than that for the BBL. As in other two-dimensional boundary layer flows, disturbances undergoing maximum amplification are infinitely elongated in the direction of the flow and take the form of streamwise-oriented vortices which induce strong variations in the streamwise perturbation velocity (streaks). The Reynolds number dependence of the maximum growth, and the best choice of scaling for the spanwise wavenumber of the perturbation causing it, are elucidated. There is good agreement between the streak resulting from OP and disturbances measured in experiments in which the asymptotic suction boundary layer is subject to free stream turbulence (FST). This agreement is shown to improve as the level of FST increases.

1. Introduction

A boundary layer subject to a wall-normal flow is encountered in many applications, e.g. filtration through porous membranes, and laminar flow control via suction through discrete holes or a permeable surface. Potential reductions in viscous drag on the order of 60% to 80% provided a strong motivation for early workers to concentrate on the latter case, for which Meridith and Griffith[2] found a general solution in the asymptotic limit of constant suction. Later Iglisch[1] extended this work to the non-similar flow arising before the asymptotic state establishes itself, and outlined a method for finding the velocity profile corresponding to an arbitrary suction distribution.

[1] Permanent address: KTH Mechanics, SE-100 44 Stockholm, Sweden.
[2] These references are taken from Schlichting (1979).

The application of optimal control theory to laminar flow control has sparked a renaissance in the field (Bewley 2001). An extensive amount of work has been done on the subject of flow control in general and the interested reader is addressed to Moin & Bewley (1994), Joslin *et al.* (1996), Joslin (1998), Lumley & Blossey (1998), Balakumar & Hall (1999), Högberg (2001), and Lundell (2003), just to mention a few works on both experimental and numerical control. Pralits *et al.* (2002) and Walther *et al.* (2001) have recently outlined methods in which modifications to the boundary layer flow by spatially-varying steady suction create conditions which stabilize linear disturbances. This approach contrasts with earlier work in which the disturbances themselves are the target of some rationally directed control activity (Abergel & Témam (1990); Bewley & Liu (1998)).

The difficulties of sensing boundary layer disturbances in an aerospace setting on the one hand, and the inherent complexity of a system capable of delivering variable suction at an arbitrary position on a lifting surface on the other, pose formidable implementation challenges with technology available today. The simple case where the boundary layer is subject to uniform, constant suction, as initially envisioned by the pioneers in the field, is far more likely to find application in practice. It is also the focus of recent experimental and theoretical work by Fransson & Alfredsson (2003), who investigated the linear stability characteristics of the flow using classical spatial stability theory (Drazin & Reid (1981); Schmid & Henningson (2001)). They determined the behaviour of Tollmien-Schlichting waves, and observed disturbances evoked by varying levels of free stream turbulence (FST, whose intensity is typically quantified by the parameter $Tu = u_{\rm rms}/U_\infty$).

Additional terms in the familiar Orr–Sommerfeld/Squire system describing linear stability appear as a consequence of the normal velocity component, however it has long been known that the change in shape of the mean streamwise velocity profile is the main reason for the altered stability characteristics of the flow (Drazin & Reid 1981). That this change is considerable is reflected by a two order of magnitude increase in critical Reynolds number (Hocking 1975). In turn, this indicates that modal Tollmien–Schlichting disturbances are significant in flows where the free stream velocity dominates the suction velocity.

At moderate flow régimes likely to arise in applications, attention must then turn to other linear growth mechanisms. Since Fransson & Alfredsson (2003) report the presence of streaks in asymptotic suction boundary layers subject to FST, it is natural to inquire whether and to what degree this flow is capable of sustaining algebraic or transient growth, of which streaks are a characteristic signature (see Westin (1997); Matsubara & Alfredsson (2001), and their references for a complete review of the phenomenon in the Blasius boundary layer (BBL)).

Algebraic growth is a consequence of the non-normality of the governing differential operator: as the normal modes are not orthogonal, constructive and destructive interference may give rise to transients before the asymptotic state described by modal theory sets in (Schmid & Henningson 2001). Butler & Farrell (1992) pioneered the study of optimal perturbations (OP) in shear flows; their findings and those of later workers indicate that the initial conditions which maximize perturbation kinetic energy are streamwise-oriented vortices which produce streaks (variations in the streamwise perturbation velocity). Ever since the transient growth and its linear physical mechanism was described by Ellingsen & Palm (1975), and Landahl (1980) a number of works has been done on the topic. Among the earlier ones are e.g. Hultgren & Gustavsson (1981), Gustavsson (1991), Reddy & Henningson (1993), and Trefethen *et al.* (1993). For more recent publications on the subject see e.g Luchini (2000), Reshotko (2001), and Andersson *et al.* (2001).

In the following, OP are sought for the asymptotic suction boundary layer (ASBL) using a direct-adjoint technique in the temporal framework. This method has been employed previously to investigate the Falkner–Skan–Cooke family of boundary layers (Corbett & Bottaro 2000, 2001). For the ASBL the parallel flow approach is exact and no local approximations are made. The results are then compared with experimental measurements made by Fransson (2001), and good agreement between the computed and measured disturbances in the boundary layer is observed.

2. Asymptotic suction boundary layer

This work focuses on events in the steady flow of an incompressible fluid over a permeable flat plate through which a normal velocity is applied, and in particular to the region where the boundary layer ceases to evolve in the streamwise direction. The general situation is depicted in figure 1. In this two-dimensional flow continuity is satisfied directly, provided the streamwise velocity varies only in y and the wall-normal velocity is constant. The subsequent simplification of the x-momentum equation permits its direct integration,

$$U(y) = U_\infty \left[1 - \exp\left(y\, V_\mathrm{w}/\nu\right)\right] \ , \tag{1}$$

where U_∞ is the free stream velocity, V_w is the normal velocity applied at the wall, and ν is the kinematic viscosity. Physical solutions are associated only with the suction case $V_\mathrm{w} < 0$ (see Schlichting 1979; White 1991, and their references for more details). The displacement and momentum thicknesses,

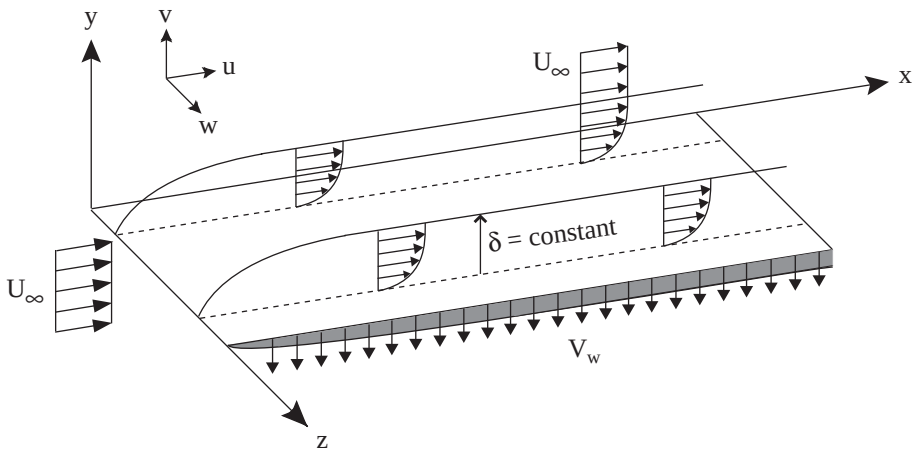

FIGURE 1. Schematic of the flow field over a flat plate subjected to constant suction. The coordinate system used in this work is shown, along with the corresponding velocity components.

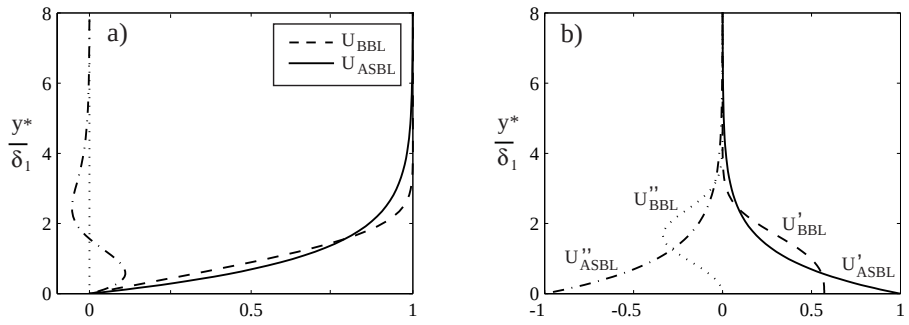

FIGURE 2. a) Velocity profiles for the asymptotic suction (ASBL) and Blasius (BBL) boundary layers, with their difference indicated by the dash-dotted line. b) First and second derivatives. Superscript $*$ indicates dimensional quantities.

$$\delta_1 = -\frac{\nu}{V_\mathrm{w}} \text{ and } \delta_2 = \frac{\delta_1}{2} \ ,$$

are constant, as is the boundary layer thickness. In this flow the wall-directed convection exactly balances the growth of the shear layer through viscous diffusion. The resulting streamwise velocity profile is fuller than the Blasius boundary layer, as shown in figure 2.

The Reynolds number based on δ_1 becomes

$$R = \frac{U_\infty \delta_1}{\nu} = -\frac{U_\infty}{V_\mathrm{w}}, \tag{2}$$

and is used throughout this investigation.

3. Optimization problem

Of interest is the transient behaviour of unsteady three-dimensional velocity perturbations $\tilde{\mathbf{u}}(x, y, z, t) = [\tilde{u}, \tilde{v}, \tilde{w}]$ in a steady incompressible parallel base flow $\mathbf{U}(y) = [\, U, V_\mathrm{w}, 0\,]$, which are described by the Navier–Stokes equations linearized about the base state. The ASBL is parallel, but to treat the spatially developing BBL as parallel is an approximation which is only valid as long as the disturbance varies on a length scale which is much smaller than that of the base flow.

Since the base flow $\mathbf{U}$ has two components, terms involving V_w arise and the classical Orr–Sommerfeld/Squire equations are no longer valid. These extra terms can easily be taken into consideration provided the unknowns are scaled with respect to U_∞ and δ_1, as V_w can then be replaced by $-1/R$ (cf. expression 2). Furthermore, the system of linearized Navier-Stokes equations describing $\tilde{\mathbf{u}}$ can be simplified considerably by eliminating the perturbation pressure and introducing the wall-normal perturbation vorticity, $\tilde{\eta} = \partial\tilde{u}/\partial z - \partial\tilde{w}/\partial x$.

The resulting system for $\tilde{\mathbf{v}} = [\tilde{v}, \tilde{\eta}]$ can, upon assuming periodicity in the stream- and spanwise directions,

$$\tilde{\mathbf{v}}(x, y, z, t) = \mathbf{v}(y, t) \exp(\mathrm{i}\alpha x + \mathrm{i}\beta z) \ ,$$

(with $\alpha, \beta \in \mathbb{R}$ the corresponding stream- and spanwise wavenumbers), be written

$$\left[\left(\frac{\partial}{\partial t}+\mathrm{i}\alpha U-\frac{1}{R}\frac{\partial}{\partial y}\right)\Delta-\mathrm{i}\alpha\frac{\mathrm{d}^2U}{\mathrm{d}y^2}-\frac{1}{R}\Delta^2\right]v = 0\ , \tag{3}$$

$$\left[\frac{\partial}{\partial t}+\mathrm{i}\alpha U-\frac{1}{R}\frac{\partial}{\partial y}-\frac{1}{R}\Delta\right]\eta = -\mathrm{i}\beta\frac{\mathrm{d}U}{\mathrm{d}y}v\ . \tag{4}$$

Here $\Delta=\partial^2/\partial y^2-k^2$ represents the Laplacian operator, where $k^2=\alpha^2+\beta^2$, and the grouping $-\frac{1}{R}\frac{\partial}{\partial y}$ represents wall-normal convective effects. Perturbations are assumed to be zero at the wall and to vanish far from the wall. As a consequence homogeneous Dirichlet boundary conditions apply to $\mathbf{v}$, and from continuity it is seen that additional homogeneous Neumann conditions apply to v.

Initial conditions $\mathbf{v}_0=\mathbf{v}_0(y)$ for (3) are sought which undergo maximum relative amplification over a given time span, $t\in[0,\tau]$. The metric used here is the growth,

$$G(\tau)=\frac{E(\tau)}{E(0)}\ , \tag{5}$$

or ratio of final to initial perturbation kinetic energy densities,

$$E(t)=\frac{1}{2}\int_0^\infty(\bar{u}\cdot u+\bar{v}\cdot v+\bar{w}\cdot w)\,\mathrm{d}y=\frac{1}{2k^2}\int_0^\infty(-\bar{v}\Delta v+\bar{\eta}\cdot\eta)\,\mathrm{d}y\ .$$

Above, overbars indicate conjugate transpose quantities.

The procedure for determining $\mathbf{v}(y,0)=\mathbf{v}_0$ which maximizes the ratio (5) while satisfying (3) and its boundary conditions is described in detail in Corbett & Bottaro (2001), to which the interested reader is referred (alternative methods in the temporal and spatial frameworks are reported in **?**Butler) and Andersson *et al.* (1999), respectively). Here it is simply noted that the constraints on the extremization of G are enforced by introducing Lagrange multipliers, or adjoint variables, for each of the constraints. An iterative procedure is then used to maximize G. One starts from an arbitrary guess for $\mathbf{v}_0$ and integrates (3) from $t=0$ to $t=\tau$. At this point transfer relations,

$$a(y,\tau)=-\frac{1}{2k^2E(0)}v(y,\tau)\ ,\ b(y,\tau)=\frac{1}{2k^2E(0)}\eta(y,\tau)\ ,$$

from $\mathbf{v}$ to its adjoint $\mathbf{a}(y,t) = (a,b)^{\mathrm{T}}$ are applied. The adjoint field's behaviour is described by,

$$\left[\left(\frac{\partial}{\partial t} + \mathrm{i}\alpha U - \frac{1}{R}\frac{\partial}{\partial y} + \frac{1}{R}\Delta\right)\Delta + 2\mathrm{i}\alpha\frac{\mathrm{d}U}{\mathrm{d}y}\right] a = -\mathrm{i}\beta\frac{\mathrm{d}U}{\mathrm{d}y} b \ , \tag{6}$$

$$\left[\frac{\partial}{\partial t} + \mathrm{i}\alpha U - \frac{1}{R}\frac{\partial}{\partial y} + \frac{1}{R}\Delta\right] b = 0 \ , \tag{7}$$

where the boundary conditions on $\mathbf{a}$ are analogous to those on $\mathbf{v}$. Integrating the adjoint system (6) from $t = \tau$ to $t = 0$, another set of transfer relations

$$v_0(y) = -\frac{2k^2E(0)^2}{E(\tau)}a(y,0) \ , \ \eta_0(y) = \frac{2k^2E(0)^2}{E(\tau)}b(y,0) \ ,$$

provides an estimate for $\mathbf{v}_0$. The procedure is repeated until $\mathbf{v}_0$ converges, which requires few iterations in general.

4. Results

Before presenting results, some nomenclature is introduced for clarity in the discussion to follow. In a mean flow parameterized by R, what distinguishes an OP for the period $t = \tau$ from all other valid initial conditions described by the wavenumber pair (α,β) is that it maximizes the growth at the end of the interval, $G(\tau)$. The procedure outlined in §3 produces a global maximum of G as argued by Luchini (2000).

Below, the words 'local' and 'global' are applied in a different context to describe OP: in the following these words will refer to periods of time. The OP for an arbitrary interval is referred to as a *local* optimal,

$$\sigma(\tau) \equiv \max_{\forall v_0(\alpha,\beta)} G(\tau) \ ,$$

whereas the largest growth achievable for perturbations described by a given wavenumber pair in the same mean flow is termed a *global* optimal,

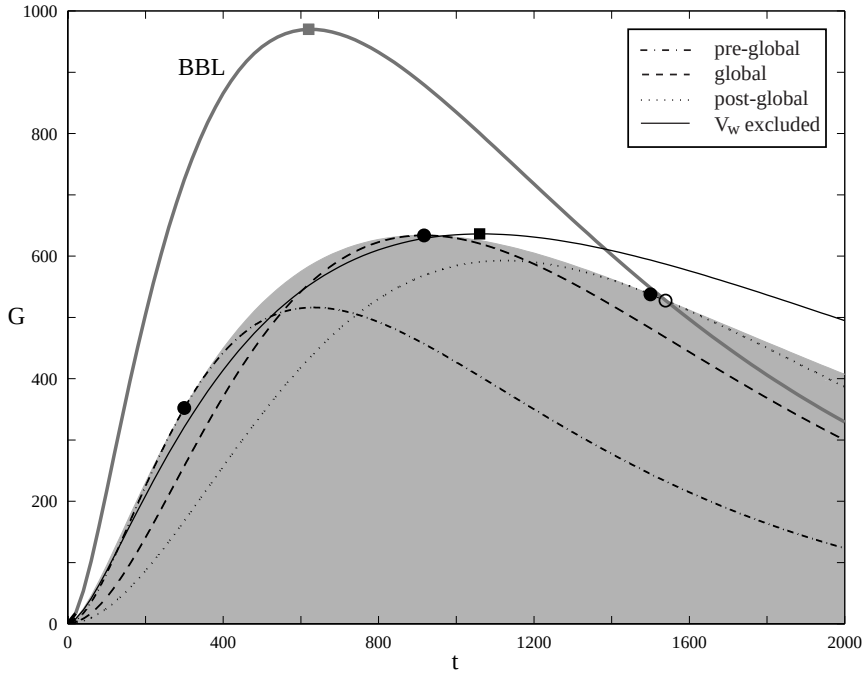

FIGURE 3. Local and global OP growth in the ASBL ($(\alpha, \beta) =$ (0,0.53) at $R = 800$, the shaded region represents the envelope of local optimum growth. The grey line is the envelope of local optimum growth in the BBL ($(\alpha, \beta) =$ (0,0.65)) at $R = 800$. The individual cases are discussed further in the text.

$$\gamma = \sigma(t_\gamma) \equiv \max_{\forall t} \sigma(t) \ ,$$

where t_γ is time at which this growth occurs. The largest transient growth possible at R is experienced by the *maximum* optimal,

$$\Gamma = \gamma(t_\Gamma) \equiv \max_{\forall \alpha, \beta} \gamma(t_\gamma) \ ,$$

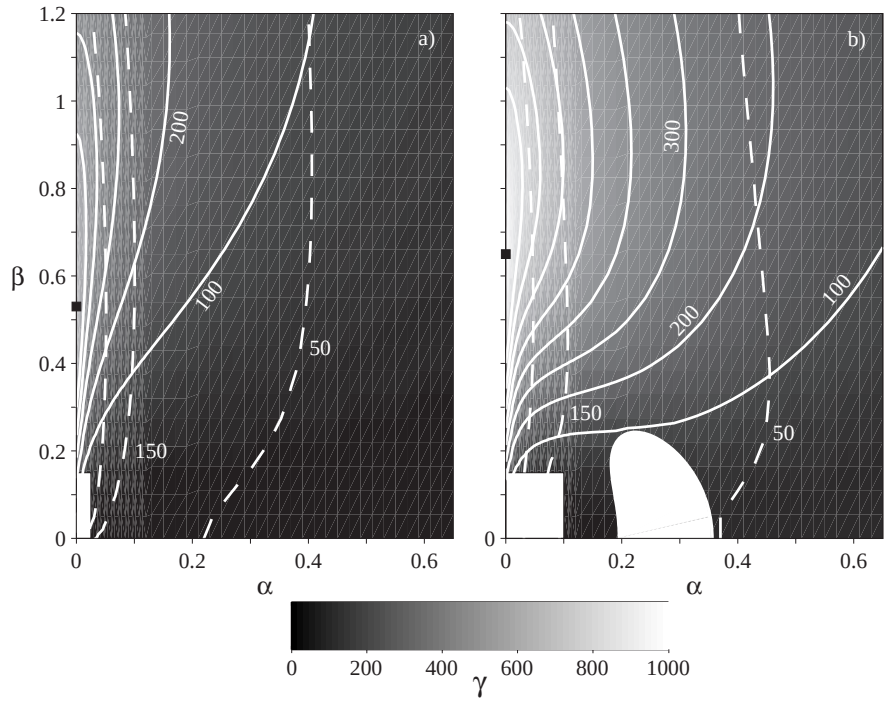

FIGURE 4. Contours of global optimal growth in the wavenumber plane at $R = 800$ for a) the ASBL, b) the BBL. The empty rectangles near the origin are uncalculated areas, and the empty region about $\alpha \approx 0.3$ in the latter case indicates the presence of exponentially amplified disturbances. Level lines of γ are solid, those of t_γ dashed. The increment between all level lines is 100.

and is a characteristic quantity of the base flow. Its parameters are denoted t_Γ, α_Γ and β_Γ. Finally, the 'response' of an optimal perturbation is the state of the disturbance at the time for which it is optimal (i.e., τ or t_γ or t_Γ).

The distinctions drawn above are illustrated in figure 3. The shaded region represents the envelope of growth attained by local optimals with $\alpha = 0$, $\beta = 0.53$ in the ASBL at $R = 800$. The three curves entirely within this region show the temporal evolution of two local optimals and the global optimal, these are denoted pre-global, post-global and global, respectively. Symbols indicate the times for which they are optimal, demonstrating that locally optimal growth seldom coincides with the maximum growth experienced by the perturbation.

The global optimal shown in figure 3 corresponds to the maximum optimal for the ASBL at $R = 800$, no other perturbation experiences more algebraic

Flow		β	γ	t_γ
BBL	max	0.65	969.9	625.7
ASBL	pre-max	0.53	352.1	300.0
	max	0.53	633.9	917.7
	post-max	0.53	537.7	1500.0

TABLE 1. Parameterization of the OP at $R = 800$ whose growth is shown in figure 3. 'Max' denotes a global maximum, the other fields denote local maxima. In all of these cases $\alpha \equiv 0$.

amplification. The solid grey curve is the analogue of the shaded region for the BBL ($\alpha = 0$, $\beta = 0.65$ at $R = 800$). Evidently, the ASBL is capable of sustaining significant transient growth on the order of that experienced in the BBL. This is in sharp contrast to the situation for modal disturbances: Hocking (1975) shows that the critical Reynolds number in the ASBL is two orders of magnitude larger than in the BBL. The strong damping effect of suction on Tollmien–Schlichting waves evidently does not carry over to algebraically excited disturbances.

The difference in transient growth characteristics between the ASBL and the BBL can be attributed to the change in shape of the mean streamwise velocity profile. The solid black line partially within the shaded area in figure 3 traces the temporal evolution of the global maximum optimal perturbation ($\Gamma = 636$ at $t_\Gamma = 1065$, with $\alpha = 0$, $\beta = 0.50$) in a hypothetical flow with no suction but an identical U-velocity profile to the ASBL. Effectively, this exercise demonstrates that the additional terms due to V_w in (3) and (6), required to obtain the correct physics, only bring about a small change in the overall result.

Transient growth is not restricted to disturbances infinitely elongated in the streamwise direction. Figure 4 shows that perturbations exhibiting periodicity in the streamwise direction also experience substantial algebraic excitation. The rapid decrease in t_γ away from the β axis shows that such perturbations reach their maximum amplitude earlier than those undergoing the most amplification, as a consequence they may play a significant role in flows subject to forcing which excites them preferentially.

The physical mechanism behind algebraic growth in the ASBL is identical to that found in previous work on transient growth (Butler & Farrell 1992; Andersson *et al.* 1999). This is seen from the optimal perturbation velocity profiles shown in figure 5 and their respective responses at t_γ for the local and global optima of figure 3 (cf. table 1 for a full parameterization of these disturbances). It is possible to discern that the OP take the form of streamwise-oriented vortices, with perturbation velocities distributed primarily in the crossflow plane.

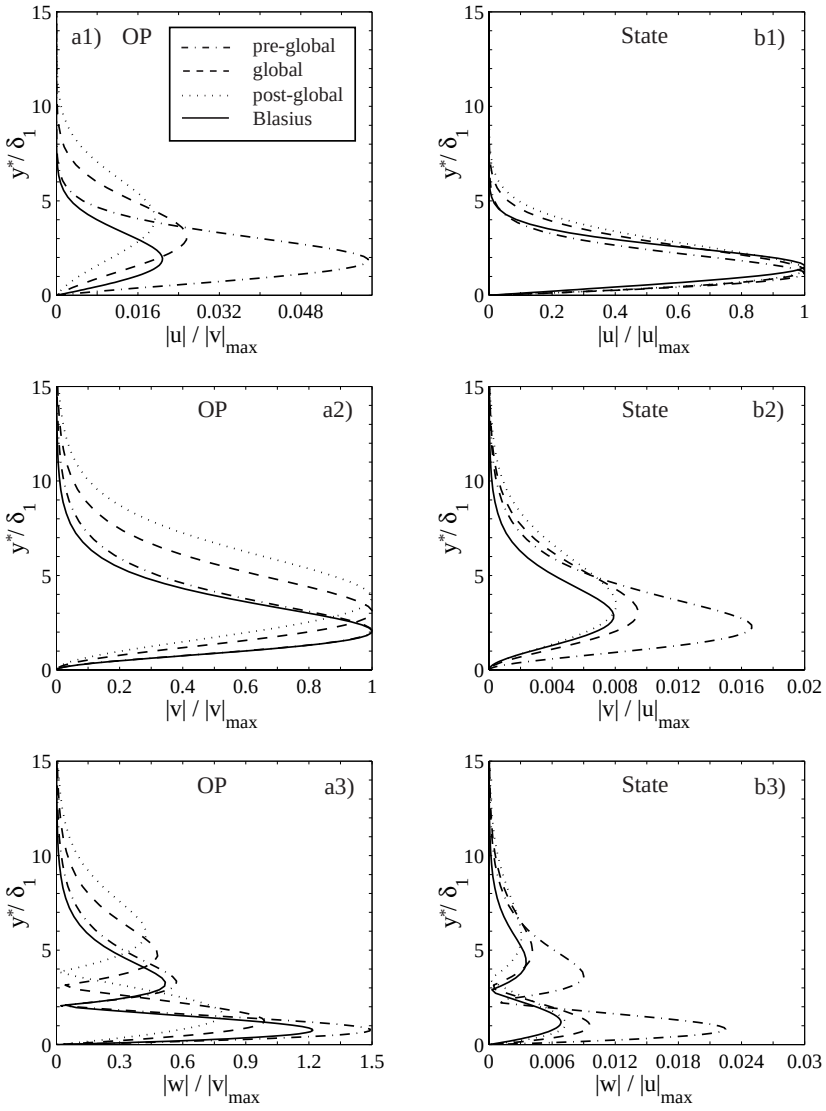

FIGURE 5. a) Perturbation velocity profiles for the pre-global, global and post-global OP in the ASBL and the global OP in the BBL at $R = 800$, b) their respective states at their respective t_γ (cf. table 1), marked with symbols in figure 3). The line-types of the pre-global, global and post-global profiles correspond to their amplification curves in figure 3.

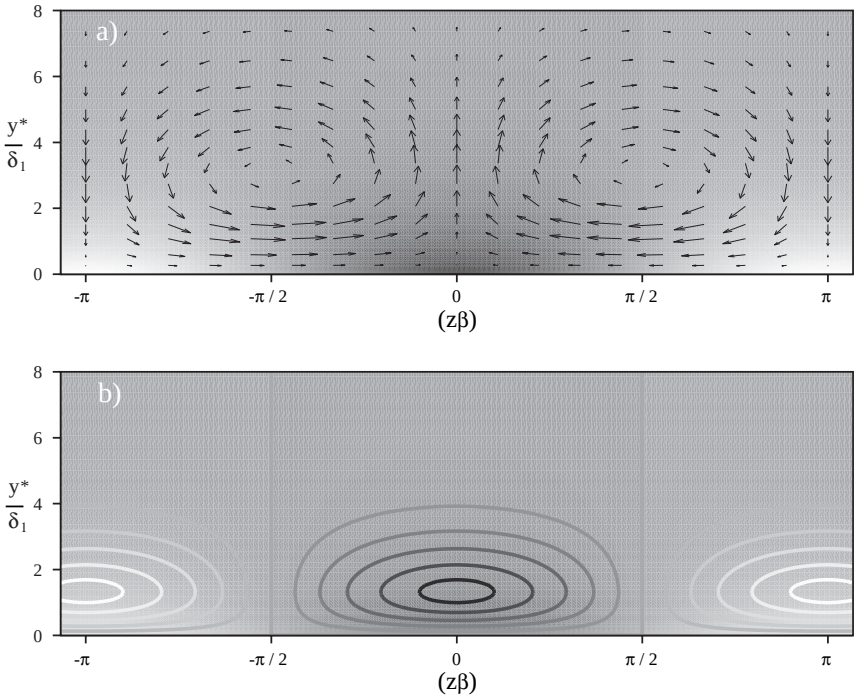

FIGURE 6. Evolution of the global OP for the ASBL at $R = 800$ in the crossflow plane, illustrating the lift-up mechanism. a) The crossflow components of the OP superposed on the perturbation pressure field (dark shading corresponds to low pressure). b) u-contours of the response (dark lines correspond to low velocity) similarly overlaid on p, at t_γ.

In contrast, the response is consistent with a streak, producing a large variation in streamwise perturbation velocity. A physical explanation for this was advanced by Landahl (1980), who noted that such initial configurations of perturbation velocity are ideally suited to 'lift-up' low-speed fluid into relatively faster flow and vice versa, exchanging momentum and generating a streak, an effect illustrated in figure 6 for the maximum optimal in the ASBL at $R = 800$. Also shown in figure 5 are the perturbation velocity profiles for the BBL (given by solid lines). It is interesting to compare the global OP in the ASBL and the BBL, i.e. the dashed and solid lines. Whereas the OP profile maxima for all ASBL cases are located higher above the plate than their BBL counterparts, the reverse holds for the u-component of the response. The time evolution of

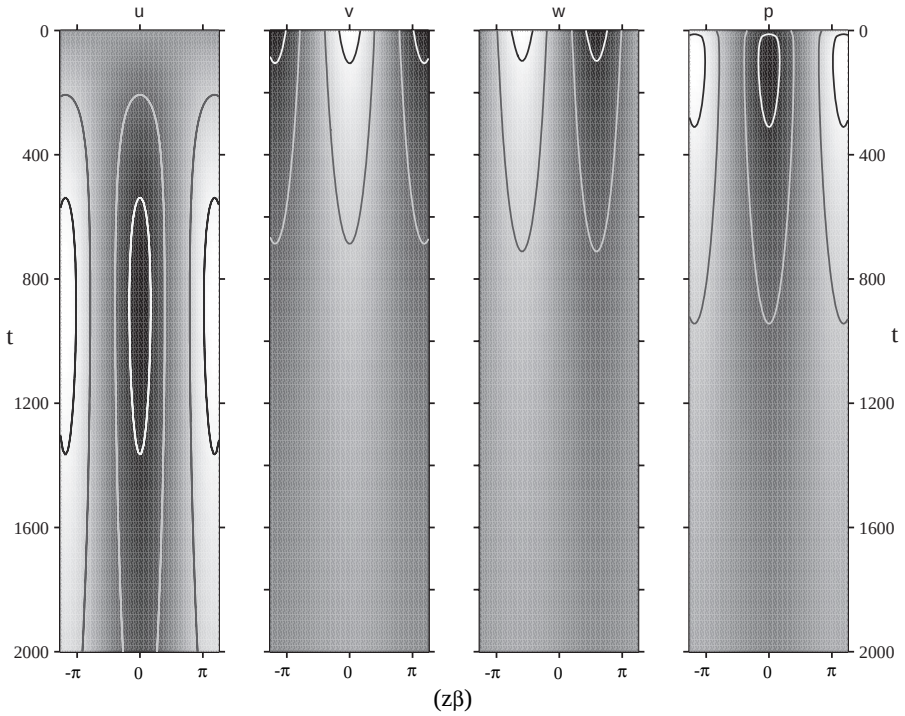

FIGURE 7. The time evolution of each perturbation component plotted in the zt-plane at the y-position above the wall where its maximum is found (normalized such that the maximum over all time is unity). Light shading indicates areas of positive perturbation quantities, and contour lines at ± 0.9 and ± 0.5 are shown. $|(u, v, w, p)|_{\max} = (10.8226, 0.25773, 0.25471, 7.4409 \times 10^{-7})$.

all perturbation components of the maximum optimal in the ASBL case is illustrated in figure 7. The strong initial v- and w-components decay quickly, while the u-component grows until reaching its maximum at $t_\gamma \approx 920$ (coinciding with the maximum energy), decaying slowly thereafter. The pressure perturbation, always largest at the surface, peaks rapidly and decays downstream.

With the scaling employed by Gustavsson (1991) to analyse the growth of the vorticity one can show that t_Γ will scale linearly and Γ quadratically with R (Schmid & Henningson 2001). These trends are confirmed for the BBL and ASBL in figure 8, where results for several different R have been reduced using both integral length scales. While either scaling is adequate to collapse the

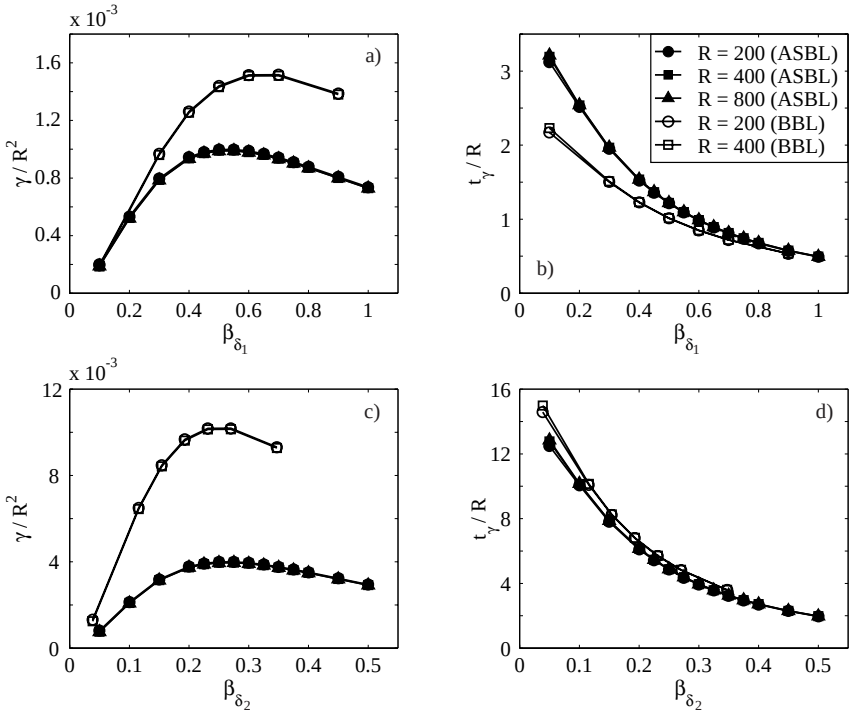

FIGURE 8. Behaviour of γ and t_γ with variations in the spanwise wavenumber. a) & b) scaled using δ_1, the displacement thickness. c) & d) using δ_2, the momentum thickness.

Flow	$\Gamma \times 10^3$	t_Γ	β
BBL, Butler and Farrell 1992	$1.50R^2$	$0.778R$	0.65
BBL	$1.51R^2$	$0.781R$	0.65
ASBL	$0.99R^2$	$1.147R$	0.53
BBL, ASBL intersection	$0.82R^2$	$1.920R$	0.53

TABLE 2. Reynolds number dependence of the maximum global optimal energy growth (Γ) and the time (t_Γ) at which this appears for the Blasius-, asymptotic suction boundary layer, and their intersection (see text).

data for a given type of boundary layer flow, it is interesting that the spanwise wavenumber associated with maximum growth is nearly independent when scaled with momentum thickness. Similar behaviour has been observed in the Falkner–Skan boundary layer (Corbett & Bottaro 2000). Considering the fact

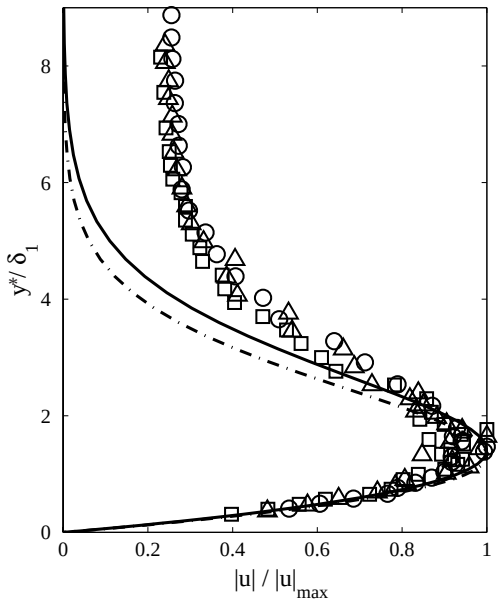

FIGURE 9. Streamwise perturbation velocity profiles at $R = 347$. Lines are OP response (i.e. disturbance at t_γ: solid line for $\beta = 0.33$, the measured streak separation; dash-dotted for $\beta = 0.53$, the maximum global optimal), symbols represent experimental data ($u_{\rm rms}$) at different downstream positions, $x = 1$m (◯), 1.6m (△), 2m (□) for a flow with $Tu = 1.4\%$. Experimental data from Fransson (2001).

that in the ASBL flow the equations are exact (i.e. no local approximation is invoked) the collapse of the curves in figure 8 indicates that boundary layer scales would be appropriate to model the physics of this problem even for R as small as 200. By transferring this argument to the BBL, this result provides a firm ground for the asymptotic (boundary-layer-based) analysis by Andersson *et al.* (1999) and Luchini (2000). Fitting the results for maximum global growth at various R, one obtains the coefficients reported in table 2. The minor discrepancy in the results reported for the Blasius case may be due to differences in optimization method, numerical discretization, or problem formulation.

From table 2 it is evident that in comparison to the case with no suction, the ASBL supports less algebraic growth and that this takes longer to develop. However, it is noticeable in figure 3 that as t becomes large more growth is experienced by the transient disturbances in the ASBL than in the BBL. The point of intersection between ASBL and BBL growth curves (cf. the ◯-symbol in figure 3) scales as t_Γ and Γ mentioned previously. As this behaviour occurs

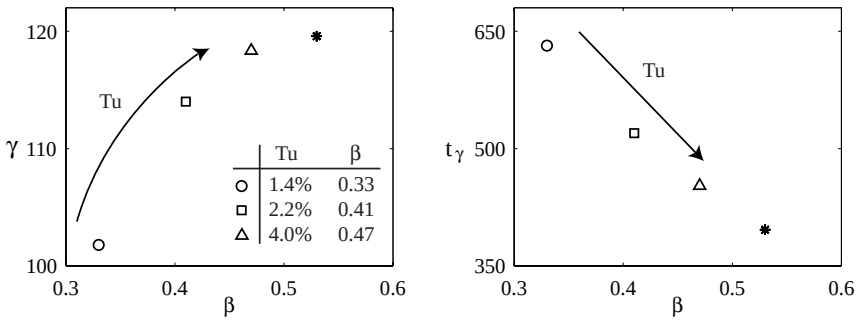

FIGURE 10. Computed γ and corresponding t_γ for four different β at $R = 347$. The open symbols indicate spanwise wavenumbers obtained from experiments at different Tu, whereas the global maximum at this R is shown by $*$.

for all R, it also occurs for all times, including the shorter intervals for which the parallel flow approximation in the BBL is a good one. The coefficients for the intersection relation with respect to t_Γ and Γ are given in table 2.

The ASBL is one case in which the algebraic growth mechanism presents the only viable linear route to transition at Reynolds numbers of practical interest. In this context it is reasonable to compare the optimal response state to disturbances measured inside the boundary layer (cf. §6 of Luchini (2000) for more details). Experiments on the ASBL subject to three different levels of FST were conducted by Fransson (2001). Three different turbulence generating grids situated upstream of the leading edge of the flat plate were used to generate the different FST intensities (Tu). The first 0.36 m of the plate is impermeable, after which uniform suction through a porous plastic plate material causes an asymptotic boundary layer to develop. The suction is such that $R = 347$ when $U_\infty = 5$ m/s, and measurements are carried out using hot-wire anemometry.

The experimentally observed streaks are not stationary in space nor in time. Thus, from two-point spatial correlation measurements a spanwise correlation function may be extracted and the position between the two probes where a distinct minimum in the correlation function is observed (which is quite clear in laminar boundary layers) may be interpreted as half the dominating spanwise wavelength of the streaks (i.e. $= \pi/\beta$). Experimentally, a small increase of the spanwise scale with the downstream distance is observed and the scale seems to vary inversely with the level of free stream turbulence (cf. Fransson & Alfredsson 2003). Figure 9 compares perturbation velocity profiles of two different OP with measurements at three different streamwise stations when $Tu = 1.4\%$. The agreement is good between the theoretical predictions, corresponding to the maximum global optimal for this flow and the global optimal at the measured streak spacing, and measurements carried out at three

x-stations. As might be expected the concordance is slightly better for the optimal whose spanwise periodicity matches the experimental conditions.

In comparing theory to measurement, differences in free-stream disturbance amplitude between the BBL and ASBL are apparent (cf. Andersson *et al.* 1999; Luchini 2000; Matsubara & Alfredsson 2001). The explanation is simple: in the BBL, perturbations within the boundary layer grow with x, and since the data is normalized to unity the free-stream disturbance amplitude decreases. In contrast, disturbance growth within the ASBL ceases as the asymptotic régime is approached for that particular suction velocity, and so a similar scaling causes the disturbance profiles to collapse in the free stream (see Fransson & Alfredsson 2003).

As mentioned above, the magnitude of Tu appears to have a significant effect on the measured streak spacing. Figure 10 shows that the theoretically predicted spanwise wavenumber for the maximum global OP is approached as Tu increases. In this figure the different β are extracted from the experiments (corresponding to a particular Tu) and used as an input to the OP-calculation. It is noteworthy that the maximum achievable growth varies little with large changes in β, on the other hand t_γ decreases dramatically.

It should be pointed out that the receptivity process giving rise to streaky structures is very complex and far from fully understood. There are many parameters influencing the process that are hard to control in an experiment when changing Tu. Amongst them are the integral and Taylor length scales of the FST that are impossible to keep constant, even when an active grid (with a variable upstream injection of secondary fluid in order to change Tu) with fixed mesh width and bar geometry is used (cf. Fransson 2001). Westin (1997) discusses whether or not any preferred spanwise scale exists that is most likely to be excited inside the boundary layer for any specific scale in the free stream. Fransson & Alfredsson (2003) report a decrease of the spanwise scale inside the boundary layer with increasing Tu for a Blasius flow, and good agreement of the spanwise scale with spatially predicted OP-scales by Andersson *et al.* (1999) and Luchini (2000). This study strengthens the hypothesis that for high enough Tu the boundary layer preferentially amplifies disturbances whose scales are close to that of the optimal disturbance. However, it should be remembered that the free stream scales are important and that the FST level does probably not set the spanwise scale inside the boundary layer by itself.

5. Conclusions

The transient behaviour of small disturbances in the asymptotic suction boundary layer (ASBL) has been investigated using a direct-adjoint approach in the temporal framework which is exact for this parallel flow. Initial disturbance configurations (optimal perturbations, OP) are found which maximize subsequent algebraic amplification of perturbation kinetic energy over a given period.

Significant algebraic growth is shown to occur, albeit less than that occurring in the Blasius boundary layer, which represents the no suction case. The difference can be attributed to the change in shape of the mean streamwise velocity profile. On the other hand, algebraically excited disturbances are shown to persist longer in the ASBL.

In accordance with other results for two-dimensional boundary layer flows, most growth occurs for disturbances which are infinitely elongated in the streamwise direction. These OP initially take the form of streamwise-oriented vortices which engender streaks, or large variations in the streamwise disturbance velocity. When scaled by momentum thickness, the spanwise wavenumber of the disturbance experiencing maximum amplification is identical to that for the Falkner–Skan family of boundary layers.

The numerical results from this work are in good agreement with experimental data obtained by Fransson (2001). That is, the velocity profile of the streak resulting from the OP undergoing the most growth is in good agreement with disturbances measured in the ASBL. The agreement is slightly better for the optimal perturbation whose spanwise wavenumber matches the streak spacing observed experimentally. Streak spacing in the experiment appears to be dependent on Tu. As the FST level increases, the streak spacing approaches the numerically determined wavenumber for the disturbance undergoing the most growth.

The asymptotic suction boundary layer is a suitable model for flows which may result from active flow control via steady suction (Walther *et al.* 2001; Pralits *et al.* 2002), amongst other applications. This work shows that algebraic disturbance amplification is a viable linear path to transition in the ASBL, and that OP for this class of flow must be taken into consideration in applications.

Acknowledgments

The authors would like to thank Profs. P. H. Alfredsson, A. Bottaro, and P. Luchini for valuable comments which lead to an improved manuscript. J. H. M. Fransson's stay in Toulouse was supported by an EU Marie Curie Training Site Fellowship in addition to his basic foundation by The Swedish Research Council (VR).

References

Abergel, F. & Témam, R. 1990 On some control problems in fluid mechanics. *Theor. Comput. Fluid Dyn.* **1**, 303–325.

Andersson, P., Berggren, M. & Henningson, D. S. 1999 Optimal disturbances and bypass transition in boundary layers. *Phys. Fluids* **11(1)**, 134–150.

Andersson, P., Brandt, L., Bottaro, A. & Henningson, D. S. 2001 On the breakdown of boundary layer streaks. *J. Fluid Mech.* **428**, 29–60.

Balakumar, P. & Hall, P. 1999 Optimum suction distribution for transition control. *Theor. Comput. Fluid Dynamics* **13**, 1–19.

Bewley, T. R. 2001 Flow control: new challenges for a new renaissance. *Progress in Aerospace Sciences* **37**, 21–58.

Bewley, T. R. & Liu, S. 1998 Optimal and robust control and estimation of linear paths to transition. *J. Fluid Mech.* **365**, 305–349.

Butler, K. M. & Farrell, B. F. 1992 Three-dimensional optimal perturbations in viscous shear flow. *Phys. Fluids A* **4**, 1637–1650.

Corbett, P. & Bottaro, A. 2000 Optimal perturbations for boundary layers subject to stream-wise pressure gradient. *Phys. Fluids* **12(1)**, 120–130.

Corbett, P. & Bottaro, A. 2001 Optimal linear growth in swept boundary layers. *J. Fluid Mech.* **435**, 1–23.

Drazin, P. G. & Reid, W. H. 1981 *Hydrodynamic stability*. Cambridge University Press.

Ellingsen, T. & Palm, E. 1975 Stability of linear flow. *Phys. Fluids* **18**, 487–488.

Fransson, J. H. M. & Alfredsson, P. H. 2003 On the disturbance growth in an asymptotic suction boundary layer. *J. Fluid Mech.* **482**, 51–90.

Fransson, J. H. M. 2001 Investigations of the asymptotic suction boundary layer. TRITA-MEK Tech. Rep. 2001:11. Licentiate Thesis, KTH, Stockholm.

Gustavsson, L. H. 1991 Energy growth of three-dimensional disturbances in plane Poiseuille flow. *J. Fluid Mech.* **224**, 241–260.

Hocking, L. M. 1975 Non-linear instability of the asymptotic suction velocity profile. *Quart. J. Mech. Appl. Math.* **28**, 341–353.

Högberg, M. 2001 Optimal control of boundary layer transition. PhD thesis, KTH, Stockholm, TRITA-MEK Tech. Rep. 2001:13.

Hultgren, L. S. & Gustavsson, L. H. 1981 Algebraic growth of disturbances in a laminar boundary layer. *Phys. Fluids* **24**, 1000–1004.

Joslin, R. D. 1998 Aircraft laminar flow control. *Annu. Rev. Fluid Mech.* **30**, 1–29.

Joslin, R. D., Erlebacher, G. & Hussaini, M. Y. 1996 Active control of instabilities in laminar boundary layers – overview and concept validation. *J. Fluids Eng.* **118**, 494–497.

Landahl, M. T. 1980 A note on an algebraic instability of inviscid parallel shear flows. *J. Fluid Mech.* **98**, 243–251.

Luchini, P. 2000 Reynolds number independent instability of the boundary layer over a flat surface: optimal perturbations. *J. Fluid Mech.* **404**, 289–309.

Lumley, J. & Blossey, P. 1998 Control of turbulence. *Ann. Rev. Fluid Mech.* **30**, 311–327.

Lundell, F. 2003 Experimental studies on bypass transition and its control. PhD thesis, KTH, Stockholm, TRITA-MEK Tech. Rep. 2003:03.

Matsubara, M. & Alfredsson, P. H. 2001 Disturbance growth in boundary layers subjected to free-stream turbulence. *J. Fluid Mech.* **430**, 149–168.

Moin, R. & Bewley, T. R. 1994 Feedback control of turbulence, part 2. *Appl. Mech. Rev.* **47**, S3–S13.

Pralits, J., Hanifi, A. & Henningson, D. S. 2002 Adjoint-based optimization of steady suction for disturbance control in incompressible flows. *J. Fluid Mech.* **467**, 129–161.

Reddy, S. C. & Henningson, D. S. 1993 Energy growth in viscous channel flows. *J. Fluid Mech.* **252**, 209–238.

Reshotko, E. 2001 Transient growth: A factor in bypass transition. *Phys. Fluids* **13(5)**, 1067–1075.

Schlichting, H. 1979 *Boundary layer theory*. McGraw-Hill.

Schmid, P. J. & Henningson, D. S. 2001 *Stability and transition in shear flows*. Springer.

Trefethen, L. N., Trefethen, A. E., Reddy, S. C. & Driscoll, T. A. 1993 Hydrodynamic stability without eigenvalues. *Science* **261**, 578–584.

Walther, S., Airiau, C. & Bottaro, A. 2001 A methodology for optimal laminar flow control. *Submitted* .

Westin, J. 1997 Laminar-turbulent boundary layer transition influenced by free stream turbulence. PhD thesis, KTH, Stockholm, TRITA-MEK Tech. Rep. 1997:10.

White, F. M. 1991 *Viscous fluid flow*. McGraw-Hill.

Paper 3

3

On the hydrodynamic stability of channel flow with cross flow

By Jens H. M. Fransson and P. Henrik Alfredsson

KTH Mechanics, SE-100 44 Stockholm, Sweden

Published in *Phys. Fluids* **15**, 436–441, 2003

We study plane channel flow with a homogeneous cross flow through porous walls mainly with respect to the stability to two-dimensional wave disturbances. Since the stability of a shear flow depends both on the velocity distribution and the Reynolds number we partly investigated this flow under the conditions that the flow Reynolds number was constant. The flow exhibits some interesting and unexpected stability characteristics. The effect of the cross flow was for certain parameter regions stabilizing and for others destabilizing. The latter result is in contrast to previous studies.

1. Introduction

A well known method for controlling wall bounded flows is to use suction or blowing through a porous part of the wall. Suction is usually associated with stabilizing the flow in the sense of hydrodynamic stability, and *vice versa* for blowing. For instance it is well known that the asymptotic suction boundary layer is much more stable than the Blasius boundary layer. In the case of a channel flow with a homogeneous cross flow, i.e. both walls are porous and fluid is injected and withdrawn with the same rate at the two walls, respectively, the effect on the stability is less obvious.

The present flow geometry can be found in a wide range of industrial applications, e.g filtration and flow in artificial kidneys are some important processes in the biomedical industry. Further, in cooling/heating applications and in boundary layer control areas the effect of cross flow is of great interest. Furthermore, the results of the present investigation extends previous studies and throws a new light on the stability of plane Poiseuille flow with uniform cross flow.

In previous works on the stability analysis of this flow, e.g. Hains (1971) and Sheppard (1972), the pressure gradient along the channel has been held constant, independent of the magnitude of the cross flow. For increasing cross flow the flow rate along the channel decreases and thereby the flow Reynolds number. For this case the cross flow has a stabilizing effect of the flow and Hains

(1967) showed that the unstable mode in plane Poiseuille flow (without cross flow) becomes completely stable as the velocity profile approaches the linear profile of Couette flow, which in turn has been proven to be stable for all infinitesimal disturbances (see e.g. Potter (1966)).

The stability of flows with suction and/or injection have been considered by e.g. Zaturska *et al.* (1988), Nicoud & Angilella (1997), Jankowski & Majdalani (2002). These authors studied continuous suction at both walls (asymmetric solutions), Couette flow with uniform cross flow, and porous channel flow with suction through the walls considering an oscillatory pressure, respectively. In Nicoud & Angilella (1997) it was shown that low rates of cross flow has a destabilizing effect on the flow, whilst high rates act stabilizing.

In the present study we have taken a slightly different approach to the problem. The stability of a shear flow is both a function of the mean velocity distribution and the Reynolds number. In the previous studies these two effects have not been separated, since the flow Reynolds number decreases when the cross flow increases, assuming the same pressure gradient. Here we chose to keep either the flow rate or the maximum streamwise velocity constant, and thereby the flow Reynolds number is also constant. This gives a different picture of the flow as compared to the previous studies and it is shown that depending on the parameter values the flow can be either stabilized or destabilized.

2. Theoretical considerations

2.1. *Mean flow distribution*

The asymptotic suction boundary layer profile is one of few exact solutions to the Navier-Stokes equations, however it is also possible to obtain an exact solution for the streamwise velocity profile in a plane channel with uniform cross flow. The shape of the profile depends on a Reynolds number, $R_v = V_0 h/2\nu$, based on the cross flow velocity ($V_0 = \text{const}$) and half the channel height $h/2$.

The velocity profile can be written as

$$u(y) = R_v \frac{y + \sinh^{-1}(R_v)\, e^{-R_v y} - \coth(R_v)}{1 - \log[R_v^{-1}\sinh(R_v)] - R_v \coth(R_v)}, \tag{1}$$

where $u(y)$ is the velocity profile made non-dimensional with the maximum streamwise velocity U_0, and y ($\in$ [-1, 1]) is the non-dimensional variable normal to the walls. For small values of R_v a series expansion of the expression (1) becomes

$$u(y) = (1 - y^2)[1 - \frac{1}{3} y R_v + (y^2 - \frac{1}{3}) R_v^2] + O(R_v^3), \tag{2}$$

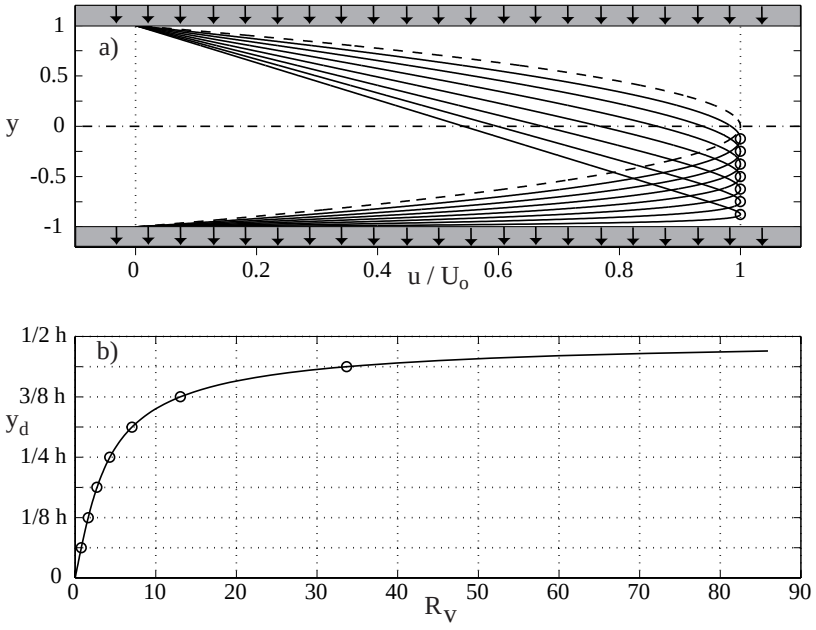

FIGURE 1. a) Velocity profiles for laminar plane channel flow with continuous cross flow when keeping U_0 constant. Dashed line is the parabolic profile achieved when the cross flow is absent and the dash-dotted indicates the centreline. b) The influence of R_v on y_d. See text for comments.

and it is clearly seen how the parabolic profile is retrieved when $R_v = 0$. The velocity profiles are plotted in Fig. 1(a). In the presence of the cross flow the position of maximum streamwise velocity (this position is denoted by y_d in the following) is displaced towards the lower (suction) wall. In Fig. 1(b) y_d is plotted versus R_v, where the y_d-values of the profiles in a) are marked with circles. Note that for high enough values of R_v the velocity profile will approach the linear Couette flow profile, except for a thin boundary layer at the suction wall. In the above expression the streamwise pressure gradient is substituted by expressing it with the maximum velocity (U_0) in the channel. The pressure gradient is plotted in terms of (U_0) in Fig. 2 versus R_v which shows that the pressure difference has to increase to keep U_0=const.

In this study the stability is considered through two other Reynolds numbers than what was used by the above references (based on constant dP/dx).

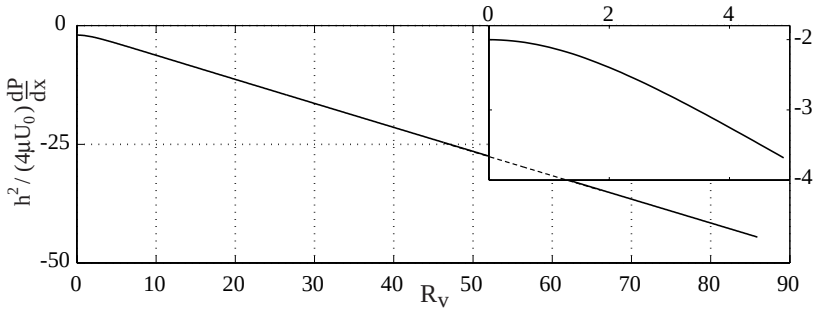

FIGURE 2. Influence of the cross flow on the streamwise pressure gradient when keeping U_0 constant.

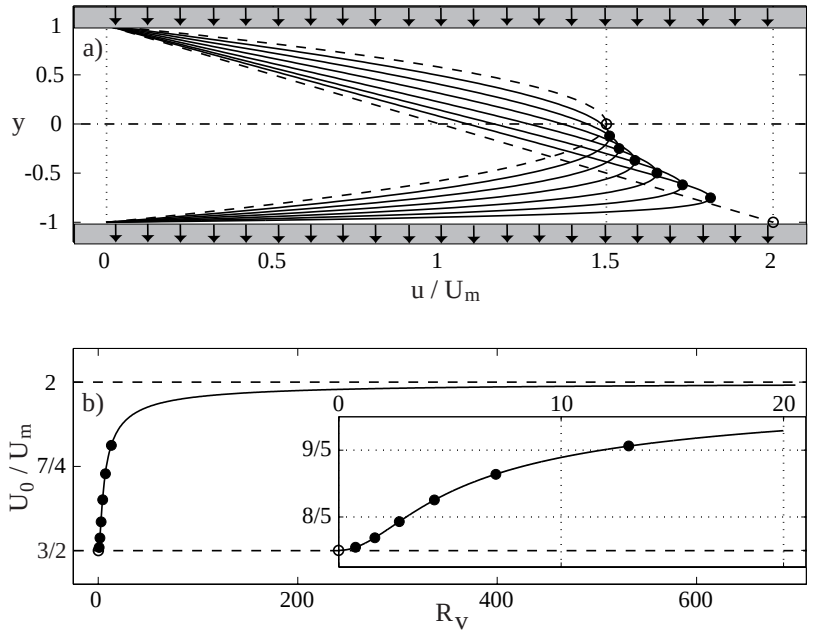

FIGURE 3. a) Velocity profiles for laminar plane channel flow with continuous cross flow and constant massflow. Dashed lines are the parabolic and linear Couette profiles whilst the dash-dotted indicates the centreline. b) Influence of R_v on U_0 for constant massflow (U_m). The markers corresponds to the same y_d as in Fig. 1

One of the Reynolds numbers, Re_0, is based on a constant U_0, whereas the other, Re_m, is based on a constant average velocity (U_m=const) defined as

$$U_m = \frac{1}{2}\int_{-1}^{1} u(y)dy.$$

This latter condition gives an increasing maximum velocity, see Fig. 3(a), with increasing cross flow velocity. In Fig. 3(b) the influence of R_v on U_0/U_m is plotted. For the parabolic profile the value is 3/2, whereas in the asymptotic limit when $R_v \to \infty$, the Couette flow limit is approached and the maximum velocity is twice the average velocity. To keep the Reynolds number constant the applied pressure gradient has to increase with increasing cross flow for both cases.

2.2. *Stability characteristics and numerical procedure*

When considering the stability of flows with cross flow the mean cross flow velocity component can also be taken into consideration in the stability equation. The implementation of this component becomes trivial when scaled with the maximum velocity in the channel and gives rise to an extra term with respect to the standard Orr-Sommerfeld and Squire equations (the sign of this term determines the direction of the cross flow), which gives

$$\left[(-i\omega + i\alpha U - \underbrace{\frac{R_v}{Re}\mathcal{D}}_{extra})(\mathcal{D}^2 - k^2) - i\alpha U'' - \frac{1}{Re}(\mathcal{D}^2 - k^2)^2\right]\hat{v} = 0 \qquad (3)$$

and

$$\left[(-i\omega + i\alpha U - \underbrace{\frac{R_v}{Re}\mathcal{D}}_{extra}) - \frac{1}{Re}(\mathcal{D}^2 - k^2)\right]\hat{\eta} = -i\beta U'\hat{v}, \qquad (4)$$

respectively. Above, $\mathcal{D}$ represents differentiation with respect to the wall-normal coordinate (y), ω is the angular frequency, α is the streamwise and β the spanwise wavenumbers and $k^2 = \alpha^2 + \beta^2$.

The stability analysis is made with a temporal approach implying that the eigenvalue problem is solved for $\omega \in \mathcal{C}$ or alternately for $c = \omega/\alpha$, being the phase velocity, $\hat{v}$ and $\hat{\eta}$ the complex eigenfunctions of normal velocity and vorticity respectively, and with the streamwise wave numbers $(\alpha, \beta) \in \mathcal{R}$. The boundary conditions chosen are that $\hat{\eta}$, $\hat{v}$, $\mathcal{D}\hat{v} = 0$ at both walls.

We have mainly devoted our attention to the least stable modes, i.e. two-dimensional wavelike perturbations according to Squire's theorem, resulting in that $\beta = 0$ in most of the calculations. Squire's theorem can be derived in the usual way by identification of terms in the two-dimensional and three-dimensional cases. For a given base flow R_v is constant (cf.eq. 1) and therefore the extra term does not give any additional condition to Squire's theorem.

The numerical method used for these calculations was a spectral method with Chebyshev expansion of the dependent variable. The solution is then represented by a truncated sum of Chebyshev polynomials according to

$$\hat{v} = \sum_{n=0}^{N} a_n \mathcal{T}_n^{(j)}(y) \quad \text{for} \quad y \in [-1, 1],$$

where N is the truncated value, a_n is the coefficient of the n:th Chebyshev polynomial and the superscript $^{(j)}$ denotes the j:th derivative of the Chebyshev polynomials.

The eigenvalue problem was solved using a built-in solver in the mathematical software Matlab. The accuracy of the code was checked through comparison with results for plane Poiseuille flow by Schmid & Henningson (2001).

3. Results

For a specific Re and wavenumber (α) the influence of R_v on the stability is analyzed. For the chosen values, which are $(Re, \alpha) = (6000, 1.0)$, the parabolic profile is unstable, i.e. $c_i > 0$. For a gradually increasing cross flow the flow is first stabilized until some critical value is reached. Increasing the cross flow further destabilizes the flow and it becomes unstable again after a certain value of R_v is reached. This threshold value will be denoted branch I, since for a further increasing R_v the flow will enter the stable region again after crossing branch II. This is seen in Figs. 4(a) and (b), where the least stable mode is followed. In Fig. 4(a) c_i is plotted versus R_v where the branches are marked in the reduction figure and in Fig. 4(b) the complex plane of the phase velocity ($c = c_r + ic_i$) is plotted where the R_v-value is given at the markers.

When keeping $Re_0 = \text{const.}$ an increasing R_v gives a decreasing Re_m. However, in order to show that the influence of the choice of Reynolds number is small, Figs. 5(a) and (b) show similar plots (as in Fig. 4) but now with Re_m

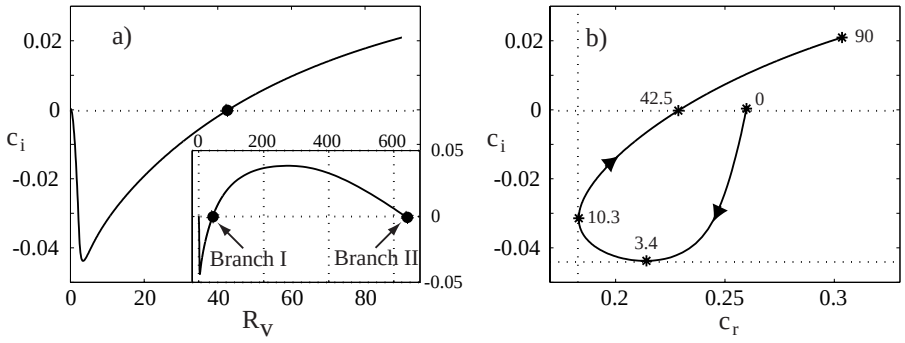

FIGURE 4. Stability calculation where the flow Reynolds number is based on the maximum velocity. Flow parameters (Re, α, β) = (6000, 1.0, 0). a) Shows the point where R_v stops being stabilizing. b) The complex phase velocity plane with corresponding R_v-values at ($*$)-markers.

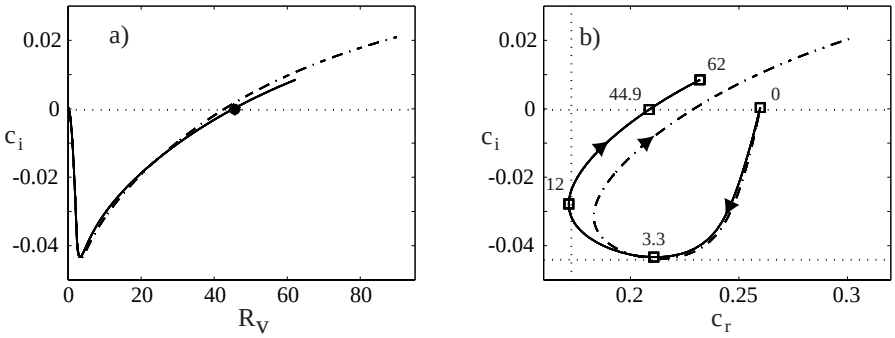

FIGURE 5. Stability calculation where the flow Reynolds number is based on the average velocity. Flow parameters (Re_m, α, β) = (4000, 1.0, 0) corresponding to $Re = 6000$ for $R_v = 0$. a) Shows the point where R_v stops being stabilizing. b) The complex phase velocity plane with corresponding R_v-values at ($\square$)-markers. For solid line c is normalized with U_0 and the dash-dotted line is the curve seen in Fig. 4(b).

= const. It is clear that the effect of the choice of Reynolds number is only marginal.

The streamwise and wall-normal disturbance amplitude distributions belonging to the least stable eigenvalue are shown in Fig. 6 for different strengths of the cross flow (here given both in terms of R_v and y_d). The distributions

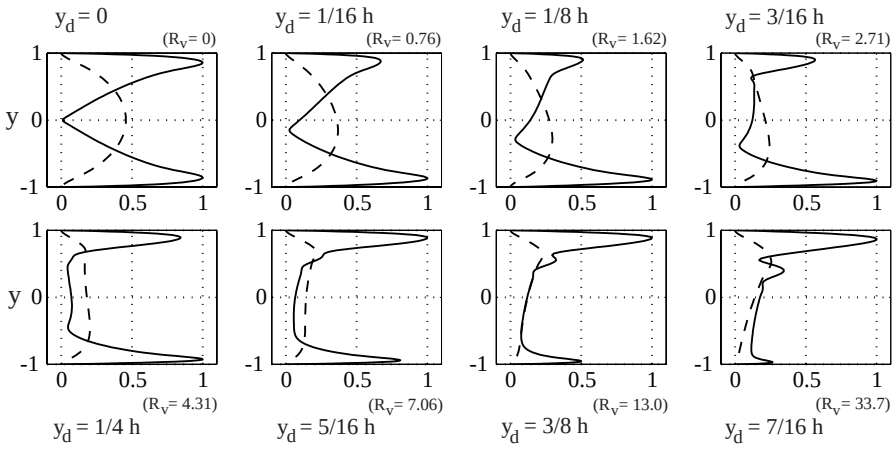

FIGURE 6. Amplitude distributions of streamwise and wall-normal disturbance function, $|\hat{u}|$ (solid lines) and $|\hat{v}|$ (dashed lines) respectively, for different strength of the cross flow. $\hat{u}$ is obtained from the continuity equation together with the definition of the vorticity, and both functions are normalized with the maximum value of $|\hat{u}|$. Flow parameters (Re, α, β) = (6000, 1.0, 0).

for the two different Reynolds number based calculations can hardly be distinguished, thus only the one based on the maximum velocity is plotted. For small values of R_v (up to 3.4 for these parameters) the flow stabilizes and the effect on $\hat{u}$ is a decreasing amplitude of the upper peak (blowing side) as compared to the suction side. The suction side peak also moves towards the wall. The distribution of the wall-normal disturbance shows a similar trend, i.e. its maximum is shifted towards the suction side. When increasing R_v further the streamwise disturbance peak at the blowing side becomes the largest and also

y_d	R_v	Re_c	α_c	c_r	R_v/Re_c
0	0	5772.22	1.02039	0.263982	0
0.0332 h	0.2	5967.01	1.01189	0.261378	3.35e-5
0.0665 h	0.4	6607.4	0.99025	0.25399	6.05e-5
0.0989 h	0.6	7902.5	0.95361	0.24148	7.59e-5

TABLE 1. Critical values for various y_d values. (See text)

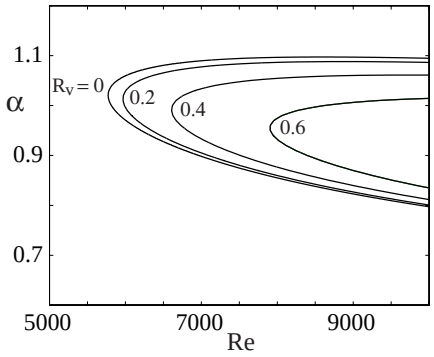

FIGURE 7. Neutral stability curves for various R_v.

the wall normal disturbance has its largest amplitude in the upper part of the channel. However at $R_v \approx 400$ the amplitude of $\hat{u}$ is the same on both sides of the channel and as R_v increases further the maximum in $\hat{u}$ occurs on the lower (suction) side.

Neutral stability curves for $R_v = 0$, 0.2, 0.4 and 0.6 are plotted in Fig. 7 to show the movement of the curves for increasing R_v. The shift of the curves towards higher Re_c and lower α_c may be observed for increasing R_v. Recall that for relatively large R_v the stability changes character and therefore the neutral stability curve will at some R_v change direction and move towards smaller Re_c. The critical values for the chosen cross flows in Fig. 7 are presented in table 1. These values are calculated with a critical-value search program developed for accurate determination of these values. The critical value for plane Poiseuille flow determined here are in agreement with e.g. Schmid & Henningson (2001).

As was shown in Fig. 4 there is a region of intermediate R_v where the cross flow makes the flow unstable. In order to elucidate this region contour plots of critical R_v with the corresponding c_r for branch I and II in the α-Re plane are shown in Fig. 8. The solid lines indicates paths of constant critical R_v-values (a,b) and c_r-values (c,d). Note that the calculated range of Re is in between 1000 and 10000. Below a certain Re the flow is absolute stable and the critical values are given in the end of this section.

In Fig. 9 the neutral stability curve for α=1.0 is plotted in the Re-R_v plane. For small values of R_v the critical Re increases dramatically from Re_c = 5814.9, marked with ($\times$) in Fig. 9, and the unstable range of wavenumbers becomes smaller[1]. Figure 7 shows that a disturbance with $\alpha = 1.0$ for low

[1]Note that this is not the critical value for plane Poiseuille flow (5772.22), since that value is obtained for $\alpha = 1.02039$.

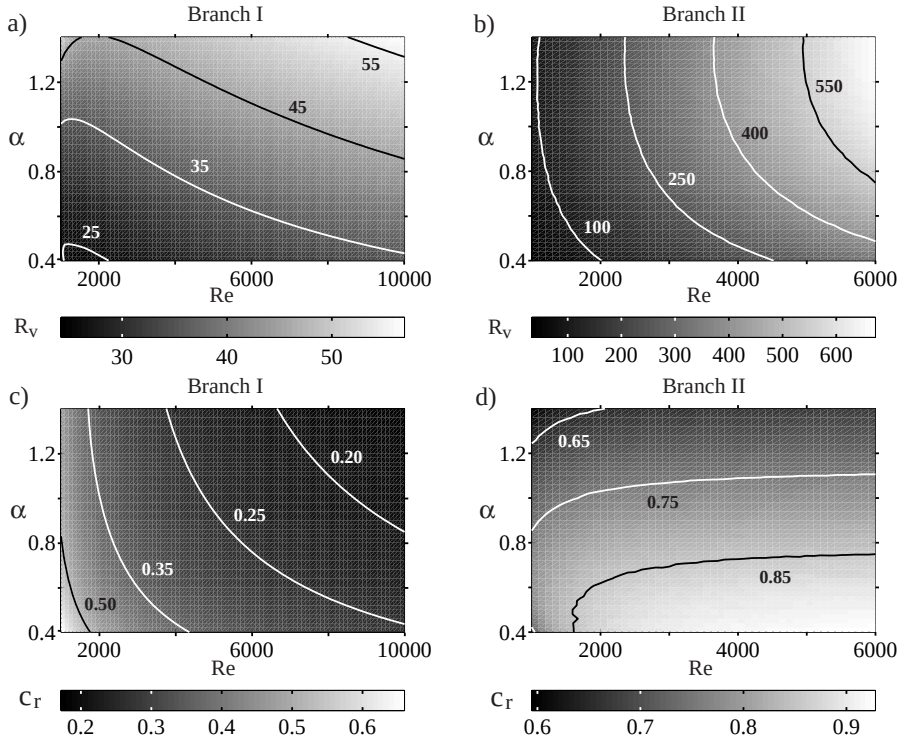

FIGURE 8. Contour plots of R_v^c and c_r in the α-Re plane for branch I. a) and c) and branch II b) and d).

R_v ($\sim \mathcal{O}(1)$) becomes stable for all Re up to a certain critical value of R_v, giving rise to a discontinuity in the neutral stability curve in Fig. 9. When R_v increases further the flow becomes more unstable and the neutral curve moves towards lower critical R_v. The ultimate critical values are determined to be $(Re_c, \alpha_c, R_v^c) = (667.4, 0.858, 38.24)$ with $c_r = 0.644$. The critical Re-value can be substantially reduced when cross flow is present and for the ultimate critical value the cross flow velocity to the maximum streamwise velocity ratio is 5.7%. The corresponding critical Re is hence lowered by an order of magnitude as compared to plane Poiseuille flow.

So far, only two-dimensional disturbance calculations have been presented. The focus has been on the most unstable mode, which can be justified since Squire's theorem is still valid despite the cross flow term. However, the stabilizing effect of three-dimensionality for a given β is smaller with increasing R_v. This is an interesting phenomenon since it would imply that three-dimensional modes could be realistic competitors to there two-dimensional counterpart in a

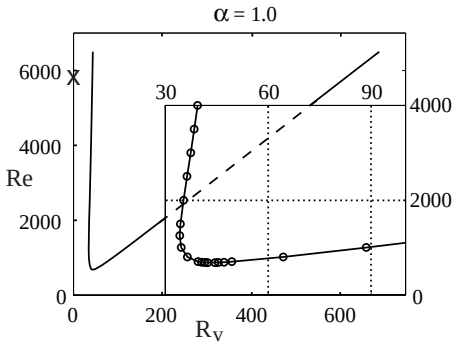

FIGURE 9. Neutral stability curve for $\alpha = 1.0$ in the Re-R_v plane.

real flow situation. For the particular case $(Re, \alpha) = (6000, 1.0)$ the growth factor (c_i) of the most unstable mode is reduced from 0.00032 to -0.00202 when β is increased from 0 to 0.5 for $R_v = 0$, and is located on branch[2] A. Considering the same case but $R_v = 10$ the reduction is from -0.03190 to -0.03257 for the corresponding most unstable mode on branch A. It should be noted however, that at $R_v \approx 1.18$ and 0.87 for $\beta = 0$ and 0.5 respectively, the overall most unstable mode has moved to branch P. Another feature that was observed is that for relatively small R_v the phase velocity of the disturbance is increased for increasing β. In contrary, for larger values of R_v the phase velocity is reduced and the change of trend occurs around $R_v = 2$.

4. Summary

We have shown that plane channel flow with homogeneous cross flow through porous walls exhibit some interesting and unexpected stability characteristics. Since the stability of a shear flow depends both on the velocity distribution and the Reynolds number we partly investigated this flow under the conditions that the flow Reynolds number was constant. The effect of the cross flow was for certain parameter regions stabilizing and for others destabilizing. The latter result is in contrast to previous studies.

Acknowledgments

This work has been financially supported by The Swedish Research Council (VR) and is gratefully acknowledged.

[2]The division of the eigenvalues into three main branches A (left), P (right), and S (center) by Mack (1976) have been used here.

References

Hains, F. D. 1967 Stability of plane Couette-Poiseuille flow. *Phys. Fluids* **10**, 2079–2080.

Hains, F. D. 1971 Stability of plane Couette-Poiseulle flow with uniform crossflow. *Phys. Fluids* **14**, 1620–1623.

Jankowski, T. A. & Majdalani, J. 2002 Laminar flow in a porous channel with large wall suction and a weakly oscillatory pressure. *Phys. Fluids* **14**, 1101–1110.

Mack, L. M. 1976 A numerical study of the temporal eigenvalue spectrum of the blasius boundary layer. *J. Fluid Mech.* **73**, 497–520.

Nicoud, F. & Angilella, J. R. 1997 Effects of uniform injection at the wall on the stability of Couette-like flows. *Phys. Fluids* **56**, 3000–3009.

Potter, M. C. 1966 Stability of plane Couette-Poiseuille flow. *J. Fluid Mech.* **24**, 609–619.

Schmid, P. J. & Henningson, D. S. 2001 *Stability and transition in shear flows*. Inc.: Springer-Verlag New York.

Sheppard, D. M. 1972 Hydrodynamic stability of the flow between parallel porous walls. *Phys. Fluids* **15**, 241–244.

Zaturska, M. B., Drazin, P. G. & Banks, W. H. H. 1988 On the flow of a viscous fluid driven along a channel by suction at porous walls. *Fluid Dyn. Res.* **4**, 151–178.

Paper 4

4

Free stream turbulence induced disturbances in boundary layers with wall suction

By Shuya Yoshioka, Jens H. M. Fransson and P. Henrik Alfredsson

KTH Mechanics, SE-100 44 Stockholm, Sweden

Submitted for publication.

An experimental investigation of free stream turbulence (FST) induced disturbances in asymptotic suction boundary layers (ASBL) has been performed. In the present study four different suction rates are used and the highest is 0.40% of the free stream velocity, together with three different FST levels (Tu= 1.6, 2.0 and 2.3%). A turbulence generating grid of active type is used and offers the possibility to vary the Tu-level while the scales of the turbulence remains almost constant. It is known that FST induces elongated disturbances consisting of high and low velocity regions, usually denoted streaky structures, into the boundary layer. The experiments show that wall suction suppresses the disturbance growth and may significantly delay or inhibit the breakdown to turbulence. Two-point correlation measurements in the spanwise direction show that the averaged streak spacing decreases with increasing FST-level, whereas the spacing in the ASBL is more or less constant in the downstream direction. This is in contrast to what is observed in a Blasius boundary layer where streaks develop and adapt their spanwise scale close to the boundary layer thickness. A hypothesis for the present observations is that the observed scale reflects the disturbances that are fed from the leading edge part into the boundary layer whereafter the structures only passively are convected downstream.

1. Introduction

Boundary layers influenced by high free stream turbulence (FST) are encountered in many technical applications, especially in various types of fluid machinery. Boundary layer transition under such circumstances is usually referred to as bypass transition. Reliable methods for the prediction of bypass transition is at present limited, (see e.g. Westin & Henkes 1997), mainly because the mechanisms of disturbance receptivity and growth as well as the breakdown process are still not fully understood. It is known that FST induces streamwise elongated disturbances consisting of high and low velocity regions (streaky

structures) into the boundary layer (Kendall 1985, 1998; Westin *et al.* 1994; Alfredsson & Matsubara 2000; Matsubara & Alfredsson 2001), which seem to resemble so called transiently growing disturbances, (see e.g. Andersson *et al.* 1999; Luchini 2000; Fransson & Corbett 2003). For boundary layers subjected to FST it has been found that the disturbance grow algebraically to a fairly high amplitude before it breaks down into turbulence and this breakdown may be caused by a secondary instability on the streaks Andersson *et al.* (2001). Westin *et al.* (1998) pointed out that the continuous forcing by FST along the boundary layer edge is necessary for the breakdown.

Distributed suction at the wall has long been known to be a possibility to stabilize laminar boundary layers with respect to instability waves (TS-waves) in order to avoid or postpone transition. Fransson & Alfredsson (2003) showed that also FST induced disturbances could be stabilized by suction at the wall, indicating that the suction is also effective to delay bypass transition.

In the present study these results are extended to other Reynolds numbers and a parametric study is made in order to understand both the receptivity to free stream turbulence of the boundary layer as well as the subsequent disturbance development.

Recent studies (e.g. Matsubara & Alfredsson 2001) indicate that the spanwise scale of the streaky structures tends towards the local boundary layer thickness far from the plate leading edge in the Blasius boundary layer (BBL). In an asymptotic suction boundary layer (ASBL) experiment it is possible to change the boundary layer thickness and Reynolds number independently. Furthermore in the asymptotic region the boundary layer thickness is independent of the downstream position. This makes it possible to study the development of the streaky structures under constant conditions, which is not possible in a growing boundary layer.

1.1. *The asymptotic suction boundary layer*

In a laminar boundary layer with wall suction, i.e. the velocity normal to the wall is negative and uniform at the wall ($-V_0$, furthermore the normal velocity is the same throughout the ASBL), the streamwise velocity distribution ($U(y)$) in the wall normal direction can be analytically obtained and expressed as follows (see e.g. Schlichting 1979)):

$$U(y) = U_\infty \left(1 - e^{-\frac{V_0 y}{\nu}}\right), \tag{1}$$

where U_∞ and ν denote free stream velocity and kinematic viscosity, respectively. It should be noted that the velocity profile is independent of streamwise

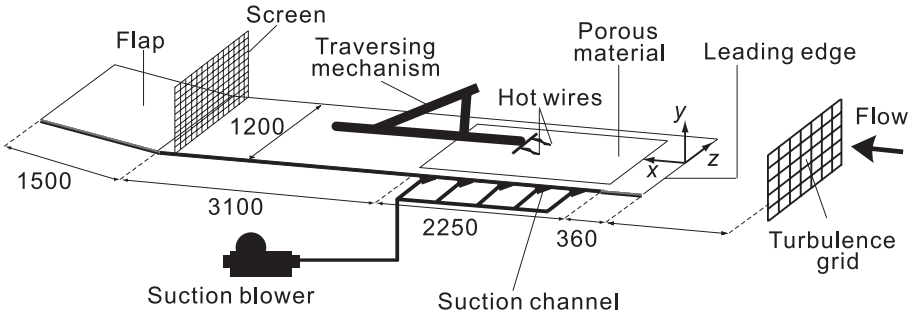

FIGURE 1. Schematic of experimental facility. Dimensions are in mm.

position x, and thus the boundary layer thickness becomes constant. The displacement thickness δ_1, momentum thickness δ_2, and shape factor H_{12} are:

$$\delta_1 = \frac{\nu}{V_0}, \quad \delta_2 = \frac{1}{2}\frac{\nu}{V_0} \quad \text{and} \quad H_{12} = 2. \tag{2}$$

The Reynolds number based on displacement thickness δ_1 is written as:

$$Re = \frac{U_\infty \delta_1}{\nu} = \frac{U_\infty}{V_0}. \tag{3}$$

As indicated by Eqs. (2) and (3), the boundary layer thickness and Reynolds number can be independently adjusted by changing U_∞ and V_0.

2. Experimental set up

The experiments were conducted in the MTL-wind tunnel at KTH and a schematic of the experimental set up is shown in figure 1. We use a coordinate system with its origin fixed at the centre of the leading edge of the plate. The x, y- and z-axes were directed in the downstream, wall normal and spanwise directions. The test section is 7 m long, 0.8 m high and 1.2 m wide and a horizontal test plate, which spans the whole width of the test section was mounted with its upper surface approximately 0.25 m from the wind tunnel floor. A porous material, 3.2 mm in thickness, covers 2.25 m (length) $\times$ 1.0 m (width) of the upper surface of the test plate. Through this porous surface, uniform suction was applied starting from x=0.36 m, see figure 1. The porous plate consists of a sintered plastic material with an average pore size of 16 μm

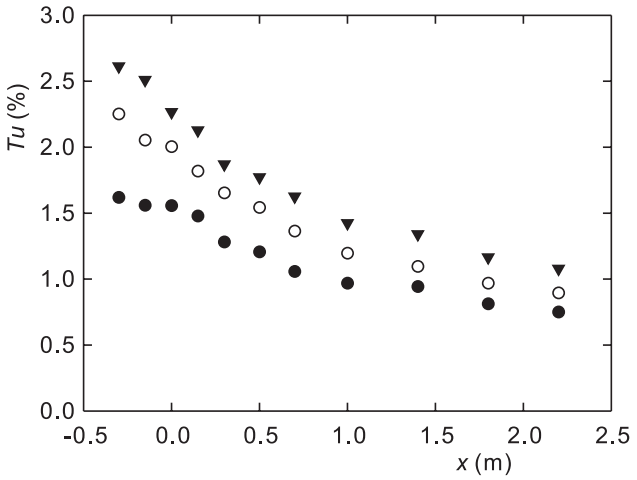

FIGURE 2. Variation of free stream turbulence level, Tu, for the three cases, ▼: G0, ○: G1 and ●: G2 at U_∞=5.0 m/s.

and can be considered hydrodynamically smooth. There is a plenum chamber below the porous plate which is connected to an electric blower through 18 holes and 9 suction channels. An extra aluminum plate section of 3.1 m was added downstream of the test plate and was followed by a trailing-edge flap. The trailing-edge flap as well as the fine-meshed screen placed just upstream the flap is used to adjust the blockage ratio between the upper and lower sides of the test plate. This makes it possible to control the position of the stagnation line at the leading edge and have it on the upper side of the plate to avoid separation. For the leading edge, an asymmetric shape was employed to minimize the pressure gradient. The pressure gradient along the porous part of the plate without suction was within ΔC_p=±0.01 by careful adjustment of the test section ceiling. For details of the plate and leading edge (see e.g. Fransson 2001).

Velocity measurements were made with hot-wire anemometry, where the sensors were single wires made from platinum with a diameter and length of 2.5 μm and 0.5 mm, respectively. The calibration is made in the free stream against a pitot tube and the calibration function used is King's law with an extra term added to take natural convection at low velocities into account (see e.g Johansson & Alfredsson 1982). The hot-wire probe was mounted on the traversing mechanism as shown in figure 1. For the evaluation of the spanwise scale of the streaky structures, two hot wire probes were used for the simultaneous measurement of the instantaneous streamwise velocity.

The free stream turbulence was generated by an active turbulence generating grid mounted upstream of the leading edge. This grid has a mesh width of 50 mm and is constructed by 13 horizontal and 20 vertical pipes with a diameter of 5 mm. A total of 254 jet orifices (diameter 1.5 mm) were drilled in the pipes and point towards the upstream direction. From these jet orifices, secondary air is ejected into the free stream. The distance from the grid to the plate is 1.4 m, which ensures a fairly homogeneous turbulence at the plate. The turbulence intensity depends on the injection rate and in the present study three cases are studied. These are denoted by G0 (without injection), G1 and G2, hereafter. In figure 2, the downstream variation of the FST level, $Tu = u_{rms}/U_\infty$ is shown. In all three cases, the FST level gradually decreases in the downstream direction. The FST level at the leading edge of the test plate,i.e. at $x = 0$ m, is 1.6%, 2.0% and 2.3% for the G0, G1 and G2 cases respectively. An advantage with using the active grid to control the turbulence level is that the turbulence scales are fairly independent of the injection rate as shown by Fransson (2001) and for the grid used the Taylor scale is approximately 8 mm.

In the present study we take advantage of the fact that for the asymptotic suction boundary layer the Reynolds number and the boundary layer thickness can be changed independently as discussed in section 1.1. In one set of measurements the free stream velocity was set to 5.0 m/s and the suction velocity V_0 was varied in the range of 0–0.4% of U_∞. In another set of measurements the free stream velocity U_∞ was varied in the range 2.0–6.0 m/s and the suction velocity was kept at 0.29% of U_∞, which gave a constant Reynolds number ($Re = 350$). In that way the boundary layer thickness, but not the Reynolds number, changes. The characteristics of the boundary layers studied can be found in Table 1.

Many different methods, which are based on the measured velocity time signal, have been deviced to determine when the flow changes between laminar and turbulent conditions (or vice versa) in a transitional flow situation, see e.g. Hedley & Keffer (1974). In this study the following simple method was used to distinguish between these different flow regimes. The method is depicted in figure 3 which in (a) shows a typical signal from the transitional region,

Experiment	Case A				Case B				
U_∞ (m/s)	5.0				2.0	3.0	4.0	5.0	6.0
V_0/U_∞ (%)	0.10	0.20	0.29	0.40			0.29		
Re	1000	500	350	250			350		
$\delta_{1,ASBL}$ (mm)	2.99	1.50	1.03	0.75	2.58	1.72	1.29	1.03	0.86

TABLE 1. Boundary layer characteristics for the different ASBL in the present study.

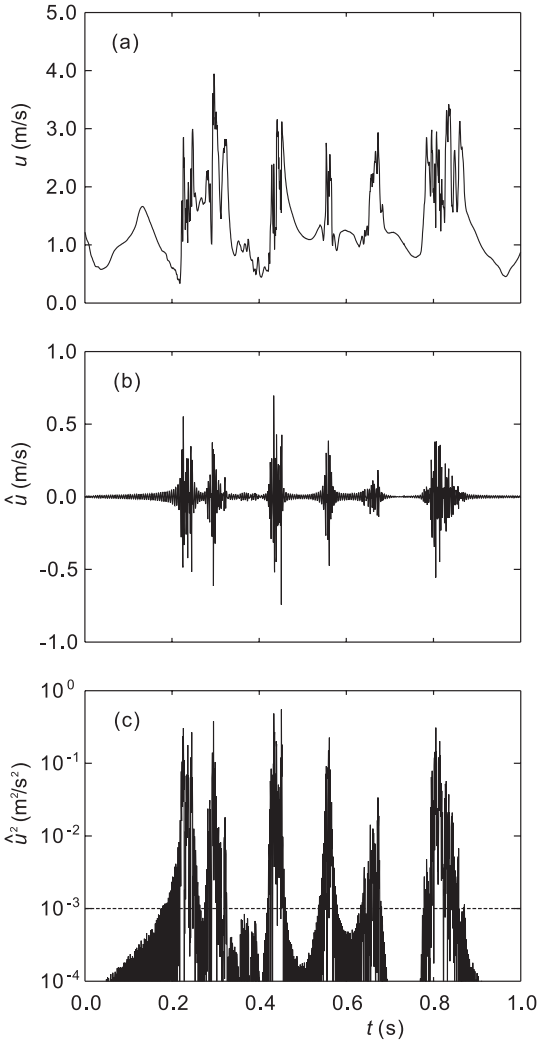

FIGURE 3. An example illustrating the sorting technique for laminar and turbulent periods in the transitional region. The measurement is made at x=1.4 m and the suction rate is 0.1% of U_∞ (=5.0 m/s), and with grid condition G2. (a) velocity signal from the position of maximum u_{rms} (b) high-pass filtered velocity signal, (c) square of high-pass filtered signal.

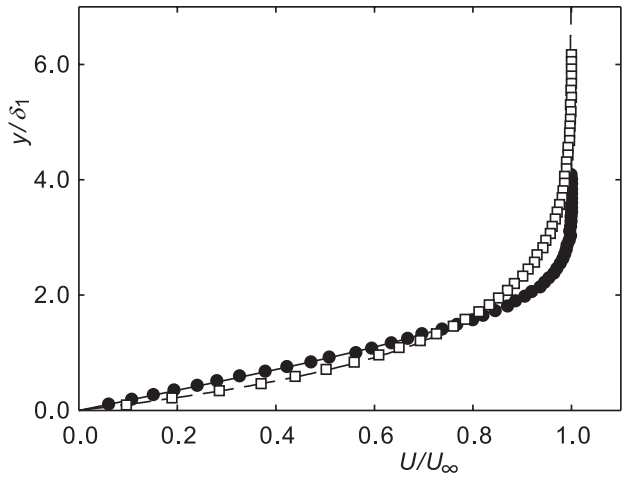

FIGURE 4. Mean velocity profiles for boundary layers with (□) and without (●) wall suction, no grid. Also the theoretical distributions for the Blasius (———) and the asymptotic suction (– – –) boundary layer profiles are shown. x=2.2 m, U_∞=5.0 m/s

characterized by turbulent spots intermixed with laminar regions. This signal was Fourier transformed whereafter the contribution below 200 Hz was set to zero. By an inverse transform the high frequency part of the signal was extracted which can be seen in figure 3(b). By squaring the high-pass filtered signal and applying a suitable threshold the turbulent sequencies of the signal were determined. Note that the vertical axis in figure 3(c) is logarithmic in order to clearly see the effect of changing the threshold. The method of course show some sensitivity to the chosen values of filter frequency and threshold and these values were chosen after a trial and error procedure, but were then kept constant for all cases. This methodology was used both to determine the intermittency factor (which was determined at the y-position of maximum u_{rms}) as well as to extract the non-turbulent parts in order to determine the spanwise spatial scale of the streaky structures in the transitional region.

3. Results and discussion

3.1. *Disturbance growth*

Typical mean velocity distributions, $U(y)$, without FST at a fixed free stream velocity of U_∞=5.0 m/s are shown in figure 4 at x=2.2 m with (V_0/U_∞ = 0.20%) and without suction. Note that the distance from the wall is normalized

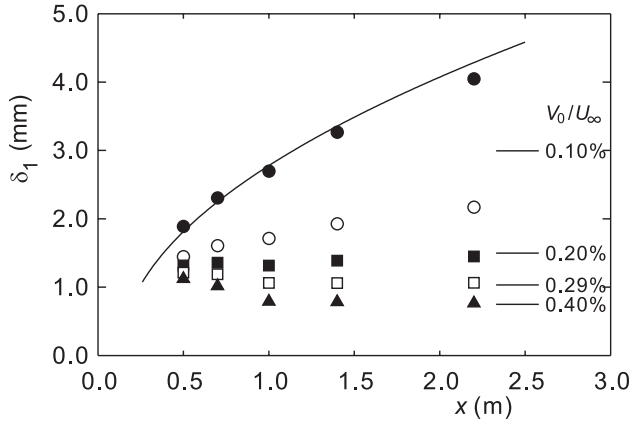

FIGURE 5. Downstream development of displacement thickness for the no suction case (●) and for the four suction ratios of Case A in Table 1. The lines indicate the theoretical development of the displacement thickness for the BBL and the asymptotic thickess for the four suction cases. There is no grid and U_∞=5.0 m/s.

by the measured displacement thickness. For the ASBL the measured value is within 3% of the theoretical one (1.45 mm as compared to 1.50 mm) whereas the discrepancy is larger for the BBL (4.05 mm as compared to 4.42 mm). The theoretical velocity profiles obtained from the Blasius solution and Eq. (1) are also shown in the figure for comparison. It is seen that both measured velocity distributions are in good agreement with theory. Figure 5 shows the development of the displacement thickness for the cases without any turbulence grid. In the no suction case the displacement thickness grows roughly as $x^{1/2}$ as expected from theory whereas it grows less or decreases for the suction cases. For suction velocities of 0.2% and higher it seems that the boundary layer reaches the asymptotic state on the test plate. The boundary layer growth with FST is similar except for the cases when it becomes transitional.

The random motion of the streaky structures gives rise to low frequency fluctuations in the streamwise velocity as sensed by a stationary hot wire. Rms-distributions of the velocity fluctuations in the boundary layer are shown in figure 6 for the case G1 at x=1.0 and 2.2 m. For x=1.0 m the flow is still laminar whereas at x=2.2 m (depending on the suction rate) the flow is either fully turbulent, transitional or laminar. Figure 6(a) shows that with increasing suction rate the u_{rms}-level inside the boundary layer decreases. At x=2.2 m, figure 6(b), the no suction case shows a distribution that is what to

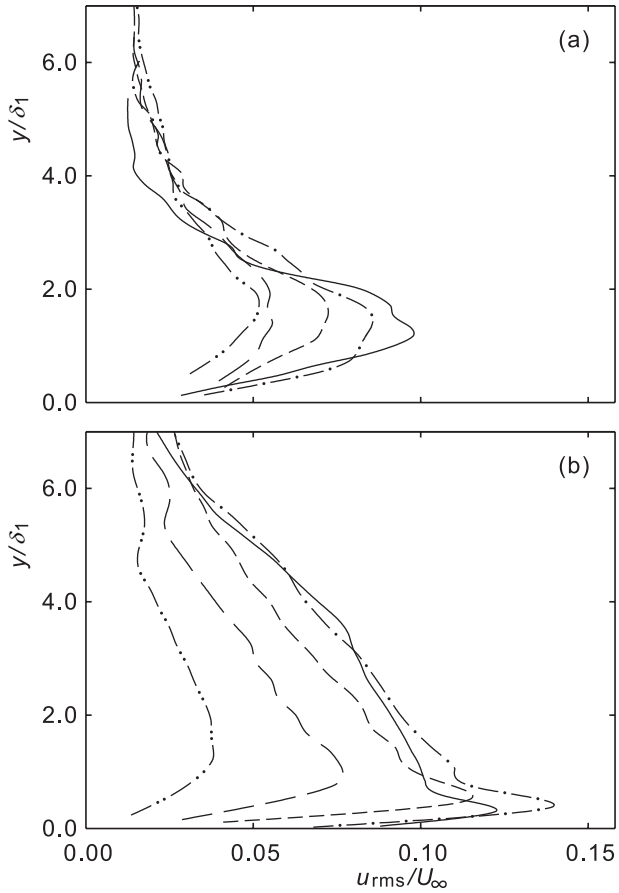

FIGURE 6. Effect of wall suction on the wall normal distributions of turbulent intensity for case G1. (a) x=1.0 m, (b) x=2.2 m. ———: no suction, – · – · –: V_0/U_∞=0.1%, – – -: 0.2%, — — —: 0.29%, – ·· – ·· –: 0.40%.

be expected by a typical turbulent boundary layer with a maximum very close to the wall. Also the maximum level is in the range which one would expect from a turbulent boundary layer. For V_0/U_∞=0.10%, the disturbance level is larger than that of the no-suction case especially in the region close to the wall. This is due to the transitional state of the boundary layer. It is obvious that a further increase of suction provides a reduction of u_{rms} across the full height

of the boundary layer, that the peak position moves away from the wall, and that the peak itself becomes broader.

The downstream evolution of the FST induced disturbance amplitude in the boundary layer is investigated next. In this case the free stream velocity was fixed to U_∞=5 m/s, and the suction velocity was changed which gives a variation of the Reynolds number as summarized in Table 1.

In figure 7 the variation of the maximum values of u_{rms} measured at each x position is shown. Figure 7(a) shows the G0 case, and without suction u_{rms} increases approximately as $x^{1/2}$ until x=2.0 m, and thereafter it increases faster due to the start of the transition process, i.e. formation of turbulent spots. This is indicated by the variation of the shape factor, H_{12}, and the intermittency factor, γ, shown in figure 8(a). Even at the most upstream position, x=0.5 m, the shape factor is $H_{12} = 2.5$, which is less than the value of the Blasius profile, $H_{12} = 2.6$. This is due to the presence of the streaky structures inside the boundary layer. The shape factor is almost constant up to x=1.5 m but decreases to $H_{12} = 2.3$ at x =2.2 m. Corresponding to this decrease, the intermittency factor γ rises from 0.0 to 0.2.

From figure 7(a) it is obvious that the development of the disturbance amplitude in the downstream direction shows less growth when suction is applied. In fact the growth of u_{rms} with downstream distance seems eliminated for a suction rate V_0/U_∞ of 0.2%, and u_{rms} is decreasing in the downstream direction, for higher suction rates. The shape factor H_{12} and intermittency factor γ for all the suction cases presented in figure 8(a) are close to $H_{12} = 2.0$ and $\gamma = 0.0$ which means that the boundary layer state is laminar and transition is inhibited.

In figure 7(b) the results obtained from the case G1, are shown. Without suction, u_{rms} first increases with downstream distance as for the G0 case. The start of the transition occurs around x=1.4 m, which is further upstream as compared to the G0 case, the highest rms-level is found around x=1.8 m, whereafter it decreases until the boundary layer has established a fully turbulent region. This development is also clearly demonstrated by the downstream variation of H_{12} and γ, shown in figure 8(b).

For the suction rates $V_0/U_\infty = 0.1\%$ and 0.2%, the growth of u_{rms} is suppressed as compared with the no-suction case, see figure 7(b). However at the end of the test region the start of transition is seen both as an increase in u_{rms} and as an increase in γ (figure 8(b)). Furthermore a corresponding decrease in the shape factor is also seen. For the two highest suction rates (0.29%, 0.40%) there is hardly any sign of transition, neither in the rms-amplitude nor in the intermittency result. For the highest suction case $V_0/U_\infty = 0.40\%$ in particular, u_{rms} decreases in the downstream direction in the same way as for the G0 case.

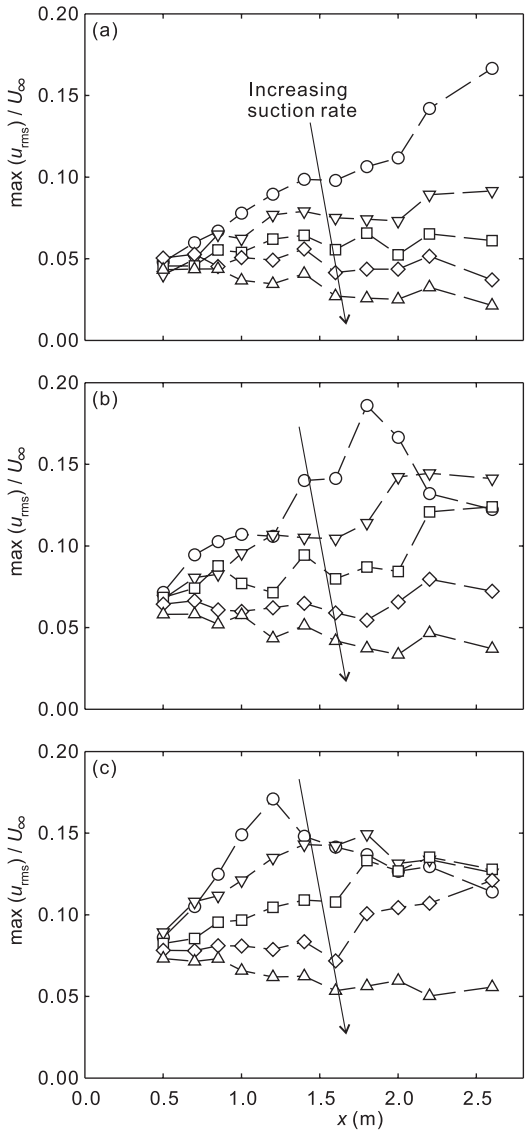

FIGURE 7. Downstream evolution of u_{rms}-maximum. (a) G0, (b) G1, (c) G2. ○, No suction; ▽, V_0/U_∞=0.1%; □, 0.2%; ♢, 0.29%; △, 0.40%. Lines are for visual aid only.

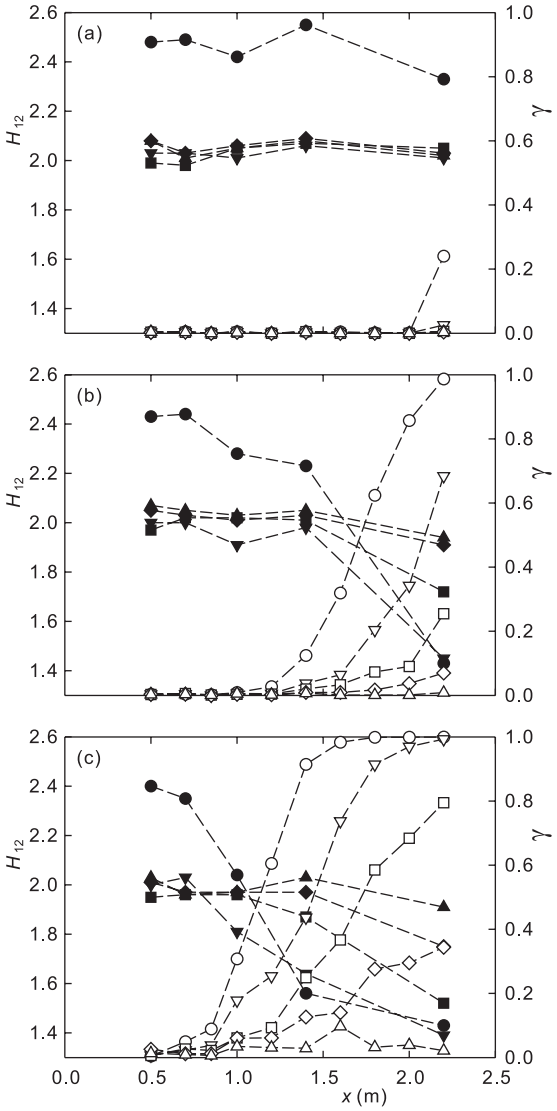

FIGURE 8. Downstream variation of the shape factor (H_{12}) and the intermittency factor (γ). (a) G0, (b) G1, (c) G2. Symbols as in figure 7. Filled symbols, H_{12}; open symbols, γ. Lines are for visual aid only.

For the highest FST level (G2) all cases except the highest suction rate become transitional in the measurement region (figures 7(c) and 8(c)). It is also clear, especially from the intermittency data, that the start of transition moves upstream as compared with the G1 case.

3.2. *Spanwise scale of streaky structures*

The spanwise scale of the streaky structures induced by FST in the Blasius boundary layer has previously been investigated by Matsubara & Alfredsson (2001). They showed that the spanwise scale (obtained both from flow visualization and two-point velocity measurements) changes in the downstream direction (it may decrease or increase depending on the grid and U_∞). They concluded, however, that the spanwise scale tended towards $3\delta_1$, which is close to the boundary layer thickness. This also means that a typical structure would have an aspect ratio close to one in the cross stream plane. So called optimal perturbation theory for spatially developing disturbances shows that the most amplified spanwise wavenumber (β) for streaky structures is β=0.775 where δ_1 is the normalizing length (see e.g. Andersson *et al.* 1999; Luchini 2000). In terms of the spanwise scale of the structures this implies a spanwise streak width of $4.1\delta_1$.

Fransson & Alfredsson (2003) also did some measurements in the asymptotic boundary layer and compared directly with the Blasius boundary layer. In that case there was no large difference between the two cases. They noted however, that the higher the FST level, the shorter the spanwise scale, coming closer to the wave length of the optimal disturbance. For the ASBL, Fransson & Corbett (2003) showed that the spanwise wavenumber (β) of the the most amplified transiently growing disturbance (the optimal disturbance in a temporal context) is β =0.53, where δ_1 is the normalizing length. This corresponds to a spanwise wavelength of $11.8\delta_1$, i.e. a streak width of $5.9\delta_1$.

In the following we will further investigate the spanwise scale of the streaks in the ASBL, by both changing the Reynolds number as well as the boundary layer thickness at a constant Re. The spanwise scale is determined from the two point correlation of the fluctuating streamwise velocity simultaneously obtained at two different spanwise positions but at the same streamwise and wall normal positions. The wall normal position was chosen as the one with highest measured rms-level and this was done through an iterative process for each measurement position. For positions where the flow is laminar this corresponds to the position for which the streaks have their maximum amplitude, however in the transitional region where turbulent spots intermittently passes, this position would move closer to the wall, since the maximum of the turbulent fluctutations is closer to the wall (cf. figure 6).

In the transitional region, the laminar periods of the fixed hot-wire were extracted and only these periods were used to determine the correlation. We

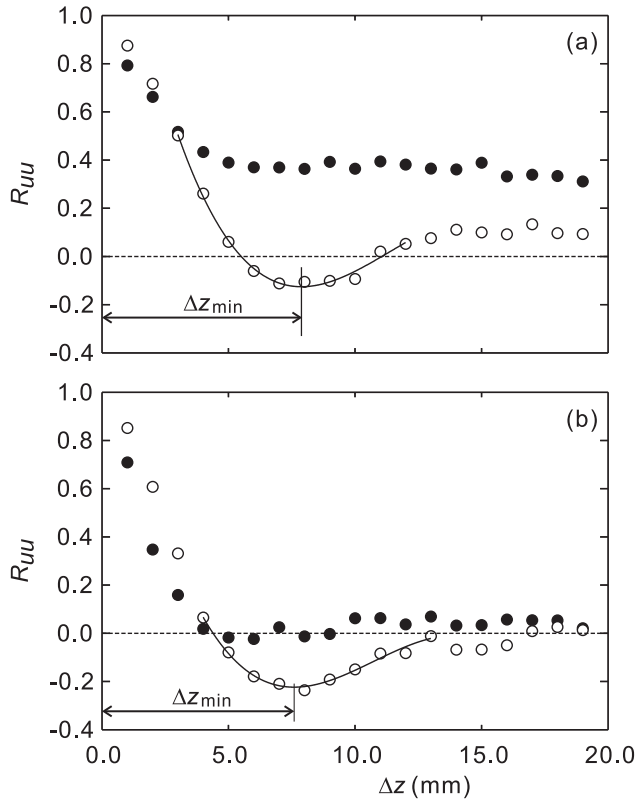

FIGURE 9. Two examples of spanwise correlation of streamwise velocity obtained for G2. ●: full signal, ○: filtered signal. The filtered correlation function is shown with a fitted third order polynomial used to determine the correlation minimum. (a): x=1.4 m, V_0/U_∞=0.10%, γ=0.44, (b): x=2.2 m, V_0/U_∞=0.29%, γ=0.34

will call this the conditional correlation. Two typical correlation functions are shown in figure 9. Both the correlation obtained from the full signal as well as the conditional correlation are shown. The full correlations show quite different behaviour in the two cases shown and the reason for this is apparent when the two hot-wire signals (separated by 8 mm) are viewed in figure 10. In the case corresponding to figure 10(a) the DC-level of the signals jumps between two levels, depending on the whether the flow is in a laminar or turbulent state. In figure 10(b) on the other hand the DC-level of the two flow regimes is the same. In the former case, even if the high frequency turbulence becomes

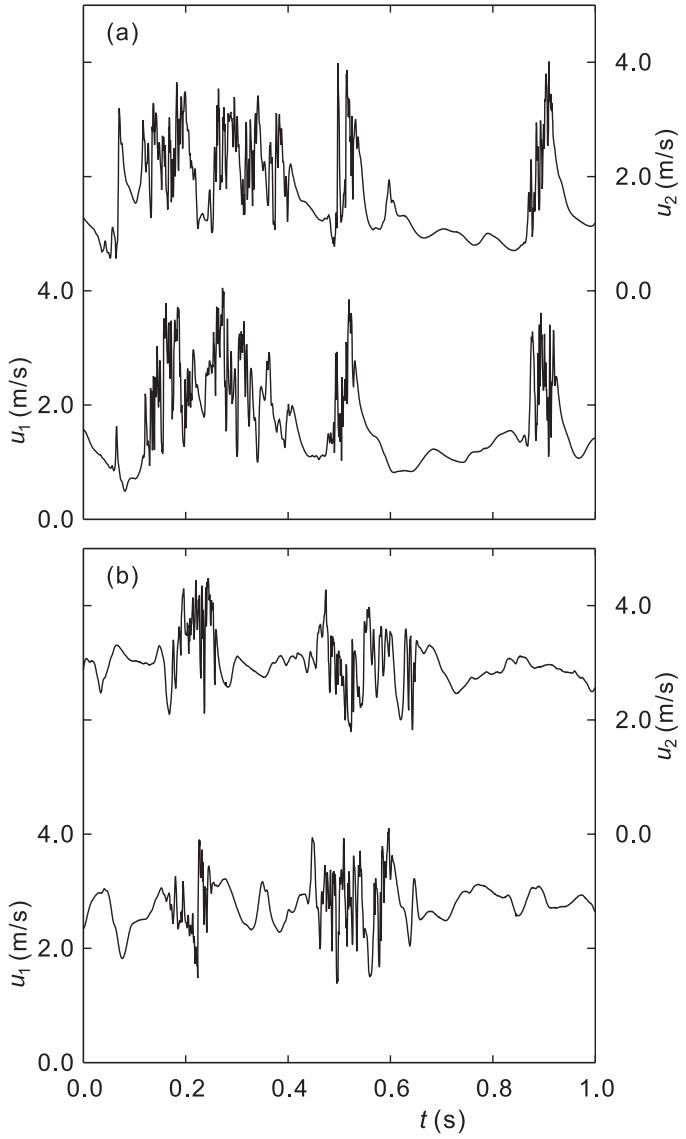

FIGURE 10. Excerpt of time signals obtained from two hot-wires separated by Δz=8 mm which were used to evaluate the correlations in figure 9. (a): x=1.4 m, (b): x=2.2 m.

uncorrelated, the signals will still show a high correlation due to the nearly simultaneous change in DC-level.

The conditional correlation has however, for both cases, a similar appearance with a clear local minimum which gives us confindence in our method. The spanwise position, Δz_{min}, of this local minimum is considered to correspond to half of the spacing of the streaky structures. In order to determine the minimum in a consistent way a third order polynomial was fitted to the ten measurement points which were closest to the minimum measured value and then the spacing was obtained from the minimum of the fitted function. This was done by an automatic process, however all correlation functions were checked by visual inspection to avoid occasional erroneous points.

In figure 11 the streamwise variation of the streak spacing Δz_{min} is shown. In the case without suction Δz_{min} increases in the downstream direction for all three FST cases (see figure 11(a)). In the cases of G1 and G2 some downstream positions are not shown because in this region transition is completed and the boundary layer is in a fully turbulent state. The data show that the streak spacing becomes wider as the boundary layer grows. In the most downstream position Δz_{min} is slightly less than the boundary layer thickness at that position. This development is in agreement with the results of Matsubara & Alfredsson (2001) and Fransson & Alfredsson (2003).

When suction is applied, see figures. 11(b)–(e), the increase of Δz_{min} is suppressed and its value stays fairly constant and falls in the range 7–10 mm in all suction cases. This suggests that for these conditions Δz_{min} is not strongly affected by the change of the boundary layer thickness due to the different rates of suction. However, the trend that higher FST gives smaller Δz_{min} is still observed for all cases.

In order to further illustrate this behaviour the data are replotted in figure 12 where instead the Δz_{min} values for each Tu-level are given in different graphs. In each subfigure the four different suction cases are shown and the data points are for five different x-positions (x=0.5, 0.7, 1.0, 1.4 and 2.2 m). First of all it can be seen that the variation for a given suction rate along the plate (i.e. at different x-positions) is quite small. It is also clear that for all four different suction cases there is no clear variation, but instead the data strongly suggest that the spanwise scale is the same (however one should also be aware of that for $Re = 1000$ the boundary layer has not reached its asymptotic state, see figure 5). A difference is however clearly seen for the different Tu-levels, the higher the Tu-level the smaller the spanwise scale. This is in accordance with similar findings by Fransson & Alfredsson (2003). A final remark is that the spanwise scale is close to the Taylor length scale of the grid.

In the above set of measurements the Reynolds number changes with the suction rate. A second set of measurements was made where the Reynolds number was kept constant by simultaneously changing the free stream velocity

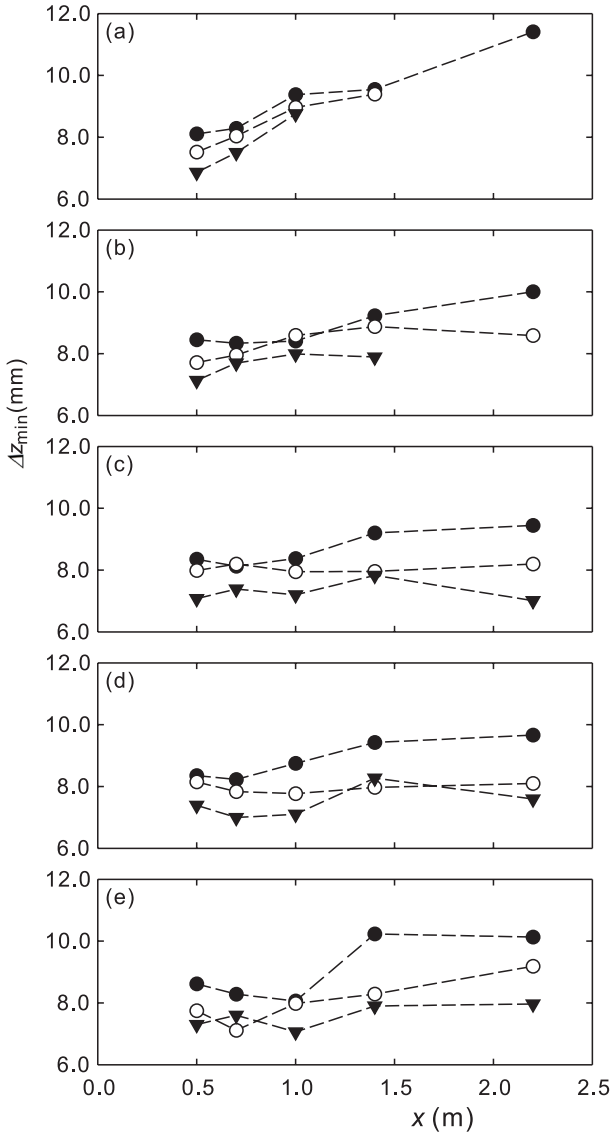

FIGURE 11. Streamwise variation of streak spacing. V_0/U_∞= (a) 0, (b) 0.10%, (c) 0.20%, (d) 0.29%, (e) 0.40%. ●: G0, ○: G1, ▼: G2. Lines are for visual aid only.

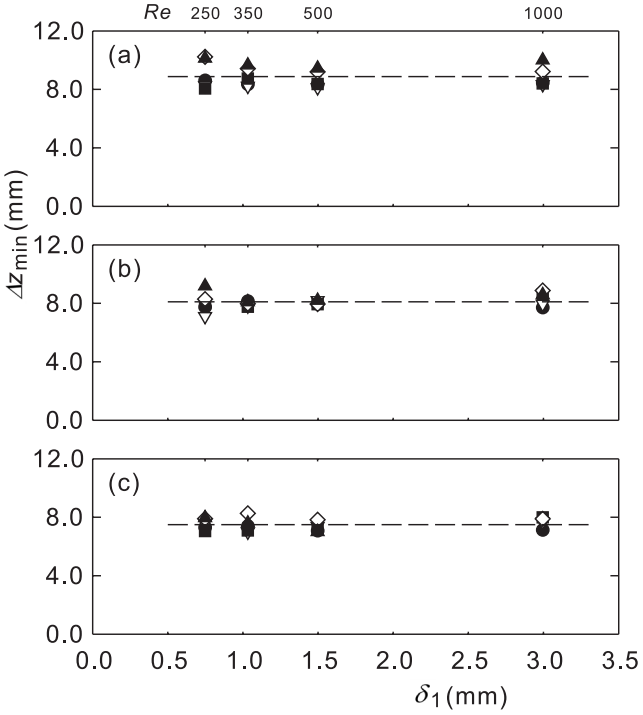

FIGURE 12. Variation of streak spacing as a function of displacement thickness (or Re). Same data as in figure 11. Lines give the average value of all measurements at each Tu. (a) G0, average value=8.9 mm, (b) G1, average value 8.1mm, (c) G2, average value 7.5 mm. Symbols mark the five different measurement positions, ●: x=0.5 m, ▽: 0.7 m, ■: 1.0 m, ◇: 1.4 m, ▲: 2.2 m.

and the suction velocity such that their ratio was constant and hence also the Reynolds number. In this way the thickness of the boundary layer changes and gives the possibility to investigate the relationship between the boundary layer thickness and the streak spacing without influence of the Reynolds number.

For the data in figure 13 U_∞ varies from 2.0 to 6.0 m/s and V_0 was adjusted to keep the Reynolds number at Re=350, see Table 1. In order to have the same turbulence level the injection rates of secondary airflow from the active turbulence grid for the G1 and G2 cases were tuned to the same Tu-levels at the leading edge to those for U_∞=5.0 m/s cases. However, since there is no tuning possibility for the G0 case only the G1 and G2 were used for this part of the study. In the figure also the curve corresponding to the spanwise width

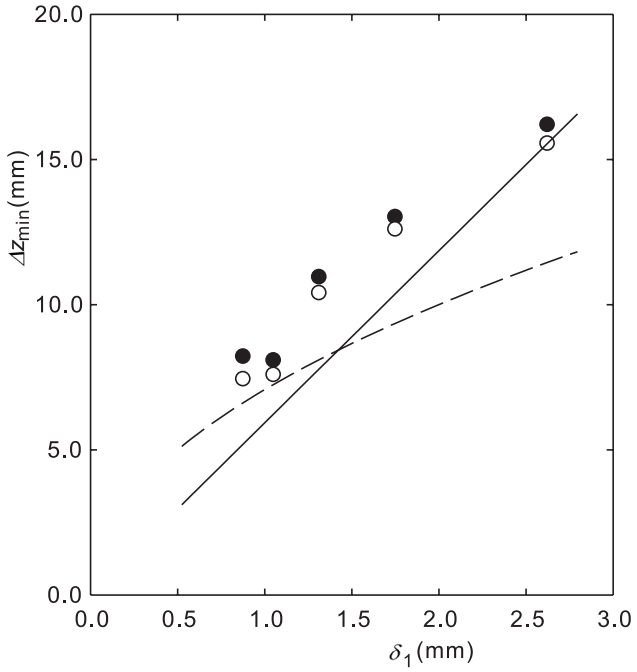

FIGURE 13. Streak spacing against displacement thickness at Re=350. ●: G1, ○: G2, — — —: optimal spacing BBL at x=0.36 m, ——: optimal spacing ASBL.

of the optimal perturbation for the ASBL has been plotted (=$5.9\delta_1$) as well as the spanwise width of the optimal perturbation for a disturbance which is assumed to develop inside a BBL up to a streamwise length corresponding to the length of the solid leading edge (=0.36 m).

For the high free stream velocities (corresponding to small δ_1 in the figure), the measured data are only slightly larger than the optimal values from the BBL, but for lower free stream velocities the difference becomes large. On the other hand the measured data comes closer to the optimal scale in the ASBL when the velocity decreases. A hypothesis explaining this behaviour is that for the high velocities the displacement thickness at the start of suction is larger than the final thickness of the ASBL and after the leading edge the velocity distribution in the near wall region of the boundary layer undergoes a strong rearrangement. This also means that the Reynolds number based on displacement thickness decreases about a factor of three. In such a situation it

seems natural that the disturbances are passively convected downstream without changing the spanwise scale as was also evident from the data in figure 12. For the U_∞=2.0 m/s case on the other hand, the displacement thickness of the BBL at the start of the suction section is approximately the same as that for the ASBL. For this case the boundary layer is already at the start of the suction section close to the final ASBL and the disturbances have the possibility to develop towards the optimal disturbance over a fairly long distance.

4. Summary and conclusions

The primary motive for the present investigation is to enhance the knowledge of the boundary layer transition scenario caused by moderate levels of free stream turbulence (FST) and to investigate how it is influenced by wall suction. The present experimental set-up is unique in the sense that it allows a change of the boundary layer thickness while keeping the Reynolds number constant. Furthermore, the active turbulence generating grid used in this work is able to maintain (roughly) the same Taylor scale while varying the intensity.

The results reported in section 3.1 show that wall suction may strongly affect and even eliminate breakdown to turbulence in a boundary layer which is affected by FST. A well known hypothesis is that in bypass transition the breakdown to turbulence is caused through a secondary instability developing on the spanwise inflectional velocity distribution formed by the streaky structures. It has also been shown that in order to obtain breakdown the streaks need to reach fairly high amplitudes. Since the growth of the streaks decreases with suction and their amplitude saturates the level where breakdown occurs may not be reached.

The experiments clearly show that with an increase of the energy at small wave numbers in the free stream there is also a decrease in the observed spanwise disturbance wave length in the boundary layer.

Two observations can be made from the measurements of the spanwise scale which can be related to recent work on optimal perturbations.

• For the case of constant U_∞=5.0 m/s the scale of the structures does not change significantly over the suction section and is for this case slightly larger than the optimal scale of BBL at the start of suction. This may be an effect of that the scales observed mainly depend on the scales which are introduced into and amplified in the boundary layer near the leading edge. Since the growth of the streaks are inhibited or even become negative in the ASBL, it may be possible that the streaks initiated at the leading edge become mainly passive disturbances which are convected by the flow.

• For a constant Re, but with varying U_∞, it seems that two competing mechanisms are at work. One is that (as above) the disturbances from the leading edge is passively convected in the downstream direction with the boundary layer. However in the case when the boundary layer displacement thickness

does not change significantly as the boundary layer reach the suction section, the streaks may develop further and their scale is observed to approach the optimal scale.

Acknowledgments

This work is supported by the Swedish Research Council (VR). SY was supported by a postdoc position financed from Carl Tryggers Stiftelse and KTH Mechanics which is greatfully acknowledged. Support was also given by the Scandinavia-Japan Sasakawa Foundation.

References

Alfredsson, P. H. & Matsubara, M. 2000 Free-stream turbulence, streaky structures and transition in boundary layer flows. *AIAA Paper* 2000-2534.

Andersson, P., Berggren, M. & Henningson, D. S. 1999 Optimal disturbances and bypass transition in boundary layers. *Phys. Fluids* **11**, 134–150.

Andersson, P., Brandt, L., Bottaro, A. & Henningson, D. S. 2001 On the breakdown of boundary layer streaks. *J. Fluid Mech.* **428**, 29–60.

Fransson, J. H. M. 2001 Investigation of the asymptotic suction boundary layer. KTH Mechanics, Licentiate thesis, TRITA-MEK 2001:11.

Fransson, J. H. M. & Alfredsson, P. H. 2003 On the disturbance growth in an asymptotic suction boundary layer. *J. Fluid Mech.* **482**, 51–90.

Fransson, J. H. M. & Corbett, P. 2003 Optimal linear growth in the asymptotic suction boundary layer. *Eur. J. Mech., B/Fluids* **22**, 259–270.

Hedley, T. B. & Keffer, J. F. 1974 Turbulent/non-turbulent decisions in an intermittent flow. *J. Fluid Mech.* **64**, 625–644.

Johansson, A. V. & Alfredsson, P. H. 1982 On the structure of turbulent channel flow. *J. Fluid Mech.* **122**, 295–314.

Kendall, J. M. 1985 Experimental study of disturbances produced in a pretransitional laminar boundary layer by weak freestream turbulence. *AIAA Paper* 85-1695.

Kendall, J. M. 1998 Experiments on boundary layer receptivity to freestream turbulence. *AIAA Paper* 98-0530.

Luchini, P. 2000 Reynolds-number-independent instability of the boundary layer over a flat surface. *J. Fluid Mech.* **404**, 289–309.

Matsubara, M. & Alfredsson, P. H. 2001 Disturbance growth in boundary layers subjected to free stream turbulence. *J. Fluid Mech.* **430**, 149–168.

Schlichting, H. 1979 *Boundary layer theory*. New York: McGraw-Hill.

Westin, K. J. A., Bakchinov, A. A., Kozlov, V. V. & Alfredsson, P. H. 1998 Experiments on localized disturbances in a flat plate boundary layer. Part 1. The receptivity and evolution of a localized free stream disturbance. *Eur. J. Mech., B/Fluids* **17**, 823–846.

Westin, K. J. A., Boiko, A. V., Klingmann, B. G. B., Kozlov, V. V. & Alfredsson, P. H. 1994 Experiments in a boundary layer subjected to free-stream turbulence. Part I. Boundary layer structure and receptivity. *J. Fluid Mech.* **281**, 193–218.

Westin, K. J. A. & Henkes, R. A. W. M. 1997 Application of turbulence models to bypass transition. *J. Fluids Eng.* **119**, 859–866.

Paper 5

5

Transition induced by free stream turbulence

By Jens H. M. Fransson Masaharu Matsubara[1] and P. Henrik Alfredsson

KTH Mechanics, SE-100 44 Stockholm, Sweden

Free stream turbulence is maybe the most important source to force by-pass transition in boundary layer flows. The present study aims at describing the initial energy growth of streamwise oriented disturbances in the boundary layer originating from the presence of turbulence intensities between 1.4% and 6.7%, but also to lay the ground for a prediction model for free stream turbulence induced transition. For this study three passive and one active turbulence generating grids were used. The active grid was built in order to vary the turbulence intensity (Tu) with only a small change of the characteristic turbulence scales. It is shown that the initial energy growth in the boundary layer is linear in the downstream distance and proportional to Tu^2, whereas the transitional Reynolds number is shown to be inversely proportional to Tu^2. The intermittency in the transitional zone was determined and it was shown that by scaling the intermittency function with the length of the transition zone a universal function could be obtained. The length of the transition zone was found to increase linearly with the transition Reynolds number, however it was also noted that the length has a minimum value. With these results we were able to formulate an expression for the spot production rate which has a better physical base than previous models.

1. Introduction

It is known from both flow visualization and hot-wire measurements that a boundary layer subjected to free stream turbulence (FST) develops unsteady streaky structures with high and low streamwise velocity (for reviews see Kendall 1998; Westin 1997). This leads to large amplitude, low frequency fluctuations inside the boundary layer although the mean flow is still close to the laminar profile. Several flow visualization photos have been published showing the presence of streaky structures in boundary layer transition induced by free stream turbulence (see e.g. Matsubara & Alfredsson 2001), and it is apparent that the free stream turbulence gives rise to longitudinal structures in the flow

[1]Permanent address: Department of Mechanical Systems Engineering, Faculty of Engineering, Shinshu University, Nagano, Japan.

with a relatively well defined spanwise scale. The streaks are subsequently seen to develop a streamwise waviness, which develops into turbulent spots. This sinuous-type of secondary instability can only take place for sufficiently high amplitudes of the streaks (experimentally when the streamwise rms-value reaches about 10% of the free stream velocity). Quantitative measurements of this scenario, especially growth rate and scales of the longitudinal streaks, are important to obtain accurate physical modeling of these processes and they are also needed for development of a reliable prediction method.

Today it is known that there exist several routes of transition to turbulence. FST induced transition is only one scenario which by-passes the classical Tollmien-Schlichting scenario. Over the past two decades several experimental studies have investigated transition under the influence of FST. Kendall (1985) observed low-frequency fluctuations in the boundary layer that grows in linear proportion to $x^{1/2}$ (i.e. proportional to the laminar boundary layer thickness, δ). He also observed the occurrence of elongated streamwise structures with narrow spanwise scales. Also Westin *et al.* (1994) made detailed measurements of a laminar boundary layer disturbed by free stream turbulence and showed among other things that the Blasius profile was only slightly modified, despite u_{rms} levels of about 10 % inside the boundary layer before breakdown. They also confirmed that the growth of u_{rms} was proportional to $x^{1/2}$. The spanwise scale of the streaks decreases with increasing turbulence intensity (Tu) and this scale seems to adopt to the boundary layer thickness after an initial mismatch (see Matsubara & Alfredsson 2001). Fransson & Alfredsson (2003) carried out FST experiments in an asymptotic suction boundary layer and could show that with a reduction of the boundary layer thickness by a factor of two the spanwise scale of the streaks was maintained, giving rise to a spanwise widening of the streaky structure relative to the boundary layer thickness. This result excludes the possibility of the boundary layer thickness itself to be an upper limit of the spanwise scale, and puts the FST scales in focus for the determination of the streak spacing.

A correct modeling of the receptivity process is important if theoretical results are to be compared with experimental ones. The natural transition scenario is complex and there is a limitation by means of measurement techniques to measure initial disturbances (they are simply too small). In case of FST induced transition experiments, the best one can do (at the present time) is to make sure that the characteristc scales generated by the turbulence generating grid are well documented. In flat plate wind tunnel experiments there are two essential factors that determines the receptivity process. Firstly, the geometry of the leading edge plays a major role (cf. e.g. Klingmann *et al.* 1993). A symmetric leading edge gives rise to a pressure suction peak, which results in a local negative pressure gradient followed by a positive one. This is the reason for several asymmetric leading edge designs (see e.g. Klingmann *et al.* 1993; Fransson 2001). Secondly, the nature of the disturbances that effects

the boundary layer is important. In case of FST disturbances these are described by the characteristic scales of the turbulence and the energy-frequency spectrum.

For reasons mentioned above, experimental results may differ, since there are many external and experimental conditions that may vary from facility to facility. To overcome the difficulties in analysing experimental data and to find clear trends there is a need of experiments with small variations of the FST scales, this in order to reduce the scale dependence. With an active grid the scales can be kept almost constant within a fairly large range of FST levels. The major part of the results in this paper is from such a grid. The present paper starts with a brief introduction of the experimental setup followed by a thorough description of the turbulence generating grid. Thereafter, a standard intermittency estimation technique with an improvement on the threshold determination is described. Finally the results are shown and discussed in terms of modelling and prediction of transition.

2. Experimental setup

The experiments were performed in the MTL wind-tunnel at KTH where a 4.2 m long test plate was mounted horizontally in the test section. Over the past decade several studies on FST induced by-pass transition have been reported from the KTH Mechanics group with roughly the same experimental setup (we refer to Matsubara & Alfredsson 2001, concerning details of the experimental setup). Briefly speaking, the test section is 7 m long with a cross sectional area of 1.2×0.8 m^2, and is equipped with a five degree traversing mechanism (see figure 1 for a schematic view of the flat plate setup). The maximum speed is around 70 m/s and the contraction ratio is 9. Recently, the flow quality of the MTL wind tunnel was re-confirmed after 10 years in operation. At 25 m/s the streamwise turbulence intensity is less than 0.025% and both the cross flow turbulence intensities are less than 0.035%. Furthermore, the total pressure and temperature variation is less than $\pm 0.06\%$ and $\pm 0.05°$, respectively. For full details of the tunnel the interested reader is refered to Lindgren & Johansson (2002).

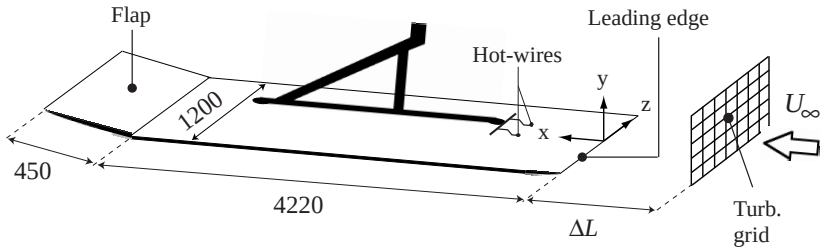

FIGURE 1. Schematic view of the experimental setup.

Grid	$\text{Bar}_{\text{geom.}}$	M (mm)	d_p (mm)	S_g	τ (mm)	Λ (mm)
A	round	36	6	...	7±1	...
B	round	23	3.5	0.28	7±1	...
E	square	50	10	0.36	7±1	...
G	round	50	5	0.19	9±1	20–50

TABLE 1. Passive (A, B, and E) and active (G) grid characteristics. See text for definitions.

The FST was generated by four different grids (three passive, grids (A, B, E), and one active grid G) mounted at different positions (ΔL=1000–1600 mm) upstream the leading edge. The free stream velocity (U_∞) was varied in the range 2–14 m/s and a variation of ΔL provided turbulence levels ($Tu = u_{rms}/U_\infty$) in the range 1.4% to 6.7% at the leading edge of the plate. In section 3 the active turbulence generating grid is described thoroughly and in Table 1 the characteristics of all four grids are summarized.

The data were collected with hot-wire anemometry of both single- and X-probe type. The single probe was calibrated in the wind tunnel against a Prandtl tube and then a modified King's law (cf. Johansson & Alfredsson 1982), taking into account the natural convection, was used for curve fitting. For the X-probe an angle calibration was carried out and a 2D fifth-order polynomial were fitted to the calibration data, giving U and V as functions of the obtained voltage pair.

3. Active turbulence generating grid

Free stream turbulence is usually generated with the use of grids, consisting of circular or square bars. The scale and intensity of the FST is related to the geometry of the grid, as for instance the mesh width (M) and the solidity, where a higher solidity gives a higher turbulence level. In order to generate different FST intensities without changing the set-up in the test section an active grid was developed. The grid is active in the sense that it ejects secondary fluid jets into the fluid upstream, i.e. counterflow injection. A study on such an active grid was carried out by Gad-El-Hak & Corrsin (1974) where both coflow and counterflow injection was compared with the zero injection case. They showed through a simple analysis that in the zero injection case the FST intensity is proportional to the square root of the coefficient of static pressure drop over the grid. Even though an expression of this coefficient may be derived for the injection case the relation to the FST intensity could not be derived. Gad-El-Hak & Corrsin (1974) concluded that the effects of injection are simply too many and complicated. One would have to consider for instance the effects on the boundary layers around the grid elements, the turbulence levels near the jet exits, and the stability of the system of jets.

Their experimental investigation revealed that coflow injection reduces the static pressure drop across the grid, hence decreases the effective solidity as well as the rod wake width. This in turn leads to a smaller turbulence level at a prescribed distance downstream. In contrast, the counterflow injection produces a larger pressure drop across the grid with increasing jet strength which increases the effective solidity and gives larger FST levels. The effective solidity was visualized by means of hydrogen bubble flow technique. The authors claim that the counterflow injection generates higher turbulence energy as well as larger scales, both events being associated with the instability of the jet system. This result is verified with the present active grid.

3.1. *Design*

The active grid was built to be placed in the test-section of the MTL wind tunnel at KTH. The grid consists of a rectangular frame with dimension 1.2×0.8 (width×height, identical with the test-section dimensions). Each side of this frame is separated from the others and consists of a brass pipe with an outer diameter of 15 mm (wall thickness = 1 mm) and has two inlets for secondary air in order to reduce the pressure drop inside the grid. A total amount of 33 brass pipes, 20 vertically and 13 horizontally, were then soldered to the frame. These pipes has a diameter (d_p) of 5 mm (wall thickness 0.9 mm) and are located to give a mesh width M=50 mm (square) which corresponds to a geometrical solidity (S_g) of 0.19. The jet orifices have a diameter of 1.5 mm and are in the present setup directed upstream. The orifices are concentrated to the middle section of the grid with a total amount of 254 (12 horizontally × 12 and 11 vertically × 10, cf. figure 2 for an illustration of the grid geometry). The secondary air is supplied to the grid through flexible rubber tubing connected to the inlets at the frame. The air is driven by a modified vacuum cleaner (1 kW) and the jet strength was regulated by a transformer. In the result part of the present study the injection rate was varied, but in this section three different rates (none, moderate and high) will be shown. These are denoted

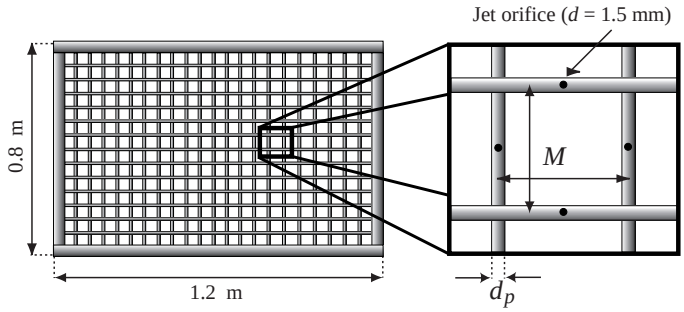

FIGURE 2. Active grid (G) with main measures.

as G0, G1 and G2, which corresponds to an upstream injection of (0, 5, 10) litre/sec or an individual jet velocity of (0, 11, 21) m/s, respectively. A fine-meshed screen (mosquito type) was positioned on the downstream side of the frame in order to improve the homogeneity of the flow.

3.2. *Characteristic data of the active grid*

3.2a. *Turbulence decay.* Downstream of the grid the turbulence decays and the typical power-law decay can be described according to

$$Tu = \frac{u_{rms}}{U_\infty} = C(x - x_0)^b, \tag{1}$$

where x_0 is a virtual origo, the constant C and exponent b are parameters to be determined through curve fit to experimental data.

In figure 3 the downstream development of Tu, of the active grid, is shown. The two different injection rates are plotted together with the zero injection case for comparison. The grid distance upstream the leading edge was in this section fixed at $x = -1400$ mm corresponding to $28M$ from the leading edge of the plate. The curve fits are done for Tu with Eq. (1) with $b = -0.5$, which can be shown to be the value for fully isotropic turbulence decay. The virtual origin has been determined consistently by taking the intersection point with

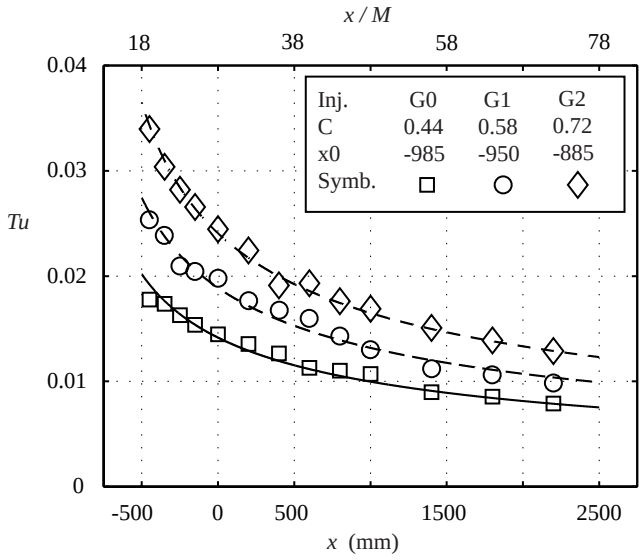

FIGURE 3. Turbulence decay for different injection rates. The curves are fitted to experimental data according to Eq. (1) for a given $b = -0.50$.

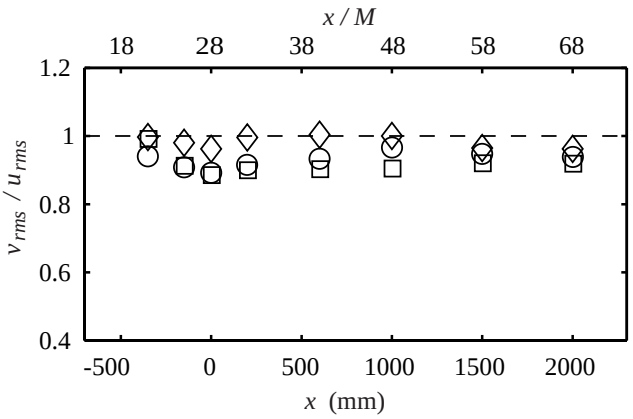

FIGURE 4. The isotropy measure v_{rms}/u_{rms} as a function of the downstream distance. (□) G0, (◯) G1, and (♢) G2.

the x/M-axis when $1/Tu^2$ is plotted versus x/M. A new virtual origin was determined for all three cases and are given in figure 3 together with the value of the constant C. This figure clearly shows the increase of Tu with increasing injection rate for all downstream positions from the grid position.

In figure 4 the isotropy measure v_{rms}/u_{rms} is plotted as a function of the downstream distance. The figure shows a nearly isotropic turbulence for all three cases at $x = -400$ mm downstream the active grid, which is in agreement

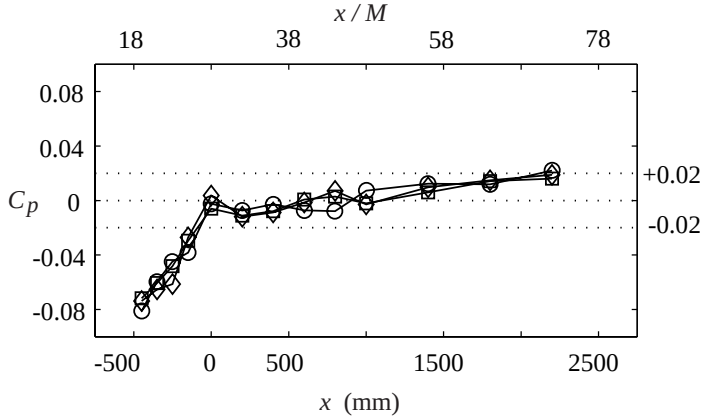

FIGURE 5. Pressure distribution vs the downstream distance for different injection rates (cf. figure 4 for symbols).

with the rule of thumb that $20M$ is needed to establish a nearly isotropic turbulence behind a grid. All three cases have an isotropy measure above 0.9 and the highest Tu seems to achieve the highest degree of isotropy. According to Groth & Johansson (1988) several investigations have reported that the turbulence behind a grid retains a small degree of anisotropy over a very large downstream distance (up to $400M$). They report fast return to a nearly isotropic state and explains that the main source for a persisting anisotropy may be large-scale anisotropic turbulence on the upstream side of the grid and that the return to isotropy depends on the macroscale (i.e. integral scale) Reynolds number.

The measurements on the active grid were carried out in connection with a flat plate boundary layer experiment and a large effort was taken to get a zero pressure gradient on the plate (starting at $x = 0$ mm). This gives rise to a small acceleration in front of the plate. However as can be seen from the pressure coefficient (C_p) plotted versus the downstream distance in figure 5 the mean flow condition stays the same despite the injection from the grid. Since the injection gives rise to a larger blockage the rotational speed of the wind-tunnel fan is increased to compensate for this such that the same velocity, measured with a Prandtl tube at a reference position, is obtained.

3.2b. *Turbulence scales.* In addition to the turbulence intensities generated by the grid, the FST scales are of interest. In a turbulent flow the scales ranges from the smallest Kolmogorov scale (which can be determined from the turbulence decay) to the largest allowed by the geometry.

The smallest energetic timescale is called the Taylor microscale (τ_t) and this scale can be estimated directly from the autocorrelation function. Also the integral (macro) timescale (Λ) can be obtained from the autocorrelation and is defined as

$$\Lambda = \int_0^\infty R_{uu}(t^*)dt^*, \tag{2}$$

where $R(t^*)$ is the autocorrelation function defined as

$$R_{ij}(t^*) \equiv \frac{\overline{u_i(t)u_j(t')}}{\overline{u_i(t)u_j(t)}},$$

with $t^* = t' - t$. Through Taylor's hypothesis (frozen turbulence approximation) the length scales can then be determined and should agree with scales determined from two point spatial correlation functions. This hypothesis holds for $u/U_\infty \ll 1$ and states that $u(t) \approx u(x/U)$. It is hard to estimate the Taylor lengthscale from spatial correlation measurements since this needs a well resolved correlation coefficient curve for small separations. Therefore the

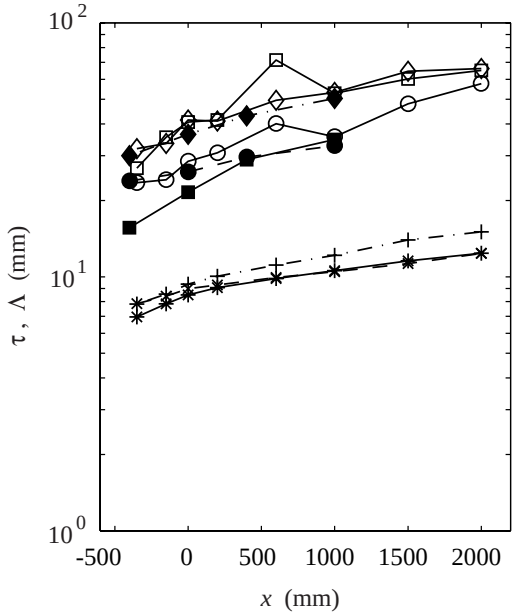

FIGURE 6. The Taylor (τ) and the Integral (Λ) lengthscale evolution. ($\Box$,$*$) G0, ($\bigcirc$,$\times$) G1, and ($\Diamond$,$+$) G2. ($*$,$\times$,$+$) denotes τ and filled markers of Λ are from spatial correlation measurements and unfilled from the autocorrelation.

timescale is usually determined and the use of Taylor's hypothesis is used to convert to a length scale.

The Taylor microscale can be defined as

$$\tau_t^2 \equiv 2\frac{\overline{u^2}}{\overline{(\partial u/\partial t)^2}}.$$

This expression is derived through Taylor series expansion of the correlation coefficient function (see e.g. Tennekes & Lumley 1997) and was used here to determine the Taylor length scale. The same procedure as Hallbäck *et al.* (1989) was used with the exception of approximating the time derivative of the signal with $\Delta u/\Delta t$. First the measured (denoted by subscript m) time scale is computed according to

$$\tau_{tm}^2 = 2\frac{\overline{u^2}}{\overline{(\Delta u/\Delta t)^2}} \tag{3}$$

for decreasing Δt (i.e. increasing sampling frequency) and then the expression

$$\left(\frac{\tau_{tm}}{\tau_t}\right)^2 = 1 + \beta\frac{\Delta t}{\tau_t} \tag{4}$$

is fitted to data in the region $0.1 < \Delta t/\tau_t < 0.35$, which was suggested in Hallbäck *et al.* (1989) (for increasing downstream distance the lower limit is though shifted towards higher values). τ_t is then accurately obtained. Hallbäck *et al.* reported that for very small Δt the effect of electrical noise and insufficient resolution in the AD-converter gives a too low value of the microscale which could be observed in the present case as well.

The autocorrelation was calculated from a 60 sec long time signal sampled at a frequency of 25 kHz. There is a relatively small difference between the three cases, although a tendency for the highest injection rate to be correlated over the longest times. It is however clear that a typical correlation time increases with downstream distance for all three cases. Similar results are obtained from spatial (in the spanwise direction) correlation measurements using two hot-wires. At $x = 40M$ the correlation functions clearly show that the scales increase with increasing injection, whereas further downstream the differences between the three cases decrease. It is also seen that the correlation extends over larger distances when x increases which is in accordance with the results obtained from the autocorrelation function.

In figure 6 the downstream evolution of τ and $\Lambda_{t,z}$, respectively, are plotted. For the calculation of Λ through expression 2 the above integration limit was truncated at $\tau_t = 0.1$ sec for the autocorrelation and $\Delta z = 70$ mm for the spatial correlation. The timescale is transformed to the length scale through Taylor's hypothesis. The integral length scales obtained from the spatial correlation is slightly smaller than the one obtained from the autocorrelation, which is in agreement with theoretical results for isotropic turbulence. The lengthscales are seen to grow in the downstream direction and the Taylor lengthscale seem to increase slightly with increasing injection which is in concordance with the results in Gad-El-Hak & Corrsin (1974).

3.2c. *Energy spectra.* The energy spectra gives a good overview of the turbulent scales for the different injection rates. If the energy distribution over the frequencies are the same it is most likely that they also share the same energetic scales, i.e. turbulent lengthscales. When plotting the energy as $f \cdot E$ versus the frequency ($\log f$) for the no-injection case it clearly shows that the main energy content moves towards lower frequencies with the downstream distance, indicating an increase (in size) of the integral lengthscale (most energetic scale).

The energy spectra (normalized to make the total kinetic energy equal to unity) for all three injection rates are compared in figure 7 at different downstream positions. This figure shows that the variation of the energy distribution

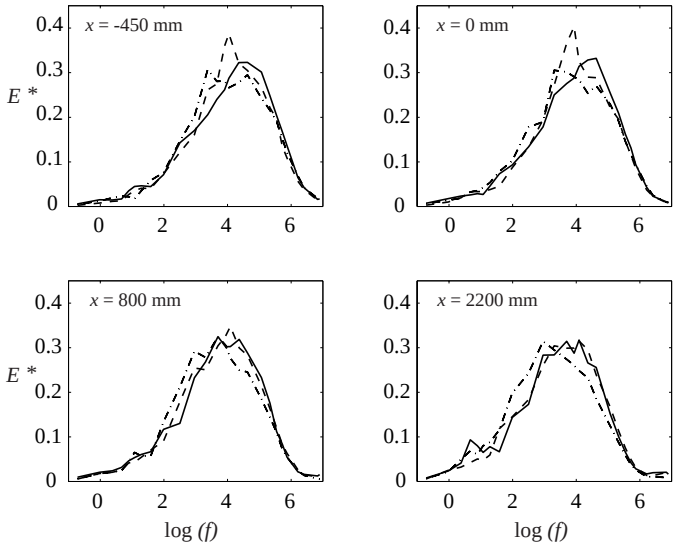

FIGURE 7. Energy spectras at different downstream positions for all three injection rates. (solid) G0, (dashed) G1, and (dash-dotted) G2. $E^* = f \cdot E / \int_0^\infty f \cdot E \ \mathrm{d}(\log f)$.

is small for the different injection rates, although a slight shift towards lower frequencies can be seen for increasing injection. It is also clearly seen that the maxima in the distributions move towards lower frequencies with downstream distance. A similar increase in the turbulence scales was observed in figure 6.

4. Intermittency estimation procedure

In analysis of transitional flows, discrimination between turbulent and laminar flow is valuable not only to estimate the intermittency (γ) function but also to obtain separated statistics of the measured data into laminar and turbulent cases, i.e. conditional sampling. In order to do this there are two essential decisions that has to be made by the evaluator, i.e. choice of detector ($\mathcal{D}$)/criterion ($\mathcal{C}$) function, and the determination of threshold value. So far there is no universal procedure accepted for these two decisions. One difficulty is that the intermittency estimate is very sensitive to the threshold value, which makes the choice of method essential and more or less suitable for a given flow.

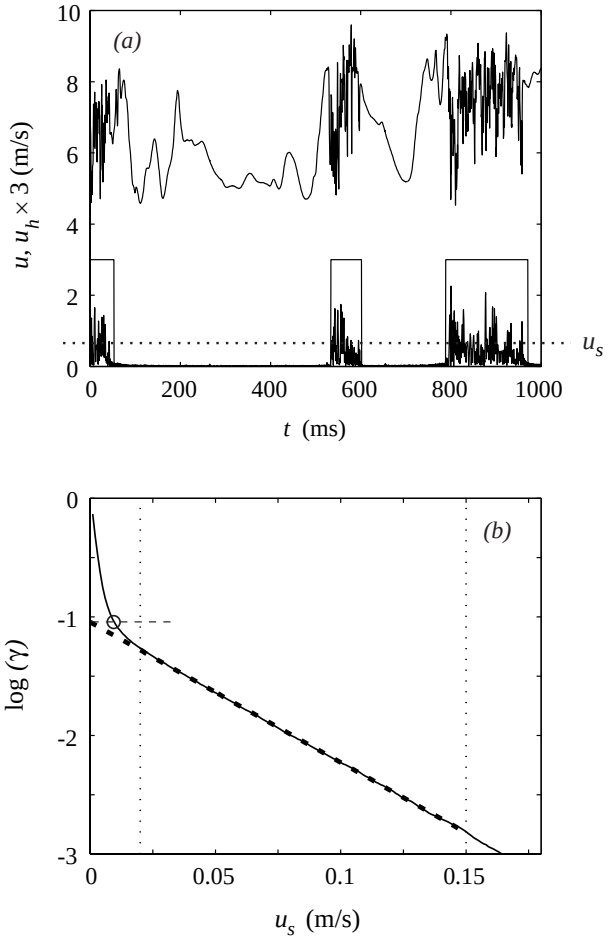

FIGURE 8. (a) Top velocity trace is the original signal (u) and the bottom is the corresponding high-pass filtered signal (u_h) (magnified by a factor of 3) with the intermittent regions marked with squares (i.e. the $\mathcal{I}_{u_s^*}$-function). u_s is a threshold value. (b) Full line corresponds to the calcualted intermittency of u_h by changing u_s, whereas the dashed line is the fitted line to obtain the intermittency at the intercept with the abscissa. The circle determines the value of u_s^*.

Hedley & Keffer (1974) stressed the difficulties in intermittency estimation and summarized many of the different $\mathcal{D}$-functions which had been used by different researchers. From this paper Kuan & Wang (1990) developed a

general method to determine the threshold, the so called "dual-slope method". In this method the second derivative of the velocity signal was adopted as the $\mathcal{D}$-function. The cumulative intermittency distribution as function of the threshold value appeared to consist of two straight lines of different slopes when plotted in a semilogarithmic diagram. The intersection of these lines was then chosen to give the threshold value.

However, with the data presented in this paper the change of slope was not always that clear, making it difficult to determine the threshold in an insensitive manner. In our case the original idea in Hedley & Keffer (1974) to use the region of maximum curvature as threshold value would have been more appropriate. However, the intermittency estimation of the data in the present paper is based on standard high-pass filtered velocity signal as $\mathcal{D}$-function and the threshold value is chosen in a fairly insensitive way. In figure 8 an example case of the intermittency estimation is illustrated. Figure 8(a) shows a velocity signal (u) with the absolute value of the corresponding high-pass filtered signal (u_h). A systematically chosen cut-off frequency (f_{cut}) for the filtering was used in order to develop an automatic γ-calculator, namely; $f_{cut} = U_\infty/(5 \cdot \delta_{99})$, where δ_{99} is the Blasius based boundary layer thickness. This expression of f_{cut}, which turned out to create a nice detector function, was selected through visual inspection of many different signals and is naturally based on the convective velocity ($\propto U_\infty$) and the streamwise scale ($\propto \delta_{99}$) of the streaky structures (cf. Matsubara & Alfredsson 2001). The $\mathcal{C}$-function is created by short-time averaging of the $\mathcal{D}$-function, this in order to get rid of the appearing zeros in the turbulent regions. Next thing is to determine the threshold value (u_s^*) that will discriminate the true turbulence from the noise and give an accurate value of the finally calculated γ. This is done by varying the level of u_s in figure 8(a) on the $\mathcal{C}$-function, producing an indicator ($\mathcal{I}$) function according to:

$$\mathcal{I}^j(t_i) = \begin{cases} 1 & \text{when} \quad \mathcal{C}(t_i) \geq u_s^j \\ 0 & \text{when} \quad \mathcal{C}(t_i) < u_s^j \end{cases}$$

here $i = 1 : n$; and $j = 1 : m$, where n and m are the number of discrete points of the signal and the amount of threshold values, respectively. From the $\mathcal{I}$-function, γ is calculated as function of u_s which is plotted in figure 8(b) as a solid line. The dashed line corresponds to

$$\gamma(u_s) = c \cdot \exp(\alpha u_s),$$

which is fitted to the calculated values between the dotted vertical lines. The intercept with the abscissa is used as the "true" value of γ. The corresponding threshold value (u_s^*) giving the same γ is marked in the figure by a circle.

5. Results

The presentation of the experimental results are divided into three sections where the first part deals with the streamwise disturbance energy growth. The streamwise disturbance level is shown to grow linearly with x and the influence of the level of Tu is discussed. The second part deals with quantitive results from the transition zone, obtained from intermittency measurements. The correlation between a transitional Reynolds number, based on the downstream distance from the leading edge, and the FST level is shown to agree according to a "recent" theory by Andersson *et al.* (1999). Finally the present intermittency data are compared with two previously published models of the transition zone (Narasimha 1957; Johnson & Fashifar 1994). The universal intermittency functions according to the above mentioned models are tested and parameters are proposed based on the present data. A new expression with a sound physical basis, based on the present measurements, for the spot production rate is also proposed.

5.1. *Disturbance energy growth*

In figure 9(a) the streamwise disturbance energy ($E = u_{rms}^2/U_\infty^2$), measured at y/δ^*=1.4 ($\delta^* = 1.72\sqrt{x\nu/U_\infty}$ is the theoretical laminar displacement thickness of the Blasius boundary layer), is plotted as function of the Reynolds number (defined as $Re_x = xU_\infty/\nu$ throughout this paper). A typical curve shows an initial, nearly linear, growth after which the disturbance energy reaches a maximum and then asymptotes to a constant level around $E = 0.007$. By inspection it is found that the maximum is closely related to the point of γ=0.5, i.e. at this point the flow alternatively consists of laminar portions and turbulent spots. The higher the Tu the smaller the Re_x for which the maximum occurs, i.e. transition occurs for smaller Re_x. Another apparent feature of figure 9(a) is that the amplitude of the maximum increases with increasing Tu, or equivalenly the maximum decreases the higher the associated Re_x. There may be several reasons for the variation of the maximum value with Re_x, such as changes in the mean velocity between the laminar and turbulent parts of the signal or changes in turbulence intensity with Re_x due to change of the measurement position with respect to the wall in terms of viscous lengths for the turbulent part of the signals. Another possibilty is simply that transition occurs at lower streak amplitudes for higher Re. However in order to get a full understanding of this behaviour further experiments and analysis have to be made.

In figure 9(b) the measured points are plotted where the x-axis has been scaled with the interpolated Re_x-value for which E=0.01 or equivalently $u_{rms} = 0.1U_\infty$. As expected all points fall nicely onto one curve, however the most interesting feature is that a line fitted through the points will cross the abscissa at some positive value of Re_x. This indicates that there is an initial region at the

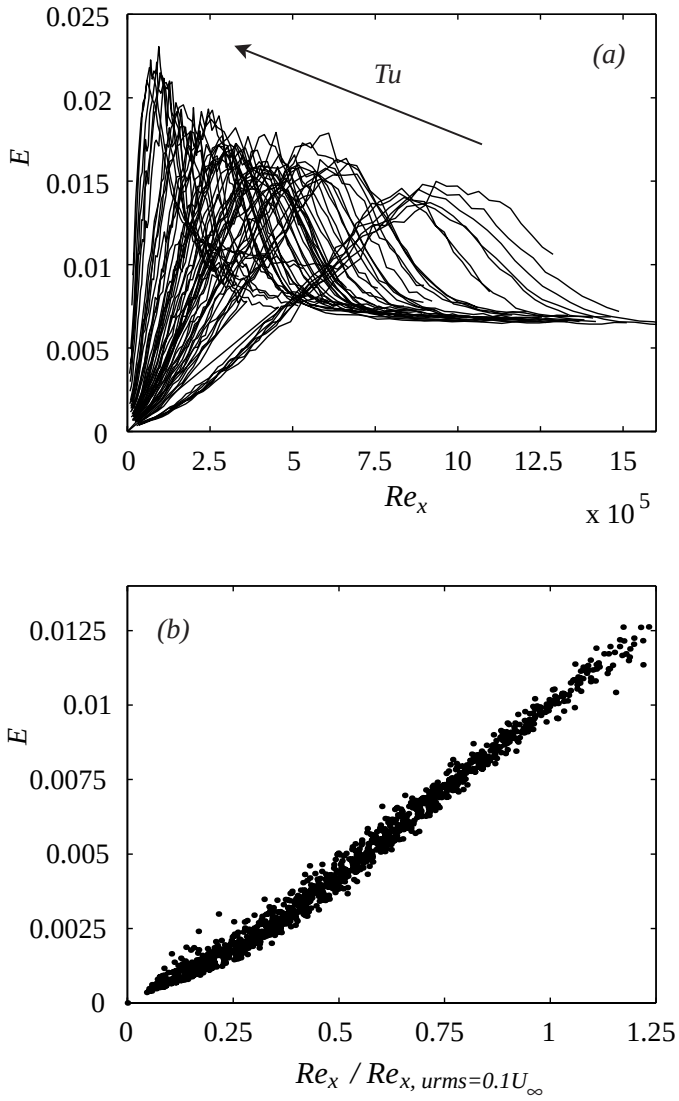

FIGURE 9. (a) Streamwise turbulent energy ($E = u_{rms}^2/U_\infty^2$) as function of Re_x for various free stream turbulence levels. Measurements are made at y/δ^*=1.4. (b) Measured points in (a) where horizontal axis is scaled with the position where u_{rms}=0.1U_∞ (i.e. E=0.01).

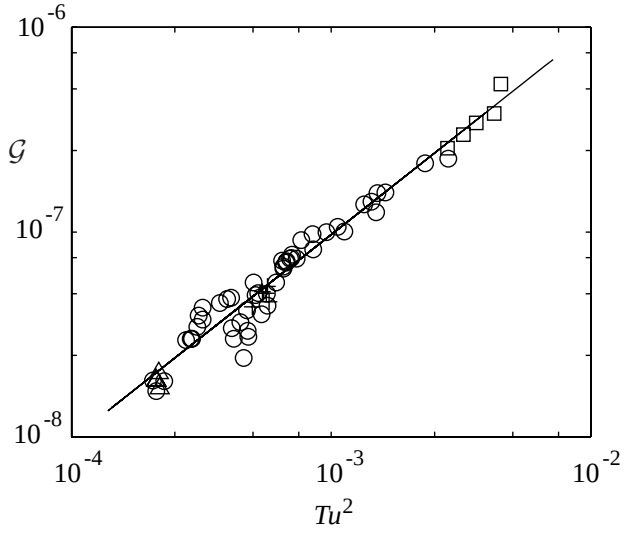

FIGURE 10. Slope of the linear growth in figure 9(a) versus Tu^2. The different symbols ($\triangle$, $+$, $\bigcirc$, $\square$) correspond to the different turbulence generating grids (B, A, G, E), respectively.

leading edge where the disturbances grow slower than further downstream. One possibility is that this is due to the receptivity process which needs a certain distance before it is completed and the disturbances have adjusted themselves to the boundary layer.

Figure 10 shows a measure of the disturbance growth ($\mathcal{G} = \mathrm{d}E/\mathrm{d}Re_x$), i.e. the slope of the linear region of a typical curve in figure 9(a). The slope is calculated by fitting a straight line in the interval of E between 0.0025 and 0.0125. Here, the lower limit is due to the above mentioned receptivity region where the disturbance evolution has another slope, and the upper energy limit is where the intermittency starts to increase from zero (for E <0.0125 γ is always less than 0.1) and deviation from the linear growth expected. It can be seen that this quantity ($\mathcal{G}$) is proportional to Tu^2. This result strongly indicates that there is a linear response between the level of FST (forcing) and the disturbance amplitude (response) in the boundary layer.

5.2. *The transition zone*

In order to investigate the transition zone further the intermittency function for the different levels of Tu were determined according to the procedure described in section IV. It is not obvious how to chose the best y-position to evaluate the intermittency. The following results were obtained by evaluating the intermittency at a position in the boundary layer where y/δ^*=1.4. However as was

shown in Matsubara *et al.* (1998) the intermittency is fairly constant up to at least y/δ^*=2.

Figure 11(a) shows the intermittency curves for seven different intensities of the FST (namely, Tu=[1.4 2.2 3.3 3.9 5.3 5.7 6.7]%). They are shown as function of $Re_x/Re_{x,\gamma=0.5}$, i.e. they will all cross the point [1,0.5] in the plot. The figure shows that the relative length of the transition region increases with increasing turbulence level. Figure 11(b) on the other hand, shows that all the intermittency curves of the grid G cases that satisfy $Tu \leq 2.6\%$ collapse on a universal function.

The intermittency functions can now be used to estimate the transition Reynolds number Re_{tr}, which we define to be the Reynolds number for which γ=0.5. Figure 12 shows the transitional Reynolds number as function of Tu for all four grids. In both figures the line corresponding to

$$Re_{x,\gamma=0.5} = C \cdot Tu^{-2}. \tag{5}$$

is also shown, which gives a good representation of the data. This is in line with the suggestion by Andersson *et al.* (1999) who proposed that for FST induced transition the breakdown to turbulence occurs when the streaky disturbances in the boundary layer reach a certain (high) amplitude. They also assumed that the input energy is proportional to the free-stream turbulence energy and that the streaky structures grow in amplitude with the optimal rate. These assumptions lead to that $Re_{x,tr}$ becomes proportional to Tu^{-2}. In that paper this idea was substantiated by comparisons with experimental data by Matsubara, Yang and Voke, and Roach and Brierley (for detailed references see Andersson *et al.* 1999). The present data give $C = 196$, which can be compared with $C = 144$ suggested in Andersson *et al.* (1999). The latter was however, based on only six experimental data points.

The length of the transition zone is also an important variable for modelling as well as basic understanding of the transition process. In our experiments this length can be estimated from the intermittency function and we chose the values of γ=0.1 and 0.9 to define the position where transition starts and ends, respectively. In the same way we define the middle of the transition zone as the position where γ=0.5. In figure 13(a) the transition length is made non-dimensional in terms of a Reynolds number ($\Delta Re_{tr} = Re_{x,\gamma=0.9} - Re_{x,\gamma=0.1}$) and plotted as function of the Reynolds number of the middle of the transition zone ($Re_{x,\gamma=0.5}$). If we now estimate that the x-position where γ=0.5 is the average value of those positions where γ=0.1 and 0.9, we can introduce a shaded area in figure 13(a) which denotes non-admissible values of the transition length Reynolds number. This relation just states that $\Delta Re_{tr} < 2Re_{x,tr}$ and is arrived at from pure geometrical reasoning. The data from Grid E and G seem to collapse on a single straight line wheras the data from grid A and grid B are above that line and thereby show a slightly longer transition zone. One should also point out that the line does intercept the vertical axis at a value of about

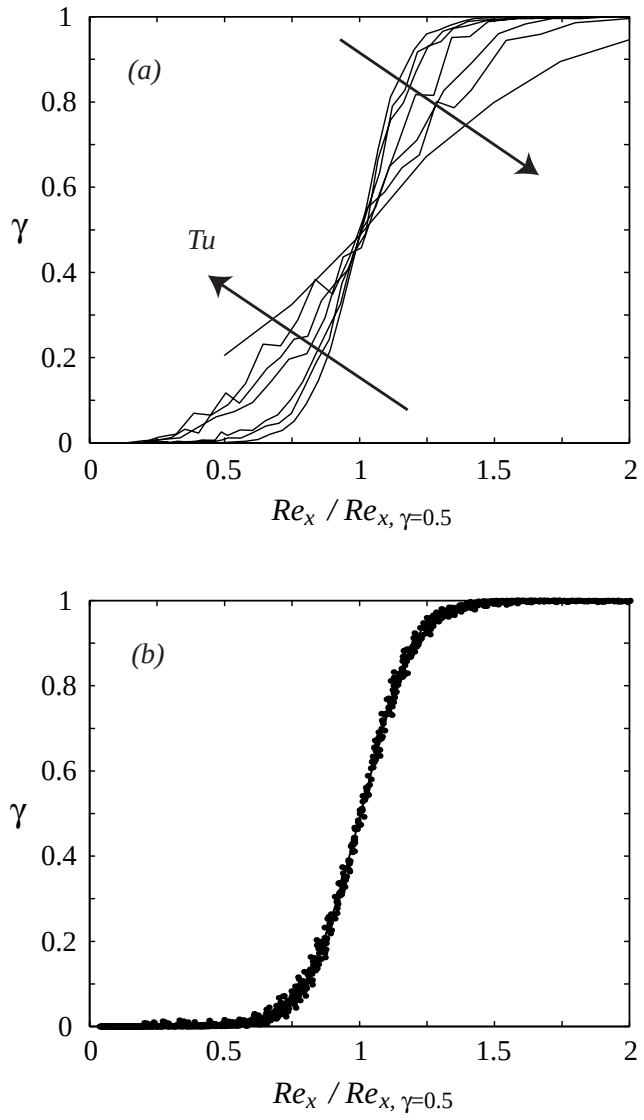

FIGURE 11. (a) Intermittency functions for different grids and Tu levels (1.4 2.2 3.3 3.9 5.3 5.7 6.7)%. (b) Intermittency functions from grid G and $Tu \leq 2.6\%$.

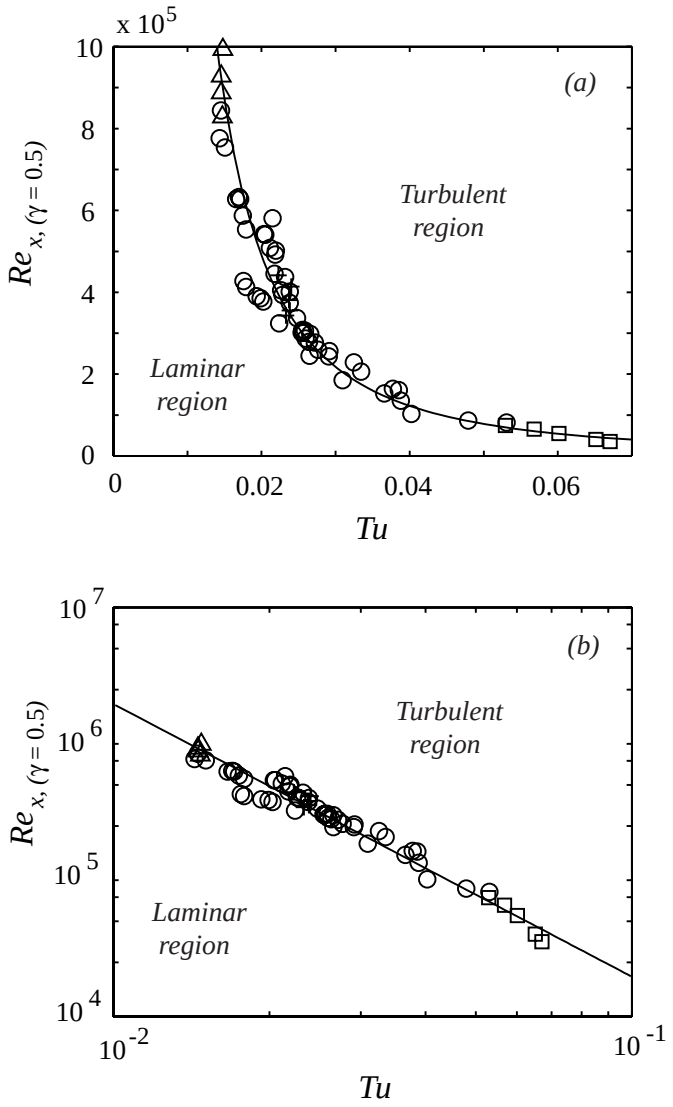

FIGURE 12. (a) Transitional Reynolds number (defined from γ=0.5) as function of the free stream turbulence level. (b) Logarithmic axes of the data in (a). See caption of figure 10 for symbols. Solid line is a curve fit to the shown symbols according to Eq. 5.

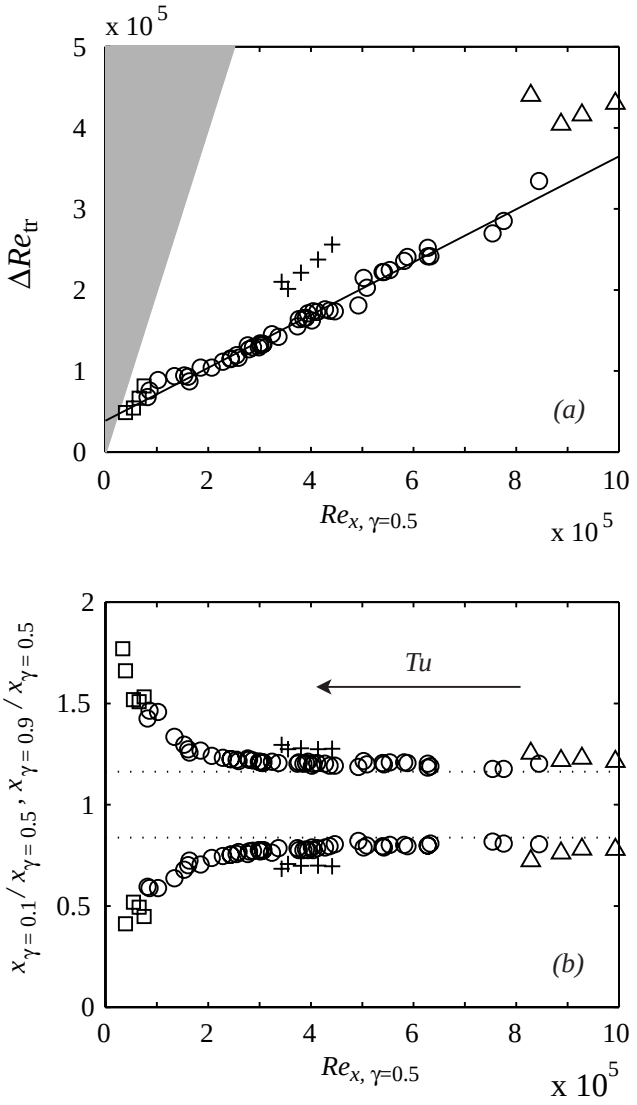

FIGURE 13. (a) Length of transition zone versus $Re_{x,\gamma=0.5}$. The shaded area denotes the nonadmissable region for which $\Delta Re_{tr} > 2Re_{x,tr}$. (b) Downstream position where γ=0.1 (lower symbol curve) and 0.9 (upper) normalized with the position where γ=0.5. The dotted lines correspond to $1\pm\frac{k}{2}$ where k=0.33. See caption of figure 10 for symbols.

3.9×10^4, showing that there is a minimum length of the transition zone also at high disturbance levels. This is of course also related to the fact that there is a minimum Reynolds number for self-sustained turbulence.

The linear variation of ΔRe_{tr} with $Re_{x,\gamma=0.5}$ can also be used to determine an expression for the relative length of the transition region. If we assume that there is a linear relation as in figure 13(a) this can be expressed as

$$\Delta Re_{tr} = \Delta Re_{tr,min} + kRe_{tr} \tag{6}$$

where $\Delta Re_{tr,min}$=3.9×10^4 is the intercept of the line with the ordinate axis and k=0.33 is the slope. With this relation we can easily calculate the relative length of the start and end of transition such that

$$\frac{x_{0.9}}{x_{0.5}} = 1 + \frac{k}{2} + \frac{\Delta Re_{tr,min}}{2Re_{tr}} \tag{7}$$

and

$$\frac{x_{0.1}}{x_{0.5}} = 1 - \frac{k}{2} - \frac{\Delta Re_{tr,min}}{2Re_{tr}} \tag{8}$$

As can be seen the relative length tends to a constant value for large transition Reynolds numbers whereas it becomes larger for small Re_{tr}. This is nicely illustrated in figure 13(b) where the individual values are plotted. As can be seen the assumption that the position of γ=0.5 is in the middle between the values of γ=0.1 and 0.9 seems to be fairly accurate.

There has been other attempts to relate the length of the transition zone with the transition Reynolds number. For instance Dhawan & Narasimha (1957) and later Narasimha (1984) suggested a power law relation such that

$$\Delta Re_{tr} = \alpha Re_{tr}^{\beta}. \tag{9}$$

The values of α and β given in Narasimha (1984) were 9.0 and 0.75, respectively, where they used the levels of γ=0.25 and 0.75 to determine the length of the transition zone. However according to Eq. 6 there is a minimum length of the transition zone and therefore the expression (9) must diverge from the experimental data for small values of Re_{tr}, i.e. high levels of Tu. In figure 14 the same data as in figure 13 are plotted, but now in logarithmic format and with ($\Delta Re_{tr} - \Delta Re_{tr,min}$) as function of Re_{tr}, where $\Delta Re_{tr,min}$=3.9×10^4. Also plotted in the figure is Eq. 9 with the values suggested by Narasimha (1984). First of all it is clear that the present data nicely follow expression (6). It is also seen that the relation suggested by Narasimha (1984) is close to the data for large Re_{tr}, whereas it diverges for small values as expected. The slighly

smaller transition zone length obtained with Eq. 9 can be explained as an effect of chosing a smaller interval of γ values to define the transition zone length.

5.3. *Intermittency models*

Emmons (1951) formulated a theory which describes the relation between a spot production function $[g(x, y, t)]$ and the intermittency factor $[\gamma(x)]$, based on probability considerations. For a steady two-dimensional flow this relation becomes:

$$\gamma(x) = 1 - \exp\left[-\int_{\mathcal{R}} g(x_0)dx_0dy_0dt_0\right], \tag{10}$$

where $\mathcal{R}$ is the dependence volume (spot sweep volume) assumed to be a cone with straight generators. However, due to the lack of available experimenal data Emmons suggested a first and simple assumption about $g(x)$, namely to be independent of x. Seven years later Narasimha (1957) improved this assumption based on new observations. These observations suggested that laminar breakdown in a two-dimensional boundary layer is nearly point-like, and that the spots originate in a restricted region (see Dhawan & Narasimha 1957 for an extended version of Narasimha 1957). In Dhawan & Narasimha (1957) they argue that $g(x)$ should have a maximum at some location and they state that experimentally this location turns out to be the start position of

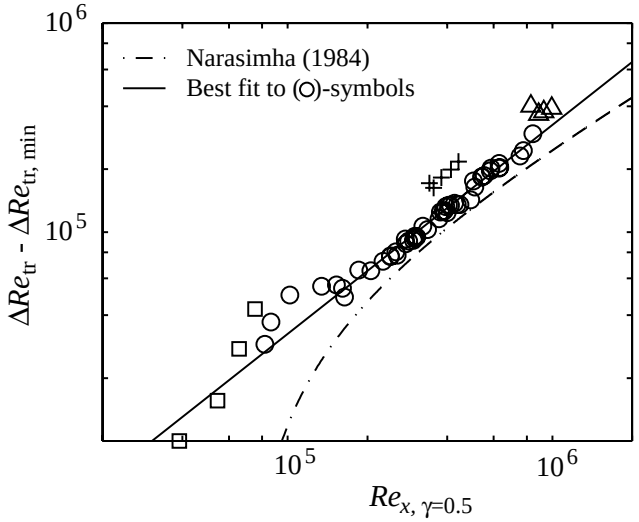

FIGURE 14. Correlation between the length of transition zone and the Reynolds number at the end of transition.

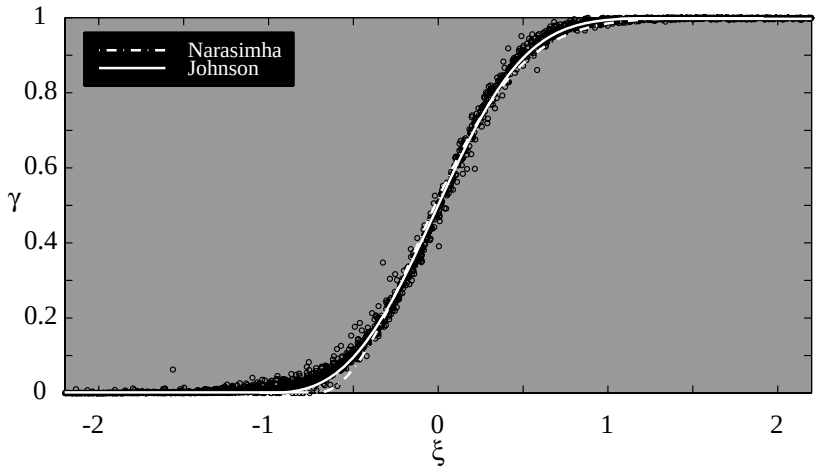

FIGURE 15. Universal intermittency functions by Narasimha and Johnson compared with all the experimental data as (∘)-symbols.

transition (x_t). Assuming a Gaussian distribution to represent $g(x)$ with its centre at x_t, they showed that the best fit of the Gaussian curve to experimental data is achieved when the standard deviation approaches zero (i.e. nearly a Dirac delta function, $\delta(x)$). Applying $g(x_0) = n\delta(x_0 - x_t)$ in Eq. (10) Narasimha (1957) derived the following expression

$$\gamma(x) = 1 - \exp\left[-(x - x_t)^2 \frac{n\sigma}{U_\infty}\right], \tag{11}$$

where $n\sigma/U_\infty$ is assumed constant with n and σ beeing the turbulent spot production rate per unit length in the spanwise direction and the Emmon's dimensionless spot propagation parameter, respectively.

Furthermore, Narasimha (1957); Dhawan & Narasimha (1957) showed that γ can be expressed as a unique function of ξ according to

$$\gamma(x) = 1 - \exp\left[-A_N(\xi + B_N)^2\right], \tag{12}$$

where $\xi = (Re_x - Re_{tr})/\Delta Re_{tr}$, and A_N and B_N are constants.

Johnson & Fashifar (1994) used a different approach resulting in an ordinary differential equation of γ. Furthermore, they assumed $n\sigma/U_\infty$ to increase linearly with x resulting in a unique function of γ like Eq. (12) but with the exponent of ξ appearing as a power of three (instead of two) according to

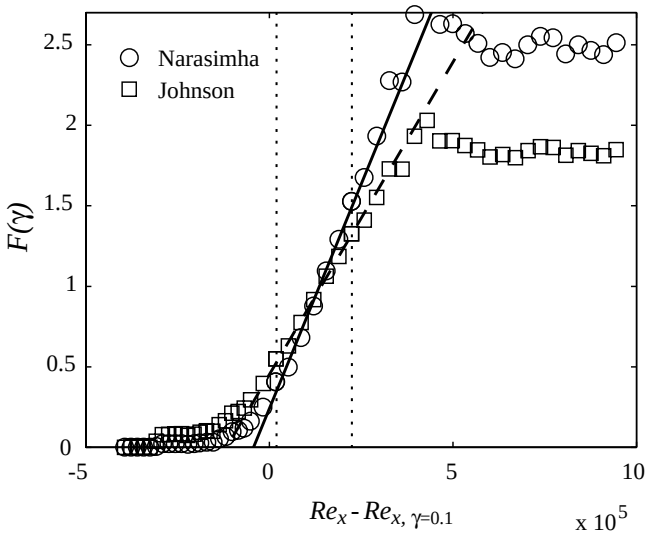

FIGURE 16. Procedure for determination of $Re_{tr,start}$. Same data is applied for the Narasimha and the Johnson models.

$$\gamma(x) = 1 - \exp\left[-A_J(\xi + B_J)^3\right], \tag{13}$$

where A_J and B_J are constants.

In figure 15 all γ-distributions corresponding to different Tu-levels are plotted and as can be seen they all show a common distribution. In the same figure both the Narasimha and the Johnson γ-functions are shown as dashed and solid lines, respectively. The best fit to all data results in $(A_N, B_N) = (1.42,\ 0.72)$ and $(A_J, B_J) = (0.60,\ 1.05)$, respectively, where the Johnson model is seen to give the best representation. It can be noted that a slightly larger exponent than 3 would give an even better fit to the data.

Finally, by introducing Re_x in Eq. (11) the Narasimha model may be transformed into a dimensionless form according to

$$\gamma(x) = 1 - \exp\left[-(Re_x - Re_{x,t})^2 \hat{n}\sigma\right], \tag{14}$$

where $\hat{n} = n\nu^2/U_\infty^3$ is a dimensionless spot production parameter. Note that comparison with Eq. (12) reveals the relation $\hat{n}\sigma \propto \Delta Re_{tr}^{-2}$.

An interesting correlation in this context is the one between the position where transition starts and the Tu-level. For this, one has to define the start

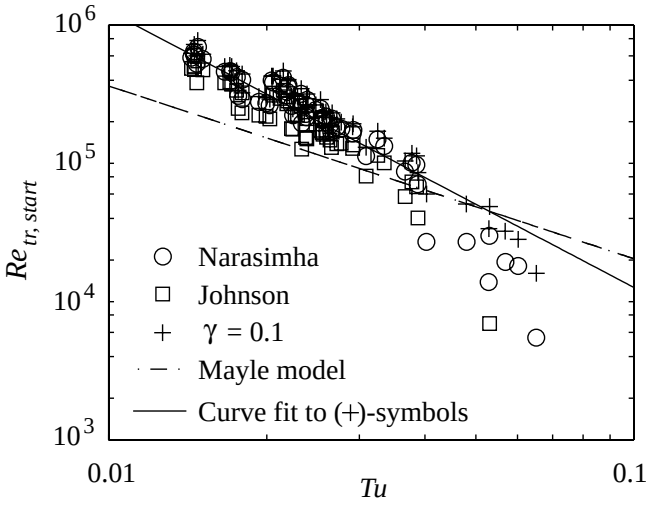

FIGURE 17. Start position of transition zone versus Tu (see text for comments).

of transition. Mayle (1991) (see his Appendix B) outlines a method in order to determine this position based on the function

$$F(\gamma) = \sqrt[p]{(-\log(1-\gamma))}$$

suggested in Narasimha (1957) (where $p = 2$). Through straight line curve fitting in the range $0.1 < \gamma < 0.9$, $Re_{x,t}$ is determined by the Re_x where the line crosses the ordinate axis (i.e. $F(\gamma)$=0). An example is shown in figure 16 where $F(\gamma)$ for both the Narasimha ($p = 2$) and the Johnson ($p = 3$) models are plotted.

This procedure is repeated for all cases (and both models) and in figure 17 the $Re_{tr,start}$ is plotted versus the Tu-level together with the Re_x where $\gamma = 0.1$ (see (+)-symbols). A best fit to the (+)-symbols according to $Re_{tr,start} = K \cdot Tu^m$ with $m = -2$ is done, resulting in $K = 126$, and compared with the model by Mayle corresponding to $(K, m) = (1148, -5/4)$. From the figure we can conclude that $Re_{x,\gamma=0.1}$ corresponds well with the Narasimha model and that the Johnson model defines the start of transition slightly earlier (i.e. for a lower γ-value). It should also be noted that for high Tu the Johnson model even produced some values of the start of transition that were located upstream the leading edge of the plate. These are of course excluded from figure 17.

From Eq. 14 it is clear that the slope of the curve corresponds to $\sqrt{\hat{n}\sigma}$, which is related to the transition length as stated above. In figure 18(a) and (b) the non-dimensional spot production rate ($\hat{n}\sigma$, obtained from the Narasimha

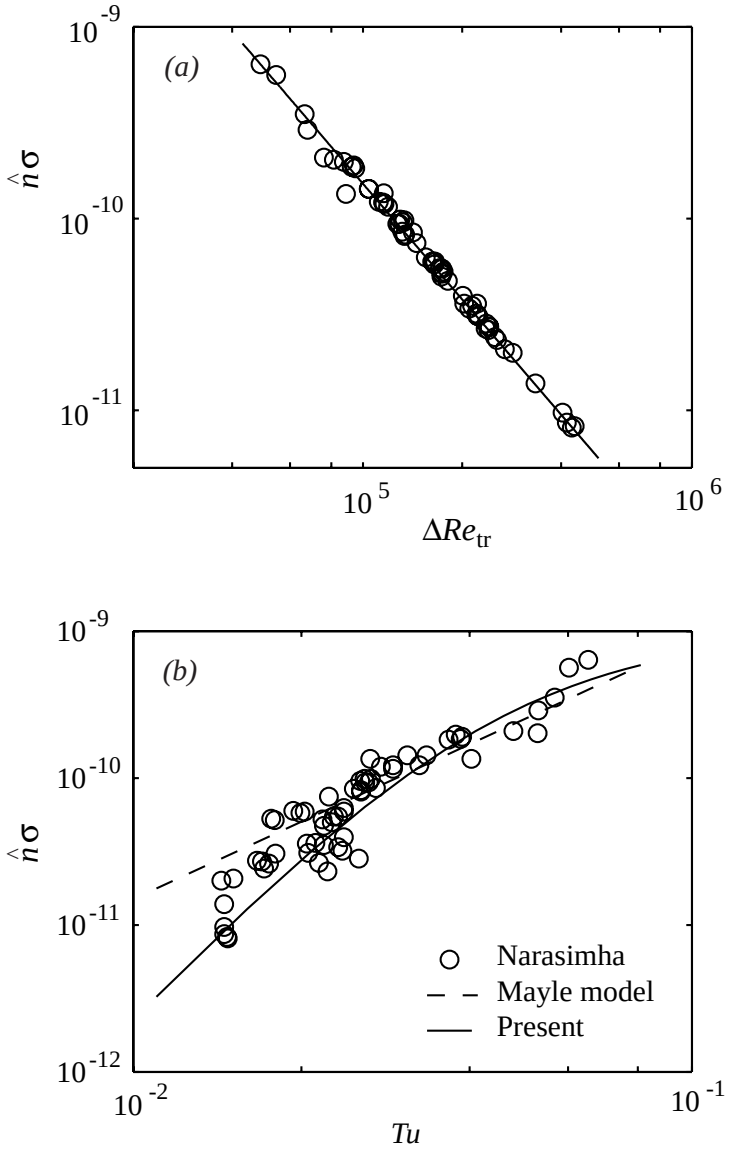

FIGURE 18. Non-dimensional spot production rate versus; (a) the extent of the transition zone, solid line is $\hat{n}\sigma = 1.52\Delta Re_{tr}^{-2}$; (b) turbulence intensity level. Solid line is $\hat{n}\sigma = 10^{-9}\left(1 + 0.00165Tu^{-2}\right)^{-2}$.

model) is plotted versus ΔRe_{tr} and Tu, respectively. Figure 18(a) simply verifies the above stated proportionality and the solid line in the figure corresponds to $\hat{n}\sigma = 1.52\Delta Re_{tr}^{-2}$. With this result, together with Eqs. 5 and 6, it is possible to write down an expression for the variation of $\hat{n}\sigma$ with Tu such that

$$\hat{n}\sigma = \frac{1.52}{\Delta Re_{tr,min}^2}\left(1 + \frac{kC}{\Delta Re_{tr,min}} Tu^{-2}\right)^{-2} \tag{15}$$

where the values of the constants have been given earlier but are repeated here; k=0.33, C=196 and $\Delta Re_{tr,min} = 3.9 \cdot 10^4$. In figure 18(b) we compare the Mayle (1991) model ($\hat{n}\sigma = 4.7 \times 10^{-8} Tu^{7/4}$) with the present data. Also included in the figure is the expression obtained from Eq. 15. It is seen that this expression follows the data better than the Mayle model, and especially seems to give the correct behaviour for low Tu, where Eq. 15 shows $\hat{n}\sigma$ to become proportional to Tu^4. For levels of Tu less than 0.5–1 %, TS-waves start to dominate the transition process and then Eq. 15 ceases to be valid.

On the other hand, high values of Tu give a constant value of $\hat{n}\sigma$. This can be seen as a result of a minimum Reynolds number for transition, i.e. for high Tu a further increase does not lower Re_{tr} and hence $\hat{n}\sigma$ seems to stay constant.

6. Summary and conclusions

This paper describes an extensive set of measurements of free stream turbulence induced transition for turbulence levels ranging from 1.4% up to 6.7% of the free stream velocity. The following points summarize the results:

- An active grid has been designed and evaluated. This grid makes it possible to change the Tu-level within a fairly large range without significantly changing the length scale of the turbulence.
- A procedure to estimate the intermittency of a velocity signal has been developed and implemented succesfully to determine flow properties in the transitional zone.
- In the initially laminar, but disturbed region, it has been found that the disturbance energy grows linearly as $Tu^2 Re_x$.
- The transitional Reynolds number was found to vary as Tu^{-2}.
- It was found that the length of the transitional zone has a minimum value and it increases linearly with Re_{tr}. This result puts earlier attempts to model the length of the transitional zone into doubt.
- The relative length of the transitional zone increases with increasing Tu.
- The intermittency function is found to have a relatively well-defined distribution, valid for all Tu.

We may also conclude that the present results seem to confirm that the initial part of the transition scenario is due to algebraically growing disturbances and that the prediction method of Andersson *et al.* (1999) rests on a sound physical basis. The present results, which are based on a larger data base than used by Andersson *et al.* (1999), give, however, a slightly different numerical value of the related constant. Finally we were able to relate Re_{tr} and Tu to the spot production rate in a way which gives a better physical description of the transitional zone than has previously been done.

Acknowledgments

This research is partly financed through VR, The Swedish Research Council. Dr Matsubara was supported by JSPS Research Fellowships for Young Scientists. J. Shiomi is acknowledged for taking part of the construction work of the active grid and for some of the initial data collection.

References

Andersson, P., Berggren, M. & Henningson, D. S. 1999 Optimal disturbances and bypass transition in boundary layers. *Phys. Fluids* **11**, 134–150.

Dhawan, S. & Narasimha, R. 1957 Some properties of boundary layer flow during the transition from laminar to turbulent motion. *J. Fluid Mech.* **3**, 418–436.

Emmons, H. W. 1951 The laminar-turbulent transition in a boundary layer–Part I. *J. Aero. Sci.* **18**, 490–498.

Fransson, J. H. M. 2001 Investigations of the asymptotic suction boundary layer. TRITA-MEK Tech. Rep. 2001:11. KTH, Stockholm, licentiate Thesis.

Fransson, J. M. H. & Alfredsson, P. H. 2003 On the disturbance growth in an asymptotic suction boundary layers. *J. Fluid Mech.* **482**, 51–90, **Paper 1**.

Gad-El-Hak, M. & Corrsin, S. 1974 Measurements of the nearly isotropic turbulence behind a uniform jet grid. *J. Fluid Mech.* **62**, 115–143.

Groth, J. & Johansson, A. V. 1988 Turbulence reduction by screens. *J. Fluid Mech.* **197**, 139–155.

Hallbäck, M., Groth, J. & Johansson, A. V. 1989 A Reynolds stress closure for the dissipation in anisotropic turbulent flows. *Seventh Symposium on Turbulent Shear Flows* **17-2**, 17.2.1–17.2.6.

Hedley, T. B. & Keffer, J. F. 1974 Turbulent/non-turbulent decisions in an intermittent flow. *J. Fluid Mech.* **64**, 625–644.

Johansson, A. V. & Alfredsson, P. H. 1982 On the structure of turbulent channel flow. *J. Fluid Mech.* **122**, 295–314.

Johnson, M. W. & Fashifar, A. 1994 Statistical properties of turbulent bursts in transitional boundary layers. *Int. J. Heat Fluid Flow* **15**, 283–290.

Kendall, J. M. 1985 Experimental study of disturbances produced in a pretransitional laminar boundary layer by weak free stream turbulence. *AIAA Paper* 85-1695.

Kendall, J. M. 1998 Experiments on boundary-layer receptivity to freestream turbulence. *AIAA Paper* 98-0530.

Klingmann, R. G. B., Boiko, A. V., Westin, K. J. A., Kozlov, V. V. & Alfredsson, P. H. 1993 Experiments on the stability of Tollmien-Schlichting waves. *Eur. J. Mech., B/Fluids* **12**, 493–514.

Kuan, C. L. & Wang, T. 1990 Investigation of the intermittent behaviour of transitional boundary layer using a conditional averaging technique. *Exp. Thermal Fluid Sci.* **3**, 157–173.

Lindgren, B. & Johansson, A. V. 2002 Evaluation of the flow quality in the MTL wind-tunnel. TRITA-MEK Tech. Rep. 2002:13. KTH, Stockholm.

Matsubara, M. & Alfredsson, P. H. 2001 Disturbance growth in boundary layers subjected to free-stream turbulence. *J. Fluid Mech.* **430**, 149–168.

Matsubara, M., Alfredsson, P. H. & Westin, K. J. A. 1998 Boundary layer transition at high levels of free stream turbulence. ASME paper 98-GT-248.

Mayle, R. E. 1991 The role of laminar-turbulent transition in gas turbine engines. *J. Turbomach.* **113**, 509–537.

Narasimha, R. 1957 On the distribution of intermittency in the transition region of a boundary layer. *J. Aero. Sci.* **24**, 711–712.

Narasimha, R. 1984 Subtransitions in the transition zone. In *Proc. IUTAM Symposium, Laminar–Turbulent Transition* (ed. V. V. Kozlov), pp. 141–151. Novosibirsk: Springer.

Tennekes, H. & Lumley, J. L. 1997 *A first course in turbulence*. The MIT Press, Cambridge.

Westin, J. 1997 Laminar-turbulent boundary layer transition influenced by free stream turbulence. PhD thesis, KTH, Stockholm, TRITA-MEK Tech. Rep. 1997:10.

Westin, K. J. A., Boiko, A. V., B. G. B. Klingmann, V. V. K. & Alfredsson, P. H. 1994 Experiments in a boundary layer subjected to freestream turbulence. Part I. Boundary layer structure and receptivity. *J. Fluid Mech.* **281**, 193–218.

Paper 6

6

On streamwise streaks generated by roughness elements in the boundary layer on a flat plate

By J. H. M. Fransson†, L. Brandt†, A. Talamelli†‡ and C. Cossu⋆

† KTH Mechanics, SE-100 44 Stockholm, Sweden
‡ DIEM, Università di Bologna, Italy
⋆ Laboratoire d'Hydrodynamique (LadHyX), CNRS-Ecole Polytechnique, F-91128 Palaiseau, France

An experimental and theoretical investigation aimed at describing the transient growth of steady and spanwise periodic streamwise streaks in a flat plate boundary layer is presented. Stable laminar streaks are experimentally generated by means of a spanwise periodic array of small cylindrical roughness elements fixed on the plate. The streamwise evolution of the streaks is measured and it is proved that, except in a small region near the roughness elements, they obey the boundary layer scalings. The maximum achievable amplitude is mainly determined by the relative height of the roughness elements. Very low intensity of the streamwise turbulent fluctuations excludes the formation of a shedding from the elements. Results are compared with numerical simulations of optimal and 'nearly optimal' boundary layer streaks. The theory is able to elucidate some of the discrepancies recently noticed between experimentally realizable transient growth and optimal perturbation theory. The key factor is found to be the wall normal location and the extension of the laminar standing streamwise vortices inducing the streaks. The differences among experimental works can finally be explained by the different streak generation mechanisms dominating in the boundary layer and can be linked to the geometry and to the ratio between the roughness height and the boundary layer scale.

1. Introduction

In the absence of external free-stream or wall perturbations the boundary layer developing on a semi-infinite flat plate immersed in a uniform flow of an incompressible viscous fluid is two-dimensional (2D) and is well described by the Blasius solution (see e.g. Schlichting 1979). The 2D Blasius solution is known to be linearly unstable to viscous Tollmien-Schlichting (TS) waves in a range of Reynolds numbers. Unstable TS waves modify the basic flow and, when they exceeds a critical amplitude of the order of 1% of the freestream velocity

U_∞, they experience a secondary instability Herbert (1988) wich finally leads to fast transition to turbulence. This transition scenario is well understood, at least in its initial part, and is often called the "classical" transition scenario. The classical transition scenario is, however, observed only with low levels of external perturbations. It has been known for many years that the presence of free-stream turbulence or wall imperfections may lead to strong 3D modulations of the boundary layer and trigger early transition (see Klebanoff *et al.* 1962; Tani 1969; Kendall 1985*a*, among others).

Lift-up and streaky structures in 2D boundary layers

In the 2D boundary layer, indeed, small amounts of streamwise vorticity are very effective in pushing low momentum fluid away from the wall and high momentum fluid towards the wall. This eventually leads to large elongated spanwise modulations of the streamwise velocity field called streamwise streaks. This 'lift-up effect' (Landahl 1980) is based on an inviscid mechanism but the effect of viscosity eventually dominates rendering the growth of the streaks only transient. Before their final viscous decay, however, the growth of the streaks may attain values of the order of the Reynolds number (Gustavsson 1991). The potential of shear flows to exhibit such large transient growths is related to the non-normal nature of the linear stability operator (see e.g. Trefethen *et al.* 1993, for a review). The optimal perturbations, i.e. the perturbation leading to maximum transient growth, have been computed for a number of wall bounded shear flows and found to consist of streamwise vortices, while the most amplified perturbation, optimally forced by these vortices, consists in streamwise streaks (for a review the reader may refer to the book by Schmid & Henningson 2001). In the non-parallel Blasius boundary layer, the disturbance present at the leading edge that are most spatially amplified consists, again, of spanwise periodic streamwise vortices which have spanwise scales of the order of the boundary layer thickness at the location where the maximum amplification is attained (Andersson *et al.* 1999; Luchini 2000). The most amplified perturbations consist of streamwise streaks.

Streamwise streaks are therefore expected to appear whenever a boundary layer is exposed to perturbations with streamwise vorticity. An extensively studied case is the boundary layer developing in the presence of free-stream turbulence. In early observations, Dryden (1937) and Taylor (1939) reported that spanwise modulations of the boundary layer thickness are generated in the presence of free-stream turbulence. These observations were confirmed and further detailed by, among others, Arnal & Juillen (1978) and Kendall (1985*a*) who coined the term 'Klebanoff modes' for the observed streaks, referring to early observations by Klebanoff (1971). The streaks forced by free-stream turbulence typically slowly oscillate in the boundary layer in a random way; their *rms* velocity profiles, however, were found to closely match the shape of the

steady streaks forced by optimal vortices (Andersson *et al.* 1999). The occurrence of bypass transition observed in the presence of free-stream turbulence was therefore related to the stability properties of boundary layers modulated by steady optimal streaks.

Influence of the presence of the streaks on boundary layer stability

The stability properties of the streaky 3D boundary layers may strongly differ from those of the Blasius 2D boundary layer and depend on the streak amplitude and shape.

For streaks of sufficiently large amplitude the inflection points, appearing in the 3D basic flow, are able to support high frequency secondary instabilities of inviscid nature. Andersson *et al.* (2001) analyzed the linear inviscid stability of a family of streaky boundary layers parametrized by the amplitude of the linearly-optimal vortices which are forced at the leading edge of the flat plate. They found that the inflectional instability sets in when the maximum streak amplitude exceeds a critical value of 26% U_∞.

The viscous stability of the same family of basic flows considered by Andersson *et al.* (2001) has been recently explored in the case of moderate amplitudes of the streaks ($< 26\% U_\infty$), which are therefore stable to inviscid instability. It was found (Cossu & Brandt 2002; Brandt *et al.* 2003; Cossu & Brandt 2003) that, in that case, the streaks have a stabilizing effect on the viscous Tollmien-Schlichting waves. It was therefore suggested to artificially force such moderate amplitude steady streaks in the Blasius boundary layer in order to delay the onset of the viscous TS instability, and the transition to turbulence to larger Reynolds numbers.

Experimental generation of steady streaks

The generation of steady vortices in the flat plate boundary layer has retained the attention of experimentalist since the early 1960'. Most of these investigations aimed at analyzing the effect of streamwise streaks on the boundary layer stability.

In the experiments of Tani & Komoda (1962) and Komoda (1967), small wings, located outside the boundary layer, were used to generate steady streamwise vortices which, upon entering the boundary layer, led to the development of steady spanwise periodic modulations of its thickness, i.e. to steady streamwise streaks. The circulation of the forced vortices was tuned by changing the incidence of the wings. Streamwise vortices may also be introduced by perturbations applied at the wall of the flat plate for instance by spanwise periodic blowing and suction through wall slots (see e.g. Kachanov & Tararykin 1987, among many others). Spanwise periodic arrays of roughness elements have also been proven very efficient to introduce steady streamwise vorticity in boundary

layers. Roughness elements would probably be simpler to manifacture in case of industrial applications based on the generation of streaks.

Bakchinov *et al.* (1995) used a spanwise periodic array of roughness elements of rectangular section, placed at the wall at some finite distance from the leading edge, to generate large amplitude streaks. For low freestream velocities (U_∞), the amplitude of the streaks was moderate and the streaks were stable up to $20\%U_\infty$. Far downstream of the roughness array these streaks were periodic, almost sinusoidal in the spanwise direction, and with a wall normal perturbation profile reminiscent of the Klebanoff mode and of the optimal streak shape, having however its maximum at $\eta \sim 2\delta$, where $\delta = \sqrt{\nu x/U_\infty}$ is the local boundary layer reference scale at the streamwise station x. The high speed parts of the streaks were located in spanwise correspondence with the roughness element, while the low speed streaks were observed to be located in correspondence to the free space between the roughness elements.

White (2002) investigated small amplitude (stable) steady streaks generated by using a spanwise periodic array of roughness elements of circular section and very small height. The far downstream shape of the streaks considered by White is also periodic in the spanwise direction and 'nearly-optimal' in the wall normal direction with, again, a maximum at 2δ. However, in that experiment, the high speed streak is found to correspond to the space between the roughness elements while the low speed streak is situated in correspondence to the roughness elements. White (2002) carefully analyzed the streamwise evolution of the streaks, starting near the roughness array, and compared his results with the characteristics of the optimal streaks predicted by the theory when optimal vortices are forced at the leading edge. He found that the experimental streaks differ from the optimal ones in, at least, two important features: (a) the streamwise position at which the peak amplitude is attained is found to be much upstream of the value predicted by optimal theory; (b) the wall normal position of the maximum perturbation velocity of the streak is closer to the wall compared to the prediction by transient growth theory.

Motivation of the present study

The initial motivation of our study was to experimentally verify the stabilizing action of streamwise streaks on TS waves found by Cossu & Brandt (2002) for optimal streaks of moderate amplitude (from 10% to $25\%U_\infty$). White (2002) results showed, however, that the streaks generated by roughness elements are likely to differ from optimal streaks in some important features. The present investigation is therefore aimed at carefully detail the evolution of streaks of amplitude larger than that considered by White (2002) and answer the following relevant questions:

1. Do the suboptimal trends reported by White (2002) for very low amplitude streaks apply also to larger amplitude streaks?

2. What are the main factors affecting the suboptimality of the experimental streaks?

The answer to the first question is important because the generation process of the large amplitude streaks reported by Bakchinov *et al.* (1995) seems to differ from that of small amplitude streaks reported by White (2002): respectively the low or the high speed region of the streaks are found far downstream behind each roughness element in these two experiments.

It is necessary to answer the second question if one wants to compare the stability of experimental and numerical streaks. Understanding the reasons leading to suboptimality could allow either to experimentally generate optimal streaks, either to numerically reproduce the experimental suboptimal streaks. For instance, it is not even a-priori known if the experimentally generated streaks verify the boundary layer scalings away from the roughness elements and in that case it would be inappropriate to compare them with optimal streaks which are solutions of the boundary layer equations.

In order to answer these questions we conducted an experimental study and then we compared the results with numerical simulations of optimal and 'nearly optimal' boundary layer streaks. The article is therefore organized as follows: In section 2 we describe the experimental setting and the particular parameters we choosed to generate the streaks. In section 3 we present the evolution of the experimentally generated streaks and we prove that they verify the boundary layer scalings except near the roughness elements. We further check whether nonlinear saturation effects are important at the considered amplitudes. In section 4 we numerically investigate the main factors leading to suboptimal behavior and compare the numerical results to the experimental findings. In section 5 we discuss the results and we finally summarize the main findings in 6.

2. Experimental setup and parameters

Test facility

The experiments were carried out at KTH Mechanics in the MTL-wind tunnel , which has a test section of 7 m in length, 0.8 m in heigh and 1.2 m in width, and the maximum speed is 70 m/s. After ten years in operation the flow quality of the MTL tunnel has been re-confirmed and the result is collected in an internal technical report by Lindgren & Johansson (2002). At 25 m/s the streamwise turbulence intensity is less than 0.025% of the free stream velocity and both the cross flow turbulence intensities are less than 0.035%. The tunnel is equipped with a heat exchanger in the return circuit just after the fan which is able to maintain the variation of the total pressure and the temperature below $\pm 0.06\%$ and $\pm 0.05^{\circ}$, respectively. Furthermore, for boundary layer measurements the tunnel is equipped with a computer controlled five degree of freedom traversing mechanism. A schematic of the experimental set-up is shown in figure 1. A 4.2

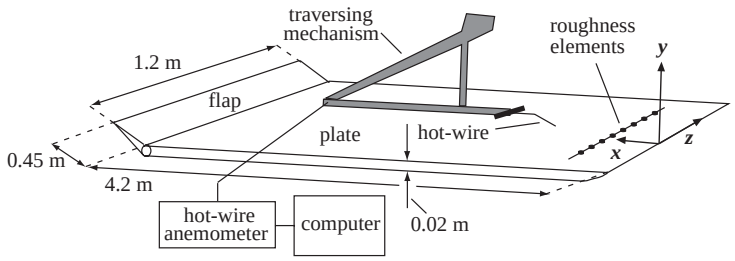

FIGURE 1. Schematic of the experimental set-up.

m long flat plate was mounted horizontally in the test section. The plate is the same as described in Klingmann *et al.* (1993) and has an asymmetric leading edge, in order get a short pressure gradient region without any suction peak at leading edge region. Further, a trailing edge flap is also used in order to regulate the stagnation streamline. The roof of the test section is adjustable making it possible to change the pressure gradient. A zero pressure gradient with a C_p-variaton of less than ± 0.01 was achieved for this set-up. A cartesian coordinate system is introduced (cf. figure 1). The origin is located on the centreline at the leading edge with $x-$, $y-$, and z-axis directed along the streamwise-, wall normal-, and spanwise direction, respectively.

Experimental setting

The streaky boundary layer was generated by means of roughness elements made of brass, obtained by cutting slices of a cylinder rod. Several preliminary tests were carried out in order to find the proper shape and dimension for the elements to generate stable and high amplitude streaks. In order to simplify these experiments the roughness elements were positioned in the middle of the plate where the boundary layer is substantially thicker. To get a good spanwise homogeneity 9 elements were periodically pasted on the plate surface. The experimental conditions are shown in the photograf of figure 2 with relevant dimensions. Here, δ is the boundary layer scale corresponding to $\sqrt{x\nu/U_\infty}$, k is the height of the roughness element, d the cylinder diameter, Δz is the spacing of the elements, and x_k is the distance from the leading edge where the elements were located. A single hot-wire probe operating at constant temperature was used to measure the streamwise velocity component (here denoted u). The probe was built at KTH Mechanics and was made of a 2.5 μm platinum wire with a distance between the prongs of approximately 0.5 mm. The calibration function proposed by Johansson & Alfredsson (1982) was used, where an extra term is added to King's law for the compensation of natural convection. This makes it suitable for low speed experiments. No temperature compensation is required due to the presence of the heat exchanger and temperature control

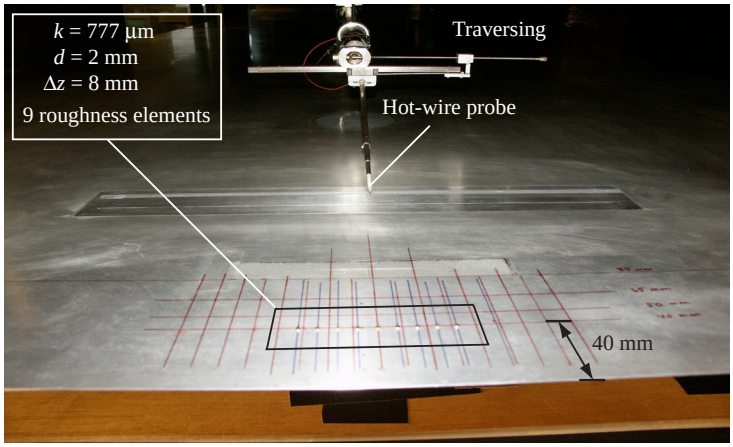

FIGURE 2. Photograf of the experimental set-up, showing the cylinder roughness elements. k = height, d = diameter, and Δz = roughness element spacing.

system. The probe is operated at 50% overheat and is calibrated against a Prandtl tube in the free stream.

Choice of parameters

Wind-tunnel experiments were performed at different free stream velocities, viz. 5, 6, 7 and 8 m/s while keeping the same height, streamwise and spanwise locations, and diameter of the roughness elements. This is a way of regulating the streak amplitude since a change of the velocity influences the height to the boundary layer scale ratio (k/δ). A stronger spanwise modulation of the boundary layer flow is achieved with an increase of velocity and vice versa. When k/δ or alternatively the roughness element Reynolds number ($Re_k = u(k)k/\nu$) becomes too large transition to turbulence occur. The critical value of Re_k for transition depends on the roughness element geometry and the flow quality of the wind-tunnel, i.e. the background disturbance level, and can be found in the range 300-1000 (cf. Klebanoff *et al.* 1992).

The selected spanwise distance between the roughness elements (Δz) sets the generated spanwise scales. However, a large Δz will induce an extra streak in between the roughness elements and initially there will be a mismatch between Δz and the spanwise wavelength of the energy dominating mode. In section 5 two different streak generation mechanisms will be discussed, and the dominating one depends on the roughness geometry, k/δ and presumably the front area (or rather z-width) of the roughness element. The dimensionless spanwise wave number is often defined as $\beta = \beta^*\delta$, where $\beta^* = 2\pi/\Delta z$. However, as mentioned above Δz does not necessarily correspond to the dominating

mode, which makes the definition delicate since comparisons are often made with the β predicted by optimal perturbation theory in where the spanwise modulation of the base flow only consists of one mode.

The Reynolds number based on the local Blasius scale (δ) at x_k ($Re_\delta = U_\infty \delta/\nu$) is a relevant stability parameter, and the critical value for amplifying Tollmien–Schlichting waves is well known to be around 300. All above mentioned parameters for the different flow cases are summarized in table 1. Numerous test-measurements with the goal to generate stable, high amplitude, and sinusoidal streaks, were made before the particular parameters in table 1 were chosen.

3. Experimental results

Perturbations induced by the roughness elements

Evolution in physical space. To follow the initial stage of the streak development, results for the configuration with $U_\infty = 7$ m/s are first presented. The stationary streamwise velocity perturbation is shown in the cross-stream (y, z) plane at different streamwise stations in figure 3. The perturbation velocity is defined as the difference of the local velocity $U(y, z)$ to the spanwise-averaged profile $U(y)$. Contours of constant streamwise velocity are also shown for comparison. Note that a region of large excess velocity is formed further downstream ($x \geq 70$ mm) straight behind the cylinders, located at $z = 0$ and 8 mm. The decay phase of the streaks is shown in the contour plot 500 mm downstream of the leading edge. The spanwise profiles change into almost sinusoidal curves as the disturbance evolves downstream and the details of the flow induced just behind the roughness elements are lost. As observed also in White (2002), a complicated disturbance is found in the region closest to the roughness array, in which the wake of each element is transformed into the periodic spanwise modulations of the streamwise velocity observed farther downstream. In the present experiments as well as in White (2002) standing cylinder roughness elements have been used, however, in the former case a

x_k^*	k^*	d^*	Δz^*	U_∞ (m/s)	δ^*	k^*/δ^*	Re_k	Re_δ	β
40	777	2	8	5	0.35	2.24	180	115	0.272
40	777	2	8	6	0.32	2.46	231	126	0.248
40	777	2	8	7	0.29	2.65	285	137	0.230
40	777	2	8	8	0.27	2.84	340	146	0.215

TABLE 1. Summary of the physical parameters. Parameters marked with an asterix are dimensional quantities in (mm). In subsequent text the $(*)$-symbols are omitted for simplicity. See text for further details.

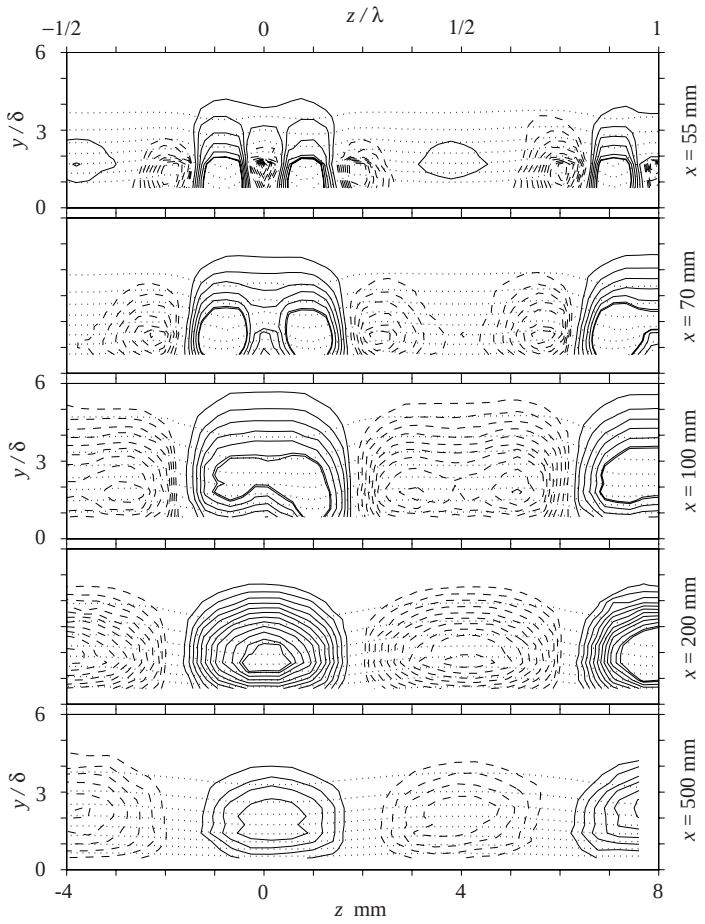

FIGURE 3. Streamwise evolution of positive and negative streamwise velocity perturbations (solid and dashed lines respectively). Dotted contour lines (0.1 U_∞ of increment) correspond to constant streamwise velocity. $U_\infty = 7$ m/s.

high speed streak is formed straight behind the element (in agreement with Kendall 1990; Bakchinov *et al.* 1995) and in the latter case a low speed streak is achieved (in agreement with Gaster *et al.* 1994; Joslin & Grosch 1995). An easy explanation of the contradictory observations is that there are different dominating generation mechanisms present (cf. section 5 for an extension of the subject). However, both mechanisms give rise to a transient growth of the energy in the downstream distance.

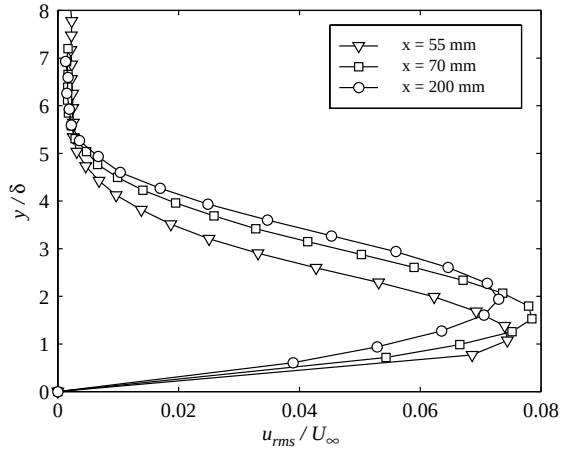

FIGURE 4. Disturbance profiles in the wall normal direction for different downstream locations. $U_\infty = 7$ m/s.

In figure 4 u_{rms}-profiles, based on the spatial $U(z)$-distribution, for three different downstream locations are compared. The positions are $x = 55, 70$, and 200 mm corresponding to 19, 45 and 206 roughness element heights downstream of the elements. It is clear from the figure that for this particular case the roughness elements induce a single peak in the u_{rms}-profile, despite the fact that it is possible to distinguish a shift in the locations of maxima in the high and low speed streaks (see figure 3 $x = 55$ mm). The reason for not observing the two peaks in the u_{rms}-profile is because all modes are superposed and the outer peak is hidden in the summation. White (2002) observed a two peak u_{rms}-distribution as far downstream as 66 roughness element heights, which is explained by the fact that the three strongest modes in that particular experiment all were of two-peak nature (cf. figure 6a) of that paper). Another observation of figure 4 is that the peak position is seen to move away from the wall in terms of y/δ.

Evolution of the spanwise harmonics. Normalized spanwise velocity profiles at the wall-normal position of maximum perturbation are displayed in figure 5. Here, the evolution into an almost sinusoidal modulation of the base flow in the downstream direction is illustrated, and the higher harmonics induced straight behind the roughness elements are lost. Fourier transform of the considered profiles is also shown in figure 5. The dominating wavelength is dictated by the roughness array periodicity already at $x > 70$ mm or beyond 45 roughness heights downstream of the elements. Relatively small energy peaks at the higher harmonics of the fundamental wavelength ($\lambda_0 = 8$ mm) can also be seen.

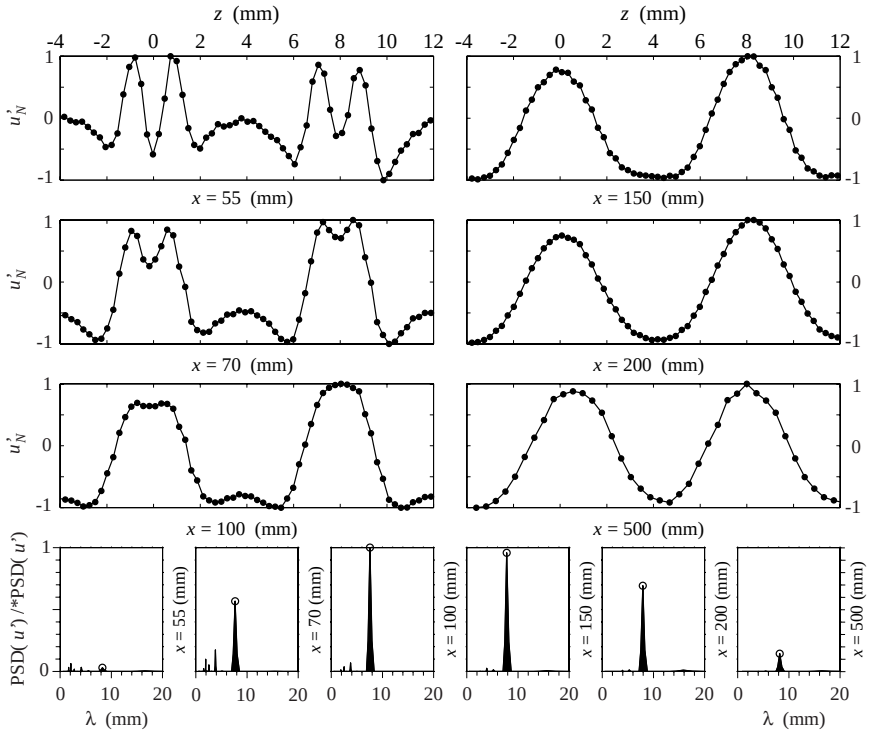

FIGURE 5. Streamwise evolution of the mean spanwise velocity profile taken at the wall normal position corresponding to the disturbance peak. a) spanwise velocity distribution normalized to ± 1, and b) spanwise power spectral density function. The normalization is such that $*$ corresponds to $\max_{\forall x}$. $U_\infty = 7$ m/s.

These harmonics reach their respectively energy maxima upstream the fundamental mode which is in concordance with theory and the results by White (2002).

In the present case, the spanwise wavelength of the streaks is unambiguously determined by the distance between the roughness elements (see figure 5). In White (2002) and White & Ergin (2003), on the contrary, the spanwise dimension (i.e. the diameter) of the roughness elements determines the dominating spanwise scale of the disturbace downstream. In White (2002) the spacing of the roughness elements is 12.5 mm and the fundamental spanwise wavelength is half of this value, while in White & Ergin (2003) similar cylindrical elements (diameter of 6.35 mm) are placed 19 mm apart. In the latter case the

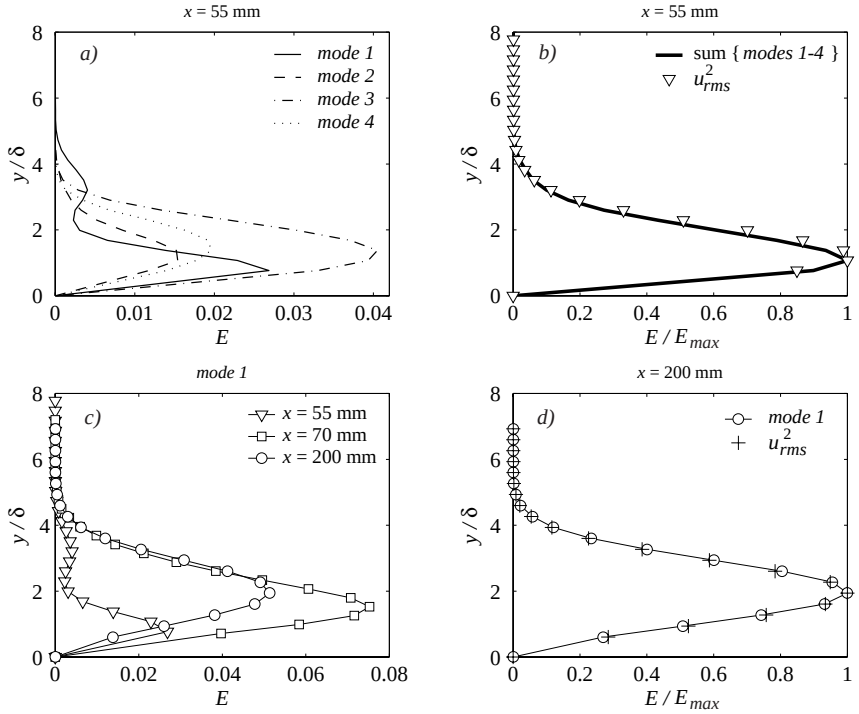

FIGURE 6. Decomposed energy mode profiles in the wall normal direction. $U_\infty = 7m/s$. a) Power Spectral Density distributions for the fundamental (1) mode $\lambda_0 = 8$ mm, and higher harmonics; (2) $\lambda_0/2$, (3) $\lambda_0/4$, and (4) $\lambda_0/5$. b) Comparison between the u^2_{rms} (figure 4) and the superposition of all four modes. c) Fundamental mode for different x-positions. d) Comparison between the u^2_{rms} (figure 4) and fundamental mode.

most energetic wavelength is one third of the spacing. For both experimental configurations the dominating scale is about 6 mm, remarkably close to the spanwise width of the elements and to the width of the induced wake.

In figure 6 the Power Spectral Density distributions in the wall normal direction is shown for different modes. Figure 6a) shows that the only mode with a two peak distribution is the fundamental mode. However, a superposition of the four modes in a) agree well with the u_{rms}-profile (see figure 4) at the same x-position since the outer peak is hidden by the other modes, this was mentioned earlier and is illustrated in figure 6b). Figure 6c) shows the evolution of the fundamental mode in the downstream direction and at $x = 70$ mm or

at 45 roughness element heights behind the elements the two peak wall normal distribution has disappeared. Finally, in d) the fundamental mode is compared with the u_{rms}-profile at the same x-position, namely $x = 200$ mm, and shows excellent agreement. This implies that there are no higher harmonics present any longer and that non-linear effects are negligible.

Streamwise evolution of the streak amplitude. In this section, we consider the downstream evolution of the streaks for the four cases under consideration, i.e. $U_\infty = 5$, 6, 7 and 8 m/s. We have shown that, except the region just downstream of the roughness, most of the perturbation energy is in the fundamental harmonic and we can therefore consider the streak amplitude in physical space. The streak amplitude A_{ST} is defined as the wall-normal maximum of the peak-to-peak difference between the streamwise velocities in the low- and high-speed regions, i.e.

$$A_{ST} = \max_y \{U(y)_{\text{high}} - U(y)_{\text{low}}\}/2$$

where $U(y)_{\text{high}}$ and $U(y)_{\text{low}}$ are the velocity profiles in the high- and low-speed regions, respectively.

The streamwise evolution of the amplitude A_{ST} is displayed in figure 7a). For the same experimental set-up, stronger streaks are induced by increasing the free stream velocity. This is due both to the increase of the cylinder height relative to the local boundary layer displacement thickness and to the increased velocity hitting on the elements. Further, it is observed that the location of maximum amplitude also moves to larger distances from the leading edge when increasing the free-stream velocity.

In figure 7b) the downstream evolution of the wall-normal position of the maximum of the steady perturbation is shown for the four cases. The dotted line represents the theoretical value obtained for the optimal perturbation at the leading edge of the flat plate $y/\delta = 2.2$ (see Andersson *et al.* 1999; Luchini 2000). In all four cases the position of maximum perturbation is seen to move upwards in the boundary layer which is in concordance with the experiments by White (2002).

Boundary layer scaling and linearity of the streaks

The data in figure 7 are here rescaled according to the boundary layer affinity property to verify whether the experimentally observed streaks also satisfy this scaling property. This property is based on th easumption of slow streamwise variation of the flow and it is therefore not valid in the vicinity of the roughness elements. However, the downstream evolution of the perturbations can still be described by the boundary layer equations. As shown in Andersson *et al.* (1999) and Andersson *et al.* (2001), steady streamwise streaks obey the boundary layer approximation and are therefore Reynolds number independent. This results in a scaling property that couples the spatial scales of the

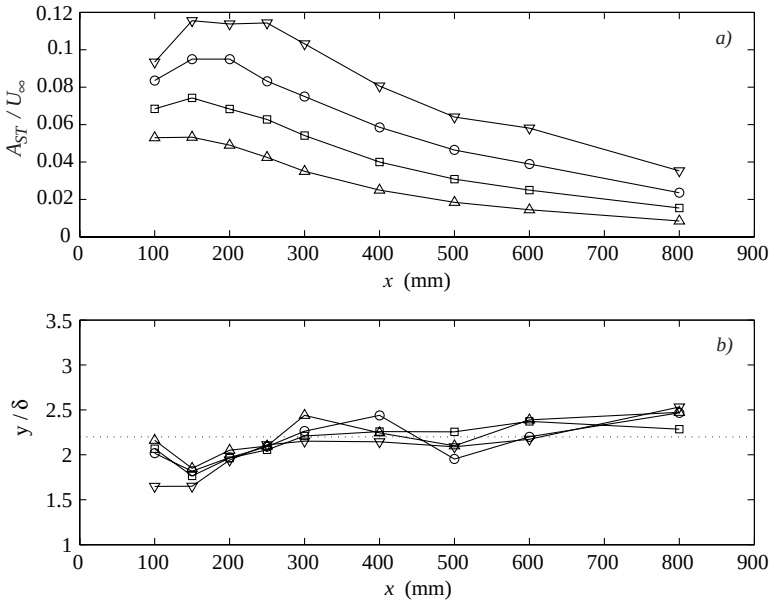

FIGURE 7. Streamwise evolution of the streaks: a) Streak amplitude A_{ST} versus x (mm). b) Wall-normal position of the maximum streak amplitude normalised with the local Blasius length scale δ. The symbols ($\triangle$), ($\square$), ($\circ$), and ($\triangledown$) correspond to $U_\infty = 5, 6, 7$, and 8 m/s, respectively.

problem to the free stream velocity and viscosity, implying that the same streak profile is obtained for every combination such that $x\beta^{*2}/U_\infty \cdot \nu =$ constant. Since β^* and ν are kept constant in the present experiment, the downstream evolution of the streaks is expected to be proportional to U_∞. This scaling implies that the same streak can be observed if the relevant flow parameters remain constant when scaled with the local boundary layer thickness. As a consequence, one can define a streamwise coordinate X such that the spanwise wavenumber β, scaled with the local δ, is the same at each station X for the four cases depicted in figure 7 and obtain the same streamwise evolution provided the scaling property holds. The streamwise coordinate X can be freely chosen. In the present case it is selected such that $\beta = 0.45$ at $X = 1$ and the results are shown in figure 8, where the streak amplitude A_{ST} is normalised with its streamwise maximum. The collapse of the different curves is remarkable despite the local β at the position of the roughness elements slightly differs for the different realizations. It should also be noted that the four configurations considered in figure 7 differ in the value of k/δ, i.e. the relative height of the roughness elements. In principle, this would break the suggested scaling

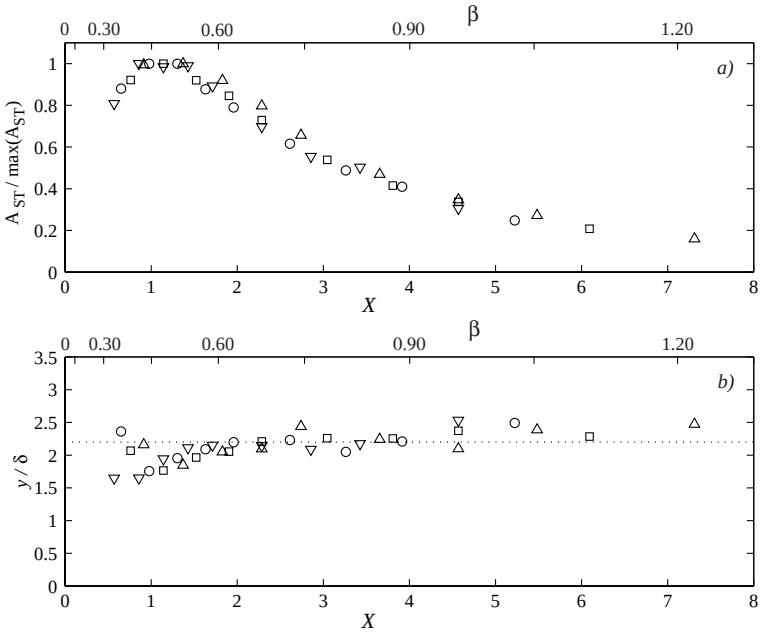

FIGURE 8. Streamwise evolution of the streaks: a) Streak amplitude A_{ST} normalised to unity versus the boundary layer streamwise coordinate X. b) Wall-normal position of the maximum streak amplitude normalised with the local Blasius length scale δ. Symbols are same as in figure 7.

property. However, it does not affect the curve collapse in the plot, where the amplitude of the streak is divided by its maximum value. Therefore, it may be inferred that the parameter k/δ mainly determines the maximum achievable streak amplitude. The maximum amplitude is attained for a local β of about 0.45 in all cases and the evolution of the wall-normal position of the maximum perturbation is also in agreement among the different experimental configurations (figure 8b). From the collapse of the curves we can also conclude that the streaks behave linearly and that the nonlinear interactions are not strong enough to induce the upstream shift of the location of the maximum amplitude noted in the simulations by Andersson *et al.* (2001) for high-amplitude nonlinearly saturated streaks. Hence, the differences between optimal perturbation and experimentally generated streaks cannot be explained by nonlinearities, as expected by the results in White (2002) where the importance of nonlinear terms can be ruled out by the small amplitudes of the measured streaks.

4. Suboptimality of the experimental streaks

The streak amplitude curves in figure 7 show only a qualitative agreement with the predictions from transient growth theory: the maxima occur farther upstream, thus at lower local β, as observed also by White (2002), and the decay downstream of the maximum is faster than for the optimal disturbances. In order to understand the physical reason for the observed differences, numerical simulations are performed on a simple theoretical model. The model is based on the work by Andersson *et al.* (1999).

Numerical method

The numerical code used in the work mentioned above is used as a basis for the present simulations. It solves the linear boundary layer equations for steady spanwise periodic disturbances. It uses Chebychev polynomials in the wall-normal direction and a fully implicit finite difference scheme in the marching direction (streamwise). The optimal perturbations are obtained by an adjoint-based optimization technique.

Influence of the streamwise position of input of the streamwise vortices

Since the disturbance is introduced by the roughness elements a certain distance downstream of the leading edge, the code used in Andersson *et al.* (1999) has been modified to optimize for initial conditions at a generic streamwise station X_0 different from the leading edge. The interested reader is referred to Levin & Henningson (2003) for a thourough account of the effect of the initial position X_0 on the transient growth of streaks. In particular, these authors show that the optimal disturbance introduced at a certain position downstream of the leading edge gives rise to a larger growth than for optimal disturbances at the leading edge.

The optimal perturbation for the experimental flow parameters at $U_\infty = 7$ m/s, corresponding to $X_0 = 0.2611$ and $\beta_0 = 0.230$, has been computed and is considered in this section. In figure 9 we display the comparison between the evolution of the disturbance energy for the optimal perturbation at the leading edge, the optimal perturbation at the actual location of the roughness element and the measured data, where we assume the square of the amplitude A_{ST} as a measure of the perturbation energy and the experimental data are arbitrarily scaled to fit in the plot. It can be seen that the growth is larger for the case of initial optimal perturbation at $X_0 = 0.26$, in agreement with the findings in Levin & Henningson (2003). The discrepancies between experimental and theoretical results are qualitatively similar and we can therefore conclude that taking into account the actual position of the perturbation generation cannot explain the observed streak behavior.

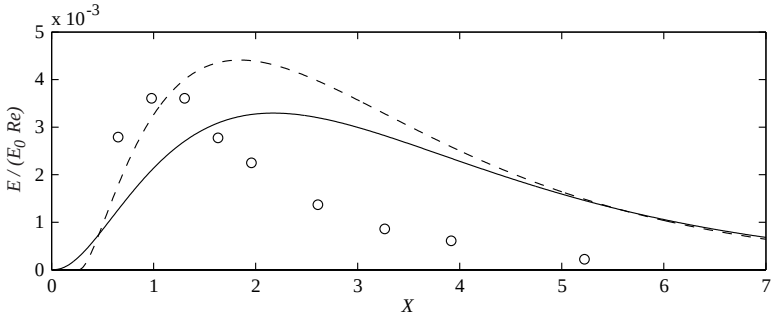

FIGURE 9. Streamwise evolution of the perturbation energy of the optimal perturbations introduced at the leading edge (solid line) and at the actual position of the roughness elements $X_0 = 0.2611$ (dashed line). The open circles indicate the square of the measured streak amplitude A^2_{ST}.

Influence of the shape of the vortices: suboptimal input vortices

The initial optimal conditions at $X_0 = 0.2611$ has zero streamwise velocity and therefore it consists only of streamwise vorticity ω_x. The latter is shown by the solid line in figure 10. It can be seen in the figure that the maximum of ω_x is located far up in the boundary layer, namely at $y/\delta = 3.55$. It was therefore decided to study the effect of changing the position of the initial streamwise vortices relative to the wall and to verify if this could be the cause of the differences between experimental data and optimal perturbations. Since $u = 0$, w may be derived directly from v through the continuity equation, and the wall-normal profile of v or alternatively of ω_x completely defines the optimal disturbance at the upstream position X_0. The wall-normal profiles of the sub-optimal initial vortices considered below are also shown for comparison in figure 10. These different conditions are obtained simply by stretching or compressing the wall-normal velocity profile of the optimal upstream perturbation. This amounts to multiply the wall normal coordinate (y) pertaining to the optimal perturbation by a factor c, so that the position of the maximum is moved to $y/\delta = 3.55c$.

It should be noted that this is the simplest approximation among the many possible initial conditions, which can be used to represent the perturbation induced by a wall-mounted cylinder. In particular, considering the discussion above on the generation mechanism, we do not consider the wall-normal vorticity associated to the cylinder wake but only the streamwise vorticity of the standing vortex forming upstream of the obstacle. However, as shown below, this approximation allows some essential features of the streak generation process to be captured.

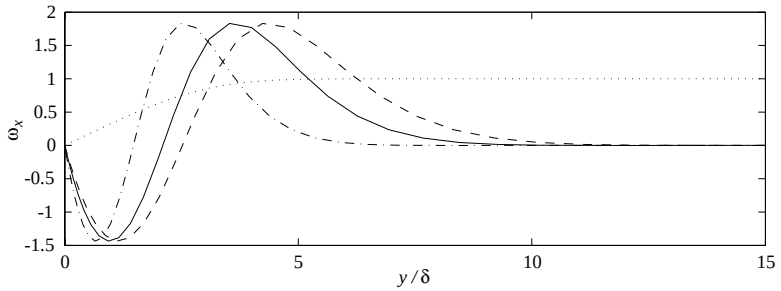

FIGURE 10. Wall-normal distribution of the streamwise vorticity of optimal disturbance at $X_0 = 0.2611$, $\beta_0 = 0.2299$ (solid line). Suboptimal initial conditions obtained by stretching or compressing the optimal disturbance by a factor c. Dashed line: $c = 1.2$; dash-dotted line: $c = 0.7$. The dotted line represents the Blasius profile.

The downstream evolution of the wall-normal maximum of the streamwise velocity, corresponding to the same streak amplitude definition as in the experiments, is displayed in figure 11a) for different values of the parameter c. The curve pertaining to the optimal perturbation (optimal at $X = 1$) is indicated by the solid line. For values of the parameter c lower than one, i.e. for initial streamwise vortices confined closer to the wall, lower amplification is obtained. Further, the location of maximum amplitude is moving upstream and a faster decay is observed downstream of the maximum. These effects become even clearer for lower values of c. Conversely, for c larger than one, i.e. for an initial vortex farther away from the wall, the location of the maximum growth moves downstream. The vortex needs a longer distance to diffuse into the growing boundary layer and to interact with the wall-normal shear of the basic flow. It is also interesting to note that the peak value is larger for $c = 1.2$. Comparing the evolution of the optimal perturbation in figure 9 and 11a), it can seen that the location of the maximum moves upstream when the streak amplitude is considered instead of the kinetic energy as a measure of the perturbation. The maximum of the wall-normal velocity is displayed in figure 11b), where the logarithmic axis is chosen to emphasise the final decay rates. It is observed that the decay is exponential and that the increase in the parameter c, corresponding to the increase in the wall-normal scale of the upstream vortices, is associated with a decrease of the downstream decay of the perturbations. This is in agreement with previous theoretical studies on the evolution of free-stream perturbations; the modes of the continuous spectrum of the linearized Navier-Stokes equations for a parallel boundary layer flow which show the lowest decay rate are in fact characterised by the largest wall-normal scales (Grosch & Salwen 1978). Note also that the damping rate of the stable modes of the discrete spectrum, i.e. of

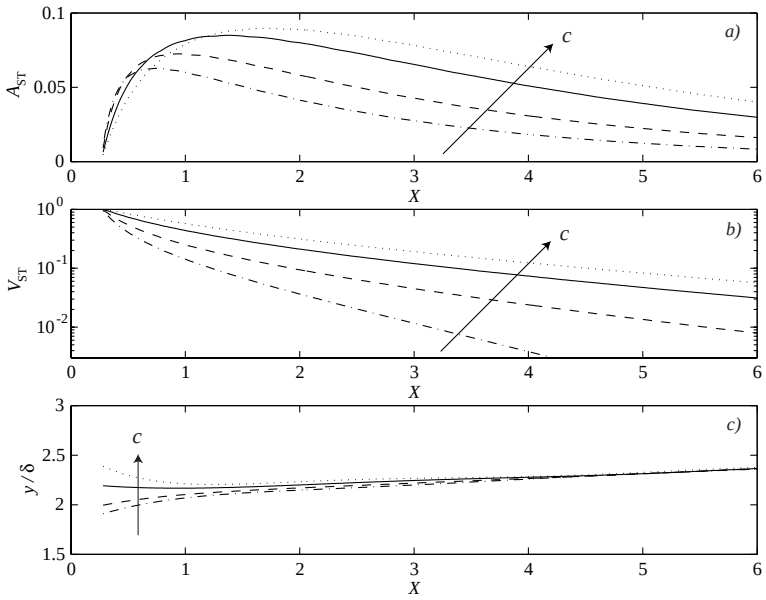

FIGURE 11. Streamwise evolution of the streak generated by initial conditions at $X_0 = 0.2611$, $\beta_0 = 0.2299$. a) Streamwise velocity amplitude; b) Wall-normal maximum of the wall-normal velocity amplitude and c) Wall-normal maximum of the streamwise velocity perturbation. Solid line: $c = 1$ (optimal disturbance); dotted line: $c = 1.2$; dashed line: $c = 0.8$; dash-dotted line: $c = 0.7$.

modes not zero inside the shear layer and decaying in the free-stream, is larger than for modes of the continuous spectrum for streamwise independent modes. The faster decay rate of the streamwise vortices can therefore explain both the reduced streak growth and the faster final decay.

The wall-normal position of the maximum of the streamwise velocity perturbation in figure 11a) is shown in figure 11c). After an initial phase in which the position of the maximum seems to be related to the location of the upstream vortices, the streak is slightly displaced away from the wall, in agreement with the experimental data. Note that for the optimal perturbation at the leading edge considered in Andersson *et al.* (1999), the position of maximum perturbation is found to be almost constant. Finally, in figure 12 we show the best fit to the experimental data. This is obtained for a value of $c = 0.78$, corresponding to the location $y/\delta = 2.75$ of the maximum of the streamwise vorticity perturbation at the position of the roughness elements. This value is remarkably close to the height of the roughness element $k/\delta = 2.65$. In figure 12a) the

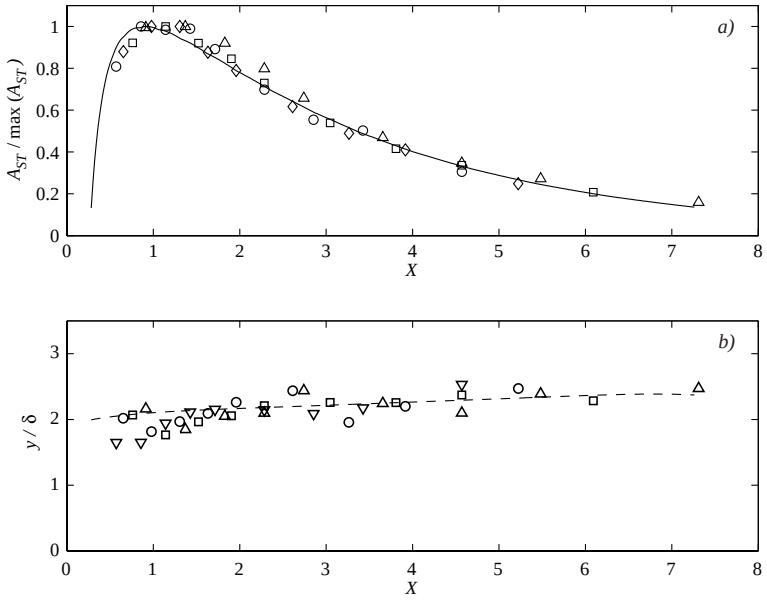

FIGURE 12. Comparison between the experimental results for all U_∞ in Table 1 and the best fitting to $U_\infty = 7$ m/s obtained using initial vortices confined closer to the wall ($c = 0.78$). a) wall-normal maximum of the streak amplitude. b) wall-normal position of the maximum perturbation.

streak decay is well captured while the position of maximum amplification is slightly upstream compared to the experiments. The downstream increase of the position of maximum perturbation is also well predicted (see figure 12b).

The wall-normal distribution of the streamwise velocity perturbation at two different streamwise stations is compared with the theoretical results in figure 13. In figure 13a) the streak profile is defined as the peak-to-peak difference in the high and low-speed region, whereas in figure 13b) it is defined as $\sqrt{E(y,\beta_0)} = \sqrt{\hat{u}^2(y,\beta_0)}$, where $\hat{u}$ is the Fourier transform in z of he streamwise velocity and β_0 the fundamental wavenumber corresponding to the roughness spacing. Both plots show a good agreement with the theoretical result.

From the results of this section we can conclude that the distance to the wall and the extension of the fundamental vortices is a fundamental parameter for the generation of steady streaks. Vortices confined into the boundary layer induce streaks, which grow less, reach their peak amplitude upstream and decay faster if compared to the optimal perturbation. Conversely, vortices displaced away from the wall create streaks, which reach higher peak amplitude but at

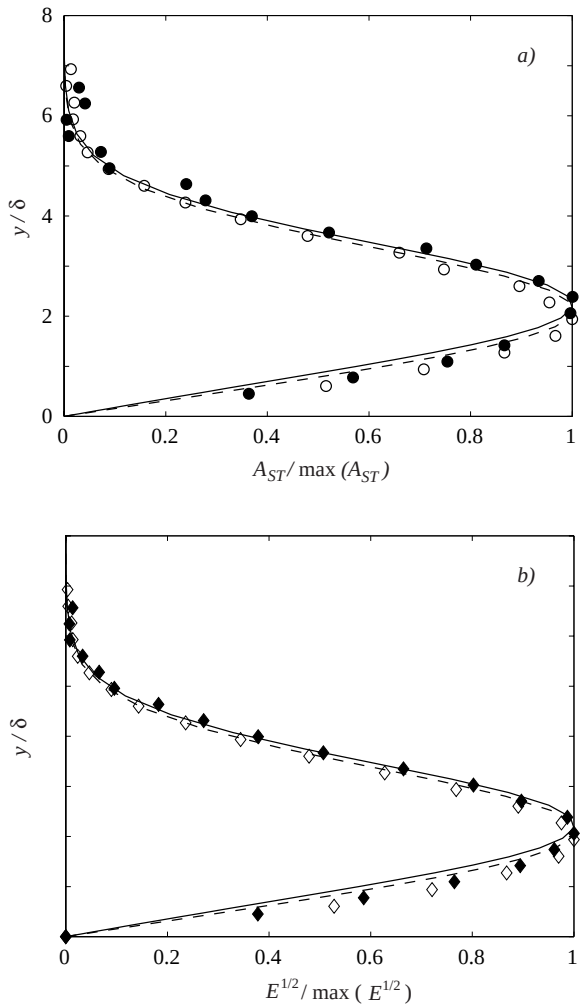

FIGURE 13. Wall-normal perturbation profiles at $x = 200$ and 500 mm (or $X = 1.31$ and 3.26) corresponding to unfilled and filled symbols, respectively. Dashed and solid lines are the corresponding theoretical profiles. a) Direct measure of amplitude (see definition of A_{ST}) and b) integrated spectral density amplitude (see text for definition of E).

positions further downstream and have a lower decay rate. We have thus identified the factor which is able to explain the difference between optimally growing perturbations and experimentally induced streaks, both in our experiment and in the study of White (2002), in spite of the different configurations.

The observed behavior is also believed to be able to explain the differences observed between optimal perturbation and streaks induced by free-stream turbulence. It is observed in Matsubara & Alfredsson (2001) that the latter streaks are characterised by a spanwise wavenumber slightly larger than the one predicted by the theory in Andersson *et al.* (1999) and Luchini (2000). Fransson & Alfredsson (2003) experimentally confirmed these results and showed that for high levels of free-stream turbulence the experimental results approaches the theoretical. The present results show, in fact, that vortices extending further above the boundary layer than the optimal vortices, and thus probably a better representation of free-stream turbulence, reach their maximum amplitude further downstream and are therefore associated to larger values of the local wavenumber β at the saturation stage. This latter type of initial conditions seems more difficult to achieve with wall-mounted actuators.

5. Discussion

Vorticity generation mechanism on the roughness elements

Comparison of the above results with similar experimental studies in literature show that two distinct flow configurations can be induced by the presence of roughness elements; They are both characterised by the formation of streamwise elongated velocity perturbations and differ in the relative position of the high- and low speed streaks with respect to the roughness elements. In the experiments by Kendall (1990), Gaster *et al.* (1994) and related simulations by Joslin & Grosch (1995), White (2002), and Asai *et al.* (2002), a region of defect velocity is formed straight behind the element. This is of course due to the presence of the wake, which persists downstream forming the low speed streak.

Conversely, in the present experiment, similarly to what was observed by Bakchinov *et al.* (1995), a high-speed region is induced behind the roughness element.

Two different generation mechanisms are therefore dominating in the two cases and we here attempt an explanation for this behaviour by considering the perturbation induced by a roughness element in a wall-bounded shear flow (see Hunt *et al.* 1978; Acarlar & Smith 1987).

A wake is formed behind the roughness element as a consequence of the momentum loss induced by the presence of an obstacle. This is associated with the wall-normal vorticity, mainly due to the spanwise variation of the streamwise velocity. This vorticity can be tilted in the streamwise variation by the wall-normal shear of the streamwise velocity profile.

Further, the presence of the wall is affecting the perturbation induced in the flow. The spanwise vorticity of the incoming shear flow is wrapped around the front part of the obstacle forming a stationary horseshoe-shaped vortex structure with the two streamwise legs pointing downstream. The vorticity

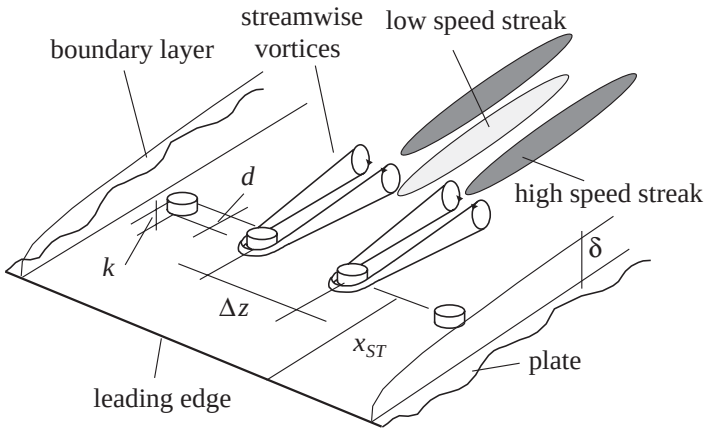

FIGURE 14. Schematic of the roughness elements disposition and conceptual view of the streaks generation mechanism.

associated with these two counterrotating streamwise vortices is such that high-speed fluid is pushed towards the wall in the region behind the obstacle and low-speed fluid is lifted on the outer sides (Hunt *et al.* 1978). The amount of vorticity concentrated in the streamwise legs of the standing vortex depends on the relative height of the element with respect the boundary layer thickness (k/δ).

It must be pointed out that the experiments by Acarlar & Smith (1987) show that the interactions between small hemispheric protuberances and a laminar boundary layer may also generate, for sufficiently high values of Re_k, a shedding of periodic hairpin vortices. The hairpin vortices are released from the roof of the roughness element. The legs of each vortex consist of two counterrotating streamwise vortices, which lift low-momentum fluid in the region between them and push high-momentum fluid towards the wall on the sides. The vortices are therefore acting so as to increase the defect velocity induced in the wake.

Nevertheless, the low level of the streamwise velocity fluctuations and the absence of any peak in the power spectra show that this phenomenon is not present in the current experiment. It may be speculated that this absence can be related to the lack of the curvature in the outer irrotational flow field, due to the geometry of the element, which is the condition for the vortex lines to concentrate forming the hairpin vortices.

It can be concluded that there is a competition between the perturbation induced by the vortex generated by the incoming vorticity upstream of the element and the wake downstream of it. In the present experiment the former mechanism is dominating and a high-speed region is located in correspondance

with the roughness element. This can be inferred from figure 3 (see also the sketch in figure 14): a region of defect velocity (wake) is induced just behind the elements, $z = 0$ and 8 mm and $x = 55$ mm.

The streamwise legs of the standing vortex cannot be seen from the streamwise velocity contour plot but their effect seems evident further downstream. The two vortices push high-momentum fluid from the upper part of the boundary layer towards the wall in the region behind the roughness elements, so that the region of defect velocity present at $x = 55$ mm is first annihilated and then replaced by the high-speed streak ($x = 70$ and 100 mm). The two vortices lift up low-momentum fluid on their sides; they start to interact with the vortices induced by the neighbouring cylinders already at $x = 100$ mm so as to induce a low-speed region centred at $z = -4$ and 4 mm, see plot at $x = 200$ mm in figure 3 where well-formed streaks are shown.

Conversely, in the experiments by Kendall (1990), Gaster *et al.* (1994) and White (2002), any given element generates a wake associated with a counterrotating vortex pair (the legs of the horseshoe vortex released when the flow is started) which decay downstream. In these cases, the steamwise vorticity of the vortex forming upstream of the obstacle are not able to overcome the defect velocity of the wake.

The studies mentioned above are all characterised by different configurations, both in terms of the shape of the roughness elements, the ratio between their spanwise width to their heigth and the local Reynolds number. However, a close examination seems to indicate that the ratio k/δ is the most relevant parameter: the wake mechanism is seen to be the most relevant for low values of k/δ, while the standing vortex is dominating for larger values of k/δ. Note also that if the latter mechanism is dominating streaks of higher amplitude are induced. In Kendall (1990) $k/\delta = 0.45$, while in White (2002) $k/\delta = 0.59$ and 0.72. In the present experiment k/δ is larger than 2 as in the work of Bakchinov *et al.* (1995). Note however that an excess velocity behind the element is also observed by Kendall (1990) in the far wake. As a consequence, one can conjecture that for relatively high elements the standing vortex is strong enough to more than balance the effect of the wake and a high-speed streak is found behind the element. In the case of lower values of k/δ, the wake of the roughness element is the dominating perturbation in the flow. The effect of the streamwise vortices generated upstream of the obstacles seems to be relevant much farther downstream and it was only detected by Kendall (1990). This is just an hypothesis which needs to be confirmed by future investigations.

6. Summary and concluding remarks

Steady, spanwise periodic streamwise streaks have been experimentally generated in a flat plate boundary layer using a spanwise array of small roughness elements of cylindrical section. All the streaks growth curves are found to collapse

when rescaled on the maximum streak amplitude and on the streamwise position where this maximum is attained. The experimentally generated streaks are hence found to satisfy the similarity property valid for perturbations satisfying the boundary layer approximation. It has however been observed, as in White (2002), that discrepancies exist between the streaks induced by the roughness elements array and the optimal streaks, in particular in the streamwise and wall normal position of the maximum streak amplitude. The same differences are observed for the large amplitude streak generated in present work. By comparing experimental data and numerical simulations, we found that these discrepancies can be mostly attributed to the fact that the streamwise vortices generated by the roughness elements are more confined into the boundary layer than the theoretically predicted optimal vortices. By considering sub-optimal vortices, theoretical predictions and experimental streak amplitude curves are seen to agree. In view of applications in the boundary layer transition delay, as recently suggested in Cossu & Brandt (2002), it has also been shown that it is possible to experimentally generate streaks of moderate amplitude, larger than those considered in White (2002), which are still stable to inflectional secondary instability.

Acknowledgments

We wish to thank Profs. Henrik Alfredsson and Dan Henningson for the helpful discussions and suggestions and Mr. Marcus Gällstedt for his assistance in the roughness elements manufacturing. C.C. acknowledges financial support from CNRS during his stay at KTH. The financial support of the Swedish Research Council (VR) is also acknowledged.

References

Acarlar, M. S. & Smith, C. R. 1987 A study of hairpin vortices in a laminar boundary layer. Part 1. Hairpin vortices generated by a hemisphere protuberance. *J. Fluid Mech.* **175**, 1–41.

Andersson, P., Berggren, M. & Henningson, D. S. 1999 Optimal disturbances and bypass transition in boundary layers. *Phys. Fluids* **11**, 134–150.

Andersson, P., Brandt, L., Bottaro, A. & Henningson, D. S. 2001 On the breakdown of boundary layers streaks. *J. Fluid Mech.* **428**, 29–60.

Arnal, D. & Juillen, J. C. 1978 Contribution expérimentale à l'étude de la reptivité d'une couche limite laminaire à la turbulence de l'écoulement général. Rapport Technique 1/5018. ONERA.

Asai, M., Minagawa, M. & Nishioka, M. 2002 The instability and breakdown of a near-wall low-speed streak. *J. Fluid Mech.* **455**, 289–314.

Bakchinov, A. A., Grek, G. R., klingmann, B. G. B. & Kozlov, V. V. 1995 Transition experiments in a boundary layer with embedded streamwise vortices. *Phys. Fluids* **7**, 820–832.

Brandt, L., Cossu, C., Chomaz, J.-M., Huerre, P. & Henningson, D. S. 2003 On the convectively unstable nature of optimal streaks in boundary layers. *J. Fluid Mech.* **485**, 221–242.

Cossu, C. & Brandt, L. 2002 Stabilization of Tollmien-Schlichting waves by finite amplitude optimal streaks in the Blasius boundary layer. *Phys. Fluids* **14**, L57–L60.

Cossu, C. & Brandt, L. 2003 On Tollmien-Schlichting waves in streaky boundary layers. *Eur. J. Mech./B Fluids* Submitted.

Dryden, H. L. 1937 Air ow in the boundary layer near plate. Report 562. NACA.

Fransson, J. M. H. & Alfredsson, P. H. 2003 On the disturbance growth in an asymptotic suction boundary layers. *J. Fluid Mech.* **482**, 51–90.

Gaster, M., Grosch, C. E. & Jackson, T. L. 1994 The velocity field created by a shallow bump in a boundary layer. *Phys. Fluids* **6**, 3079–3085.

Grosch, C. E. & Salwen, H. 1978 The continuous spectrum of the Orr-Sommerfeld equation. Part 1.The spectrum and the eigenfunctions. *J. Fluid Mech.* **87**, 33–54.

Gustavsson, L. H. 1991 Energy growth of three-dimenisonal disturbances in plane Poiseuille flow. *J. Fluid Mech.* **224**, 241–260.

Herbert, T. 1988 Secondary instability of boundary-layers. *Annu. Rev. Fluid Mech.* **20**, 487–526.

Hunt, J. C. R., Abell, C. J., Peterka, J. A. & Woo, H. 1978 Kinematical studies of the flows around free or surface-mounted obstacles; applying topology to flow visualization. *J. Fluid Mech.* **86**, 179–200.

Johansson, A. V. & Alfredsson, P. H. 1982 On the structure of turbulent channel flow. *J. Fluid Mech.* **122**, 295–314.

Joslin, R. D. & Grosch, C. E. 1995 Growth characteristics downstream of a shallow bump: Computation and experiment. *Phys. Fluids* **7**, 3042–3047.

Kachanov, Y. S. & Tararykin, O. I. 1987 Experimental investigation of a relaxating boundary layer. *Izv. SO AN SSSR, Ser. Tech. Nauk* **18**.

Kendall, J. M. 1985*a* Experimental study of disturbances produced in a pretransitional laminar boundary layer by weak free-stream turbulence. *AIAA Paper* 85-1695.

Kendall, J. M. 1990 The effect of small-scale roughness on the mean flow profile of a laminar boundary layer. In *Instability and transition* (ed. Hussaini & Voigt), pp. 296–302.

Klebanoff, P. S. 1971 Effect of free-stream turbulence on the laminar boundary layer. *Bull. Am. Phys. Soc.* **10**, 1323.

Klebanoff, P. S., Cleveland, W. G. & Tidstrom, K. D. 1992 On the evolution of a turbulent boundary layer induced by a three-dimensional roughness element. *J. Fluid Mech.* **237**, 101–187.

Klebanoff, P. S., K.D.Tidstrom & Sargent, L. 1962 The three-dimensional nature of boundary layer instability. *J. Fluid Mech.* **12**, 1–34.

Klingmann, B. G. B., Boiko, A., Westin, K. J. A., Kozlov, V. V. & Alfredsson, P. H. 1993 Experiments on the stability of Tollmien-Schlichting waves. *Eur. J. Mech.* B*/Fluids* **12**, 493–514.

Komoda, H. 1967 Nonlinear development of disturbance in a laminar boundary layer. *Phys. Fluids Suppl.* **10**, S87.

Landahl, M. T. 1980 A note on an algebraic instability of inviscid parallel shear flows. *J. Fluid Mech.* **98**, 243–251.

Levin, O. & Henningson, D. S. 2003 Exponential vs algebraic growth and transition prediction in boundary layer flow. *Flow, Turbulence and combustion* (In press).

Lindgren, B. & Johansson, A. V. 2002 Evaluation of the flow quality in the mtl wind-tunnel. Technical Report KTH/MEK/TR–02/13–SE. KTH, Department of Mechanics, Stockholm.

Luchini, P. 2000 Reynolds-number independent instability of the boundary layer over a flat surface. Part 2: Optimal perturbations. *J. Fluid Mech.* **404**, 289–309.

Matsubara, M. & Alfredsson, P. H. 2001 Disturbance growth in boundary layers subjected to free stream turbulence. *J. Fluid. Mech.* **430**, 149–168.

Schlichting, H. 1979 *Boundary-Layer Theory*. McGraw-Hill, New York.

Schmid, P. J. & Henningson, D. S. 2001 *Stability and Transition in Shear Flows*. Springer, New York.

Tani, I. 1969 Boundary layer transition. *Annu. Rev. Fluid Mech.* **1**, 169–196.

Tani, I. & Komoda, H. 1962 Boundary layer transition in the presence of streamwise vortices. *J. Aerospace Sci.* **29**, 440.

Taylor, G. I. 1939 Some recent developments in the study of turbulence. In *Proc. 5th Intl. Congr. Appl. Mech.* (ed. J. Hartog & H.Peters), pp. 294–310. Wiley.

Trefethen, L. N., Trefethen, A. E., Reddy, S. C. & Driscoll, T. A. 1993 Hydrodynamic stability without eigenvalues. *Science* **261**, 578–584.

White, E. B. 2002 Transient growth of stationary disturbances in a flat plate boundary layer. *Phys. Fluids* **14**, 4429–4439.

White, E. B. & Ergin, F. G. 2003 Receptivity and transient growth of roughness-induced disturbances. *AIAA Paper* 03-4243.

Paper 7

7

Flow around a porous cylinder subject to continuous suction or blowing

By J. H. M. Fransson†, P. Konieczny‡ and P. H. Alfredsson†

† KTH Mechanics, SE-100 44 Stockholm, Sweden
‡ Institut de Mécanique des Fluides de Toulouse, Allée du Pr. Camille Soula, F-31400 Toulouse, France

Submitted for publication.

In the present experimental investigation the surface pressure distribution, vortex shedding frequency, and the wake flow behind a porous circular cylinder are studied when continuous suction or blowing is applied through the cylinder walls. It is found that even moderate levels of suction/blowing ($\lesssim 5\%$ of the oncoming streamwise velocity) have a large impact on the flow around the cylinder. Suction delays separation contributing to a narrower wake width, and a corresponding reduction of drag, whereas blowing shows the opposite behaviour. Both uniform suction and blowing display unexpected flow features which are analysed in detail. Suction has a persisting stabilizing influence on the turbulence intensity in the wake whilst blowing only shows an effect up to five diameters downstream of the cylinder. The drag on the cylinder is shown to increase linearly with the blowing rate, whereas for suction there is a drastic decrease at a specific suction rate. This is shown to be an effect of the separation point moving towards the rear part of the cylinder, similar to what happens when transition to turbulence occurs in the boundary layer on a solid cylinder. The suction/blowing rate can empirically be represented by an effective Reynolds number for the solid cylinder, and an analytical expression for this Reynolds number representation is proposed and verified.

Flow visualizations expose the complexity of the flow field in the near wake of the cylinder, and image averaging enables the retrieval of quantitative information, such as the vortex formation length.

1. Introduction

The phenomenon of vortex shedding from bluff bodies still remains a challenging and interesting problem. The canonical configuration of the motion of a fluid past a circular cylinder is still of relevance to a large number of flows found in industrial applications (the flow past moving vehicles, pylons of bridges, buildings, etc.), as well as in natural settings. Recently, interest has

focussed on the ability to manipulate the wake of a bluff body to reduce drag, increase heat transfer or mixing, and enhance combustion.

There is an aboundance of studies in the literature on the flow past a circular cylinder, starting with Strouhal (1878) and von Karman (1912). A complete overview of the field will not be attempted here; for the interested reader there are several recent reviews available, e.g. Williamson (1996), Buresti (1998) and Norberg (2003), as well as a comprehensive two volume monograph published recently Zdravkovich (1997, 2003).

The characteristics of the flow around a cylinder depends strongly on the cylinder Reynolds number ($Re = U_\infty D/\nu$, where U_∞ is the free stream velocity, D is the cylinder diameter and ν the fluid kinematic viscosity). For low Reynolds numbers ($4 \lesssim Re \lesssim 47$) a pair of counter-rotating vortices is formed behind the cylinder, and for $Re \gtrsim 47$ these become unstable and the region up to $Re \approx 200$ is usually called the laminar periodic regime. For slightly higher Re the wake becomes unstable and irregular. Roshko (1961) provided a definition of different flow regimes based on measurements of velocity fluctuations and spectra for $Re > 1000$. These regimes can be identified depending on the behaviour of the boundary layer on the cylinder and are called: subcritical (purely laminar separation), precritical (laminar separation followed by turbulent asymmetric reattachment, $Re = 1.5 \times 10^5$ to 3.8×10^5), supercritical (symmetric reattachment, transition and turbulent separation, $Re = 3.8 \times 10^5$ to 3×10^6) and postcritical.

In the present study we focus on Reynolds numbers of the order of 10^4, which is in the subcritical regime (also known as the shear-layer transition regime). In these conditions the boundary layers on the cylinder are still laminar, they separate from the body and instabilities develop. Many studies have been focusing on the subcritical range, e.g. a compilation of more than 70 references can be found in Cantwell & Coles (1983). Although a cylinder mounted perpendicular to the free stream may seem as a simple generic case, the exact flow behaviour may still be influenced by various flow and geometry factors, for instance the turbulence level of the free stream, the surface roughness of the cylinder, the blockage ratio as well as the aspect ratio of the cylinder. For low Reynolds numbers, very large aspect ratios are needed to have results that are independent of it. For flows in the subcritical range there is less influence (see Norberg 1994).

1.1. *Control of vortex shedding*

It is of great interest for technical applications to be able to control the vortex shedding from a body, as well as its wake. At low Reynolds numbers (< 300) several techniques have been shown to have a potential to suppress vortex shedding or shift the shedding frequency. One such method is to oscillate the cylinder in rotary motion Berger (1967) at a suitable frequency and amplitude.

Another is to heat the cylinder Wang *et al.* (2000) thereby changing the viscosity close to the cylinder surface, giving rise to a change in the effective Reynolds number. A different approach is to use feedback control, as demonstrated in both experiments and numerical simulations by Roussopoulos (1993) and Park *et al.* (1994), respectively. In the experiments the actuation was acoustically induced through a loudspeaker (in a wind tunnel) as well as by vibrating the cylinder (in a water channel), whereas in the numerical study blowing and suction slots on the rear part of the cylinder were utilized. No blowing and suction experiments exist for this Reynolds number range (< 300) since the size of the cylinder for typical velocities in air or water would be very small and it would not be possible to implement such a device at this scale.

For higher Reynolds number flows (larger cylinders) a possible form of (passive) control consists in modifying the geometry in order to affect the vortex shedding. Experiments along this line for flow past a circular cylinder were reported by Roshko (1955, 1961); he simply placed a splitter plate on the centreline behind the cylinder. With a proper length of the splitter plate the flow behaviour can change from the alternating shedding mode to a symmetrical mode, with two closed recirculation regions on each side of the plate.

In the subcritical range of interest in this study, Tokumaru & Dimotakis (1991) carried out experiments on circular cylinders executing forced rotary oscillations. They managed to obtain a significant drag reduction of up to 80% at $Re = 15000$ for certain ranges of frequency and amplitude of the sinusoidal rotary oscillation. Computational results Shiels & Leonard (2001) have verified these experimental observations and there are indications that this kind of control could be even more efficient at higher Reynolds number.

1.2. *Porous cylinders with suction or blowing*

Other studies have considered a flow manipulation consisting in the application of suction or blowing. Early experiments on porous cylinder made of sintered bronze were carried out by Pankhurst & Thwaites (1950). They made experiments with continuous suction, but also combined suction with a flap in the form of a short splitter plate placed at various angles. At an angle of 180°, i.e. along the downstream symmetry line, and for sufficient suction, the separation is entirely prevented and a remarkably close approximation to the potential flow solution is achieved, as attested by the pressure distribution and by mean flow velocity profiles of the wake. They concluded from their experiments that values of $C_q\sqrt{Re}$ larger than ≈ 10 were needed to avoid separation[1]. They also reported values of the drag coefficient but did not do any time resolved measurements to determine the vortex shedding frequency. Boundary layer measurements on the same porous cylinder were performed by Hurley & Thwaites

[1]Here C_q is a suction coefficient defined as the suction velocity per unit area divided by the free stream velocity.

(1951) and in general good agreement was found with laminar boundary layer theory.

Continuous blowing on the whole surface has also been studied experimentally by Mathelin *et al.* (2001*a*,*b*). The cylinder in these experiments is 16.2 mm in outer diameter and is made of sintered-stainless-steel, with 30% of porosity and 30 μm average pore diameter (see Mathelin *et al.* 2001*a*, for the detailed description of the set-up). Among the effects observed, we note the presence of a wider wake and a decrease of the Strouhal number. The decrease in Strouhal number is linear with the injection rate until saturation occurs. For a 5% injection at $Re = 3900$ the reduction is for example 25%. Taking into account this reduction of the vortex shedding frequency, and the Strouhal-Reynolds curve for low Reynolds number (between 50 and 300), the flow submitted to blowing would have the same characteristics in terms of instability as a flow at a lower Reynolds number, and an analytical relation was determined to provide the equivalent Reynolds number of the canonical case which produces the same behaviour as the case with blowing.

A different type of blowing can be achieved through the use of synthetic jets, which provide a localized addition of momentum normal to the surface. Glezer & Amitay (2002) show that synthetic jets on selected positions over the cylinder can give a delay of separation for different Reynolds number (i.e. both for a turbulent and a laminar boundary layer). They argued that this delay was caused by increased mixing within the boundary layer. In addition, the interaction between the jet and the cross flow has a profound effect both on the separated shear layer and on the wake; the magnitude of the Reynolds stresses is reduced indicating that the delay in separation is not merely the result of a transition to turbulence in the boundary layer.

1.3. *Present study*

The objectives of our study is, partly, to complement the investigations just cited by considering both the effect of uniform suction and blowing, on a very smooth, porous cylinder. We will document the changes of the flow in the subcritical regime, in terms of mean and fluctuating velocity profiles in the wake through hot-wire anemometry, pressure distributions and vortex shedding for different blowing and suction rates. Smoke visualizations of the flow complement the study providing a clear picture of the flow behaviour under parametric variations. Attention to the effects of free stream turbulence will also be paid, and comparison will be made with the known results of the canonical case for which the behavior of the critical transition thresholds with free-stream turbulence is known (see e.g. Kiya *et al.* 1982).

Finally, it is shown here that the suction/blowing rate can empirically be represented by an effective Reynolds number for the solid cylinder, and an

analytical expression for this Reynolds number representation is proposed and verified.

2. Experimental set-ups and flow visualization technique

Most of the experiments were performed in the $S4$–wind tunnel at IMFT in Toulouse, which is a low speed closed circuit tunnel. It is provided with a three-dimensional traversing mechanism and allows automatized computer controlled measuring and traversing in one direction (y) with an accuracy of 1/80 mm. The background streamwise disturbance level without filtering amounts to 0.5% and 0.1% at a free stream velocity of 2.5 and 25 m/s, respectively. The dimension of the test-section is 1800 × 700 × 600 mm (length(L) × height(H) × width(W)). Measurements were made with hot-wire anemometry using a single wire Dantec probe, with 5 μm and 1.25 mm in wire diameter and prong separation, respectively. The calibration was done against a Pitot tube using the standard King's law and was carried out on the centreline, 400 mm upstream of the cylinder. The diameter (D), wall thickness (t) and the porous length of the cylinder were 50, 2.5 and 600 mm, respectively.

The end parts of the cylinder are made of brass with four inlets for tube connections. The four tubes from the inlets are then confluenced before connection to a flow meter (rotameter type), which in turn is connected to a pressure source (vacuum cleaner or high pressure air depending on whether suction or

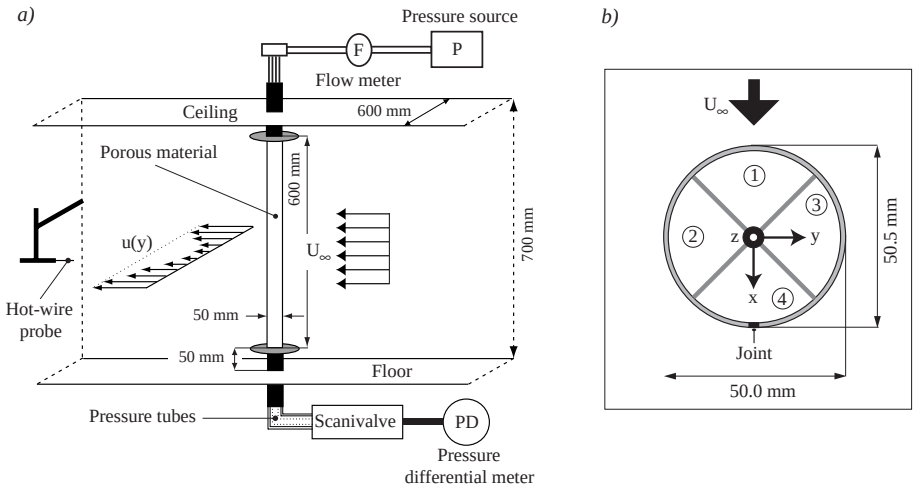

FIGURE 1. a) Experimental set-up of the porous cylinder, and b) the interior of the cylinder with four separate pressure chambers.

blowing is required). The cylinder is mounted vertically in the test-section with end plates located at a distance $\Delta = 50$ mm from the ceiling and floor. This is done to minimize three dimensional end effects that are created from the boundary layers developing on ceiling and floor (cf. Szepessy & Bearman 1992, for a thorough investigation of the effect of end plates); see figure 1a) for the experimental set-up. The blockage and aspect ratios of this set-up are 0.083 ($= D/W$) and 12 ($= (H - 2\Delta)/D$), respectively.

The inside of the cylinder consists of four isolated chambers, as shown in figure 1b), in order to achieve varying suction rates through different portions of the cylinder, in view of future planned experiments. Furthermore, the co-ordinate system of the present investigation is defined in this figure. There are 16 surface pressure taps (inner diameter 0.5 mm) positioned around the cylinder, which are shifted along the length of the cylinder forming a spiralling pattern in order to minimize mutual interference. The pressure holes can be moved relative to the oncoming flow by rotating the cylinder, and the pressure tubings are connected to a Scanivalve to facilitate the measurements.

Some of the experiments were also made with a turbulence generating grid placed at the inlet of the test section. The grid has a mesh width of 25 mm and the bars are of rectangular cross section with a width and a thickness of 4 and 3 mm, respectively.

2.1. *Characteristics of the porous material*

The porous cylinder is made of a sintered plastic material with an average pore size of 16 μm. Previous surface roughness measurements on a similar but flat porous plate Fransson & Alfredsson (2003) show a deviation of ± 1 μm from the mean surface. For the present case the surface can be considered to be hydraulically smooth. The cylinder is made from a flat plate which is bent to form a circular cylinder. This means that there is a joint in the axial direction along the whole cylinder, and this gives rise to a small asymmetry with a 0.5 mm larger diameter in average when measured over the joint, see figure 1b). The joint is therefore in most cases positioned 180° away from the oncoming flow in order to avoid any flow asymmetry.

To determine the permeability of the material the pressure difference (ΔP) over the cylinder wall and the flow rate ($Q = V \times S$, where V and S are the velocity through the porous material and the surface area, respectively) are measured, when suction is applied. Through Darcy's law the permeability (k) is then determined to be $k = \mu t V/\Delta P = 2.31 \times 10^{-7}$ m^2, by best line fitting to the data (μ is the dynamic viscosity).

2.2. *Flow visualization technique*

The flow visualizations were carried out in the *BL*–wind tunnel at KTH in Stockholm. For all technical information about this wind tunnel the interested reader is referred to Lindgren & Johansson (2002).

For the flow visualizations the same cylinder setup was used as for the hot-wire and pressure measurements (with a new porous cylinder section because of transport damages from France to Sweden, and without end plates to avoid camera view reduction) and in figure 2 the flow visualization setup is shown. A horizontal smoke sheet was created by injecting smoke through a slot in a wing-profile, which was located over the whole spanwise distance in the stagnation chamber of the wind tunnel. The profile has two tubing inlets, one on each side close to the walls. The smoke was generated by heating a glycol based liquid with a disco smoke generator, JEM ZR20 Mk II, and forced by a small fan through the tubing into the profile enabling a steady leakage of smoke through the slot.

The light source was a continuous Ar–ion laser, LEXEL 95–4, which gave the high light intensity needed for the short camera shutter times. The laser beam (1.5 W) was aligned through a cylinder lens creating a light sheet intersecting with the smoke sheet from the side (perpendicular to the flow field and the test section). The collection of flow visualization images was taken with a digital video camera, SONY TRV900 576×720 pixels, with a shutter time of 2 ms and with a rate of 20 images per second.

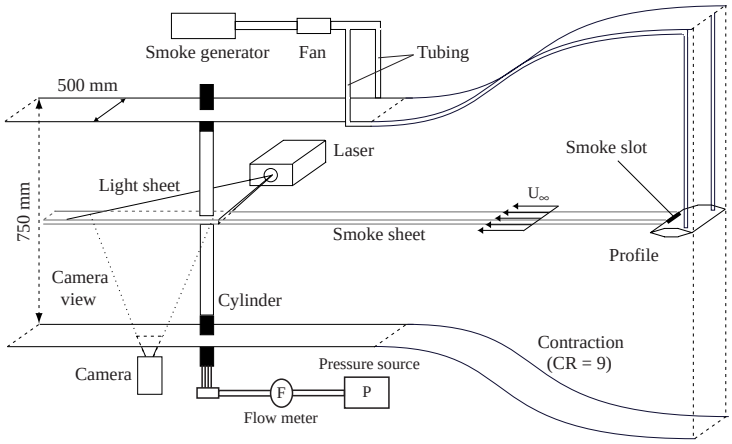

FIGURE 2. Flow visualization set-up of the porous cylinder.

3. Measurement results

In the present work the cylinder Reynolds number ($Re = U_\infty D/\nu$) is kept constant at $Re = 8300$ unless otherwise stated, whereas the suction and blowing rates are varied. This rate is expressed through the parameter $\Gamma = (V/U_\infty) \times 100$, where V is the velocity through the porous material, negative for suction and positive for blowing, and U_∞ is the oncoming streamwise velocity. At $Re = 8300$ the oncoming mean flow velocity is $U_\infty = 2.5$ m/s and the range of Γ investigated in this section is $-4 < \Gamma < +6$. The Reynolds number would, for the case of a solid cylinder, produce a laminar boundary layer and separation with a turbulent wake.

3.1. *Suction and blowing distributions*

The surface pressure distribution varies around the circumference of the cylinder when exposed to an oncoming flow, and this gives a non-uniform suction/blowing if the pressure inside the cylinder is constant. This is the case when the chambers are connected to a single tube through which suction/blowing is performed. A possible remedy to obtain uniform velocity at the surface is to divide the inner part of the cylinder into a large number of chambers that are individually regulated; this, however, would be an unpractical solution. In the present experiments the four chambers are connected to the same tubing, and hence have the same pressure. For the suction case the largest suction velocity occurs along the front stagnation line and then it decreases towards the rear. In the separated region the suction velocity is fairly constant and for $\Gamma = -1.4$ the suction velocity is about 6% smaller in this region as compared to the front. For larger suction rates the difference becomes smaller. In contrast, for the blowing case the smallest blowing velocity is along the frontal stagnation line and then increases and becomes constant from about 65° and downwards. In this case the maximum variation is less than 6% and the variation decreases with increasing Γ.

3.2. *Effect of suction/blowing on the pressure distribution*

Simply by analyzing the change of the surface pressure distribution when the cylinder is subject to continuous blowing or suction, some important conclusions can be drawn.

In figure 3a) the effect of different Γ-values on the C_p-distribution is shown and compared with the potential flow solution (dash-dotted line). There are three major remarks that can be made; firstly, one can observe how $C_{p,min}$ is reduced down to a value close to -2 for $\Gamma = -2.6$ and tends to -1 for $\Gamma = +2.6$; secondly for suction the separation point (ϕ_s) moves towards larger angles ($\phi_s \approx 105^o$ for $\Gamma = -2.6$), and when blowing is applied, the flow is seen to separate at lower angles; thirdly the base pressure coefficient ($C_{p,B}$) is increased for the case of suction producing a significant increase in the adverse pressure

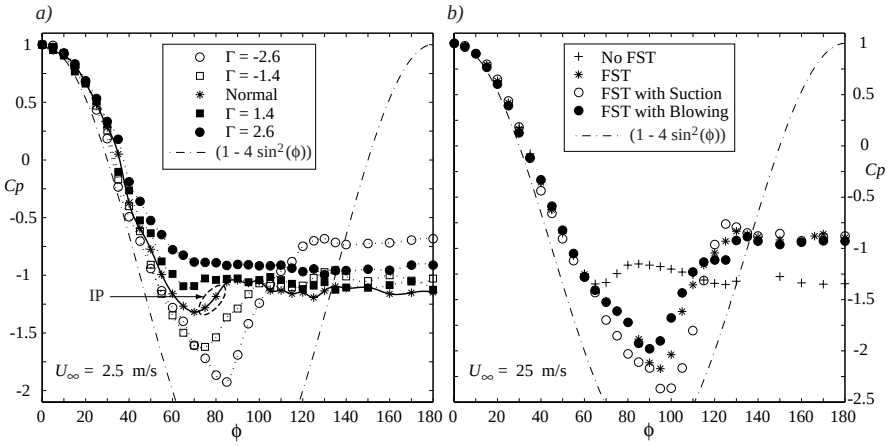

FIGURE 3. The pressure distribution around the cylinder is shown for different Γ-values. a) shows the effect of blowing/suction with a laminar oncoming flow ($U = 2.5$ m/s, $Re = 8300$, $Tu = 0.5\%$). b) shows the effect of free stream turbulence generated by a turbulence generating grid, the blowing/suction is $\Gamma = \pm 0.4$ ($U = 25$ m/s, $Re = 83000$, $Tu = 3\%$). Dash-dotted line is the potential flow solution.

recovery ($C_{p,B} - C_{p,min}$), whilst for the case of sufficiently large blowing rates, the recovery region is eliminated.

The inflection point in region IP on the C_p-curve, marked with a dashed ellipse in figure 3a), is often used to estimate the location of the separation point and this is the criterion employed in the preceding paragraph. Suction makes the boundary layer profile fuller and hence more resistant to separation, in analogy to high Reynolds number flow. At $Re \sim 10^5$ transition in the boundary layer occurs (the exact Re-value depends on the flow quality and the surface roughness) and the separation point moves from the front part of the cylinder to the rear part, due to the turbulent boundary layer that can make the flow adhere longer to the surface. In figure 3b) the free stream velocity is increased ten times and the C_p-distribution is compared with results when a turbulence intensity ($Tu = u_{rms}/U_\infty$) of 3% is present (causing transition in the boundary layer at subcritical Reynolds numbers); this was done by putting a turbulence generating grid at the inlet of the test-section. It is clearly seen, by comparing the ($\circ$)-symbols in figure 3a) with the ($*$)-symbols in b), that suction and high levels of free stream turbulence have the same impact on the C_p-distribution. Furthermore, in b), one can observe how a small blowing/suction rate ($\Gamma = \pm 0.4$) effects the location of $C_{p,min}$ and consequently the separation point, but not the base pressure coefficient.

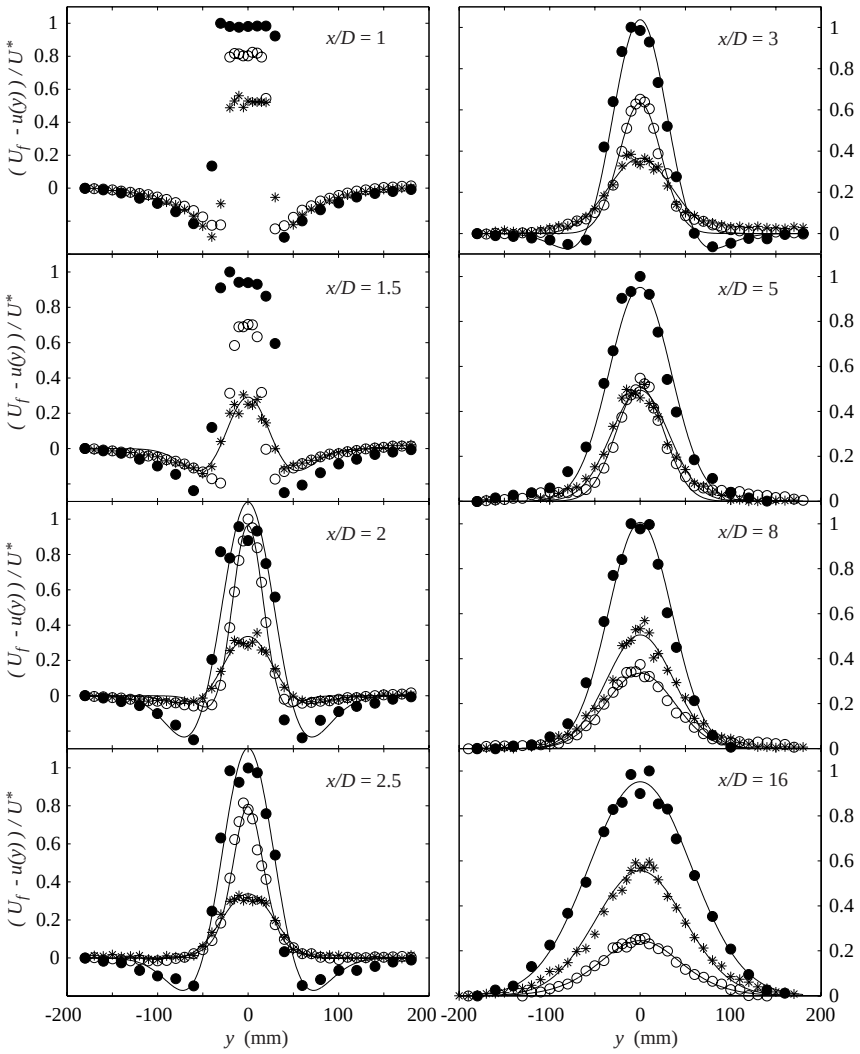

FIGURE 4. Mean velocity profiles at different positions behind the cylinder for the normal, the suction, and the blowing case. ($*$,$\circ$,$\bullet$) denotes Γ = (0,-2.6,+2.6). U_f is the mean velocity far from the cylinder in the y-direction and $U^* = \max(U_f - u(y))$ for all Γ at each x/D-position. The solid lines are curve fits to data.

3.3. *Effect of suction/blowing on the surrounding flow*

In figure 4 the mean velocity profiles for the normal case ($\Gamma = 0$), one suction case ($\Gamma = -2.6$), and one blowing case ($\Gamma = +2.6$) are plotted across the wake for different x/D-positions (see caption for symbols). Close to the cylinder (x/D small), one can observe the presence of negative values of the velocity (i.e. speeds higher than the free stream velocity). This is the effect of the shoulder acceleration around the cylinder, which for higher x/D-values is seen to disappear and the profiles approaches the Schlichting's far wake shape (see e.g. Zdravkovich 1997, chapt. 9.7). For the blowing case the shoulder acceleration is, however, quite persistent and may be observed down to $x/D = 3$.

When suction is applied, the velocity decreases close to the cylinder compared to the normal case, but farther away it actually becomes larger. This is due to the presence of low speed regions in the normal case, as shown in figure 5 for $\Gamma = 0$, where the contours represents the mean streamwise velocity normalized with U_∞. The dotted, dash-dotted, dashed, and solid contour lines correspond to $u/U_\infty = 0.8$, 0.9, 1.0, and 1.1, respectively. The gray regions correspond to $u_{rms}/U_{local} \geq 0.30$, which is a zone that has to be considered with caution since the hot-wire results may be significantly affected by large flow angles and even backflow. Note that some of the profiles in figure 4 also become affected. For successively decreasing Γ (increasing suction) the mean streamwise velocity behind the cylinder decreases at first, but at $\Gamma \approx -2.6$ there is a sudden change of trend and the velocity starts to increase. This can be observed in the contour plots of figure 5. The reason for a sudden change in the mean velocity component is the fact that suction affects the boundary layer around the cylinder and delays the separation as pointed out earlier. A

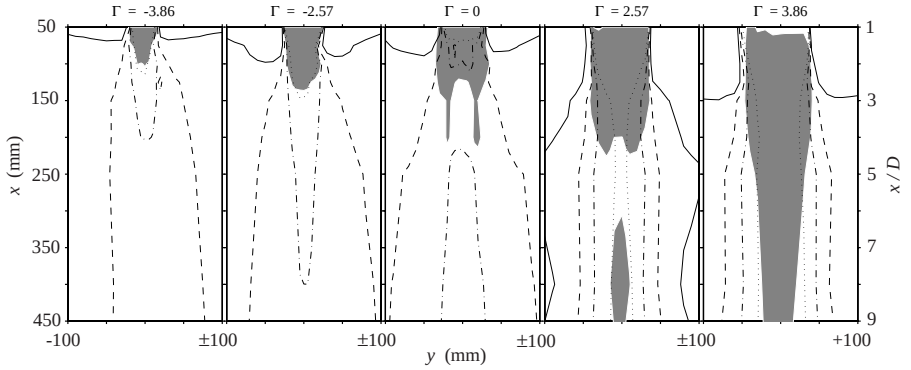

FIGURE 5. Contour plots of $u(x, y)/U_\infty$ in the xy-plane. Dotted, dash-dotted, dashed, and solid contour lines correspond to $u/U_\infty = 0.8$, 0.9, 1.0, and 1.1, respectively. Gray filled regions correspond to measured values of $u_{rms}/U_{local} \geq 0.30$.

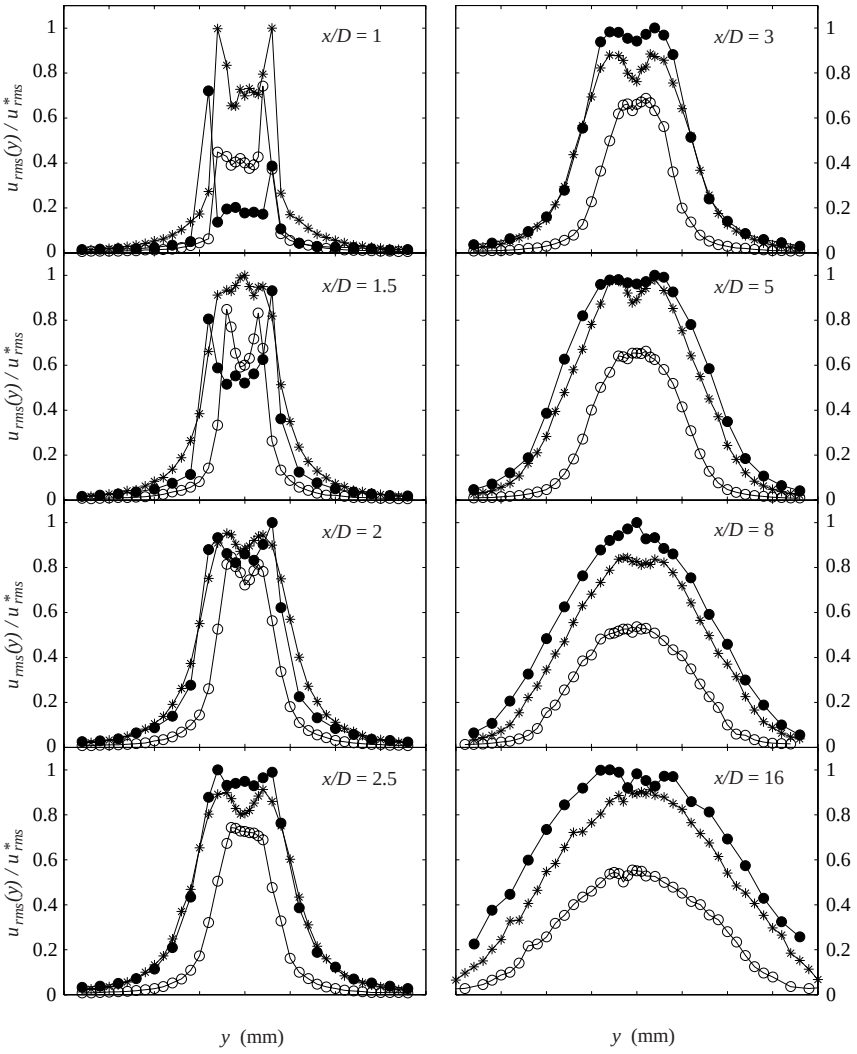

FIGURE 6. u_{rms}-profiles at different positions behind the cylinder for the normal, the suction, and the blowing case. ($*$,$\circ$,$\bullet$) denotes Γ = (0,-2.6,+2.6). u^*_{rms} is max(u_{rms}) for all Γ at each x/D-position.

possible explanation is that suction also stabilizes the wake and that less mixing occurs. With increasing suction the separation point on the cylinder is moved from the front to the rear part of the cylinder implying a decrease of the shoulder acceleration (see figure 5), a narrower wake, and thereby an increase

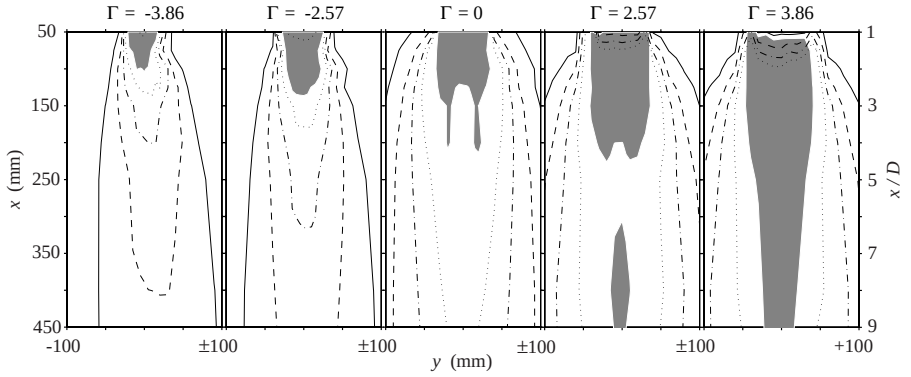

FIGURE 7. Shows contour plots of Tu in the xy-plane. Solid, dashed, dash-dotted, and dotted contour lines correspond to $Tu = u_{rms}/U_\infty = 0.02, 0.04, 0.06$, and 0.08, respectively. Gray filled regions correspond to $u_{rms}/U_{local} \geq 0.30$.

of the velocity in the wake. For very high suction rates the flow would stay attached to the cylinder giving rise to a potential-like solution, and hence the wake will be less pronounced. This hypothesis is corroborated by inspection of figure 3a).

Contrary to suction, blowing causes the flow to separate earlier, also observed in figure 3a). Despite the direct injection of air behind the cylinder the effect of the separation point is much larger and the mean velocity is reduced in the wake. Increasing blowing widens the wake and the shoulder acceleration is seen to amplify leaving low speed fluid close behind the cylinder as the wake grows. This can be observed in figure 5.

In figure 6 u_{rms}-profiles corresponding to the mean velocity profiles in figure 4 are shown, whereas figure 7 displays the contour plots of the turbulence intensity (Tu) for different values of Γ. Solid, dashed, dash-dotted, and dotted contour lines correspond to $Tu = u_{rms}/U_\infty = 0.02$, 0.04, 0.06, and 0.08, respectively. Gray filled regions are the same as in figure 5 ($u_{rms}/U_{local} \geq 0.30$), and the quantitative results in these regions should be viewed with caution. Note that some of the profiles in figure 6 also become affected. The Tu-level consistently decreases for increasing suction and it is possible to discern a more narrow wake. Furthermore, one can observe a strengthened formation of the two-peak disturbance distribution across the wake, which are seen to move towards the cylinder for increasing suction (see also figure 6).

In figure 8 the turbulence intensity Tu is plotted along the centreline (CL) behind the cylinder for different Γ. The low Tu-level close to the cylinder when blowing is applied is well illustrated in figure 8b) (as discussed in the last paragraph). It is clearly shown that blowing only effects the very near wake up

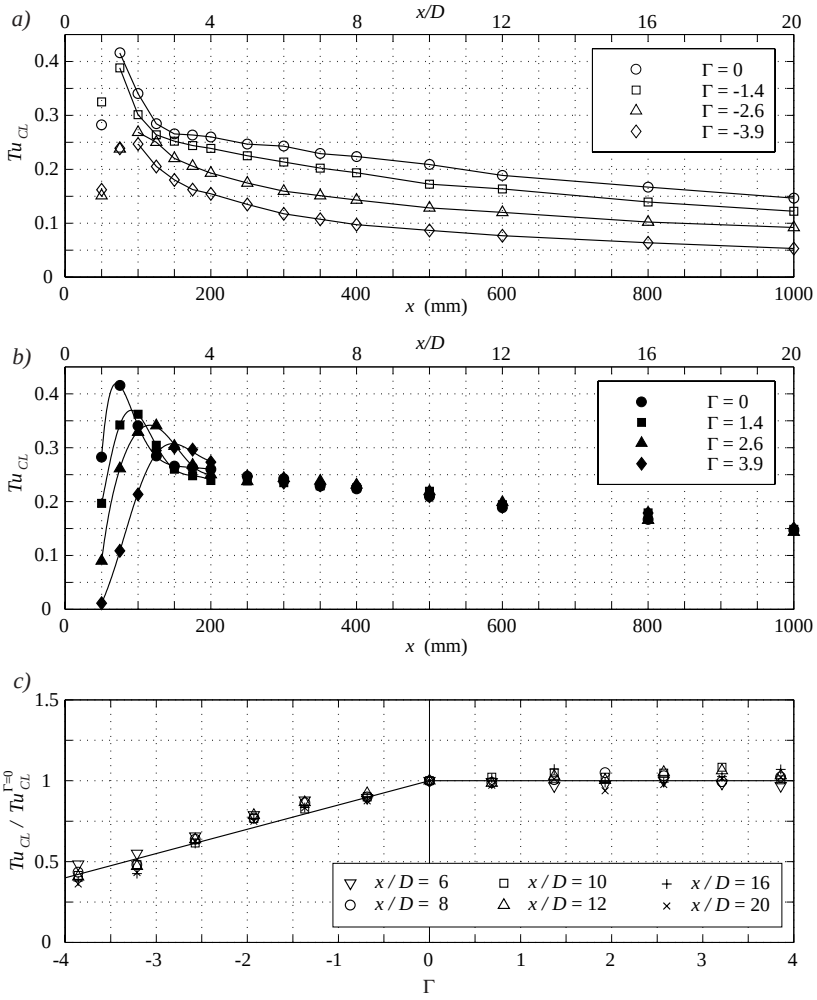

FIGURE 8. Tu_{CL}-distribution on the centreline (CL) behind the cylinder. a) and b) show the effect of increasing suction and blowing, respectively, inside the wake. c) shows how the suction decays with $Tu_{CL}^{\Gamma=0}$ and the independence of the blowing for $Tu_{CL}^{\Gamma=0}$.

to $x = 250$ mm ($5D$) (cf. figure 8b), whilst suction has a persisting stabilizing effect on the flow behind the cylinder (cf. figure 8a).

In figure 8c) some of the Tu_{CL}-data in figure 8a) and b) are used together with new data to show the independence of different x/D-positions on blowing/suction (Γ). The Tu_{CL}-data is normalized with $Tu_{CL}^{\Gamma=0}$ and decays linearly

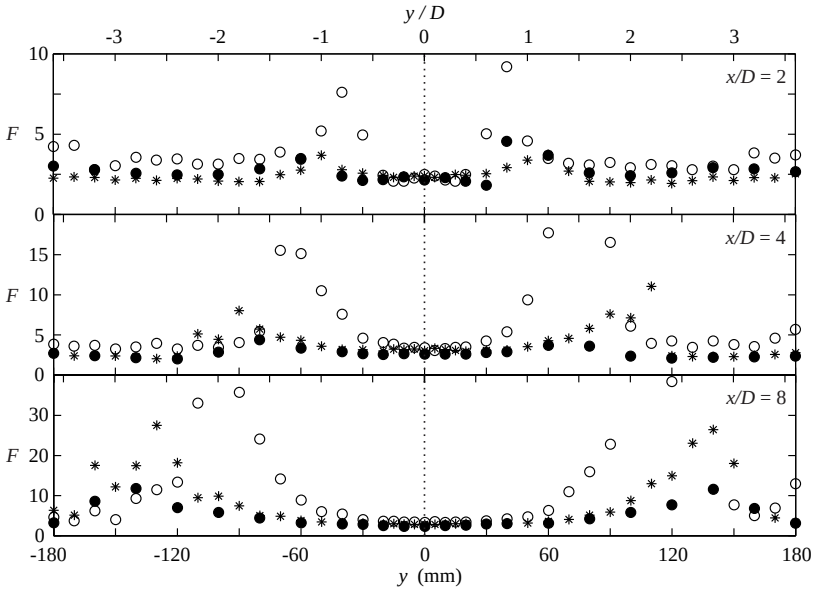

FIGURE 9. The flatness distribution across the wake is shown for different x/D-positions. The different symbols corresponds to the normal, the suction, and the blowing case. ($*$,$\circ$,$\bullet$) stand for Γ = (0,-2.6,+2.6), respectively.

with increasing suction for any fixed x/D-position, whereas the blowing has no effect from $x/D = 5$ and forward.

An additional way to illustrate the widening and narrowing of the wake is to look at the flatness ($F = \overline{(u - \overline{u})^4}/\overline{u^2}^2$) evolution, since one would expect high intermittency peaks at the wake edge (laminar/turbulent edge). In figure 9 the flatness is plotted for the three cases at different downstream positions. From this figure one can clearly see a trend of earlier departure of the F-values from the centre with suction, and a corresponding delay with blowing, compared to the normal case. The peak level difference between the three cases can be explained by an amplitude increase of the vortex shedding frequency when suction is applied and *vice versa* for the blowing case. The peak in F for the suction case is clearly seen to appear close to the centre, corresponding to a narrower wake. This narrowing and widening could also be observed directly from the profiles in figure 4 and from the contour plots in figure 6. The error in calculating the flatness due to rectification seems to be small. The questionable data in the profiles is found within $1.5D$ centred around the wake symmetry axis. The data corresponding to the normal and the suction cases at $x/D = 4$

and 8 are unaffected while the region width of possibly affected data decreases with x/D in the blowing case (cf. figure 5 or 7).

3.4. *Effect on the vortex shedding frequency*

Applying continuous blowing or suction can be interpreted as a decrease or increase, respectively, of an effective Reynolds number (related to an effective diameter), which is in contrast to intuition. This is demonstrated in the following section, where a function of an effective Reynolds number (Re_{eff}) vs the parameter Γ is derived and verified.

In figure 10a) several different collections of data of the Strouhal number ($St = f_K D/U_\infty$, where f_K is the von Karman vortex shedding frequency) are

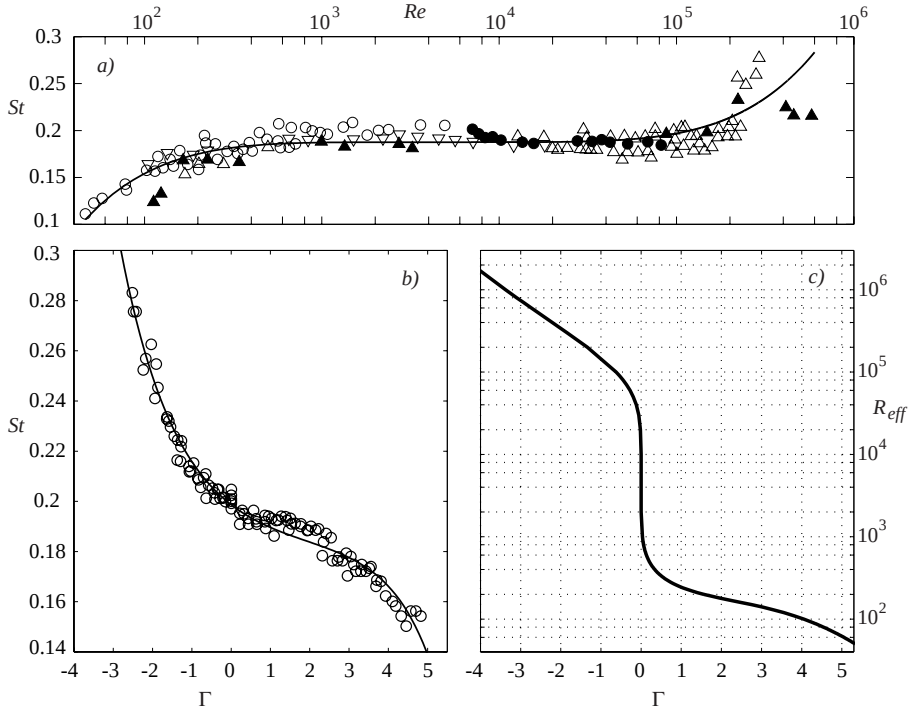

FIGURE 10. a) and b) shows the Strouhal number (St) effect on Reynolds number (Re) and blowing/suction (Γ), respectively. a) is data taken from: ($\bigtriangledown$) Strouhal, ($\bigtriangleup$) Relf, ($\circ$) Tyler, ($\blacktriangle$) Drescher, ($\bullet$) Etkin et al.; figure 13.9 in Zdravkovich (1997). b) present data (where both Re and V were varied). c) shows the effective Reynolds number (Re_{eff}) vs Γ (cf. equation 3).

shown vs the Reynolds number (see caption for reference). For the collection of those data the probe was positioned approximately one diameter downstream of the cylinder and outside the shear layer. If one assumes a constant value of St ($\lesssim 0.2$) in a wide range of Re one can fit an σ^{th} degree Re-curve (two terms) to the data according to:

$$St(Re) = m + n[\log_{10}(Re) + k]^{\sigma}. \tag{1}$$

Furthermore, in figure 10b) St is plotted vs Γ from the present measurements, where both Re and V are varied. The f_K is determined by selecting the frequency, where the distinct energy peak appears in the power spectrum. The more suction/blowing is applied, the more diffuse becomes this energy peak (which is in accordance with Re-dependent results both for high and low Re), however in figure 10b) only data where a distinct frequency can be detected are shown. From this figure it is seen that suction increases the St of about 50% for $\Gamma \approx -2.5$. In contrast to suction, blowing decreases the St with around 25% for $\Gamma \approx +5$ (in agreement with Mathelin *et al.* 2001*b*), i.e. the effect on the absolute change is smaller than for suction.

An analytical expression of $Re_{eff}(\Gamma)$ can be derived by making use of equation (1) and after assuming the following relation between St and Γ:

$$St(\Gamma) = d + \frac{\mathrm{e}^{a(\Gamma+e)} - \mathrm{e}^{b(\Gamma+e)}}{c}. \tag{2}$$

The curve fit in figure 10b) is done with equation (2). After simple manipulations of the equation $St(Re) = St(\Gamma)$ (equations (1) and (2)), the expression of $Re_{eff}(\Gamma)$ can be written as:

$$\begin{aligned}\log_{10}(Re_{eff}(\Gamma)) \quad = \quad & -k \pm \mathrm{abs}\Big\{\Big(\Delta S - m + d + \\ & + \frac{2}{c}\exp\Big[(\Gamma+e)\frac{(a+b)}{2}\Big]\sinh\Big[(\Gamma+e)\frac{(a-b)}{2}\Big]\Big)/n\Big\}^{1/\sigma}\end{aligned} \tag{3}$$

and is plotted in figure 10c). Here ΔS is the needed Strouhal shift for an equal value of the equations (1) and (2) with $Re \sim 10^3 - 10^4$ and $\Gamma = 0$, respectively. The (+)-sign in equation (3) is for $(\Delta S - m + St(\Gamma)) > 0$ and the (−)-sign for $(\Delta S - m + St(\Gamma)) < 0$. Note, that the relation between Re_{eff} and Γ described by equation (3) spans a large range of Reynolds numbers, i.e. from $Re \sim 10^2$ to $Re \sim 10^6$. In table 1 all the parameters used in the curve fits are given.

a	b	c	d	e	m	n	k	σ	ΔS
0.942	-0.691	290	0.182	-2.31	0.188	0.0024	-3.69	5	0.0111

TABLE 1. The parameter values in functions 1, 2 and 3.

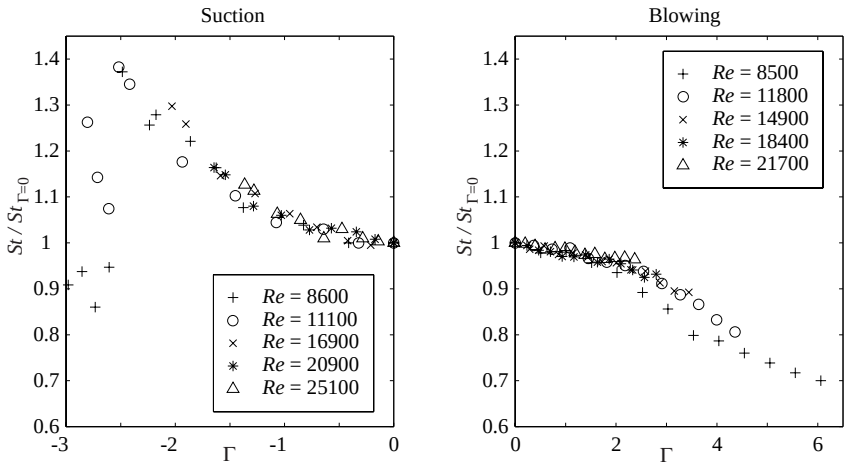

FIGURE 11. a) and b) shows the Strouhal number (St) effect on Reynolds number (Re) with blowing and suction, respectively.

In figure 10b) all Re are plotted together, however there is a small Re-dependence which can be illustrated by normalizing St with $St_{\Gamma=0}$, as done in figure 11a) and b) for the suction and blowing cases respectively. It can be observed that in the suction case the Re-dependence is quite weak, whereas it is somewhat stronger for the blowing case. For large suction the frequency peak of the vortex shedding in the power spectra is strongly reduced and is no longer a dominating frequency. The drop observed in figure 11a) is due to the fact that lower frequencies are detected with more energy content, and these are omitted in figure 10b). For moderate ($\Gamma \approx +5-6$) to large blowing and low Reynolds number ($Re = 8500$) it is possible to discern the beginning of the saturation level reported by Mathelin *et al.* (2001*b*), which is reached at $\Gamma \approx +10$. In the case of blowing the Re-dependence was first noted by Mathelin *et al.* (2001*b*), which in the present Γ-investigation is quite small and considered to have a negligible effect in the outcome of above effective-Reynolds-number analysis.

3.5. *Drag enhancement/reduction*

The momentum equation can be used to calculate the drag coefficient (C_D) from the velocity distribution across the far wake (i.e. for large values of x/D) according to:

$$C_D = \frac{2}{D}\int_{y_1}^{y_2} \frac{(U_f - u)u}{U_f^2} dy, \tag{4}$$

where $y_2 - y_1$ is the wake width. This was made for different Γ-values and the result is plotted in figure 12 with ($\circ$)-symbols. The use of the momentum formula, equation (4), to calculate the total drag can render significant errors if meausred to close to the cylinder. At $x/D \approx 30$ the positive contribution of the Reynolds normal stresses to the total drag becomes zero whereafter there is a small negative contribution (cf. Antonia & Rajagopalan 1990, for details). However, in all the present drag measurements the x/D-positions were beyond 15, which would in the case of $\Gamma = 0$ render an error that is smaller than 8% (see Antonia & Rajagopalan 1990). At $x/D = 20$ the error is less than 5%.

The shape of the drag distribution vs Γ may be compared with that obtained for different Reynolds numbers in the case of a solid cylinder, see e.g. Schlichting & Gersten (2000) (page 19 figure 1.12.) with experimental data from Wieselsberger. Now, by applying equation (3) interpolated data from Wieselsberger is mapped into figure 12 with ($\bullet$)-symbols. From the figure it is evident that the blowing/suction rate can be replaced with an effective Reynolds number through equation (3), and this relation is valid in a large range of Reynolds numbers (i.e. $Re \sim 10^2 - 10^6$). Due to a limited length of the wind tunnel there is a mismatch of the data, e.g. one would expect a collapse of the data for $\Gamma = 0$ and $Re \approx 8300$ which is not the case. The drag coefficient approaches a saturation level for increasing x/D, and in the present case (suction: $x/D = 20$; blowing: $x/D = 16$) one can observe that the saturation level is not yet reached. The two data-sets have an excellent qualitative agreement, only a shift (correction) of the absolute values is needed

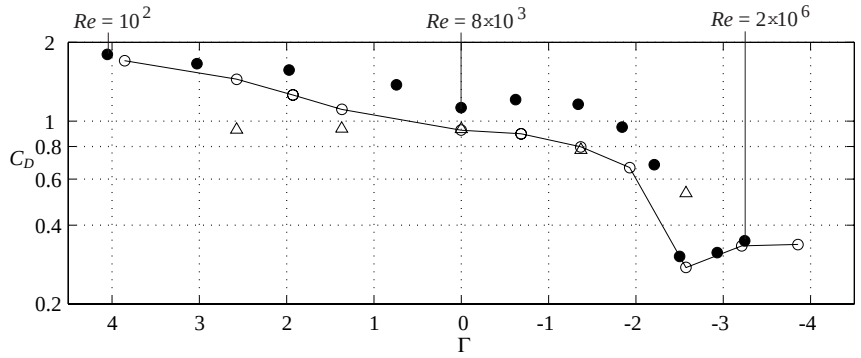

FIGURE 12. Shows the effect of C_D when blowing or suction is applied. ($\circ$)-symbols and ($\triangle$)-symbols are calculated using expression 4 and by direct integration of the pressure distribution in figure 3a), respectively. ($\bullet$)-symbols are data from *Wieselsberger* mapped through expression 3 using Re = [100 140 180 280 8000 10^5:10^5:10^6 2×10^6], which corresponds to the symbols from left to right (see text for reference).

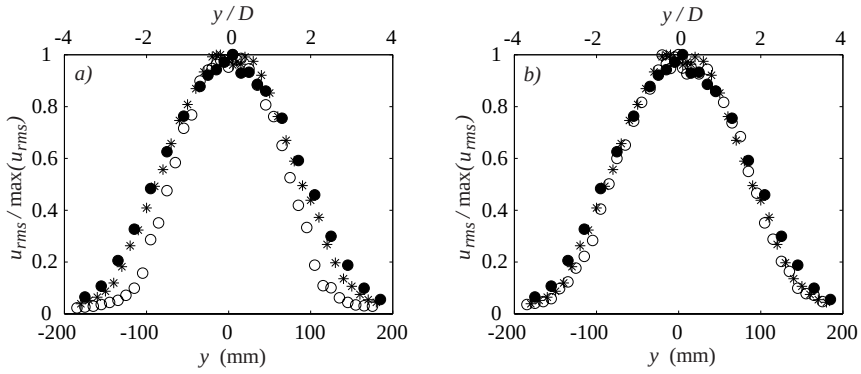

FIGURE 13. Shows that the u_{rms}-profiles scales with the effective diameter related to the effective Reynolds number. (∗,○,●) denotes Γ = (0,-2.6,+2.6). In a) $x/D = 8$ for all three cases, and in b) (∗,●) are shown at $x/D = 8$ and (○) at $x/D = 12$, respectively.

for total collapse. However, the absolute level drop of C_D at $\Gamma \approx -2.5$ seems to be the same, and one reason for this collapse could be the fact that the flow situation is different and a smaller x/D is needed to reach the saturation level of C_D. The drop is related to the shift of the separation point as described previously in connection with figure 3, which is also present for high Reynolds numbers ($Re \sim 10^5$) due to the laminar-turbulent boundary layer transition. Both the turbulent profile and the fuller laminar profile due to suction are more resistent to separation which is the actual cause for the shift. The drag coefficient was also calculated by direct integration of the pressure distribution (cf. figure 3a) and is plotted with (△)-symbols in figure 12. The agreement with the C_D-value calculated through equation (4) is good, which is expected, since the friction contribution to the total drag can be estimated from $C_{D,f} = 2/\sqrt{Re}$ (cf. Zdravkovich 1997, page 92) and becomes approximately 2% of the total drag at $Re = 8300$. Note that the difference becomes significant for lower Reynolds numbers (or positive values of Γ), which is in agreement with the above mentioned formula and the present results (see figure 12). However, the most common technique for drag measurements is to measure directly the force with a balance and this method takes all contributions into account, just as equation (4) does, if applied at $x/D = 30$.

In figure 13 the effective diameter (connected to the effective Reynolds number) is used to plot and compare the profiles at the same x/D_{eff}. For $x/D_{eff} = 8$ one achieves the x-positions 363, 400, and 569 mm for the blowing, the normal, and the suction case respectively. Figure 13b) shows the profiles at x = 400, 400, and 600 mm (which are close to the desired locations) for

the blowing, the normal and the suction case respectively, and it is clear from the figure that the appropriate profile scaling has been found. The difference is small in the mean velocity profile, which is the reason why the u_{rms}-profiles have been chosen to be displayed here.

4. Flow visualizations of the near wake

Flow visualization images were taken close behind the cylinder in the near wake. The Reynolds number was $Re = 3300$ (with $U_\infty = 1$ m/s) and the range of Γ investigated was $-5 < \Gamma < +5$ for these flow visualizations. In figure 14 instantaneous flow visualization images are shown for five different values of Γ, namely $0, \pm 2.6$ and ± 5.0. These images verify the previously presented measurement results, i.e. with suction the wake shrinks and with blowing it enlarges. In addition, they are able to provide size information of the small eddies formed in the very near wake, and the extent of the vortex formation length.

As the instantaneous images all are unique, it is not possible to draw any firm conclusion about the physical behaviour of the flow from inspection of one image. Therefore, 200 images were digitally averaged for each Γ studied (13 values), to be able to extract some quantitative information of the vortex formation length. A typical averaged image is shown in figure 15a). The settings (such as contrast and shading) of the averaged images were then all equally changed for a clearer image view. The asymmetry of the image is due to the cylinder shading the light coming from the left hand side in the figure. The same contour line (corresponding to a chosen value of the light intensity) of the averaged images was then analyzed, and in figure 15a) the result of the image averaging (and its contour line) of the $\Gamma = 0$ case is shown. In figure 15b) the contour lines for $\Gamma = +5, +3.9, +3.2, +2.6, \pm 1.4, \pm 1.9$, and 0 are plotted with alternately dash-dotted and solid lines for increasing $|\Gamma|$. The intersection of the contour lines with the streamwise axis (dotted line in figure 15b) has been chosen to represent the vortex formation length (L_F); this is plotted versus Γ in figure 15c) with ($\circ$)-symbols. The resulting estimation of the vortex formation length (L_F) is however strongly affected by the value of the chosen contour line.

Usually the peak of the velocity fluctuation level ($Tu = u_{rms}/U_\infty$) downstream of the cylinder is used as a definition of the vortex formation length (see e.g. Williamson 1996). Therefore the value of the contour line was here chosen to match $L_F = 80$ mm extracted from figure 8b) in the $\Gamma = 0$ case. Note that the Reynolds number is not the same in the two cases (measurements and visualizations), but are, nonetheless, in the same flow regime. The absence of contour lines for $\Gamma = -2.6, -3.2, -3.9$ and -5 in figure 15b) is due to the fact that the smoke is too dense, because of the wake reduction (cf. figure 14), and there will not be any visible lines for the chosen contour value. However, by applying another value of the contour line one obtains the tiny $\square$-symbols in

figure 15c). Then the three values of $\Gamma = 0, -1.4$ and -1.9 are shifted by an average distance ΔL to collapse with the $\circ$-symbols for the same Γ (i.e. the first chosen value of the contour lines). The same shift ΔL is then applied to the other data as well to give the large $\square$-symbols in figure 15c).

The data in figure 15c) clearly show how the vortex formation length decreases with increasing suction and vice versa for blowing. The data show an almost linear decrease with Γ although L_F is lower for $\Gamma = -1.37$ than for $\Gamma = -1.93$. This is most probably connected to the complicated mean flow behaviour with suction discussed previously (cf. section 3.3). Furthermore, for $\Gamma = -5$ (maximum suction investigated) it seems that the wake has disappeared since the vortex formation length obtained is at the cylinder edge (cf. figure 15c).

Verification of the relative increase of L_F obtained from the flow visualization can be done using the hot-wire measurements. For the blowing case, in

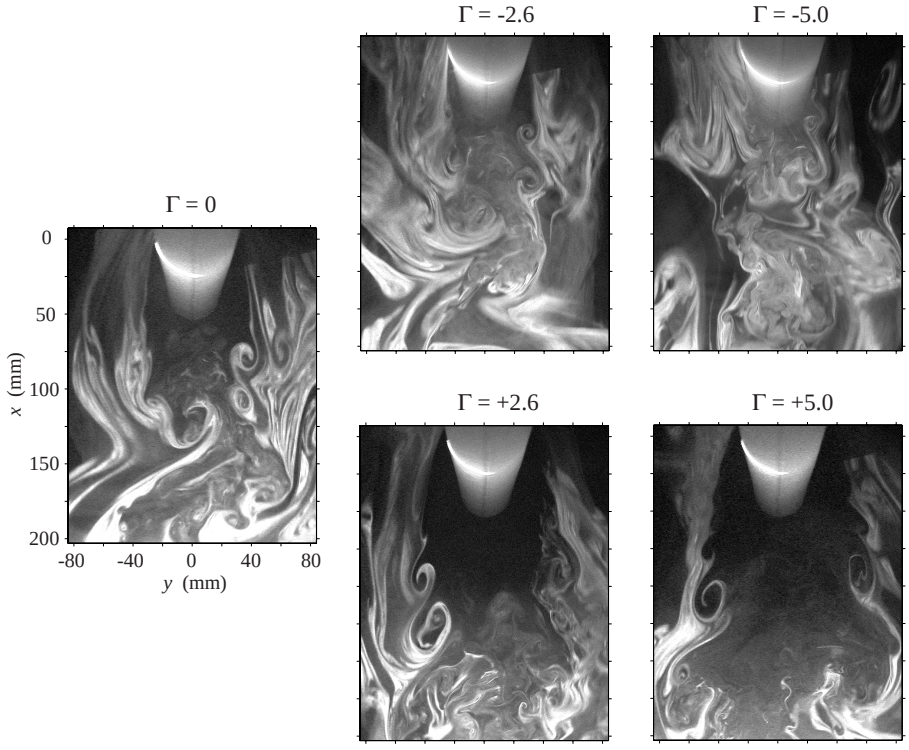

FIGURE 14. Instantaneous flow visualization images in the near wake of a porous cylinder subject to continuous suction or blowing for $Re = 3300$.

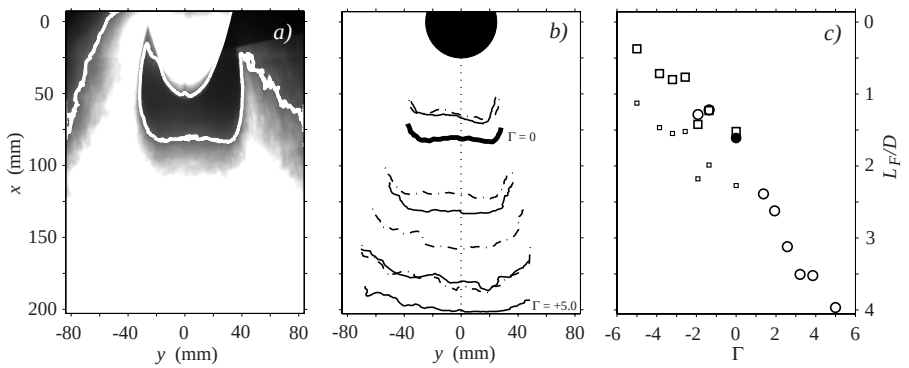

FIGURE 15. Variation of the vortex formation length vs Γ. a) Digital averaging of 200 images for $\Gamma = 0$ with the chosen color contour line. b) The contour lines for some values of $\Gamma(= +5, +3.9, +3.2, +2.6, \pm 1.4, \pm 1.9, 0)$. Bold solid line corresponds to $\Gamma = 0$ whereafter the contour lines are plotted alternately with dash-dotted and solid lines for increasing $|\Gamma|$. c) Vortex formation length versus Γ. (○)-symbols corresponds to the intersection points of the contour lines in b) with the centreline. (●) belongs to $\Gamma = 0$ (see text for (□)-symbols).

figure 8b), the peak appears very distinct and moves from $x/D \approx 1.5$ to 3 with an increase of Γ from 0 to +3.9. Using the values extracted from the flow visualization images one observes an L_F-increase to $x/D \approx 3.5$ in the same blowing interval, which is deemed acceptable considering the resolution in figure 8b).

5. Summary

The flow around a porous cylinder subject to continuous suction or blowing has been experimentally studied for Reynolds numbers of the order of 10^4. It is shown that even moderate levels of the secondary flow, i.e. $\lesssim 5\%$ of the oncoming streamwise velocity, have a large impact on the flow around the cylinder, both for suction and blowing.

Strong enough suction moves the separation line to the rear part of the cylinder in a similar way as it does when the cylinder boundary layer becomes turbulent (resulting in a narrower wake). This is shown in a qualitative way through the drastic reduction of C_D (up to 70%) above a specific value of Γ (≈ -2.5) and by a direct check of the C_p-distribution. When blowing is applied the separation point moves to smaller angles and the drag is shown to increase linearly with increasing magnitude of blowing. Correspondingly this is shown to result in a widening of the wake.

A measure of the vortex formation length has been defined from flow visualization images and used for investigating relative changes of this length when suction or blowing is applied. For instance, the vortex formation length is decreased by 75% and increased by 150% for $\Gamma \approx -5$ and $+5$, respectively. For the suction case the decrease in formation length may be directly coupled to the rearward motion of the separation point and vice versa for the blowing. It is notable that the turbulence on the wake centreline decreases throughout the whole measured downstream distance ($x/D = 20$) if suction is applied on the cylinder, whereas there is hardly any effect from blowing beyond $x/D = 5$.

The Strouhal number increases strongly with suction (up to 50% for $\Gamma \approx -2.5$), whereas blowing has the opposite effect (decrease of around 25% for $\Gamma \approx +5$). This can be seen to be coupled to an apparent diameter of the cylinder, which is decreased for suction and increased for blowing as compared to the solid cylinder. However, another interpretation of the change of Strouhal number is that the effective Reynolds number changes with suction and blowing. In fact it was shown that it was possible to find a relation between an effective Reynolds number and the blowing/suction rate. This relation was verified in a large Reynolds number range ($Re \sim 10^2 - 10^6$).

Acknowledgments

The authors would like to thank Prof. A. Bottaro for hosting the experiment in Toulouse and for valuable comments on the manuscript. We also want to thank Mr. Ulf Landén at KTH Mechanics for his skilful construction work of the cylinders. The work is part of a large research program "Control and modelling of turbulent and transitional flows" supported by the Swedish Research Council (VR). J.H.M. Fransson's six-month stay in Toulouse was supported by an EU Marie Curie Training Site Fellowship. P. Konieczny's three-month stay in Stockholm was supported by IMFT and KTH.

References

Antonia, R. A. & Rajagopalan, S. 1990 Determination of drag of circular cylinder. *AIAA J.* **28**, 1833–1834.

Berger, E. 1967 Suppression of vortex shedding and turbulence behind oscillating cylinders. *Phys. Fluids* **10**, S191–S193.

Buresti, G. 1998 Vortex shedding from bluff bodies. *Wind Effects on Buildings and Structures.* Riera & Davenport (eds.), Balkema, Rotterdam, pp. 61–95.

Cantwell, B. & Coles, D. 1983 An experimental study of entrainment and transport in the turbulent near wake of a circular cylinder. *J. Fluid Mech.* **136**, 321–374.

Fransson, J. H. M. 2001 Investigations of the asymptotic suction boundary layer. TRITA-MEK Tech. Rep. 2001:11. Licentiate Thesis, KTH, Stockholm.

Fransson, J. H. M. & Alfredsson, P. H. 2003 On the disturbance growth in an asymptotic suction boundary layer. *J. Fluid Mech.* **482**, 51–90.

Glezer, A. & Amitay, M. 2002 Synthetic jets. *Annu. Rev. Fluid Mech.* **34**, 503–529.

Hallbäck, M., Groth, J. & Johansson, A. V. 1989 A Reynolds stress closure for the dissipation in anisotropic turbulent flows. *Seventh Symposium on Turbulent Shear Flows*, 17.2.1–17.2.6.

Hurley, D. G. & Thwaites, M. A. 1951 An experimental investigation of the boundary layer on a porous circular cylinder. *Brit. Aero. Res. Council,* Rep. and Memo. 2829.

Karman, T. 1912 Über der mechanismus des wiederstandes, den ein bewegter körper in einer flüssigkeit erfährt. *Göttingen Nachr., Math.-Phys. Klasse* pp. 547–556.

Kiya, M., Suzuki, Y., Arie, M. & Hagino, M. 1982 A contribution to the free-stream turbulence effect on the flow past a circular cylinder. *J. Fluid Mech.* **115**, 151–164.

Lindgren, B. & Johansson, A. V. 2002 Design and evaluation of a low-speed wind-tunnel with expanding corners. TRITA-MEK Tech. Rep. 2002:14, KTH, Stockholm.

Mathelin, L., Bataille, F. & Lallemand, A. 2001*a* Near wake of a circular cylinder submitted to blowing - I Boundary layers evolution. *Int. J. Heat Mass Transf.* **44**, 3701–3708.

Mathelin, L., Bataille, F. & Lallemand, A. 2001*b* Near wake of a circular

cylinder submitted to blowing - II Impact on the dynamics. *Int. J. Heat Mass Transf.* **44**, 3709–3719.

Norberg, C. 1994 An experimental investigation of the flow around a circular cylinder: influence of aspect ratio. *J. Fluid Mech.* **258**, 287–316.

Norberg, C. 2003 Fluctuating lift on a circular cylinder: review and new measurements. *J. Fluids Struc.* **17**, 57–96.

Pankhurst, R. C. & Thwaites, M. A. 1950 Experiments on the flow past a porous circular cylinder fitted with a Thwaites flat. *Brit. Aero. Res. Council,* Rep. and Memo. 2787.

Park, D. S., Ladd, D. M. & Hendricks, E. W. 1994 Feedback control of von Karman vortex shedding behind a circular cylinder at low Reynolds numbers. *Phys. Fluids* **6**, 2390–2405.

Roshko, A. 1955 On the wake and drag of bluff bodies. *J. Aeronaut. Sci.* **22**, 124–132.

Roshko, A. 1961 Experiments on the flow past a circular cylinder at very high Reynolds number. *J. Fluid Mech.* **10**, 345–356.

Roussopoulos, K. 1993 Feedback control of vortex shedding at low Reynolds number. *J. Fluid Mech.* **248**, 267–296.

Schlichting, H. & Gersten, K. 2000 *Boundary layer theory*. Springer.

Shiels, D. & Leonard, A. 2001 Investigation of a drag reduction on a circular cylinder in rotary oscillation. *J. Fluid Mech.* **431**, 297–322.

Strouhal, V. 1878 Über eine besondere Art von Tonerregung. *Physikalisch-medicinischen Gesellschaft* pp. 216–251.

Szepessy, S. & Bearman, P. W. 1992 Aspect ratio and end plate effects on vortex shedding from a circular cylinder. *J. Fluid Mech.* **234**, 191–217.

Tokumaru, P. T. & Dimotakis, P. E. 1991 Rotary oscillation control of a cylinder wake. *J. Fluid Mech.* **224**, 77–90.

Wang, A.-B., Travnicek, Z. & Chia, K.-C. 2000 On the relationship of effective Reynolds number and Strouhal number for the laminar vortex shedding of a heated circular cylinder. *Phys. Fluids* **12**, 1401–1410.

Williamson, C. H. K. 1996 Vortex dynamics in the cylinder wake. *Annu. Rev. Fluid Mech.* **28**, 477–539.

Zdravkovich, M. M. 1997 *Flow around circular cylinders, Vol 1: Fundamentals*. Oxford University Press.

Zdravkovich, M. M. 2003 *Flow around circular cylinders, Vol 2: Applications*. Oxford University Press.

Paper 8

8

PIV–measurements in the wake of a cylinder subject to continuous suction or blowing

By Jens H. M. Fransson

KTH Mechanics, SE-100 44 Stockholm, Sweden

The present experimental investigation analyses the effect on the wake when applying continuous suction or blowing, through the cylinder surface, by means of PIV-measurements. Part of the cylinder is made of a porous material with a hydraulically smooth surface. Particular attention has been given to the vortex formation length behind the cylinder. Both the position of maximum back-flow and the position of the confluence point of the two stationary vortices, which appears in a mean field view, have been used as a measure of the vortex formation length. These are shown to be related by a factor of 1.4 in average. Peculiar peaks in the integrated streamwise energy across the wake was found at fixed downstream positions, and was observed to be strenghend with suction in particular. These energy peaks are hypothesized to be attributed to inflectional instability of the mean streamwise velocity profile.

1. Introduction

A flow configuration that has attracted researchers and scientists over many years is the flow past bluff bodies. This configuration offers the interaction of three shear layers to be studied (cf. e.g. Williamson 1996), namely the boundary layer on the body, the separating free shear layer, and the wake flow. From a fundamental research point of view it is a very complex flow geometry that can give many flow phenomena in different Reynolds number ranges, such as boundary layer separation, periodic vortex shedding, wake transition, boundary layer transition, flow reattachment, separation bubbles etc. These flow phenomena are of direct relevance to many practical and industrial applications, where the vortex shedding in particular plays an important role, such as in telecom masts, aircraft and missile aerodynamics, civil and wind engineering, marine structures, and underwater acoustics. The periodic vortex shedding can lead to devastating structural vibrations that finally lead to material fatigue and structural failure.

The vortex shedding instability is a self excited oscillation that will set in even if all sources of noise are removed (see Gillies 1998), and can be shown to be attributed to the local stability property of the two-dimensional mean

velocity wake profile behind a bluff body. Monkewitz (1988) identified a sequence of stability transitions by using a family of wake profiles, that resulted in $Re_C < Re_A < Re_K$, where Re_C (≈ 5), Re_A (≈ 25), and Re_K (≈ 47) are critical Reynolds numbers that mark the onset of convective, absolute, and von Kármán shedding instability, respectively. This sequence was in fully agreement with the qualitative model predictions by Chomaz *et al.* (1988) the same year. The onset of the global von Kármán shedding mode occurs via a so-called supercritical Hopf bifurcation (see e.g. Provansal *et al.* 1987). For a review on the stability properties of open flows in general the interested reader is referred to Huerre & Monkewitz (1990), and for reviews on cylinder flows in particular see e.g. Williamson (1996); Buresti (1998); Norberg (2003); Zdravkovich (1997, 2003).

1.1. *Vortex shedding control*

The ability to control the wake and the vortex shedding of a bluff body can for instance be used to reduce drag, increase heat transfer and mixing, and enhance combustion. Over the second half of last century there have been a number of successful attempts to control the shedding wake behind bluff bodies with the practical goal of reducing the pressure drag on the body.

1.1a. *Rectangular-based forebody.* A control approach that has shown to be effective in reducing the average strength of the vortices and the shedding frequency is base bleed (cf. e.g. Wood 1967; Bearman 1967). For successively increasing bleeding rates the regular shedding of vortices ceases, intermittently at first, and then completely. Hannemann & Oertel (1989) performed numerical simulations on the effect of uniform blowing from the base, and reported a critical value[1] ($c_q = 0.214$) for which vortex shedding was suppressed. Uniform suction from the base was considered numerically by Hammond & Redekopp (1997) and they report a continuous decline of the wake shedding frequency with a gradual increase of suction until an abrupt suppression occurs at a sufficiently high suction rate.

1.1b. *Cylinder.* A simple passive control method is to place a thin splitter plate aligned in the streamwise direction on the centreline of the near wake (see Roshko 1955, 1961). For a specific length of the splitter plate the sinuous von Kármán mode is altered for a varicose mode that causes a pair of twin–vortices to be formed, one on each side of the plate. More recently, Grinstein *et al.* (1991) carried out numerical simulations on the effect of an interference plate in the wake of a plate and found that the base pressure coefficient could decrease by a factor of 3 depending on the length of the plate and its separation from the base.

[1] $c_q = m^*/U_\infty D^*$, were m^* is the mass flow rate divided by density and for unit depth which is blown into the wake at the base of the plate, U_∞ is the free stream velocity, and D^* is the thickness of the plate.

Experiments on circular cylinders with forced rotary oscillations have shown to give a drag reduction of up to 80% at $Re = 15000$ for certain ranges of frequency and amplitude of the sinusoidal rotary oscillation (see Tokumaru & Dimotakis 1991). Shiels & Leonard (2001) performed numerical simulations of this control approach in where the above experimental findings were verified and showed indications that this kind of control could be even more efficient at higher Re.

Control approaches using feedback control have also been attempted. Roussopoulos (1993) carried out experiments in a wind tunnel with acoustic waves from a loudspeaker as actuation as well as by vibrating the cylinder. In a numerical study by Park *et al.* (1994) blowing and suction through slots on the rear part of the cylinder were utilized as actuation. However, this investigation were performed at relatively low Reynolds numbers (< 300) and so far it does not exist any results on higher Re-flows.

Glezer & Amitay (2002) used synthetic jets, which provide a localized addition of momentum normal to the surface, on selected positions over the cylinder in order to delay separation in both laminar and turbulent boundary layers. They argued that this delay was caused by increased mixing within the boundary layer. In addition, the interaction between the jet and the cross flow has a profound effect both on the separated shear layer and on the wake; the magnitude of the Reynolds stresses is reduced indicating that the delay in separation is not merely the result of a transition to turbulence in the boundary layer.

Experiments with suction or blowing through the entire surface of the cylinder in order to control the vortex shedding have been considered by e.g. Pankhurst & Thwaites (1950); Hurley & Thwaites (1951); Mathelin *et al.* (2001*a*,*b*); Fransson *et al.* (2003). Pankhurst & Thwaites (1950) made combined experiments with continuous suction through the surface and a flap in form of a short splitter plate at different angles. They showed through surface pressure and wake velocity measurements that with the flap directed in the streamwise direction and for sufficient suction[2] ($C_q\sqrt{R} \gtrsim 10$) the separation is entirely prevented and a remarkable close approximation to the potential flow solution is achieved. Further, Hurley & Thwaites (1951) performed boundary layer measurements on the same porous cylinder and found in general good agreement with laminar boundary layer theory. However, no time resolved measurements to determine the vortex shedding frequency were reported.

The von Kármán frequency is Reynolds number dependent, whilst the dimensionless frequency known as the Strouhal number is constant (≈ 0.2) in the range $10^2 \lesssim Re \lesssim 10^5$. Mathelin *et al.* (2001*a*,*b*) considered the case of continuous blowing through the entire cylinder surface (see Mathelin *et al.* 2001*a*, for

[2]Here C_q is a suction coefficient defined as the suction velocity per unit area divided by the free stream velocity.

a detailed description of the experimental set-up). Among the effects observed are the wider wake and a decrease of the Strouhal number with increasing blowing. They report an analytical relation of an equivalent Reynolds number of the canonical case which produces the same flow characteristics in terms of vortex shedding instability as the case with blowing versus the blowing rate. The result is that the Strouhal number decreases with blowing, which was experimentally verified by Fransson *et al.* (2003), who also considered the effect of continuous suction which turns out to have the contrary effect on the Strouhal number. Note that uniform suction from the base of a rectangular-based forbody, interestingly, gives the opposite behaviour (cf. Hammond & Redekopp 1997). In Fransson *et al.* (2003) the changes in the flow due to blowing or suction were analyzed in terms of mean and fluctuating velocity profiles in the wake through hot-wire anemometry, pressure distributions on the cylinder, and drag and vortex shedding measurements. Furthermore, smoke visualizations of the flow field in the near wake of the cylinder for different blowing or suction rates were reported. Image averaging enabled the retrieval of quantitative information, such as the vortex formation length, which showed that the vortex formation length is decreased by 75% and increased by 150% for 5% of suction and blowing of the free stream velocity, respectively.

This paper deals with the wake effect, in particular the effect of the vortex formation length, behind a porous cylinder when different rates of continuous suction or blowing are applied through the entire cylinder surface. The Reynolds number is around 4000 which is in the subcritical regime (cf. Roshko 1961), implying laminar boundary layers around the cylinder with a purely laminar separation, and the data presented can be seen as a suitable test case for comparison with numerical simulations, which can be used to develop accurate CFD (Computational Fluid Dynamics) schemes and models. Further, this investigation complement the above cited investigations by providing full velocity field information using PIV, which provides accurate velocity measurements also very close to the cylinder.

2. Experimental set-up and measurement technique

2.1. *Wind tunnel*

The experiments were performed in the BL wind tunnel[3] at KTH Mechanics, Stockholm. The cross sectional area of the test section is 0.5×0.75 m^2, and it is 4.2 m long with a maximum speed of 48 m/s. The flow quality in this tunnel is considered good with a turbulence intensity (of all three components) of less than 0.04% of the free stream velocity. The tunnel is equipped with a heat exchanger and the desired temperature is easily set by the user on the computer controlling the tunnel. At 25 m/s the temperature variation over the cross section area is less than ± 0.07 °C and the variation over a time period

[3]Boundary Layer or Björn Lindgren named after its designer.

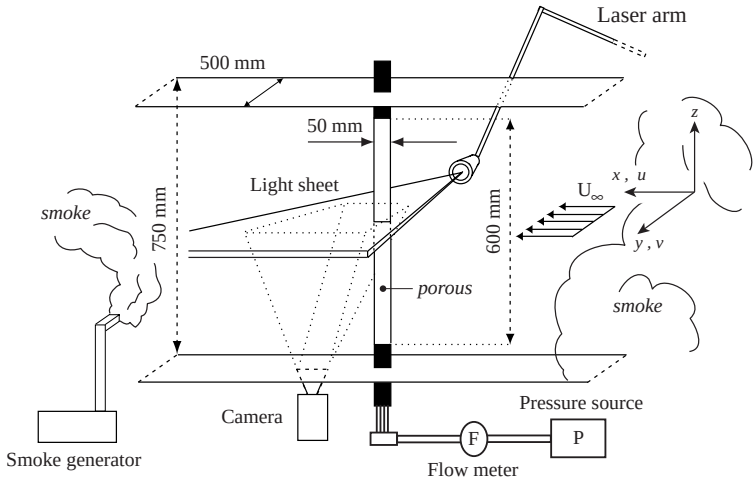

FIGURE 1. Schematic of the experimental set-up. Flow is from right to left.

of 4 hours is less than ± 0.03 °C. At this speed the total pressure variation is less than $\pm 0.1\%$. The tunnel was successfully designed with expanding corners (larger outlet than inlet cross section area) in order to reduce the total wind tunnel circuit length with only a negligible increase of the total pressure loss. The interested reader is referred to Lindgren (2002) for further details.

2.2. *Cylinder*

The same porous cylinder as was used by Fransson *et al.* (2003) for flow visualization was used in the present investigation. The cylinder consists of a cross profile made of brass as an inner skeleton. A sintered plastic material shaped to a cylinder is then slided over the brass profile and sealed, creating four isolated chambers through which different amount of blowing or suction may be applied. The end parts were made of brass pieces and act as plugs on each side of the cylinder. These were equipped with four inlets for tube connections that were confluenced before connected to a flow meter (rotameter type), which in turn was connected to a pressure source (vacuum cleaner or high pressure air depending on whether suction or blowing is required).

In figure 1 a schematic of the experimental set-up is shown with relevant measures. The cylinder was mounted vertically in the test section and has a diameter of 50 mm and a porous length of 600 mm. The porous material is a sintered plastic material with an average pore size of 16 μm, and the thickness

is 2.5 mm. Previous surface roughness measurements on a similar but flat porous plate (see Fransson & Alfredsson 2003) showed a deviation of ± 1 μm from the mean surface, which for the present case can be considered to be hydraulically smooth. The cylinder is made from a flat plate which is bent to form a circular cylinder. This means that there is a joint in the axial direction along the full length of the cylinder, and this gives rise to a small asymmetry with a 0.5 mm larger diameter in average when measured over the joint. The joint is therefore positioned at 180°, i.e. behind the cylinder in the streamwise direction, in order to avoid any flow asymmetry.

To determine the permeability of the material the pressure difference (ΔP) over the cylinder wall and the flow rate ($Q = V \times S$, where V and S are the velocity through the porous material and the surface area, respectively) are measured, when suction is applied. Through Darcy's law the permeability (k) is then determined to be $k = \mu t V/\Delta P = 2.31 \times 10^{-7}$ m^2, by best line fitting to the data (μ is the dynamic viscosity). Furthermore, a non-uniform suction/blowing rate is expected through the cylinder surface since the static pressure around the circumference of the cylinder varies when exposed to an oncoming flow and the fact that the tubing from the different chambers are confluenced before connected to the pressure source. However, the influence can be shown to be rather small. For the suction case the largest suction velocity occurs along the front stagnation line and then it decreases towards the rear. In the separated region the suction velocity is fairly constant and for a suction rate of 1.4% of the free stream velocity the suction velocity is about 6% smaller in this region as compared to the front. For larger suction rates the difference becomes smaller. In contrast, for the blowing case the smallest blowing velocity is along the frontal stagnation line and then increases and becomes constant from about 65° and downwards. In this case the maximum variation is less than 7% and the variation decreases with increasing blowing rate (see figure 2b).

2.3. *Measurement technique*

For the velocity measurements a Particle Image Velocimetry (PIV) system was used. The advantage of this technique is the allowance to capture a whole field of instantaneous velocities. On the other hand a drawback would be the relatively poor temporal resolution when compared with hot-wire for instance. The PIV-system used consists of a Spectra Physics 400 mJ double pulsed Nd:Yag laser operating at 15 Hz as a light source, and the camera is a double-frame Kodak ES1.0 8-bit CCD camera with 1018×1008 pixels. Further, a laser arm is connected to the laser which facilitates traversing of the laser sheet. The air was seeded with smoke particles generated by heating a glycol based liquid with a disco smoke generator, JEM ZR20 Mk II. The smoke inlet to the tunnel was in the open cross section between the end of the test section and the diffuser.

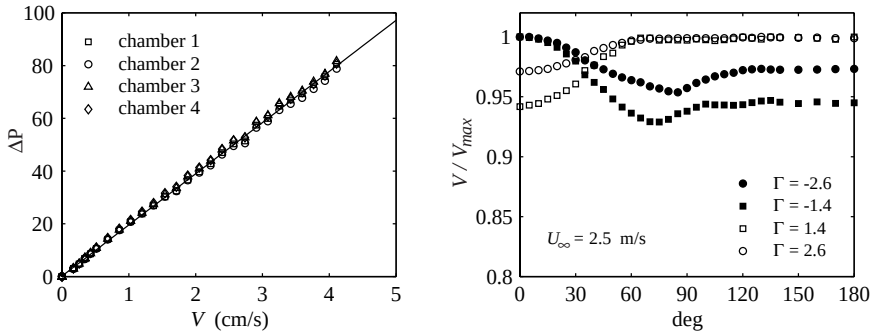

FIGURE 2. a) Permeability determination of the porous material (repeated for all chambers). Solid line is the best fit to all data. b) Suction/blowing distribution due to the static pressure variation around the circumference of the cylinder.

Before the measurements the smoke was recirculated in the tunnel until the air became homogeneuously seeded. See figure 1 for an illustration.

In the post-processing of the measured data conventional validation criteria were applied. Displacements of the particles larger than 25% of the interrogation area length was not allowed, in order to avoid low-velocity bias due to loss-of-pairs. This criterion is set before the measurements by choosing the appropriate time between the two consecutive captured images. Furthermore, spurious measurement errors were eliminated by applying a Peak-Value-Ratio (PVR) of 1.2, that is the ratio of the highest to the second highest peak in the cross-correlation is not allowed to be smaller than 1.2.

3. Experimental results

The amount of suction or blowing applied through the cylinder surface is characterized by the parameter Γ. This parameter is simply defined as the velocity through the cylinder surface $V_{\text{surf.}}$ (being negative for suction and positive for blowing) in percentage of the free stream velocity U_∞, i.e. $\Gamma = 100 \times V_{\text{surf.}}/U_\infty$. In the present experiments the free stream velocity has been kept constant at 1 m/s, corresponding to a Reynolds number based on the cylinder diameter and the free stream velocity of 3700.

The results are aimed at describing the effect of the vortex formation length for different blowing and suction rates, and to map the effect on the u_{rms} and the v_{rms} velocity fluctuation components as well as the Reynolds stress ($\overline{uv}$). See figure 1 for the coordinate directions, the origin of the system is however not shown in the figure which is located at the symmetry axis of the cylinder. The statistical quantities for all the different suction and blowing rates are based

on at least 1056 image pairs, and in the following vector and contour figures in the (x, y)-plane the data have been smoothed. Note that all contour levels can be seen as dimensional or as dimensionless form (normalized with U_∞) since $U_\infty = 1$ m/s. The measurements in the suction and in the blowing cases are not taken at the same position. In the blowing case the measurement field is slightly enlarged and moved downstream in order to follow and capture the confluence point of the two stationary vortices that are formed in an averaged perspective.

3.1. *Suction*

As reported in Fransson *et al.* (2003) suction decreases the size of the wake, both in terms of the extension of the vortex formation length as well as the width of the wake, contributing to a decrease of the total drag. In figure 3 instantaneous vector velocity fields (left column) and their corresponding back-flow coefficient maps (right column) are shown for $\Gamma = 0, -1.4, -2.6$, and -5.0. The black region in the left of the figures is the cylinder. The figures (left column) illustrates the roll up of the shear layers into distinct von Kármán eddies. Note that the shown fields only extends to 2.5 diameters downstream of the cylinder's symmetry axis, which implies that the back-flow regions only appear in the very near-wake of the cylinder according to the right column of figure 3, where the instantaneous back-flow ($U < 0$) is shown with (+)-symbols. Here, the indication of a larger back-flow region at $\Gamma = -5$ compared to $\Gamma = -2.6$ is simply an artefact of a snapshot of a turbulent velocity field dominated by large coherent structures.

In figures 4-5 the mean vector velocity fields (left column) and their corresponding mean back-flow coefficient maps (right column) are shown for $\Gamma = 0, -1.4, -1.9, -2.6, -3.2, -3.9, -5.0$, and -6.5. The figures show that the averaged velocity field consists of two stationary vortices with a stagnation point where they confluence. At some distance upstream of this point the maximum back-flow is achieved. The filled contours of the back-flow coefficient (right column) correspond to an increment of 0.1, from 0 (white = no back-flow in average) to 1 (black = back-flow at all times). The white bullet, in all figures (right column), correspond to the maximum value of the back-flow coefficient. For increasing suction this point moves towards the cylinder and in the corresponding vector velocity fields (left column) the two stationary vortices are seen to move along. The vertical (y/D) position of the cores of the two stationary vortices seem to be unaffected for low suction rates but for increasing suction the vortices are seen to be compressed in this direction implying an enlarged region of high back-flow velocities in between the cores before the vortices totally are suppressed (see $\Gamma = -6.5$ case).

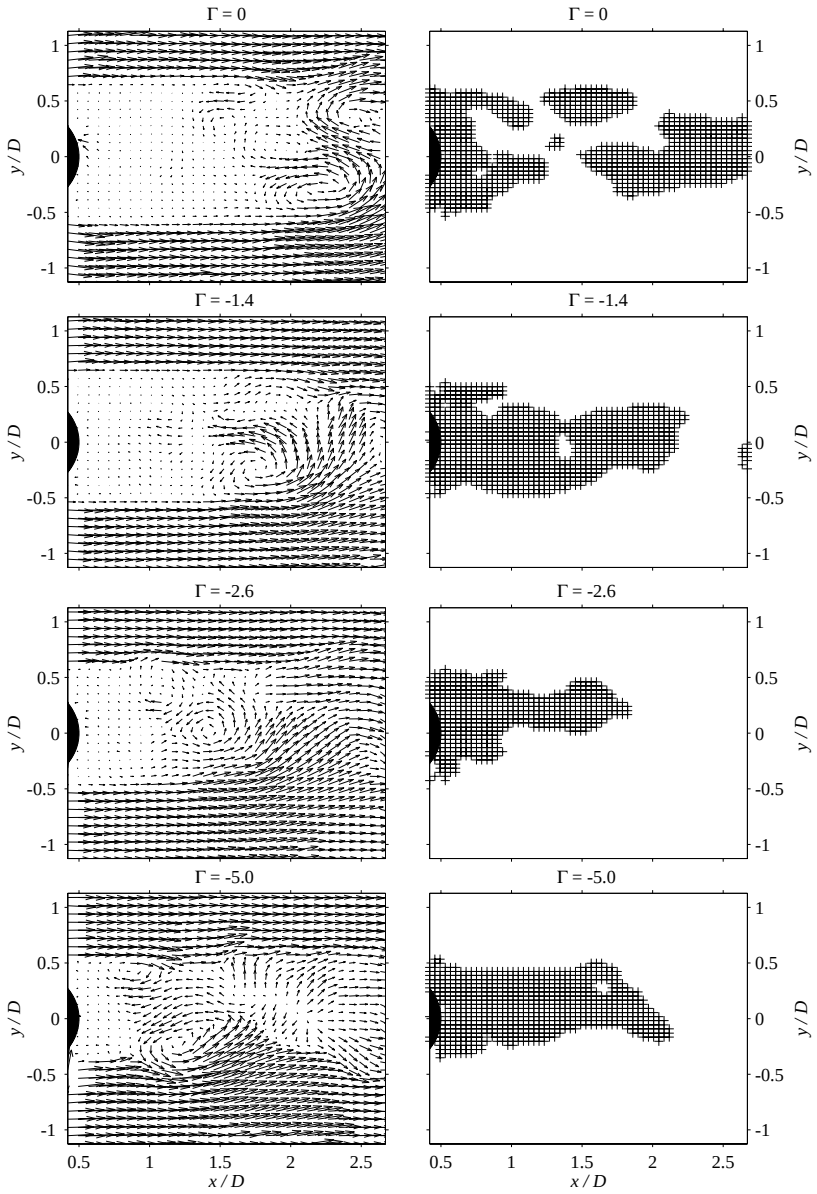

FIGURE 3. Instantaneous vector velocity fields (left column) and their corresponding back-flow coefficient maps (right column) for different suction rates.

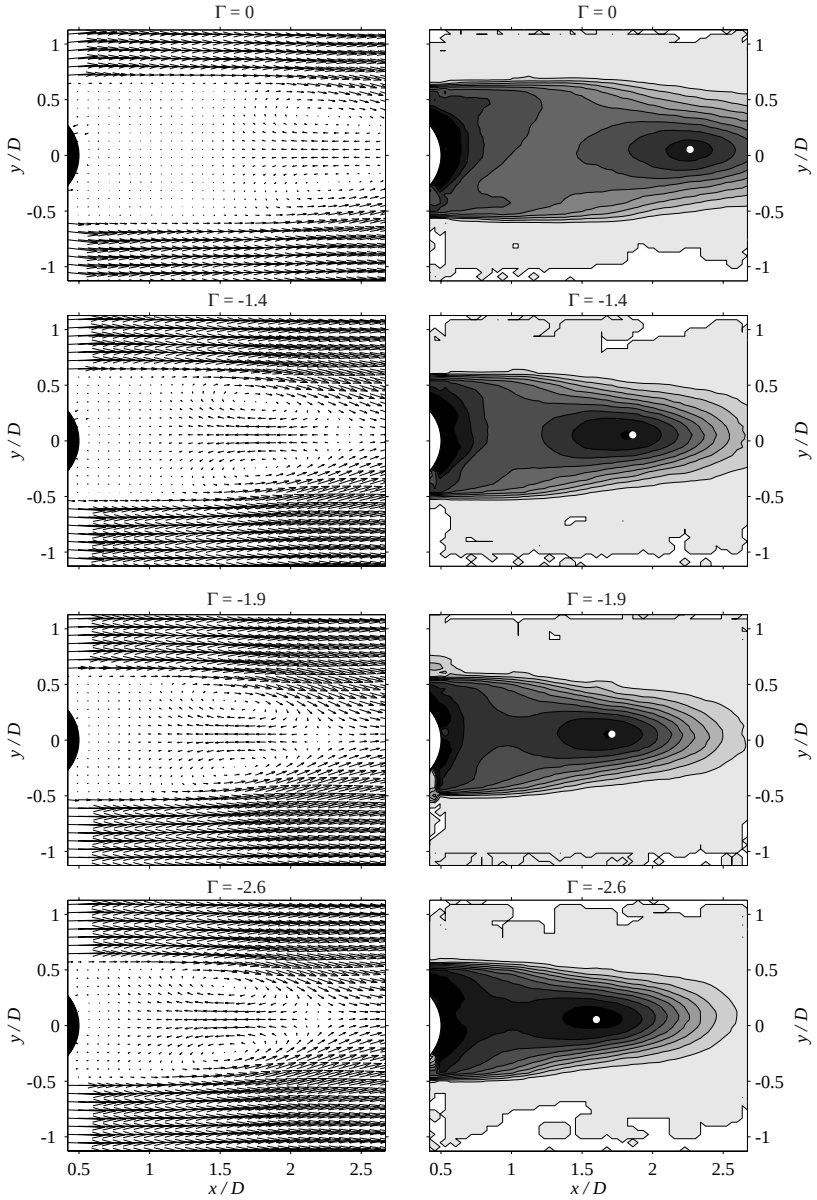

FIGURE 4. Mean vector velocity fields (left column) and their corresponding mean back-flow coefficient maps (right column) for different suction rates. The filled contours (right column) correspond to an increment of 0.1, from 0 (white) to 1 (black).

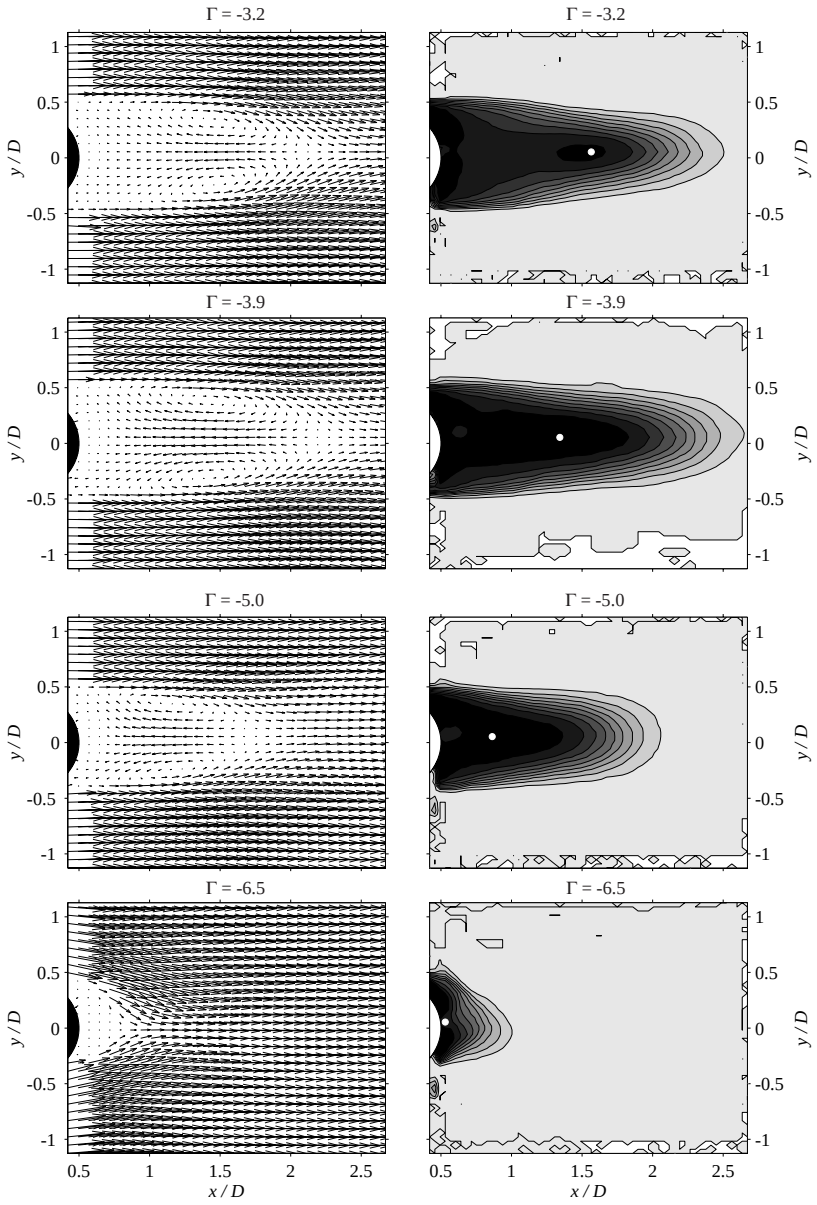

FIGURE 5. For caption see figure 4.

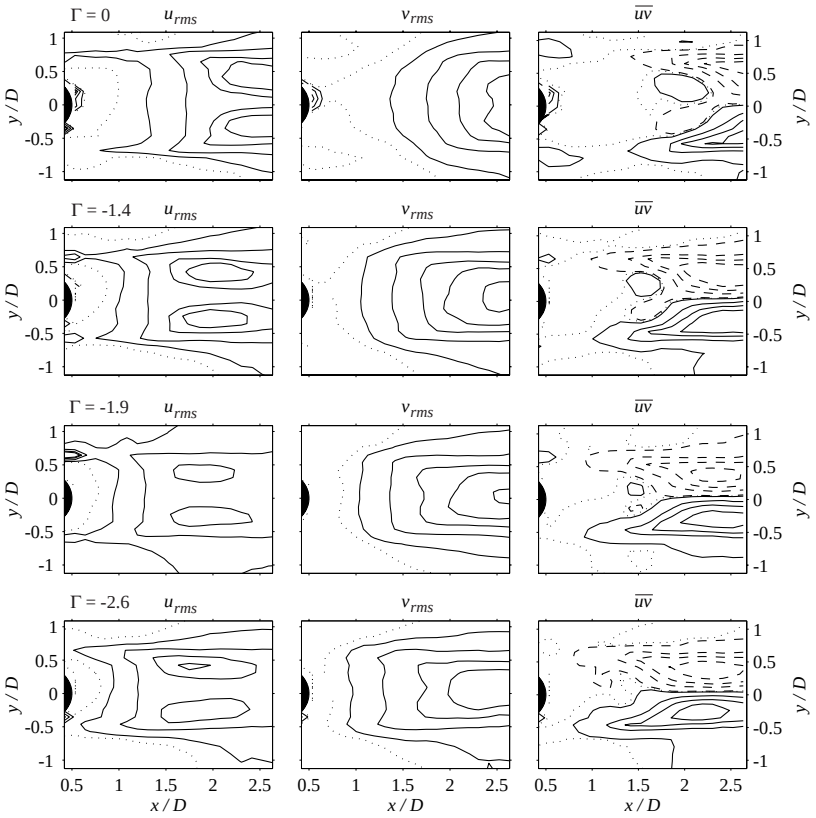

FIGURE 6. Root mean square of the u and v velocity fluctuations and the uv-Reynolds stress component in the (x, y)-plane for different suction rates.

Figures 6-7 show the u_{rms}, v_{rms}, and uv-Reynolds stress component in the (x, y)-plane for $\Gamma = 0, -1.4, -1.9, -2.6, -3.2, -3.9, -5.0$, and -6.5. The dotted contour lines in the u_{rms} and v_{rms} figures correspond to 0.05 and the solid lines to 0.1, 0.2, 0.3, and 0.35 with increasing values to the closed regions. For $\overline{uv}$ the dotted lines correspond to the zero contour and the dashed and solid contour lines correspond to negative and positive values of 0.002 0.02 0.035 0.05, respectively, with increasing values to the closed regions. For increasing suction the two peaks in u_{rms} move towards the cylinder and decreases in size which is illustrated in the figure with the approaching contour lines, since the same contours are plotted in all figures. In v_{rms} a single peak is observed which approaches the cylinder with increasing suction. The $\overline{uv}$ shows the asymmetric behaviour with positive (solid) and negative (dashed) contour lines.

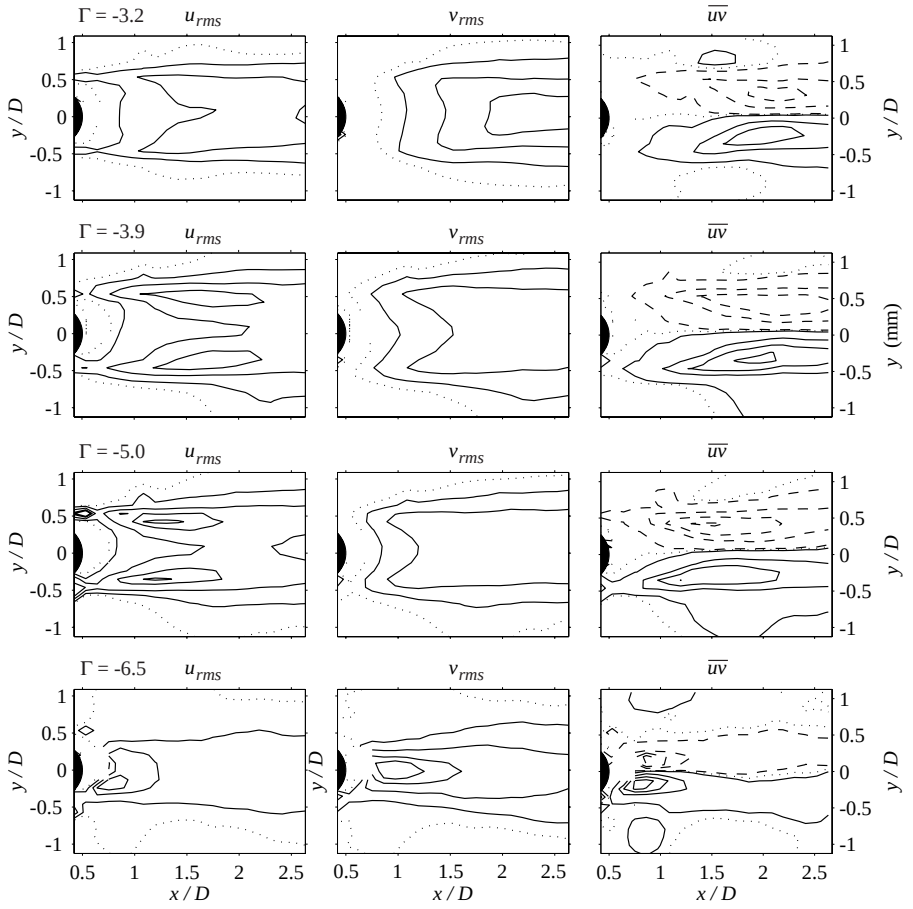

FIGURE 7. For caption see figure 6.

The wake energy evolution in the streamwise direction is shown in figure 8. E_u, E_v, and E_{uv} are defined as

$$E_u = \int \left\{ \frac{u_{rms}}{U_\infty} \right\}^2 \mathrm{d}y \ , \quad E_v = \int \left\{ \frac{v_{rms}}{U_\infty} \right\}^2 \mathrm{d}y \ , \ \text{ and } \ E_{uv} = (E_u + E_v)/2 \ ,$$

respectively. Where E_{uv} denotes the "total energy" (w-component missing) at a prescribed distance downstream of the cylinder. From figure 8a) it is clear that the level of E_u decreases monotonically with increasing suction in the region beyond approximately $2.1D$ behind the cylinder. From inspection of

figure 8a) one may conclude that the suction suppresses the transient energy distribution behind the cylinder and moves the maximum closer to the cylinder. This is probably also the scenario of E_v, see figure 8b), where the maximum is shifted about $0.5D$ downstream. A large energy peak at $x/D = 1.1$ can be observed in E_u which is also present in E_v but 3-5 times smaller depending on the suction rate. The total energy E_{uv} is plotted in figure 8c) and resembles what is just stated, but the x/D-position where a monotonic decrease of the energy with increasing suction is observed has moved slightly downstream (to ≈ 2.25) due to the shifted maximum in E_v.

3.2. *Blowing*

The effect of blowing has previously been shown (cf. Fransson *et al.* 2003) not only to increase the wake width but also to increase the velocity deficit that is encountered behind the cylinder. This causes an almost linear increase of the drag coefficient with increasing blowing. In figure 9, snapshots of the vector velocity field (left column) is shown for $\Gamma = 0, 1.4, 2.6$, and 5.0 together with

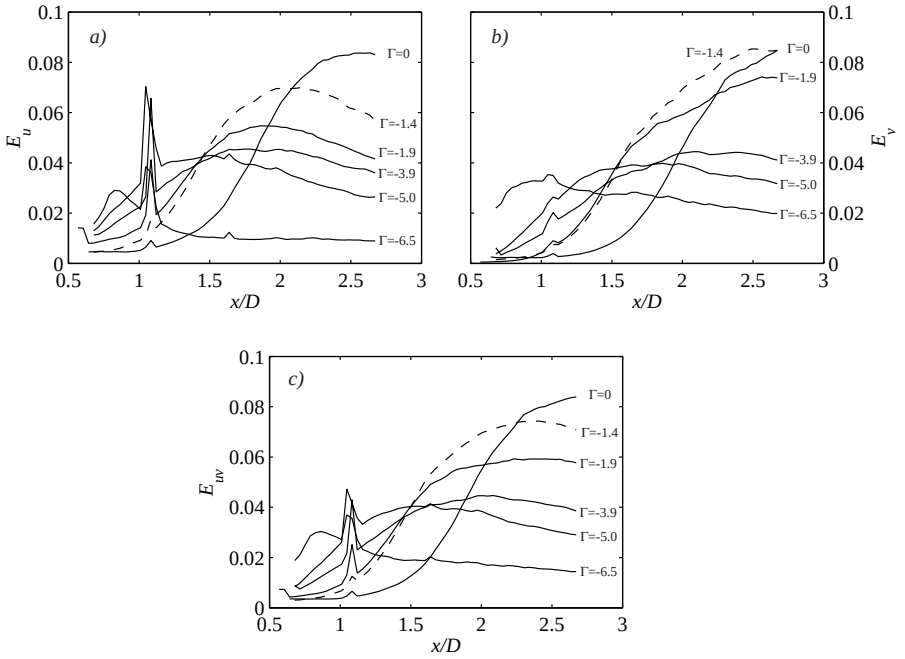

FIGURE 8. Wake energy evolution in the streamwise direction for different suction rates. a) E_u: the energy of the u-component. b) E_v: the energy of the v-component. c) Total energy $E_{uv} = E_u + E_v$.

their corresponding back-flow map (right column), which gives a representative view of the flow. Large indistinct von Kármán vortices are observed in the figure (left column) and the region of back-flow gives an impression to increase with blowing. Figures 10-11 show the mean vector velocity fields (left column) and their corresponding mean back-flow coefficient maps (right column) for $\Gamma = 0, 1.4, 1.9, 2.6, 3.2, 3.9, 5.0$, and 6.5. The y/D-position of the cores of the two stationary vortices seem to be unaffected for blowing rates up to $\Gamma = 3.2$, whereafter the distance between the two cores start to grow. However, already at low blowing rates there is a notable movement in the streamwise direction of the stagnation point and the position of maximum back-flow (for contour information of the back-flow coefficient see the corresponding suction case). The growth of the vortices with increasing blowing are best illustrated by the enlarged regions of maximum back-flow in the contour plots of figures 10-11. Here, the white bullets, again, illustrate the movement of the position of maximum back-flow.

Figures 12-13 show the u_{rms}, v_{rms}, and uv-Reynolds stress component in the (x, y)-plane for $\Gamma = 0, 1.4, 1.9, 2.6, 3.2, 3.9, 5.0$, and 6.5. The dotted, dash-dotted, dashed, and the solid contour lines in the u_{rms} and v_{rms} figures correspond to 0.15, 0.20, 0.30, and 0.35 respectively. The dotted contour lines of $\overline{uv}$ correspond to the zero level, and the dashed and solid to negative and positive contour lines, respectively (of $\pm 0.002, \pm 0.02, \pm 0.035$, and ± 0.05 with the increment towards the closed regions). The opposite effect of all three quantities is observed when compared to the suction case. The two peaks in the u_{rms}-distribution move away from the cylinder but a blowing rate of at least $\Gamma = 3.2$ is needed in order to observe an effect of blowing. The same tendency is seen for the v_{rms} and $\overline{uv}$. However, from $\Gamma = 3.9$ to 5.0 there is a large change in all three quantities, rendering the positive and negative maxima in $\overline{uv}$ out of the image.

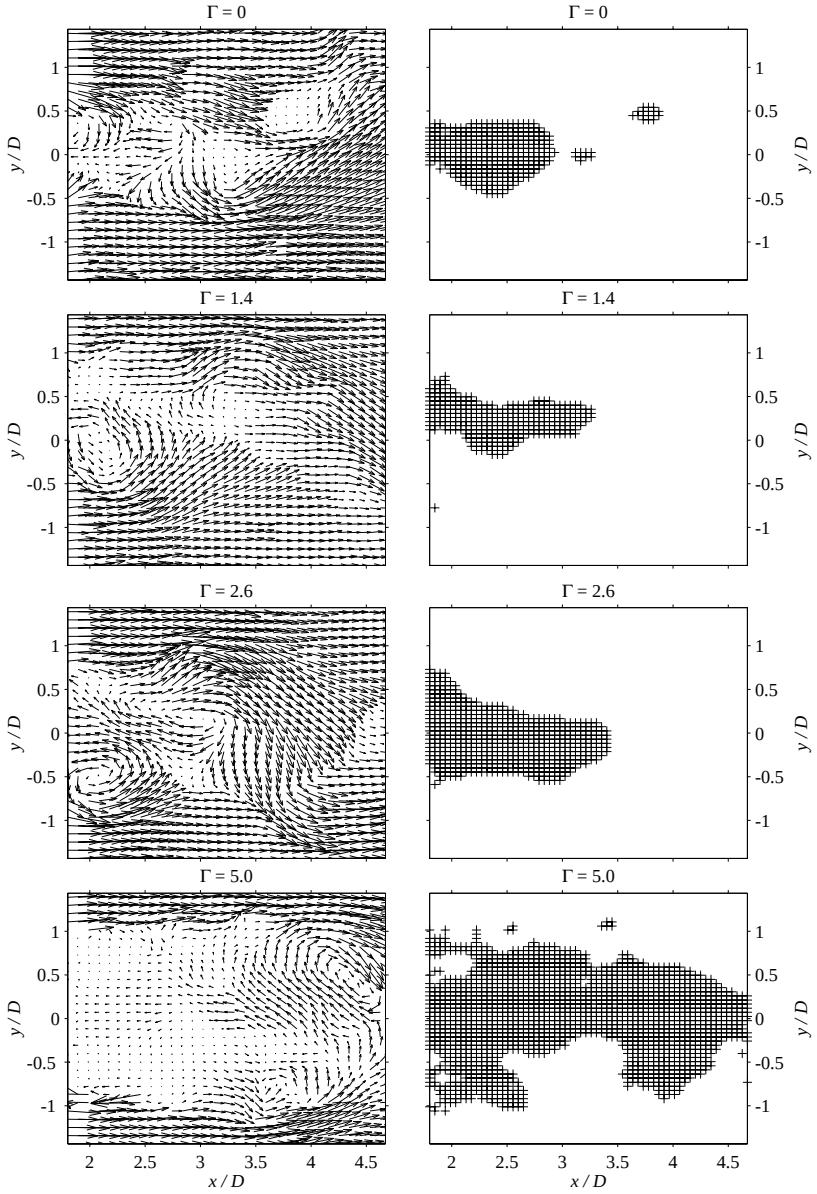

FIGURE 9. Instantaneous vector velocity fields (left column) and their corresponding back-flow coefficient maps (right column) for different amount of blowing.

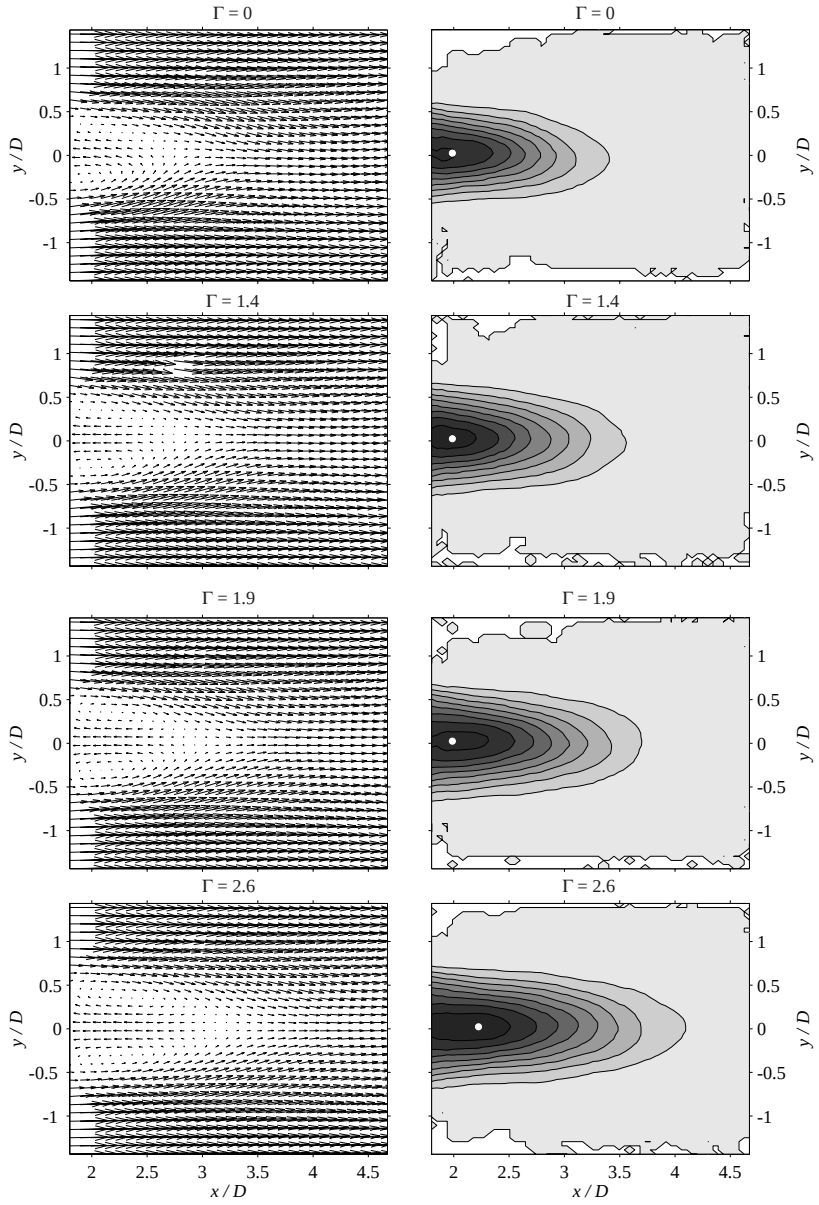

FIGURE 10. Mean vector velocity fields (left column) and their corresponding mean back-flow coefficient maps (right column) for different blowing rates. The filled contours (right column) correspond to an increment of 0.1, from 0 (white) to 1 (black).

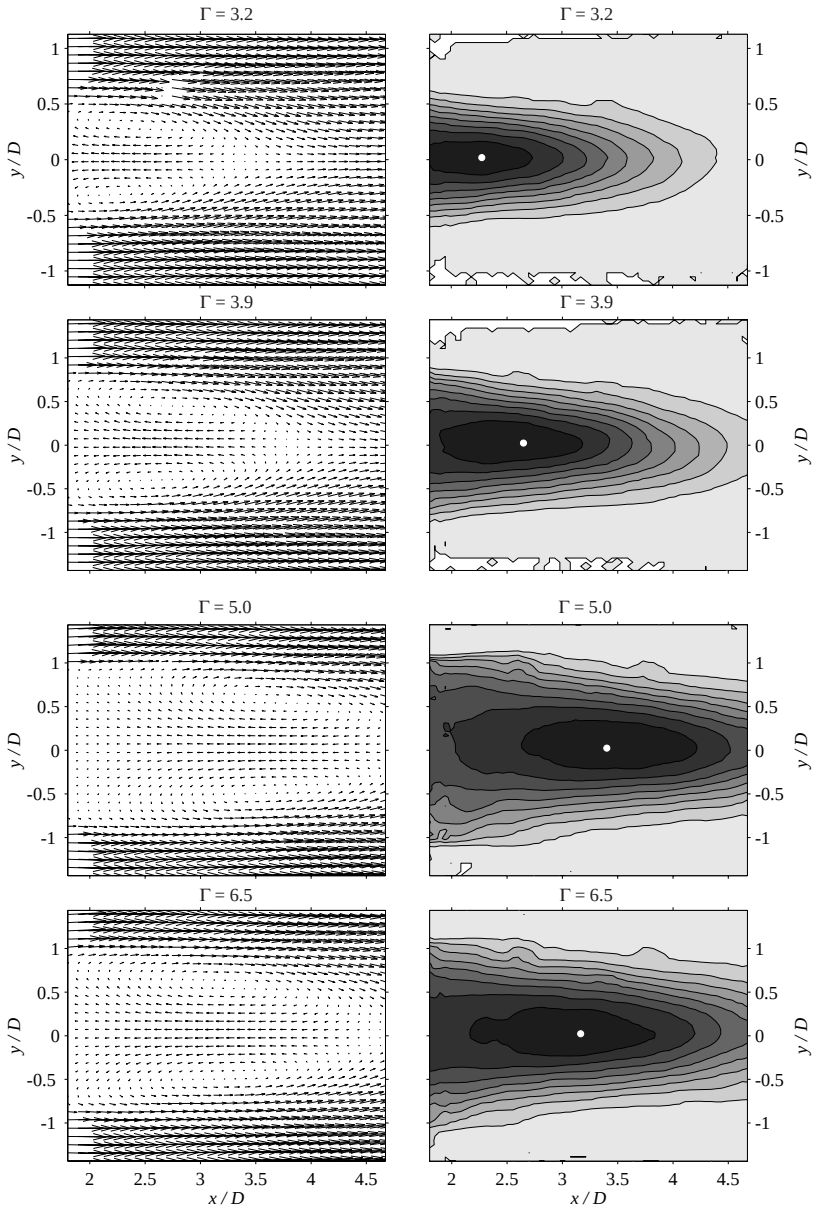

FIGURE 11. For caption see figure 10.

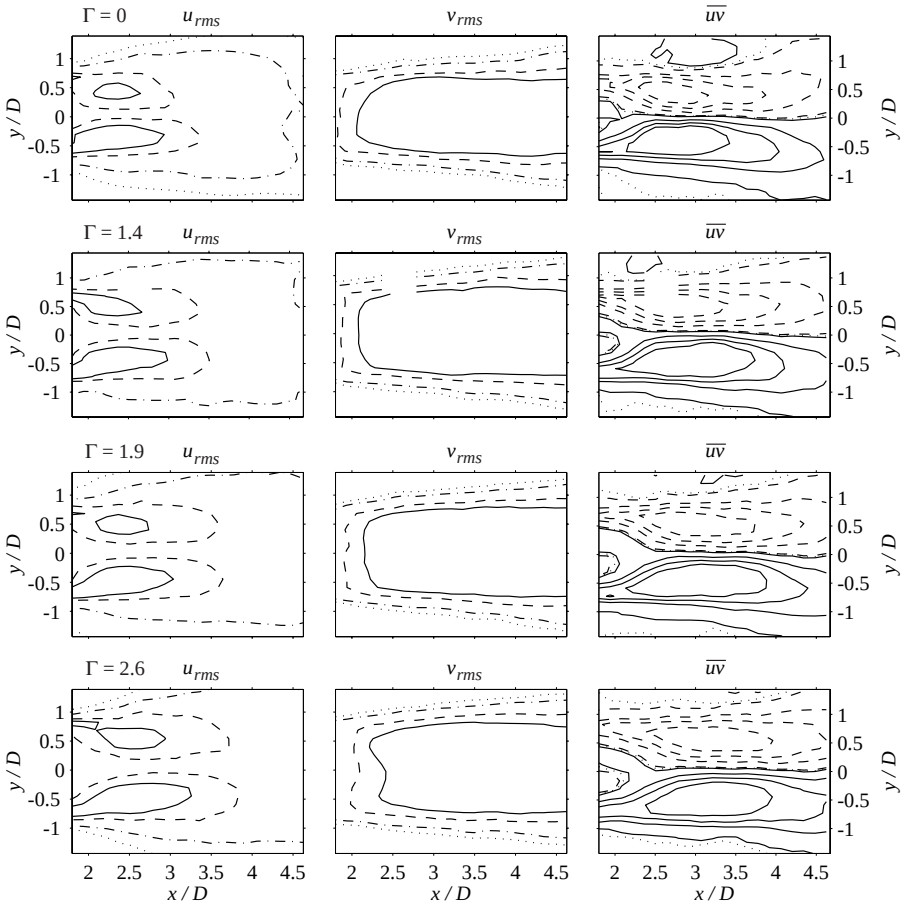

FIGURE 12. Root mean square of the u and v velocity fluctuations and the uv-Reynolds stress component in the (x, y)-plane for different blowing rates.

For increasing blowing the trends of the energy distribution is similar but not as clear as in the suction case. The E_u is monotonically increasing with blowing at $x/D = 4.7$, which can be observed in figure 14a). The maximum value of E_u moves away from the cylinder with increasing blowing and between $\Gamma = 3.0$ and 5.0 it seems to be a large shift downstream. Note that for $\Gamma = 6.5$ it looks like if the trend has been reversed when compared with $\Gamma = 5.0$. Figure 14b) shows the E_v evolution, which shows a clear shift of the maximum towards higher x/D with increasing blowing. The lower energy level distributions for $\Gamma = 5.0$ and 6.5 compared to $\Gamma = 0$ is most certain due to the delay of the energy growth when blowing is applied and the former two Γ-values will

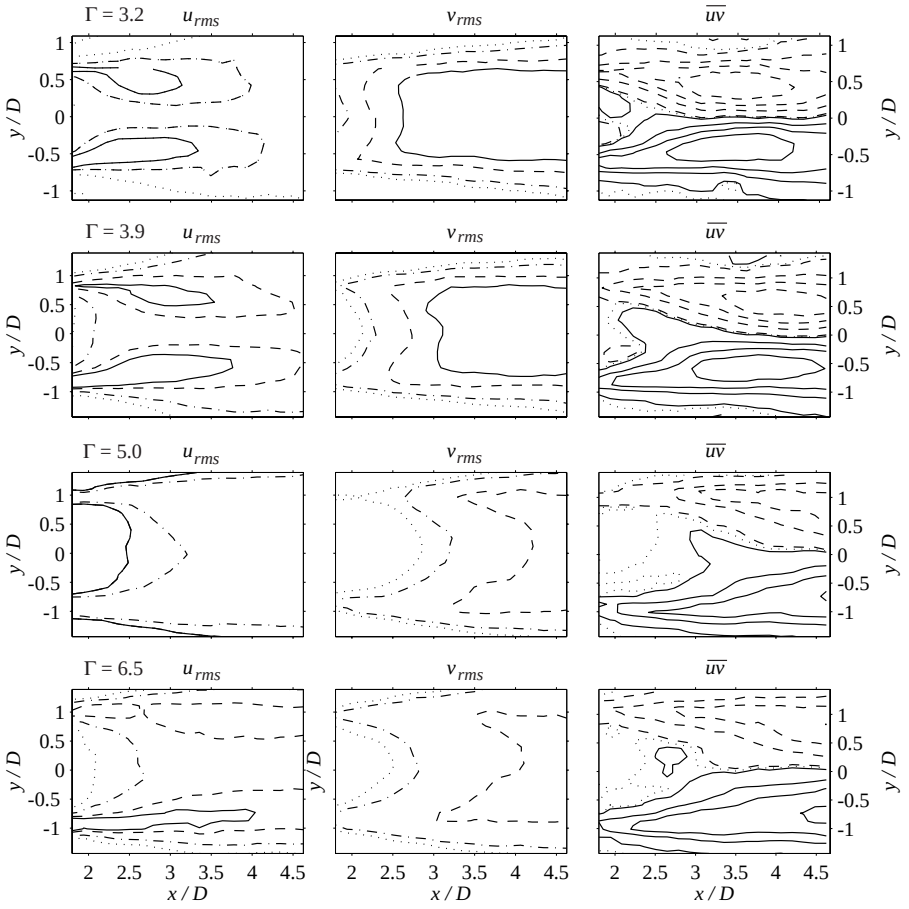

FIGURE 13. For caption see figure 12.

reach their respective maxima far out of the image in the downstream direction and therefore the intersection with $\Gamma = 0$ is not observed in the figure. In figure 14c) the "total energy" E_{uv} is shown in where the energy peaks located at $x/D = 2.65, 3.40$, and 3.75 come from E_u alone.

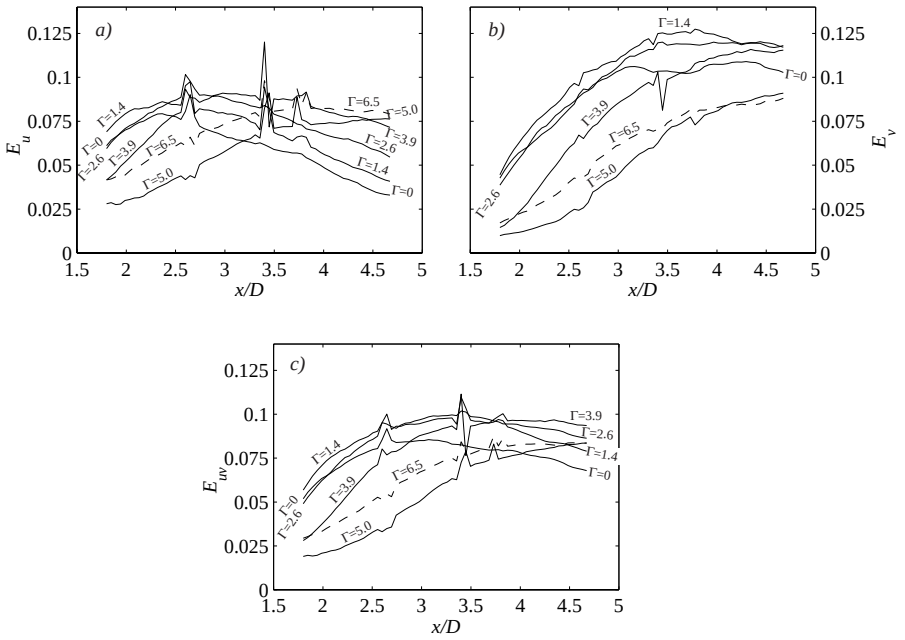

FIGURE 14. Wake energy evolution in the streamwise direction for different blowing rates. a) E_u: the energy of the u-component. b) E_v: the energy of the v-component. c) The total energy $E_{uv} = E_u + E_v$.

3.3. *Suction and blowing*

In figure 15 the x/D-positions of maximum back-flow (white bullets in figures 4-5 & 10-11) and the stagnation point, corresponding to the confluence point of the two stationary vortices, are plotted versus Γ. Both these quantities can be seen as a measure of the vortex formation length. The ratio of the two quantities is fairly constant, implying that the absolute size in the streamwise direction of the recirculating region is not significantly effected by suction nor blowing. However, a compression and an extension of the vortices in the y/D-direction could be observed for high enough suction and blowing rates, respectively (cf. figures 4-5 & 10-11). From figure 15 it is clear that suction reduces the extent of the near-wake, and the maximum back-flow and the stagnation point measures decrease with 60% and 32%, respectively, at $\Gamma = -5$ compared to $\Gamma = 0$. In contrast, blowing increases the near-wake extension with 70% and 66%, respectively, at $\Gamma = 5$ compared to $\Gamma = 0$. These measurements do not contradict the results by Fransson *et al.* (2003), where the vortex formation length was achieved from an averaged photo technique, who

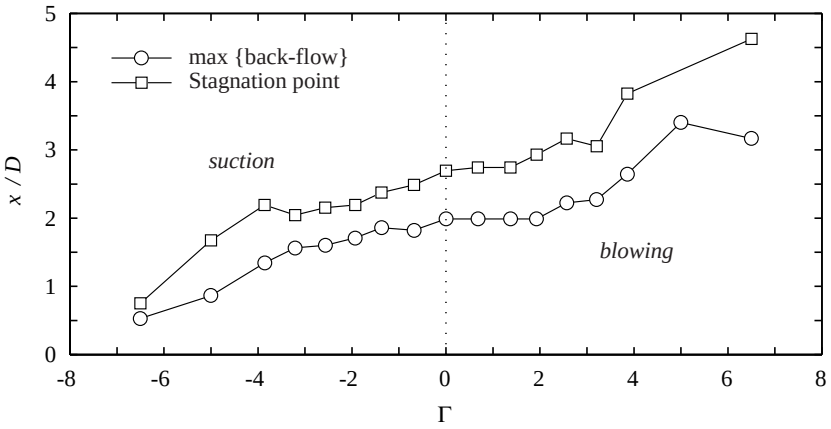

FIGURE 15. The effect of suction and blowing on the near-wake extension. Both the position of maximum back-flow and the stagnation point (or the confluence point of the two stationary vortices) can be seen as a measure of the vortex formation length. The averaged ratio between the two is 1.42.

reported a decrease of 75% and an increase of 150% at Γ-values of -5 and 5, respectively. The choice of measure is sensitive to the relative changes, which is reflected in this analysis of the present two different measures. Furthermore, in Fransson *et al.* (2003) the Reynolds number was two times larger than in the present experiments, and a Reynolds number dependence may be possible.

Figure 16 show the mean streamwise velocity profiles on the centreline behind the cylinder for some chosen ±Γ-values. The dotted lines correspond to the x/D-positions where the energy peaks in figures 8-14 appear. A possible explanation for the appearance of peaks in the y-integrated energy is inflectional instability of the mean velocity profile. In both the suction and the blowing cases (cf. figures 8-14) the energy peak is strongest in E_u, why the streamwise profiles are shown here. The change of the inflection point of the mean velocity profile in figure 16 seems to correspond with the peak strength and position in the energy distribution.

4. Summary

In the present investigation the effect on the wake behind a porous cylinder, subject to continuous suction or blowing through the cylinder surface, has been studied. The Reynolds number was 3700, implying laminar boundary layers around the cylinder with a purely laminar separation.

The effect of suction and blowing of the statistical quantities are easily summarized by saying that suction pulls the wake towards the cylinder and

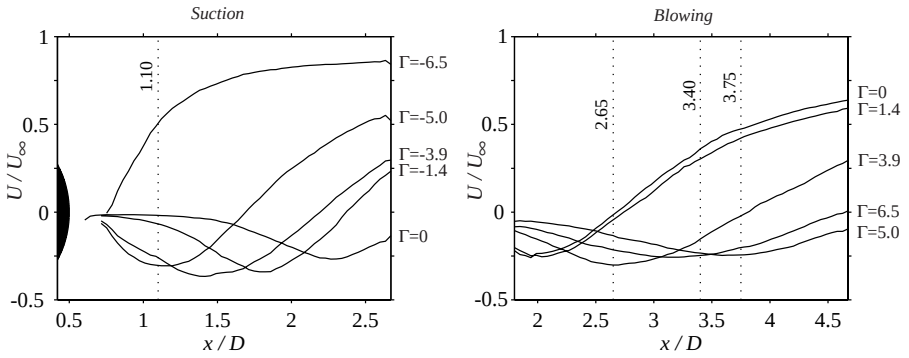

FIGURE 16. Mean streamwise velocity profiles on the centre line behind the cylinder. Left and right figures correspond to suction and blowing, respectively, and the dotted lines show the x/D-positions where the energy peaks in figures 8-14 appear.

blowing pushes it away. Furthermore, the wake width is compressed by suction and enlarged by blowing, which is revealed by inspection of vector velocity fields, and for high enough suction the mean field around the cylinder is not far from a potential flow field.

The vortex formation length is documented by means of two different measures, which in average are related by a factor of 1.4. These are the position of maximum back-flow behind the cylinder and the position where the two stationary vortices (appearing in the mean field) confluence, i.e. the stagnation point in the flow field. The choice of measure has been shown to be sensitive to relative changes, why further analysis is needed in order to define an appropriate measure of the vortex formation length. This measure may be used as a benchmark for numerical simulations, which is the main reason why this has been emphasised in the present investigation.

A tentative explanation of the appearance of energy peaks, at particular x/D-positions, in the integrated streamwise energy over the wake width is that they can be attributed to inflectional instability of the mean streamwise velocity profile.

Further analysis on the present data will be done, where comparison with absolute instability theory and probability density distributions of the vortex sizes will be given attention.

Acknowledgments

The author would like to thank Prof. Henrik Alfredsson for valuable comments and ideas. This work was financed by the Swedith Research Council (VR).

References

Bearman, P. W. 1967 On vortex street wakes. *J. Fluid Mech.* **28**, 625–641.

Buresti, G. 1998 Vortex shedding from bluff bodies. *Wind Effects on Buildings and Structures,* pp. 61–95, Riera & Davenport (eds.), Balkema, Rotterdam.

Chomaz, J. M., Huerre, P. & Redekopp, L. G. 1988 Bifurcations to local and global modes in spatially developing flows. *Phys. Rev. Lett.* **60**, 25–28.

Fransson, J. H. M. & Alfredsson, P. H. 2003 On the disturbance growth in an asymptotic suction boundary layer. *J. Fluid Mech.* **482**, 51–90, **Paper 1**.

Fransson, J. H. M., Konieczny, P. & Alfredsson, P. H. 2003 Flow around a porous cylinder subject to continuous suction or blowing. *J. Fluids Struc.* (Submitted) **Paper 7**.

Gillies, E. A. 1998 Low–dimensional control of the circular cylinder wake. *J. Fluid Mech.* **371**, 157–178.

Glezer, A. & Amitay, M. 2002 Synthetic jets. *Annu. Rev. Fluid Mech.* **34**, 503–529.

Grinstein, F. F., Boris, J. P. & Griffin, O. M. 1991 Passive pressure-drag control in a plane wake. *AIAA J.* **29**, 1436–1442.

Hammond, D. A. & Redekopp, L. G. 1997 Global dynamics of symmetric and asymmetric wakes. *J. Fluid Mech.* **331**, 231–260.

Hannemann, K. & Oertel, H. 1989 Numerical simulation of the absolutely and convectively unstable wake. *J. Fluid Mech.* **199**, 55–88.

Huerre, P. & Monkewitz, P. A. 1990 Local and global instabilities in spatially developing flows. *Annu. Rev. Fluid Mech.* **22**, 473–537.

Hurley, D. G. & Thwaites, M. A. 1951 An experimental investigation of the boundary layer on a porous circular cylinder. *Brit. Aero. Res. Council,* Rep. and Memo. 2829.

Lindgren, B. 2002 Flow facility design and experimental studies of wall-bounded turbulent shear-flows. PhD thesis, KTH, Stockholm, TRITA-MEK Tech. Rep. 2002:16.

Mathelin, L., Bataille, F. & Lallemand, A. 2001*a* Near wake of a circular cylinder submitted to blowing - I Boundary layers evolution. *Int. J. Heat Mass Transf.* **44**, 3701–3708.

Mathelin, L., Bataille, F. & Lallemand, A. 2001*b* Near wake of a circular

cylinder submitted to blowing - II Impact on the dynamics. *Int. J. Heat Mass Transf.* **44**, 3709–3719.

Monkewitz, P. A. 1988 The absolute and convective nature of instability in two–dimensional wakes at low Reynolds numbers. *Phys. Fluids* **31**, 999–1006.

Norberg, C. 2003 Fluctuating lift on a circular cylinder: review and new measurements. *J. Fluids Struc.* **17**, 57–96.

Pankhurst, R. C. & Thwaites, M. A. 1950 Experiments on the flow past a porous circular cylinder fitted with a Thwaites flat. *Brit. Aero. Res. Council,* Rep. and Memo. 2787.

Park, D. S., Ladd, D. M. & Hendricks, E. W. 1994 Feedback control of von Karman vortex shedding behind a circular cylinder at low Reynolds numbers. *Phys. Fluids* **6**, 2390–2405.

Provansal, M., Mathis, C. & Boyer, L. 1987 Benard-von Karman instability: transient and forced regimes. *J. Fluid Mech.* **182**, 1–22.

Roshko, A. 1955 On the wake and drag of bluff bodies. *J. Aeronaut. Sci.* **22**, 124–132.

Roshko, A. 1961 Experiments on the flow past a circular cylinder at very high Reynolds number. *J. Fluid Mech.* **10**, 345–356.

Roussopoulos, K. 1993 Feedback control of vortex shedding at low Reynolds number. *J. Fluid Mech.* **248**, 267–296.

Shiels, D. & Leonard, A. 2001 Investigation of a drag reduction on a circular cylinder in rotary oscillation. *J. Fluid Mech.* **431**, 297–322.

Tokumaru, P. T. & Dimotakis, P. E. 1991 Rotary oscillation control of a cylinder wake. *J. Fluid Mech.* **224**, 77–90.

Williamson, C. H. K. 1996 Vortex dynamics in the cylinder wake. *Annu. Rev. Fluid Mech.* **28**, 477–539.

Wood, C. J. 1967 Visualization of an incompressible wake with base bleed. *J. Fluid Mech.* **29**, 259–272.

Zdravkovich, M. M. 1997 *Flow around circular cylinders, Vol 1: Fundamentals*. Oxford University Press.

Zdravkovich, M. M. 2003 *Flow around circular cylinders, Vol 2: Applications*. Oxford University Press.

Paper 9

9

Errors in hot-wire X-probe measurements induced by unsteady velocity gradients

By Jens H. M. Fransson and K. Johan A. Westin

KTH Mechanics, SE-100 44 Stockholm, Sweden

Published in *Exp. Fluids* **32**, 413–415, 2002

Errors in hot-wire X-probe measurements due to unsteady velocity gradients are investigated by a comparison of hot-wire and LDV-measurements (Laser Doppler Velocimetry). The studied flow case is a laminar boundary layer subjected to high levels of free stream turbulence, and the hot-wire data shows a local maximum in the wall-normal fluctuation velocity inside the boundary layer. The observed maximum is in agreement with existing hot-wire data, but in conflict with the present LDV-measurements as well as existing results from numerical simulations. An explanation to the measurement error is suggested in the paper.

1. Introduction

It is well known that strong spatial mean velocity gradients can distort measurements obtained by hot-wire X-probes if the size of the probe can not be considered small as compared to the flow structures in question. In some cases correction procedures can be applied with success, for example Cutler & Bradshaw (1991) applied a linear correction procedure to correct X-probe measurements of the spanwise velocity component in a boundary layer[1]. In a recent paper by Talamelli *et al.* (2000) errors observed when measuring the wall-normal component in a boundary layer was thoroughly investigated using a special probe which allowed a continuous variation of the relative displacement of the two wires of the probe. Both first and second order correction terms could be estimated, and successful corrections of the mean normal velocity ($\overline{V}$) as well as the turbulent shear stress ($\overline{uv}$) were shown.

The free stream turbulence (FST) induces unsteady streaky structures of high and low streamwise velocity inside the boundary layer (for more details, see e.g. Westin 1997; Matsubara & Alfredsson 2001). This can be observed as a large amplitude low-frequency fluctuation primarily in the streamwise component (see figure 1). However, most available measurements of the wall-normal

[1] In the present paper the streamwise, wall-normal and spanwise directions are denoted by x, y and z, and the corresponding velocities with U, V and W.

fluctuations (Arnal & Juillen 1978; Roach & Brierley 1992; Westin 1997), which are all obtained using X-wire probes, also reveal a local maximum in v_{rms} inside the boundary layer. This is in contradiction to both large eddy and direct numerical simulations (Voke & Yang 1995; Rai & Moin 1991; Jacobs & Durbin 2001), which have not been able to reproduce this peak in v_{rms}. In addition to that, theoretical studies based on the concept of nonmodal disturbance growth (often denoted transient growth, see e.g. Andersson *et al.* 1999) do not predict any spatial amplification of the wall-normal disturbance energy.

To clarify this discrepancy between experimental results and computations it was decided to compare measurements with hot-wire anemometry (HWA) and Laser Doppler Velocimetry (LDV) in a laminar boundary layer subjected to FST (sometimes denoted a pseudo-laminar boundary layer). In addition to experimental results, an explanation to the observed measurement error is suggested.

2. Experimental and evaluation techniques

The experiments were carried out in the MTL wind tunnel at KTH. The results shown in figure 1, which in the following will be denoted the "old" data, were measured on a 4 m long flat plate with a turbulence level of 1.5% at the leading edge. For more details about the experimental set-up and the grid generated turbulence, see Westin *et al.* (1994). The so-called "new" results shown in figure 2 were obtained on a slightly different 6 m long flat plate, but otherwise the two experimental set-ups were similar.

In the HWA-technique an X-probe was used to measure the streamwise and wall-normal velocity components operating in CTA mode. The probe was made of 2.5 μm platinum wires and had a measurement volume less than 1 mm^3 (side length $\leq$ 1 mm) for the new data (figure 2). The old data (figure 1) was taken with a smaller probe with a wire separation of 0.5 mm. The calibration was done at different angles and flow velocities, and two fifth-order polynomials were fitted to the calibration data, giving U and V as functions of the obtained voltage pair (E_1,E_2).

In the LDV-measurements an integrated one dimensional laser-optics unit was used, including a 10 mW He-Ne laser of wavelength 632.8 nm. A beam expander was mounted to the lens to reduce the measurement volume, which can be approximated as an ellipsoid with axes lengths 0.14 mm and 2.4 mm. To be able to measure the wall-normal component close to the wall the probe has to be inclined. This causes an error which in the present case was estimated to be less than 0.2%. To provide a uniform seeding smoke from a smoke generator was injected downstream of the test section in the closed-loop wind tunnel.

The LDV-data presented are residence time weighted, i.e. each particle is weighted with its transit time. The LDV-unit only allows fixed bandwidths to be changed by the user, and the choice influences the background noise level

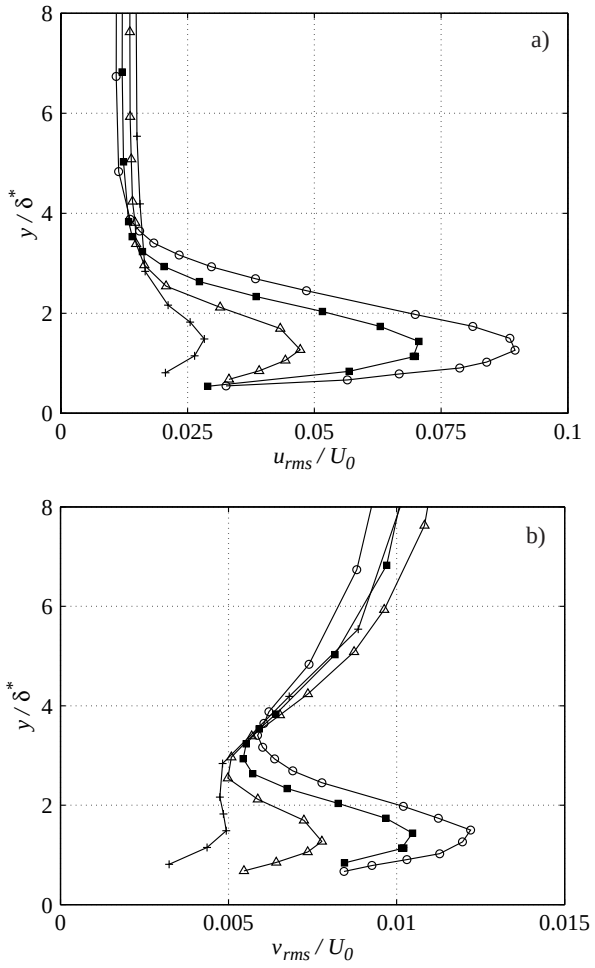

FIGURE 1. Profiles of a) u_{rms} and b) v_{rms} in the pseudo-laminar boundary layer at $Tu = 1.5\%$ ($U_0 = 8$ m/s). The different x-positions are 100 mm ($R = 400$) (+), 250 mm ($R = 630$) (△), 500 mm ($R = 890$) (■) and 800 mm ($R = 1120$) (○).

in the measured data. In the present flow case with a dominant mean flow direction along x it was possible to choose a more narrow (and better suited) bandwidth for the wall-normal component than for the streamwise one. In the present study two different bandwidths were used for the measurements of the streamwise component. However, to compensate for the background noise the u_{rms}-profile is corrected by subtracting an appropriate constant noise level

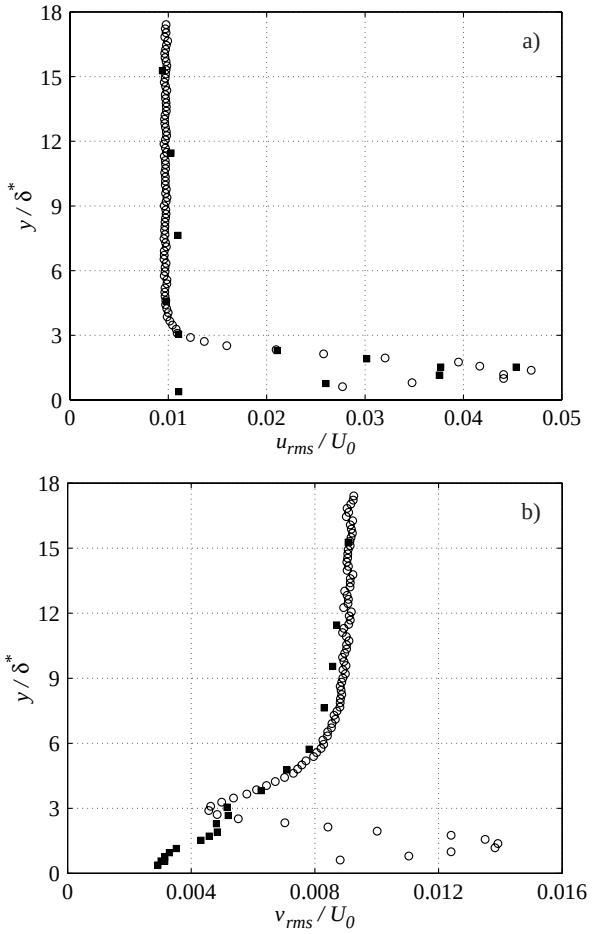

FIGURE 2. Profiles of a) u_{rms} and b) v_{rms} in the pseudo-laminar boundary layer at $Tu = 1.5\%$ ($U_0 = 4.5$ m/s) and x = 700 mm ($R = 790$). ∘ HWA-data; ■ LDV-data.

which was chosen in order to fit the free stream values to the corresponding HWA-data.

3. Results and discussion

Due to the presence of the wall the V-fluctuations in the free stream are damped when approaching the wall (see e.g. Hunt & Graham 1978). In figure 1b and 2b the damping can be seen also outside the boundary layer edge (which is located at $y/\delta^* \approx 3$). Inside the boundary layer both the HWA and the LDV predict a large amplitude peak in the u_{rms}, and after the correction of the LDV-data to

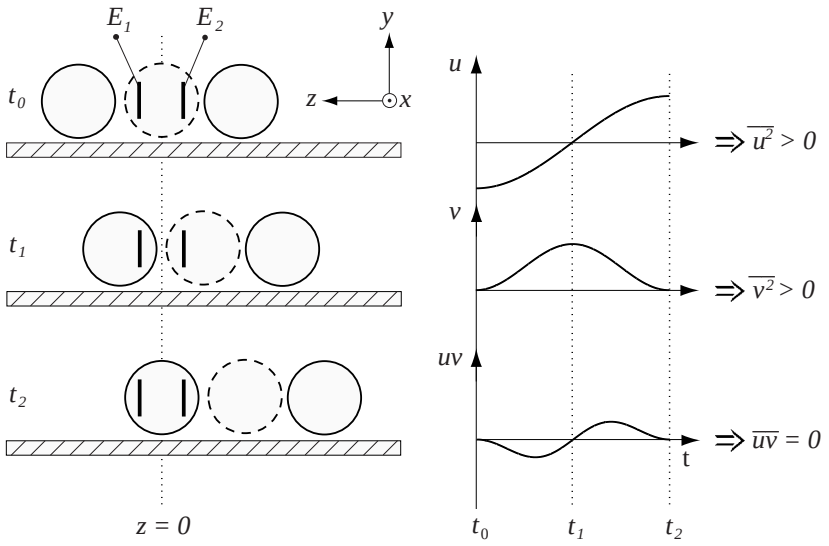

FIGURE 3. Illustration of the moving high- and low-velocity streak in relation to the stationary X-probe. By assuming a positive wall-normal velocity component ($E_1 > E_2$) the effect of the moving streaks on the Reynolds stresses is illustrated.

obtain a correct rms-level in the free stream both methods showed a maximum amplitude inside the boundary layer of approximately 4.5% (see figure 2a).

When comparing the v_{rms}-profiles the two measurements agree quite well in the damped region outside the boundary layer edge, but closer to the wall it is evident that the HWA-data generates a virtual maximum. The LDV-data is damped all the way down to the wall, which is in agreement with DNS-data (see e.g. Rai & Moin 1991; Jacobs & Durbin 2001). It is also interesting to note that the relative magnitude of the erroneous peak in $v_{rms}$is larger in figure 2b than in 1b, i.e. the larger probe size in the new measurements results in larger errors.

The explanation to the virtual maximum in v_{rms} obtained with HWA can be understood if one considers that the disturbances in the pseudo-laminar boundary layer is dominated by longitudinal streaks with high and low streamwise velocity. This is illustrated with solid and dashed circles in figure 3. Since the V-component is obtained from the voltage difference between the two wires, a spanwise gradient in U will be erroneously detected as a wall-normal component. Depending on the sign of $\partial U/\partial z$ and the direction of the movement of the streaks four different scenarios are possible of which one is shown in figure 3. The outcome of the other three is similar. It can be seen that the off diagonal element $\overline{uv}$ in the Reynolds stress tensor becomes zero, while there are non-zero

contributions to both u_{rms} and v_{rms}. Since in this simplified illustration both v_{rms} and $\overline{uv}$ should be zero, it is clear that the error due to unsteady spanwise gradients primarily will appear in measurements of the wall-normal fluctuation level.

In the present study only laminar boundary layers subjected to FST have been considered, which is a case where the described error becomes clearly visible due to the very small level of wall-normal fluctuations. However, the same gradient effect will distort measurements also in other cases. For example in the near-wall region of a turbulent boundary layer u-velocity streaks are common, and v_{rms}-profiles obtained with HWA in this region are certainly overestimated. The smaller spanwise scales in the turbulent boundary layer as compared to the pseudo-laminar one further enhances the effect of the measurement error.

Acknowledgments

The authors would like to thank Prof. Henrik Alfredsson for valuable comments and ideas.

References

Andersson, P., Berggren, M. & Henningson, D. S. 1999 Optimal disturbances and bypass transition in boundary layers. *Phys. Fluids* **11**, 134–150.

Arnal, D. & Juillen, J. C. 1978 Contribution expérimentale à l'etude de la receptivité d'une couche limite laminaire, à la turbulence de l'écoulement general. ONERA Rapport Technique No 1/5018 AYD.

Cutler, A. D. & Bradshaw, P. 1991 A crossed hot-wire technique for complex turbulent flows. *Exp. Fluids* **12**, 17–22.

Hunt, J. C. R. & Graham, J. M. R. 1978 Free-stream turbulence near plane boundaries. *J. Fluid Mech.* **84**, 209–235.

Jacobs, R. G. & Durbin, P. A. 2001 Simulations of bypass transition. *J. Fluid Mech.* **428**, 185–212.

Matsubara, M. & Alfredsson, P. H. 2001 Disturbance growth in boundary layers subjected to free-stream turbulence. *J. Fluid Mech.* **430**, 149–168.

Rai, M. M. & Moin, P. 1991 Direct numerical simulation of transition and turbulence in a spatially evolving boundary layer. *AIAA-91-1607-CP* .

Roach, P. E. & Brierley, D. H. 1992 *The influence of a turbulent freestream on zero pressure gradient transitional boundary layer development.* Part I: Test cases T3A and T3B, In Numerical Simulation of Unsteady Flows and Transition to Turbulence.

Talamelli, A., Westin, K. J. A. & Alfredsson, P. H. 2000 An experimental investigation of the response of hot-wire X-probes in shear flows. *Exp. Fluids* **28**, 425–435.

Voke, P. R. & Yang, Z. 1995 Numerical study of bypass transition. *Phys. Fluids* **7**, 2256–2264.

Westin, J. 1997 Laminar-turbulent boundary layer transition influenced by free stream turbulence. PhD thesis, KTH, Stockholm, TRITA-MEK Tech. Rep. 1997:10.

Westin, K. J. A., Boiko, A. V., B. G. B. Klingmann, V. V. K. & Alfredsson, P. H. 1994 Experiments in a boundary layer subjected to freestream turbulence. part i. boundary layer structure and receptivity. *J. Fluid Mech.* **281**, 193–218.

Paper 10

10

Leading edge design process using a commercial flow solver

By Jens H. M. Fransson

KTH Mechanics, SE-100 44 Stockholm, Sweden

In the present work the design process of an asymmetric leading edge, for laminar stability measurements in a flat plate boundary layer, is reported. It is well known that a symmetric leading edge gives rise to an undesired pressure suction peak, which effects the receptivity process and in turn the stability characteristics of the flow. The aim of the study is to design and construct a leading edge with a short adverse pressure gradient region and without the suction peak. Wind tunnel testing of the leading edge shows a successful design and is here verified by means of measured mean velocity profiles and the pressure coefficient distribution.

1. Introduction

The ideal flat plate does not have any leading edge, it is simply an infinitely thin plate with a zero pressure gradient everywhere. When placing an obstacle in a flow the fluid will accelerate around it causing the static pressure to decrease. First when the fluid is allowed to decelerate the pressure can start to recover. In figure 1 a symmetric "leading edge" generated by a two-dimensional source and a rectilinear flow (known as *half body*) with potential flow theory is shown with a solid line. The velocities are easily calculated for the above problem (see e.g. Massey 1998) from where the pressures may be achieved via Bernouilli's equation. The pressure coefficient (C_p) possessing an exact solution for this half body then becomes

$$C_p = \frac{\sin 2\theta}{\theta} - \frac{\sin^2 \theta}{\theta^2},$$

given in polar coordinates ($\theta = 0$ is the stagnation point), and is also plotted with a dashed line in figure 1. At the stagnation point ($x/L = 0$) C_p is equal to unity according to its definition. Thereafter C_p is reduced as long as the fluid is accelerating around the nose, but as soon as the curvature starts to decrease

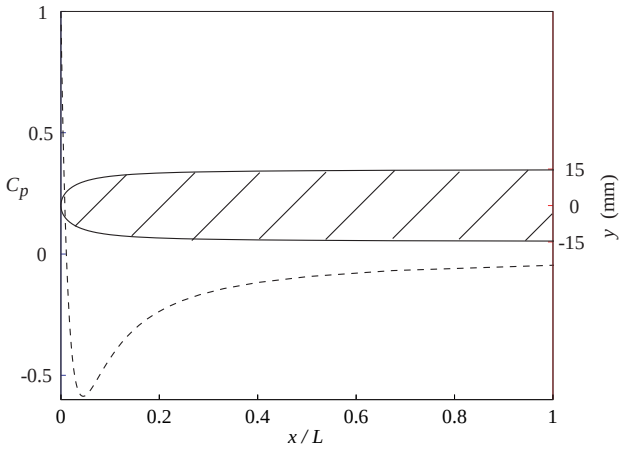

FIGURE 1. Symmetrical leading edge generated by a 2D source in a uniform velocity field with potential flow theory (L=0.215 m).

the pressure starts to recover. This minimum of C_p is the well known suction peak giving rise to a local negative pressure gradient followed by a positive one.

During the last decade several laminar to turbulent transition scenarios have been studied in the MTL wind tunnel at KTH Mechanics. Klingmann *et al.* (1993) was the first study and dealt with Tollmien-Schlichting wave instability in a flat plate boundary layer. That investigation ended the discussion whether the disagreement between modal theory and experiments was to be attributed to the parallel approach or if there was some other assumption that had been overlooked. Apart from the low background disturbance level of the MTL wind tunnel one of the reasons for being able to experimentally verify existing linear parallel theory was the design of an asymmetric leading edge. After this investigation in 1993 the plate together with the leading edge has been used successfully in a number of investigations (see e.g. Matsubara & Alfredsson 2001; Fransson *et al.* 2003*b*,*a*).

There are not many studies on asymmetric leading edges found in the literature, but receptivity studies on symmetric, both elliptic and super elliptic, leading edges have been carried out. Saric *et al.* (2002) discuss the leading-edge effects and mention that even small discontinuities in the juncture between the leading edge and the flat plate can effect the stability properties of the flow. They also summarize some works on the effect of the receptivity coefficient for different symmetric leading edge geometries. Bake *et al.* (2002) studied both experimentally and theoretically the effect of localized surface vibrations in zero and favourable pressure gradient boundary layers . Both boundary layers

were found to be more receptive to three-dimensional perturbations than to two-dimensional ones. Further, the favourable pressure gradient was found to enhance the vibration receptivity amplitudes in the range of parameters studied, and the effect increased with growing spanwise wavenumber.

The large pressure gradient prevents the evolution of a Blasius profile in this region and effects the stability characteristics of the boundary layer flow, as discussed by Klingmann *et al.* (1993). In their investigation the importance of the leading edge design was highlighted and it was shown that an asymmetric leading edge together with a trailing edge flap to adjust the stagnation line can reduce the influence that a leading edge really has on the flow.

The asymmetric leading edge presented here is a removable part from the accompanying flat plate and is 260 mm long, 30 mm thick, and 1200 mm wide. It was specially designed for the experimental set-up reported in Fransson (2001) (later published by Fransson & Alfredsson 2003), and resulted in a relatively short pressure gradient region without any suction peak at the leading edge. The leading edge is described analytically by a parameter based polynomial and a commercial flow solver was used in the design process with the criteria to minimize the pressure gradient region and to eliminate the pressure suction peak on the upper side of the plate. The leading edge was tested in a wind tunnel and the pressure coefficient distribution was found to be within ± 0.01 40 mm downstream of the leading edge. Furthermore, the wall-normal distribution of the mean velocity measured as close as 100 mm from the leading edge was very close to the Blasius profile, which shows that the present design of the leading edge (thickness = 30 mm) was successful. The performance of the previously reported asymmetric leading edge by Klingmann *et al.* (1993) was used as a challenge in the present design process, even though there was a criterion on a 58% thicker leading edge compared to that one.

2. Flow calculations

Navier-Stokes equations were solved with the commercial flow solver CFX 4.2 in the design process of the leading edge. CFX uses a conservative finite-difference method as discretisation and the equations are solved in the fixed Cartesian directions on a non-staggered grid. The test section of the MTL wind tunnel, i.e. the ceiling and the floor of the test section, was simulated in CFX together with the plate. Since the plate is not positioned in the centre of the test-section the ceiling (upper wall) and floor (lower wall) exert an influence on the pressure distribution which can not be neglected. Furthermore, the tuning of the stagnation point at the leading edge could be done by simulating the effect of a trailing flap by changing the outflow ratio between the upper (I) and lower (II) outlet (cf. figure 3). In this way the full length of the plate does not need to be simulated and the computational box can be reduced. For the present calculations the computational box, consisting of 18500 mesh points, was divided into 6 different computational blocks in order to achieve a well

resolved region around the leading edge with a smooth mesh transfer from one block to another.

Two cubic Bézier-curves connected at the nose tip were used to describe the upper and the lower sides of the leading edge. A cubic Bézier-curve is a parameter based polynomial consisting of two interpolation points ($[\bar{p}_1, \bar{p}_2]$ and $[\bar{p}_2, \bar{p}_3]$ for the lower and upper parts, respectively) and two steering points ($[\bar{b}_l, \bar{c}_l]$ and $[\bar{b}_u, \bar{c}_u]$ for the lower and upper parts, respectively). The interpolation points are shown in figure 2. In the connection point between the upper and lower curves the two curves were forced to have the same first derivate (expressed by the $\bar{K}_{2l}$ and $\bar{K}_{1u}$ vectors) in order to make the transition smooth.

A systematic parameter study was performed by applying different total areas (or weights) of the leading edge. The varying parameters are nose position ($\bar{p}_2$), starting points of curvature on lower and upper side ($\bar{p}_1$ and $\bar{p}_3$ respectively), and the steering points ($2\times\bar{b}$ and $2\times\bar{c}$), i.e. totally 7 parameters. First an area (or weight) of the leading edge was chosen and then the steering points were varied for different $\bar{p}$-vectors, thereafter the total area (weight) was changed and the procedure was repeated.

The result of the extensive and systematic parameter study, performed in order to minimize the pressure gradient region, is shown below with the parameters of the final shape of the leading edge (lower ($_l$) and upper ($_u$) part)

$$\begin{aligned} \bar{r}_l &= (1-t)^3\bar{p}_1 + 3t(1-t)^2\bar{b}_l + 3t^2(1-t)\bar{c}_l + t^3\bar{p}_2, \quad 0 \le t \le 1 \\ \bar{r}_u &= (1-t)^3\bar{p}_2 + 3t(1-t)^2\bar{b}_u + 3t^2(1-t)\bar{c}_u + t^3\bar{p}_3, \quad 0 \le t \le 1 \end{aligned}$$

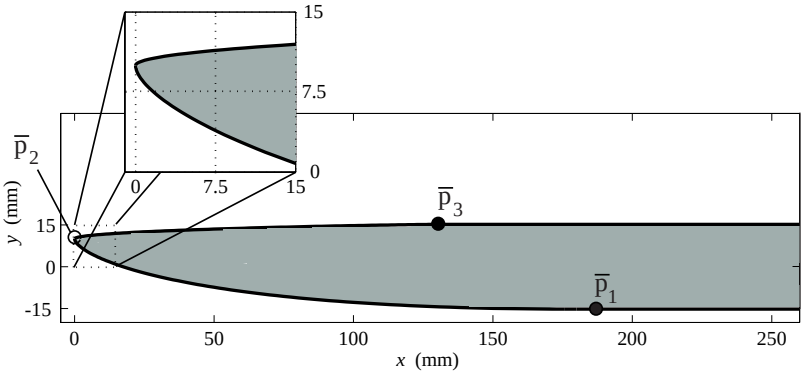

FIGURE 2. Final shape of the leading edge. The profile is described by the Bézier curves $\bar{r}_l$ and $\bar{r}_u$ given in the text.

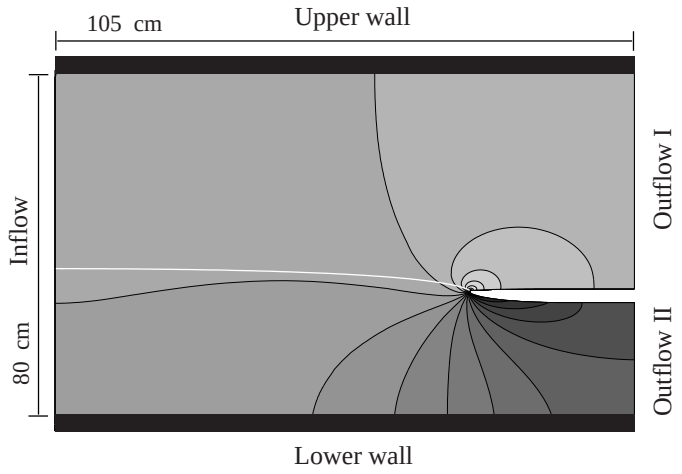

FIGURE 3. View of the computational domain. The filled contour plot shows the pressure distribution in this particular run. The white line denotes the stagnation streamline.

$$\begin{aligned} \bar{b}_l &= \bar{p}_1 + \alpha_l \bar{K}_{1l}; \quad & \bar{b}_u &= \bar{p}_2 + \alpha_u \bar{K}_{1u}; \\ \bar{c}_l &= \bar{p}_2 - \gamma_l \bar{K}_{2l}; \quad & \bar{c}_u &= \bar{p}_3 - \gamma_u \bar{K}_{2u}; \end{aligned}$$

$$\bar{p}_1 = [0.18 \;\; -0.015]; \qquad \bar{p}_2 = [0 \;\; 0.01]; \qquad \bar{p}_3 = [0.13 \;\; 0.015];$$

$$\begin{aligned} \bar{K}_{1l} &= [\text{-}1 \quad 0]; \quad \bar{K}_{2l} = [0 \quad 1]; \quad \alpha_l = 0.15; \quad \gamma_l = 0.0046; \\ \bar{K}_{1u} &= [0 \quad 1]; \quad \bar{K}_{2u} = [1 \quad 0]; \quad \alpha_u = 0.0033; \quad \gamma_u = 0.0110; \end{aligned}$$

and is plotted in figure 2. α and γ (above) are positive numbers representing the "strength" of the steering points and gives the actual steering points for fixed $\bar{p}$-vectors.

In figure 3 a view of the flow domain and geometry in the computational box is shown. The filled contour plot represents the pressure distribution for a particular run and the white solid line shows the stagnation streamline. A homogeneous velocity of 5 m/s was used as inlet condition in all runs, on the walls the 'no slip' condition was used, and the outlet conditions was set by specifying the massflow ratio between outflow (I) and (II).

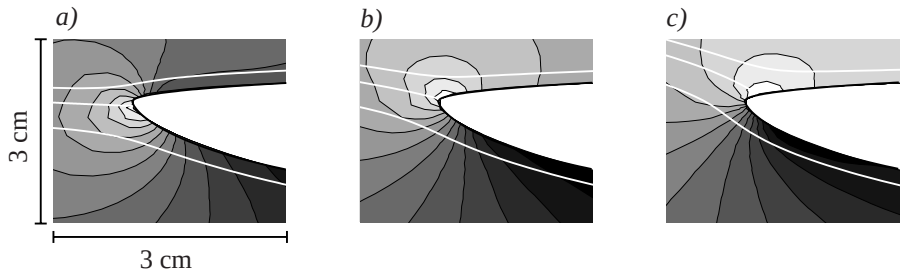

FIGURE 4. Illustration of the effect upon the stagnation point when the massflow below the plate is increased 2.5% in each figure from a) to c).

In figure 4 the effect upon the stagnation point is illustrated when increasing the massflow below the plate with 2.5% in each figure from a) to c). The 2.5% of massflow change corresponds approximately to a flap angle change of 1^{o} of a one meter long flap. The filled contours show the pressure distribution with low and high pressures as light and dark colors, respectively. The three white lines in figures 4a)-c) correspond to representative streamlines under and above the stagnation streamline, i.e the middle streamline.

3. Experimental testing

In figure 5 the experimental pressure distribution along the leading edge is shown. The pressure coefficient (C_p) was calculated from the velocity, obtained from hot-wire measurements, using Bernouilli's equation. The velocity used

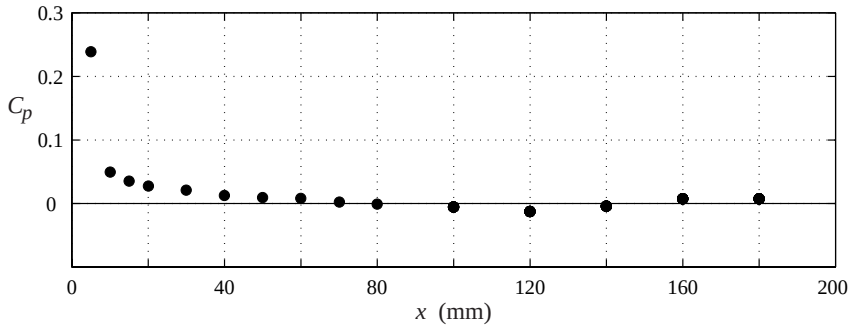

FIGURE 5. Pressure distribution close to the leading edge calculated from hot-wire data by applying Bernoulli's equation (see text for comments).

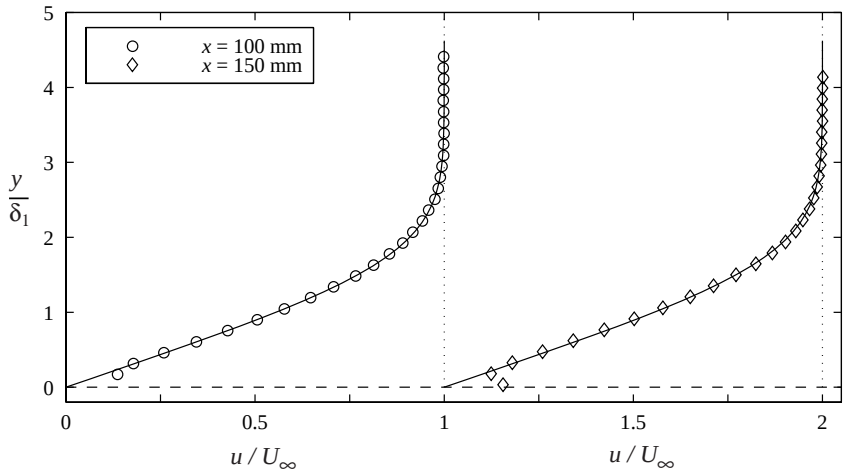

FIGURE 6. Velocity profiles measured relatively close to the leading edge. Solid line is the Blasius profile and the markers denote measured profiles. The corresponding displacement thicknesses for x=100 and 150 mm are δ_1=0.91 and 1.14 mm, respectively.

for this calculation is the velocity just outside the boundary layer edge and it has been obtained by traversing the probe through the boundary layer and then the position with a subsequent negligible velocity change is chosen. The non-dimensionalized pressure distribution is found to be within ±0.01 downstream of x = 40 mm, which is judged to be very good for a plate of this thickness (= 30 mm).

Another check of the flow around the leading edge is how Blasius-like the flow is close to the leading edge. In figure 6 two profiles are plotted at x=100 and 150 mm, and the corresponding measured displacement thicknesses (δ_1) are 0.91 and 1.14 mm, respectively. The measured displacement thicknesses are within 3% and 1% of the theoretical Blasius values, respectively, which correspond to virtual origins at x_{virt}= 6.78 and 3.71 mm, respectively.

4. Summary

For stability and transition wind tunnel studies a well designed and constructed leading edge is crucial for the outcome of the experiments, and the thicker the plate is the more important is obviously the design. For controlled transition experiments there is a need to eliminate as many external and internal disturbance sources as possible that take part in the receptivity process. In this

context external disturbances are attributed to for instance free stream turbulence or sound waves and internal disturbances are connected to surface roughness, vibrations, or the geometry design (such as the leading edge). Spending work on the leading edge design is a good investment, since it can provide long series of experiments with reliable and controlled data without any pressure suction peak effect. This is of particular importance in Tollmien-Schlichting wave measurements.

In the present paper a method is outlined for the design work of an asymmetric leading edge. The quality of the design and construction work is verified successfully by wind tunnel tests, and are presented in the paper. Furthermore, this design has already been used in a number of studies in connection with a porous suction plate and is reported in e.g. Fransson (2001), Fransson & Westin (2002), Fransson & Alfredsson (2003), and Yoshioka *et al.* (2003).

Acknowledgments

The author would like to thank Dr. Ola Widlund for his ideas and comments on the practical use of CFX and Prof. Henrik Alfredsson for valuable comments on the manuscript. Marcus Gällstedt in the KTH Mechanics workshop is acknowledged for manufacturing the leading edge. The work has been financially supported by The Swedish Research Council (VR) and is gratefully acknowledged.

References

Bake, S., Ivanov, A. V., Fernholz, H. H., Neemann, K. & Kachanov, Y. S. 2002 Receptivity of boundary layers to three-dimensional disturbances. *Eur. J. Mech. B/Fluids* **21**, 29–48.

Fransson, J. H. M. 2001 Investigations of the asymptotic suction boundary layer. TRITA-MEK Tech. Rep. 2001:11. Licentiate Thesis, KTH, Stockholm.

Fransson, J. H. M. & Alfredsson, P. H. 2003 On the disturbance growth in an asymptotic suction boundary layer. *J. Fluid Mech.* **482**, 51–90, **Paper 1**.

Fransson, J. H. M., Brandt, L., Talamelli, A. & Cossu, C. 2003*a* Steady streaks in a flat plate boundary layer **Paper 6**.

Fransson, J. H. M., Matsubara, M. & Alfredsson, P. H. 2003*b* Transition induced by free stream turbulence **Paper 5**.

Fransson, J. H. M. & Westin, K. J. A. 2002 Errors in hot-wire X-probe measurements induced by unsteady velocity gradients. *Exp. Fluids* **32**, 413–415, **Paper 9**.

Klingmann, R. G. B., Boiko, A. V., Westin, K. J. A., Kozlov, V. V. & Alfredsson, P. H. 1993 Experiments on the stability of Tollmien-Schlichting waves. *Eur. J. Mech., B/Fluids* **12**, 493–514.

Massey, B. 1998 *Mechanics of fluids*, 7th edn. Stanley Thornes, Cheltenham, U.K.

Matsubara, M. & Alfredsson, P. H. 2001 Disturbance growth in boundary layers subjected to free-stream turbulence. *J. Fluid Mech.* **430**, 149–168.

Saric, W. S., Reed, H. L. & Kerschen, E. J. 2002 Boundary-layer receptivity to freestream disturbances. *Ann. Rev. Fluid Mech.* **34**, 291–319.

Yoshioka, S., Fransson, J. H. M. & Alfredsson, P. H. 2003 Free stream turbulence induced disturbances in boundary layers with wall suction. (Submitted for publication) **Paper 4**.